Rivista Internazionale Ufficiale del
Gruppo Italiano Frattura

Anno VII
Numero 24
Aprile 2013

ISSN 1971-8993

Gruppo Italiano Frattura

FRATTURA ED INTEGRITÀ STRUTTURALE

The International Journal of the Italian Group of Fracture

igf

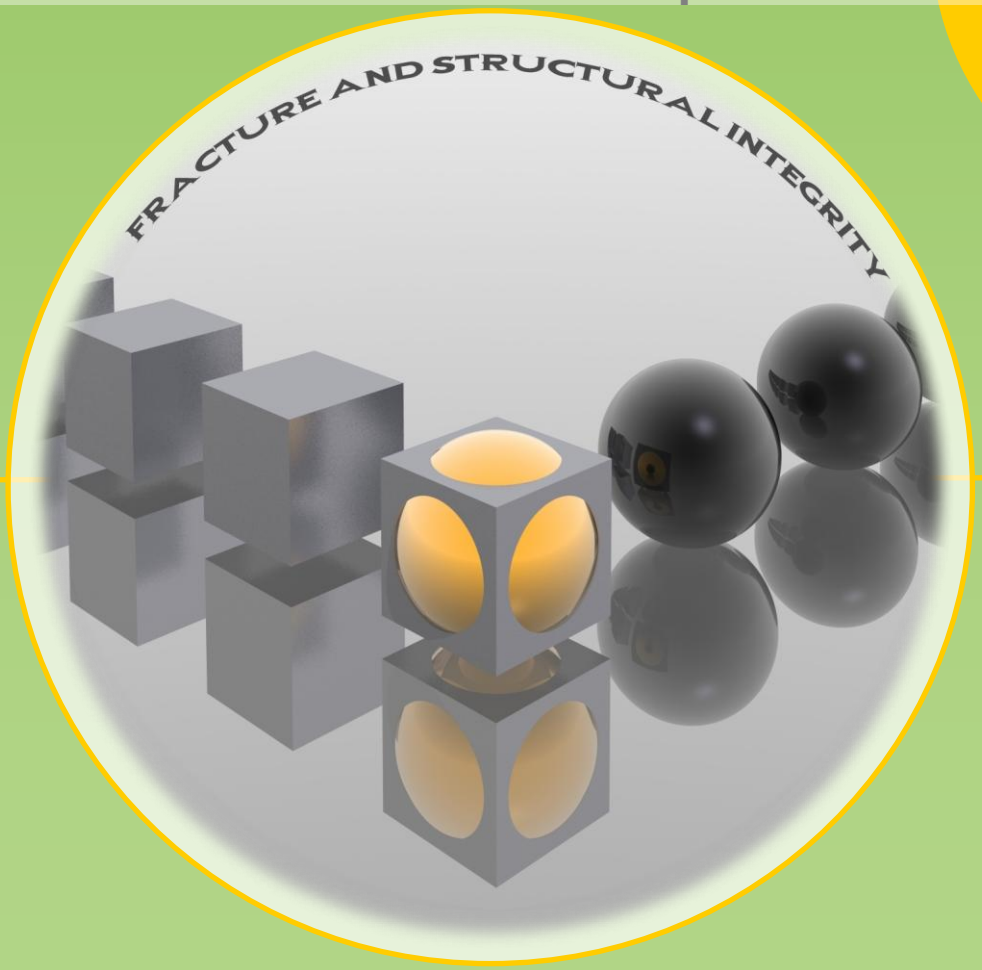

www.gruppofrattura.it

Sommario

Descrizione e scopi

Frattura ed Integrità Strutturale è la rivista ufficiale del *Gruppo Italiano Frattura*. E' una rivista open-access pubblicata on-line con periodicità trimestrale (luglio, ottobre, gennaio, aprile).
Frattura ed Integrità Strutturale riguarda l'ampio settore dell'integrità strutturale, basato sulla meccanica della fatica e della frattura, per la valutazione dell'affidabilità e dell'efficacia di componenti strutturali. Scopo della rivista è la promozione di lavori e ricerche sui fenomeni di frattura, nonché lo sviluppo di nuovi materiali e di nuovi standard per la valutazione dell'integrità strutturale. La rivista ha un carattere interdisciplinare e accetta contributi da ingegneri, metallurgisti, scienziati dei materiali, fisici, chimici e matematici.

Contributi

Frattura ed Integrità Strutturale si prefigge la rapida disseminazione di contributi originali di natura analitica, numerica e/o sperimentale riguardanti la meccanica della frattura e l'integrità strutturale. Si accettano lavori di ricerca che contribuiscano a migliorare la conoscenza del comportamento a frattura di materiali convenzionali ed innovativi. Note tecniche, lettere brevi e recensioni possono essere anche accettati in base alla loro qualità. L'*Editorial Advisory Board* sollecita anche la pubblicazione di numeri speciali contenenti articoli estesi presentati in occasione di conferenze e simposia tematici.

Istruzioni per l'invio dei manoscritti

I manoscritti devono essere scritti in formato word senza necessità di utilizzare un particolare stile e devono essere inviati all'indirizzo iacoviello@unicas.it. Il lavoro proposto può essere in lingua Italiana (con riassunto in inglese di almeno 1000 parole e didascalie bilingue) o Inglese. La conferma della ricezione avverrà entro 48 ore. Il processo di referaggio e pubblicazione on-line si concluderà entro tre mesi dal primo invio.

Journal description and aims

Frattura ed Integrità Strutturale (Fracture and Structural Integrity) is the official Journal of the Italian Group of Fracture. It is an open-access Journal published on-line every three months (July, October, January, April).
Frattura ed Integrità Strutturale encompasses the broad topic of structural integrity, which is based on the mechanics of fatigue and fracture, and is concerned with the reliability and effectiveness of structural components. The aim of the Journal is to promote works and researches on fracture phenomena, as well as the development of new materials and new standards for structural integrity assessment. The Journal is interdisciplinary and accepts contributions from engineers, metallurgists, materials scientists, physicists, chemists, and mathematicians.

Contributions

Frattura ed Integrità Strutturale is a medium for rapid dissemination of original analytical, numerical and experimental contributions on fracture mechanics and structural integrity. Research works which provide improved understanding of the fracture behaviour of conventional and innovative engineering material systems are welcome. Technical notes, letters and review papers may also be accepted depending on their quality. Special issues containing full-length papers presented during selected conferences or symposia are also solicited by the Editorial Board.

Manuscript submission

Manuscripts have to be written using a standard word file without any specific format and submitted via e-mail to iacoviello@unicas.it. The paper may be written in English or Italian (with an English 1000 words abstract). A confirmation of reception will be sent within 48 hours. The review and the on-line publication process will be concluded within three months from the date of submission.

Publisher

Gruppo Italiano Frattura (IGF)
http://www.gruppofrattura.it
ISSN 1971-8993
Reg. Trib. di Cassino n. 729/07, 30/07/2007

Special issue

Gentilissimo lettore,
il presente numero è prevalentemente dedicato alla prestigiosa Scuola Russa di Meccanica della Frattura. L'obiettivo del numero è quello di offrire un aggiornamento su alcune delle linee di ricerca seguite in questo immenso paese, non tentando nemmeno di essere esaustivi (sarebbe stato necessario un numero certamente ben più corposo), ma cercando di offrire degli spunti di riflessione e, magari, dei riferimenti per possibili collaborazioni.
Il numero è inoltre arricchito da alcuni lavori non legati alla "special issue". Preferiamo mantenere i quattro appuntamenti annuali, conservando la tempistica di pubblicazione dei lavori presentati al di fuori delle special issue (massimo tre mesi dal primo invio). Come nel precedente numero di *Frattura ed Integrità Strutturale*, i lavori appartenenti alla special issue sono quindi contraddistinti da una scritta nella prima pagina in alto a destra.

Infine, qualche informazione riguardante il prossimo Convegno IGF XXII (Roma 1-3 luglio 2013). Il convegno si terrà presso la Facoltà di Ingegneria dell'Università di Roma "Sapienza", nell'Aula del Chiostro (via Eudossiana 18). Al fine di agevolare il processo di indicizzazione, la lingua preferenziale degli atti è l'inglese. Sono comunque accettati anche lavori in italiano, ma con abstract lungo in inglese (almeno 800 parole). Nel sito IGF sono disponibili i template per la preparazione degli atti.
Le prossime scadenze sono:
- 10.04.2013: invio Abstract
- 15.04.2013: accettazione Abstract
- 31.05.2013: invio memorie

Francesco Iacoviello
Presidente IGF
Direttore Frattura ed Integrità Strutturale

Preface

It gives me a great pleasure to present a special issue of Fracture and Structural Integrity devoted to research carried out in the Russian Federation. The history of mechanics and material science has a long tradition in Russia. Mechanics was initiated in 1736 with the work *Mechanica sive motus scientia analytice exposita* by Leonhard Euler, who worked at that time in the St. Petersburg Academy of Sciences. In the 19th century, the development of mechanics in Russia was associated with the names of Gabriel Lamé, Benoit Clapeyron, and Mikhail Ostrogradskii, who were appointed professors at the Institute of the Corps of Railroad Engineers in St. Petersburg. The foundations of modern fracture mechanics were laid down by the prominent Russian/Soviet physicist Abram Fedorovich Ioffe. In 1924, Ioffe and Griffiths, two renowned scientists, independently set forth the idea of the influence of surface cracks on the overall strength of materials.

The establishment of the National Committee on Theoretical and Applied Mechanics in 1956 gave strong impetus to the development of mechanics in Russia. The full member of the USSR Academy of Sciences Nikolai Muskhalishvilli was the first chairman of this Committee. At present, the Committee brings together people from research and educational organizations and individuals with diverse research interests. One of the objectives of the Committee is to expand and develop relations between Russian and foreign scientists.

The Russian National Committee on Theoretical and Applied Mechanics expresses the hope that this Issue will be of interest to the Italian scientific community and will provide a stimulus to new personal contacts and to Russian - Italian scientific cooperation. The Issue contains the latest results of experimental and theoretical studies on deformation and fracture, simulation results, and the results of structural investigation of metals and alloys. Some papers review the development of modern concepts of mesomechanics, destruction incubation time theory, and new models of crack mechanics.

The Issue is not intended to be an exhaustive overview of all major trends of scientific work in Russia. It presents only a small part of studies performed at scientific centers of Moscow, St. Petersburg, Yekaterinburg, Perm, Novosibirsk, Nignii Novgorod and Tomsk. The Issue includes the articles written both by young scientists and experts in fracture mechanics.

We hope that the contributions selected for this Issue will help readers to gain a deeper insight into various aspects of fracture mechanics and structural integrity currently developed in Russia, and we wish them profitable reading.

Irina G. Goryacheva
Professor, Ph.D, DSc, Academician of RAS
President of the Russian National Committee in
Theoretical and Applied Mechanics

Relay-race deformation mechanism during uniaxial tension of cylindrical samples of carbon steel: using digital image correlation technique

T.V. Tretiakova, V.E. Vildeman

Center of Experimental Mechanics, Perm National Research Polytechnic University, 614990, Komsomolsky av., 29, Perm, Russia

ABSTRACT. The work deals with experimental study of macro localization of plastic yielding occurrences of structural carbon steel, research of singularity of deformation wave processes by complex use of contemporary test equipment and high effective digital image correlation method. Evolution of nonuniform axial strain fields on surface of cylindrical samples during uniaxial tension was registered, time dependences were drawn, and a 'relay-race' mechanism of material deformation was found out at the stage of yield plateau forming. Strain concentration ratio was estimated for several material deformation stages.

KEYWORDS. Digital image correlation; Wave effects; Strain localization; Carbon steel.

INTRODUCTION

A great number of scientific literature deals with experimental study issues of plastic strain in solid bodies, specifically, authors repeatedly point out that plastic strain develops nonuniformly both in space (strain localization) and in time (time evolution of localization) [1, 2]. Striking examples of plastic strain localization on macroscopic level are Chernov-Lüders Lines, initiation and evolution of necking effect on postcritical deformation stage [3, 4], and also waves of localized plastic strain.

The aim of this research was experimental investigation of regularities of plastic yielding macro localization for structural steel, study of singularities of wave deformation processes by complex use of contemporary testing equipment and non-contact strain measuring facilities.

MATERIAL AND TEST PROCEDURE

Structural carbon steel 20 (GOST 1050-88) was chosen as the research subject. Mechanical tests on uniaxial tension of solid cylindrical samples (test portion length of 16 mm, sample's diameter of 9.5 mm) were conducted on Instron 8850 universal biaxial servo-hydraulic testing system with constant kinematic loading speed of 2%/min. Non-contact registration and displacement and strain fields review were carried out by three-dimensional Vic-3D digital optical system (Fig. 1). Video-system's software is based on digital image correlation technique (DIC). DIC is a highly effective non-contact, computer-vision-based method for measuring displacement and strain fields on specimen's surface by correlating digital images captured during loading or exploitation process [5].

The digital optical system can be used for problem solving of deformable solid mechanics: experimental investigation of nonuniform strain fields and analysis of failure conditions in bodies with concentrators of different geometry [6, 7], research of inelastic material deformation processes in complex strain-stress conditions, study of displacement and strain fields evolution during crack initiation, damage accumulation and material failure [8–10], etc. The video-system contains

digital monochrome cameras, sample illumination systems, calibration grids, synchronizing hardware for communication with the test system, and specialized software which allows programming of video recording (Vic-Snap) and mathematical treatment of test data (Vic-3D). In Tab. 1 these parameters are shown.

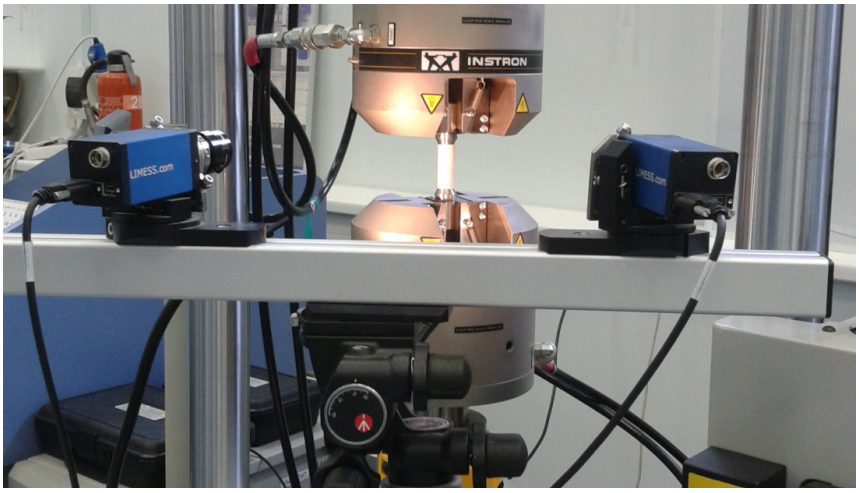

Figure 1: The non-contact three-dimensional digital optical system Vic-3D.

Hardware	2 digital b/w DCP cameras
Resolution	4 Mp
Maximum videotaping speed	15 image/s
Videotaping speed in current tests	0.2 image/s
Software	3D digital image correlation (Vic-3D)
Subset	19 pixels
Step	4 pixels
Correlation criteria	NSSD
Tensor type (strain calculation)	Lagrangian finite strain tensor

Table 1: Technical parameters of strain field registration.

Correlation of digital images was carried out by NSSD criteria (normalized sum of squared difference), which offers the best combination of flexibility and results.

$$\chi^2_{NSSD} = \sum\left(\frac{\sum F_i G_i}{\sum G_i^2} G_i - F_i\right)^2 \tag{1}$$

In the software the Lagrangian finite strain tensor was used for strain field estimation:

$$\varepsilon_{ij} = \frac{1}{2}\left(u_{i,j} + u_{j,i} + u_{k,i}u_{k,j}\right) \tag{2}$$

TEST RESULTS

Tests on uniaxial tension were carried out on 5 solid cylindrical samples. The tensile test diagram for carbon steel is shown in Fig. 2. The load-extension curve includes yield drop (II) and yield plateau (III–V) forming stages, and also an extensive post-critical deformation stage (VII–VIII).

Evolution of nonuniform axial strain fields for marked dots (I–VIII, Fig. 2), calculated by using the Vic-3D system, is illustrated in Fig. 3. At the elastoplastic deformation stage at the moment of transition through an upper yield point (point

II), initiation and evolution of axial strain wave front (points III–V) was captured lengthwise the sample axis. Plastic strain is becoming macro localized during further loading at the material hardening stage (points VI, VII), which causes the necking effect in center part of the sample. At point VIII the deformed state of cylindrical samples equals its limit, at which macro scale destruction of material occurred.

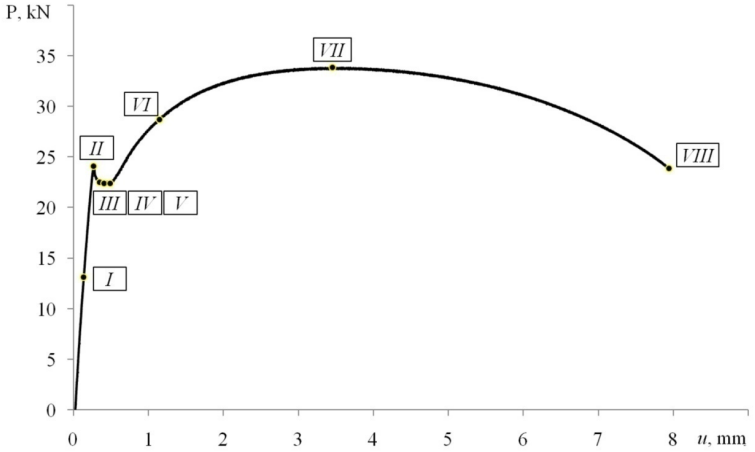

Figure 2: The tensile test diagram for carbon steel.

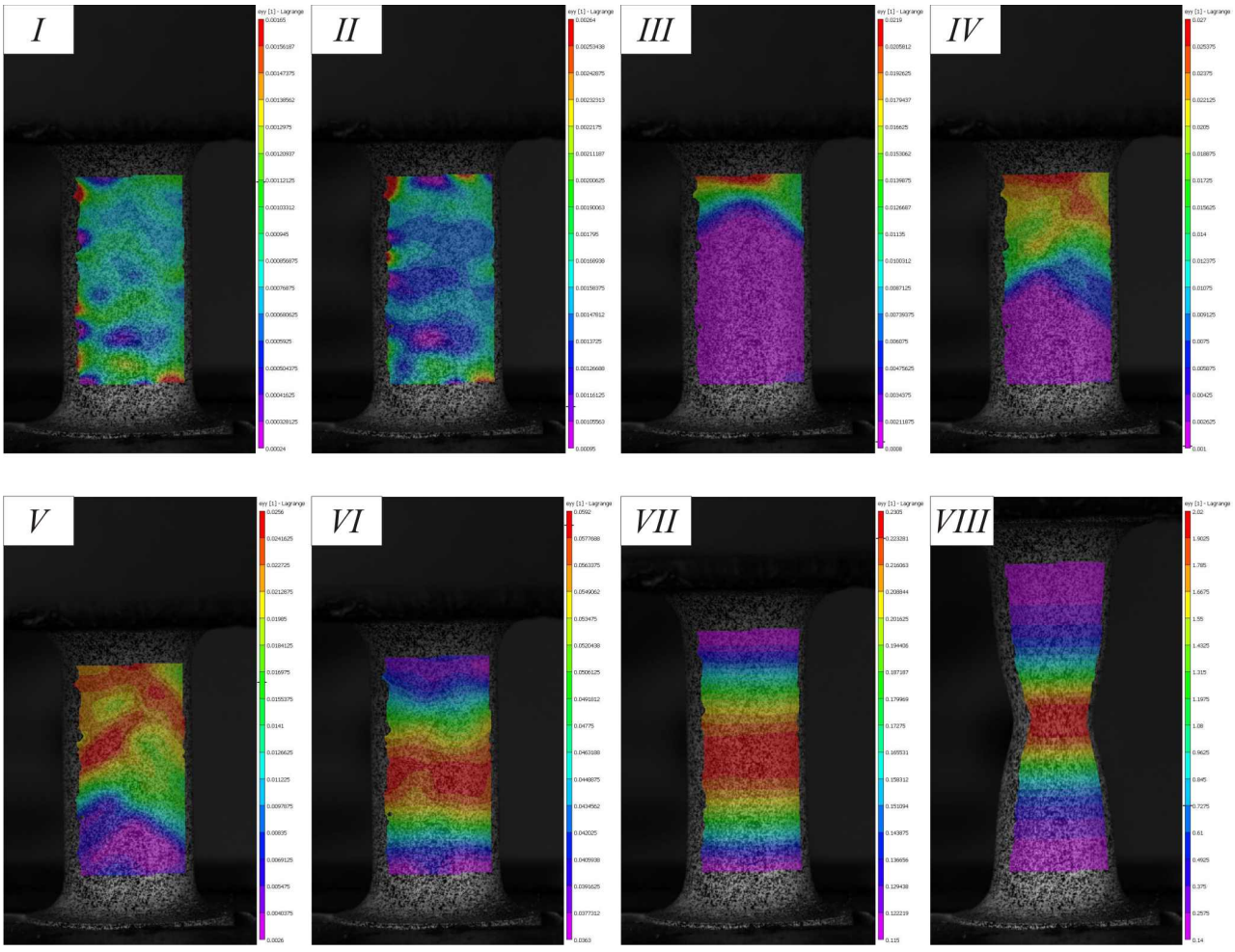

Figure 3: Evolution of axial strain fields during uniaxial tension of cylindrical sample.

Axial strain distributions were drawn to appraise inhomogeneity of the material deformation process on sample surface (Fig. 4). Designation of curves (*I–VIII*) coincides with points on the tensile test diagram (Fig. 2). It is clear that at the moment before sample destruction, significant strain localization is observed in the central part and is about $\varepsilon_{yy} = 200\%$, while average strain is 32%. The elasto-plastic material deformation stage demands for a more thorough study, specifically at the moment of yield drop and yield plateau forming (Fig. 5).

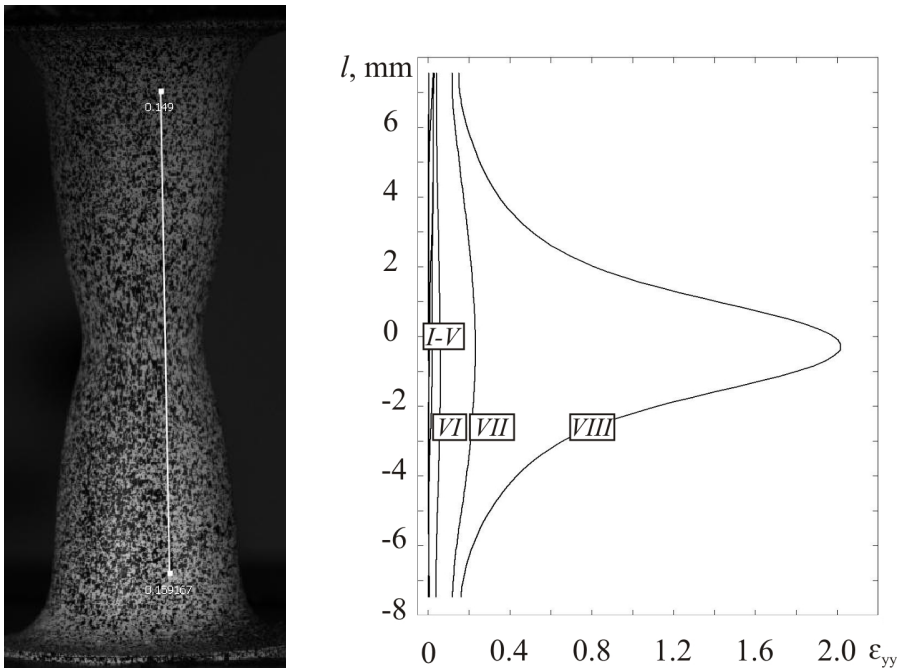

Figure 4: Axial strain distributions on surface of cylindrical sample.

At the elastic stage deformation of material was happening macro-homogeneously along the full sample length. As was mentioned above, the abrupt strain flash appeared (curve *III*, Fig. 5) at the moment of transition through an upper yield point (point *II*, Fig. 2), and a wave front of axial strain was initiated. The wave front is going from one grip to another with the speed of about 12-15 mm/min. Macro loading speed of the sample is 0.32 mm/min.

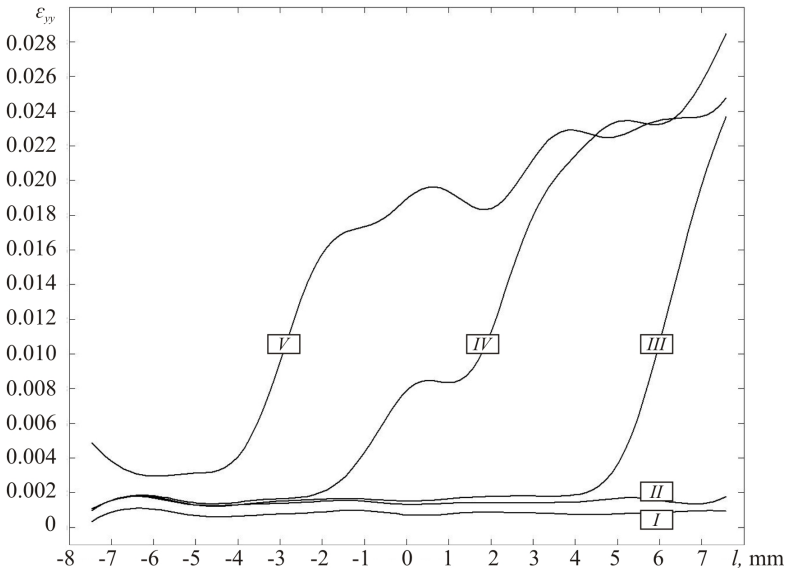

Figure 5: Axial strain distributions at the elasto-plastic deformation stage.

On the basis of experimental data time dependences of axial strain were determined for five areas of material, marked on the surface of sample test portion (Fig. 6). At the material hardening stage and postcritical stage as well, the center point (1) speed of deformation is considerably higher than the other; at the same time, equidistance points (1 and 5, 2 and 4) deform with equal speed.

Time inhomogeneity on elasto-plastic stage has wave-like behavior (Fig. 7). The step-by-step involvement of parts of cylindrical samples into the material deformation process is observed (1–5, Fig. 7). Point 1, which is located at the edge of the sample test portion, starts first. When it reached a certain level of axial strain, the material stopped deforming in this area. During the deformation process, next point (2) is engaged, and so on. This effect can be named the 'relay-race mechanism' of deformation, which happens at the stage of yield plateau forming. During further loading at the material hardening stage the axial strain level increased at point 3. This fact confirms the occurrence of localization process in the center area of solid cylindrical sample test portion.

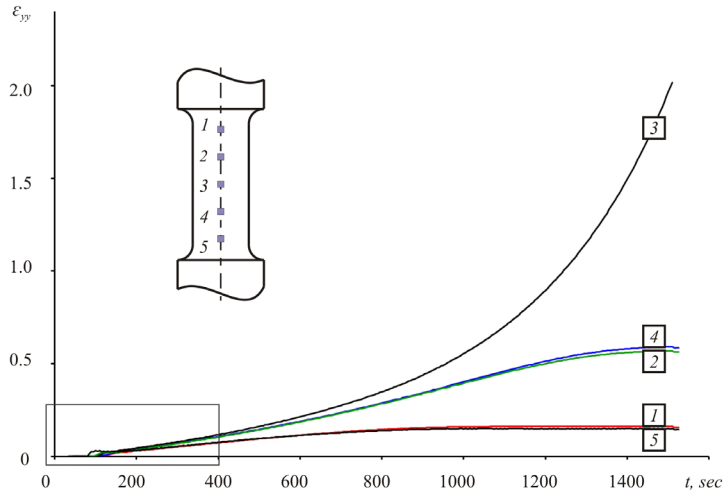

Figure 6: Time dependences of axial strain for five areas of material.

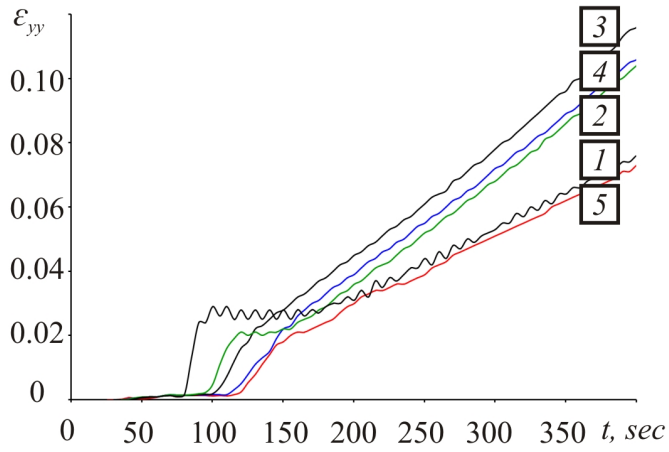

Figure 7: Time dependences of axial strain at the stage of yield plateau forming and at the material hardening stage.

In turn, the elastic unloading of peripheral specimen parts was registered at the postcritical deformation stage (*1*, *5*). The elastic unloading for the first area was about 0.120%, for area *5* it was 0.135%.

With the aim of quantitative estimation of axial strain concentration, which is caused by localization of plastic yielding in material, the following coefficient was considered:

$$k = \varepsilon_{yy}^{\max} / \varepsilon_{yy} \qquad (3)$$

where ε_{yy} is the average value of axial strain, determined by using the complementary module of video system's software 'virtual extensometer'; ε_{yy}^{max} is the maximum value of axial strain on sample surface. The 'virtual extensometer' differs from mechanical extensometers generally in that the former is used after the testing procedure, during post processing, while the latter is used in real-time mode. With the help of the 'virtual extensometer' it is possible to simulate the use of several 'extensometers' on the same specimen [8]. Tab. 2 given below shows results of estimation of axial strain concentration for different material deformation stages (points *I*–*VIII* at the tensile test diagram for carbon steel).
High value of axial strain concentration coefficient is observed at the material softening stage, and also at the moment of transition through an upper yield point, which was demonstrated in this paper.

Point	Load, *kN*	ε_{yy}, %	ε_{yy}^{max}, %	*k*
I	13.134	0.086	-	1.0
II	24.057	0.148	-	1.0
III	22.504	0.360	2.580	7.2
IV	22.326	1.013	2.962	2.9
V	22.389	1.484	2.626	1.8
VI	28.742	4.503	5.935	1.3
VII	33.974	14.156	23.105	1.6
VIII	23.980	32.719	201.978	6.2

Table 2: Estimation of axial strain concentration, which is caused by localization of plastic yielding in material.

CONCLUSION

The findings confirm the existence of space-time inhomogeneity in material inelastic deformation process; specifically the 'relay-race mechanism' of axial strain contribution was discovered and quantitatively investigated at the stage of yield plateau forming on the surface of a cylindrical carbon steel sample. The degree of strain macro localization was analyzed under the conditions of initiation and evolution of necking effect during uniaxial tension. Though there is significant reduction of cross-section area in the sample center, inhomogeneity of deformation process at the post critical stage is commensurable with inhomogeneity initiated by motion of axial strain wave front. Therefore, on the basis of these findings we can make a conclusion about the efficiency of digital image correlation technique and the noncontact 3-D video system. Issues of exposure of automodel parameters of inelastic deformation processes (loading-rate effect, loading conditions, shape effect) are not fully determined and require further complex investigation.

REFERENCES

[1] L.B. Zuev, V.I. Danilov, S.A. Barannikova, Plastic flow macrolocalization physics, (2008) 328.
[2] L.B. Zuev, V.I. Danilov, S.A. Barannikova, V.V. Gorbatenko, Physics of Wave Phenomena, 17(1) (2009) 66.
[3] V.E. Vildeman, J. Appl. Maths Mechs, 62(2) (1998) 281.
[4] V.E. Vildeman, A.V. Ipatova, M.P. Tretyakov, T.V. Tretyakova, Bulletin of Lobachevsky Nizhny Novgorod University, 4(5) (2011) 2063.
[5] M.A. Sutton, J.-J.Orteu, H.Schreier, Image Correlation for Shape, Motion and Deformation Measurements, (2009) 364.
[6] V.E. Vildeman, T.V. Sannikova, M.P. Tretyakov, Problems of mechanical engineering and machine reliability, 5 (2010) 106.
[7] V.E. Vildeman, T.V. Tretyakova, D.S. Lobanov, Perm State Technical University. Mechanics Bulletin, 4 (2011) 15.
[8] T.V. Tretyakova, M.P. Tretyakov, V.E. Wildemann, Perm State Technical University. Mechanics Bulletin, 2 (2011) 92.
[9] V.E. Vildeman, T.V. Tretyakova, D.S. Lobanov, Perm State Technical University. Mechanics Bulletin, 2 (2012) 34.
[10] T.V. Tretyakova, V.E. Vildeman, Factory Laboratory. Diagnostic materials, 6 (2012) 54.

The healing of damage after the plastic deformation of metals

S.V. Smirnov
Institute of Engineering Science, Ural Branch of Russian Academy of Sciences
34 Komsomolskaya st., Ekaterinburg, 620219, Russia.
svs@imach.uran.ru

ABSTRACT. The general regularities of damage healing during the annealing after cold deformation of metal materials are presented in this paper. In categories of damage mechanics the kinetic equations of damage healing during recovery and recrystallization are formulated. Diagrams of damage healing for some metal alloys are presented. The example of use of investigation results for optimization of industrial technology of pipes drawing is presented.

KEYWORDS. Deformation damage; Metal forming; Fracture; Healing of damage; Prediction of fracture.

INTRODUCTION

According to the current conception of metal physics, the fracture of metal materials is not a one-act catastrophic phenomenon, but a regular process of appearance and development of defects, which is in mechanics referred to as damage accumulation (plastic loosening, damageability, cracking, etc.). Pure brittle damage is possible only in metals with a large covalent component in the interatomic bond. The form and shape of defects, as well as the velocity of their propagation, depend on metal behaviour and thermomechanical loading conditions; however, the active role of plastic deformation is invariant here, and it reveals itself on the macro or micro scale.

So the technological cold plastic deformation of metal (rolling die-forging, etc.) from the first stages is accompanied by microscopic defects of continuity. The development of damage with the accumulation of deformation can result in the appearance of macroscopic defects or even the division of the body under deformation into separate parts, i.e. in defective products: this is definitely inadmissible. Macroscopic defects can be revealed easily (external by visual observation, internal by an introscopy method), but correction is either impossible or requires that the defective bulk of the metal should be removed. One of the methods for avoiding macro-damage is multi-stage deformation, with intermediate annealing at the end of every stage, which provides metal softening and, above all, the restoration of metal plasticity (i.e. the ability of the metal to be deformed without fracture). The amount of deformation in a separate stage is established intuitively, proceeding from one's practical experience. To understand the technology of manufacturing cold-deformed products with annealing, it is necessary to give a mathematical description (within the above-mentioned model) of how the restoration of the reduction of micro-damage proceeds under annealing.

As distinct from macro-defects, micro-discontinuities are harder to detect under service conditions. Industry lacks the means of checking micro-flaws, so, therefore all metal products have micro-flaws which can affect the efficiency of machine parts. It has been ascertained hat they influence fatigue life [1]. Therefore it is important to study the mechanisms of eliminating (or healing) micro-flaws, i.e. the mechanisms for the restoration of the margin of metal plasticity by heat treatment and the ways of making it more efficient. This is the subject matter of the present paper.

DAMAGE MODEL

The deformational criteria of damage and the phenomenological theories based on a certain hypothesis of damage accumulation are widespread in mechanics [1-8]. In the description of damage under developed plastic conditions, the deformational approach is also popular (see, for example, the survey found in [9]). Historically, the problem of damage in plastic deformation was initially considered in terms of technological interests on the basis of empiric criteria and fracture models. This approach allowed some simple applied problems to be solved, but hampered the study of the general rules of metal damage under the complex stress-strain state. In mechanics, the progress in the development of the notion of metal damage under plastic deformation is connected with the appearance of kinetic theories of dispersed fracture (damage mechanics) [1, 4-12].

The process of damage under plastic deformation can be represented in a different way in terms of the damage mechanics as

$$\frac{d\omega}{d\Lambda} = f\left(\omega, s_1, s_2, ...\right) \tag{1}$$

where ω is a characteristic of metal damage; S_1 and S_2 are thermomechanical loading parameters depending on the loading conditions. Before loading $\omega = 0$ while $\omega = 1$ when the fracture happens. Intermediate values of ω characterize a level of development of micro-defects.

The kinetic equation Eq.1 was first proposed by L.M. Kachanov [2, 3] to describe damage in creep, and was later used by a number of authors to describe damage under plastic deformation. The most well-known model of metal damage under plastic deformation to be used for making practical calculations is the linear model authored by V. L. Kolmogorov [1, 4, 7]

$$\frac{d\omega}{d\Lambda} = \frac{1}{\Lambda_f} \tag{2}$$

where Λ_f is metal plasticity defined as limiting (at the instant of fracture) accumulated amount of shear strain Λ in deformation under constant stress state characterized by the stress state index k_1 and the Lode-Nadai parameter k_2:

$$k_1 = \frac{\sigma\sqrt{3}}{\sigma_S};\ k_2 = \frac{2\sigma_2 - \sigma_1 - \sigma_3}{\sigma_1 - \sigma_3} \tag{3}$$

where $\sigma = (\sigma_1+\sigma_2+\sigma_3)/3$ is mean normal stress; $\sigma_1, \sigma_2, \sigma_3$ are main normal stresses; σ_s is equivalent stress.

Note that in the literature there is no consensus on the form of the kinetic equation, and it is generally chosen by authors on the basis of hypothetical ideas or published fragments of metal-physic research data. Therefore in this paper we will use an adaptive model of damage accumulation [12, 15]. This model has been formulated from the analysis of experimental data on changes in metal density under plastic deformation and heat treatment after plastic deformation.

A general adaptive model of damage was formulated to describe damage accumulation under conditions of the experimental stepwise change in the stress-strain state, at a later date model was developed in some others forms. When the stress state changes, the rate of damage variation on the adaptation portion is evaluated as follows:

$$\frac{d\omega}{d\lambda} = \left[1 + c_1\left(1 - e^{-c_2\Delta k_{1i}}\right)\left(1 - \frac{\lambda}{\lambda_a}\right)^{c_3}\right]\frac{1}{\Lambda_f} \tag{4}$$

where Δk_{1i} is the increment of the stress state index at i-stepwise of loading; $\lambda = 0 \ldots \lambda_a$ is a current amount of shear strain on the adaptation portion; λ_a is the length of the adaptation portion; c_1, c_2 and c_3 are empiric factors.

When the direction of deformation changes, the rate of damage accumulation decreases, and on the adaptation portion it can be determined by the formula

$$\frac{d\omega}{d\lambda} = \left\{1 - c_4\left|\vartheta_i\right|\left(1 - \omega_{i-1}\right)^{c_5} e^{-c_6(i-1)}\right\}\frac{1}{\Lambda_{fi}} \tag{5}$$

where ϑ is the angle characterizing the change in the loading path in Ilyushin's phase space of deformations, which can be taken as a parameter for the quantitative evaluation of deformation non-monotonicity; ω_{i-1} is the damage on the portion

preceding the *i*-th change in the direction of deformation; c_5, c_6 and c_7 are empirical coefficients. The linear model and adaptive model yield identical results at the simple monotonic deformation.

INVESTIGATION TECHNIQUE

To investigate the general regularities of damage healing during the annealing after cold deformation was the purpose of this paper. Notice that the restoration of the margin of plasticity in metals alter cold deformation has been studied for a number of years, the results being published in [5, 7, 13, 14]. The following technique [13, 14] has been developed for solving this problem (Fig. 1).

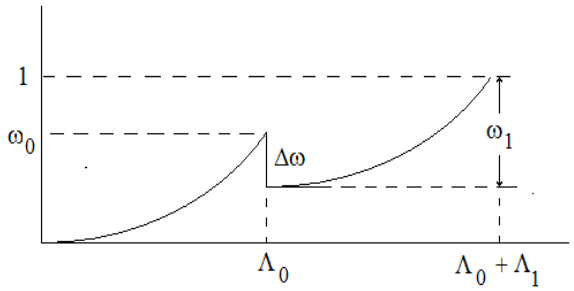

Figure 1: To definition of the damage healing under annealing after deformation

Tests are performed on metal, with plasticity $\Lambda_f = \Lambda_f(k_1, k_2)$ already known. Test specimens undergo different amounts of plastic strain Λ_0, each specimen being deformed to different amounts of damage ω_0. Therefore, all the specimens undergo annealing in accordance with the chosen regime (T is temperature and t is annealing duration). Damage decrease by the value $\Delta\omega$ takes place in annealing. After annealing once again, all the specimens undergo plastic deformation in the same direction up to fracture. Value of $\Delta\omega$ for each specimen can be calculated from a facture criterion

$$\omega_0 - \Delta\omega + \omega_1 = 1 \tag{6}$$

where:

$$\omega_0 = \int_0^{\Lambda_0} \frac{d\Lambda}{\Lambda_f(k)} \; ; \; \omega_1 = \int_{\Lambda_0}^{\Lambda_0+\Lambda_1} \frac{d\Lambda}{\Lambda_p(k)}$$

$\Lambda_0 = 2\sqrt{3}\ln(d_0/d_1)$; $\Lambda_2 = 2\sqrt{3}\ln(d_1/d_f)$; d_0, d_1 and d_f are the initial diameter, diameter before annealing and diameter after fracture of specimens.

The stress state index for cylindrical specimens is calculated as [4, 8]

$$k = \left(1 + \frac{3}{4}\frac{d}{R}(\Lambda)\right) \tag{7}$$

where $\frac{d}{R}(\Lambda)$ is a Bridgman's parameter which characterizes a neck form of specimen.

RESULTS AND DISCUSSION

An example of the damage-time history for low-carbon 0.2%C steel at a temperature of 600°C is shown in Fig 2. The lower curve $\omega = 0$ illustrated that the annealing of the blank to be deformed, for example, of hot-rolled metal, can lead to higher plasticity due to the healing of the micro-damage that appears in the hot rolling stage. The curves have three distinctive parts: AB is a rapid exponential decrease of damage due to a recovery processes; BC is a considerable deceleration (and even stopping) of healing due to incubation period of the recrystallization; and CD is further acceleration of the process due to a recrystallization.

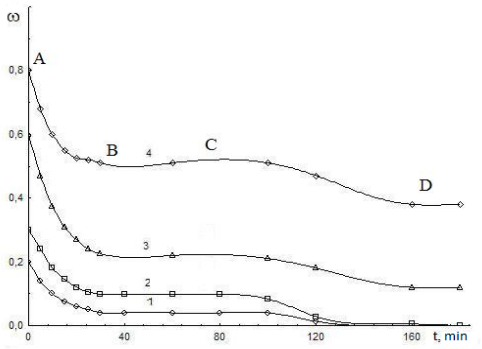

Figure 2: Damage healing during annealing (at 6000C) of carbon steel 0.2%C.

A decrease of damage due to a recovery processes can be described by the equation

$$\omega = \omega_0 \exp\left[\frac{t}{t_{rv}^2}\left(2t_{rv} - t\right)\ln\frac{\omega_{rv}}{\omega_0}\right] \tag{8}$$

where t_{rv} is recovery period, ω_{rv} is the bottom limit level of healing of the damage due to the recovery.

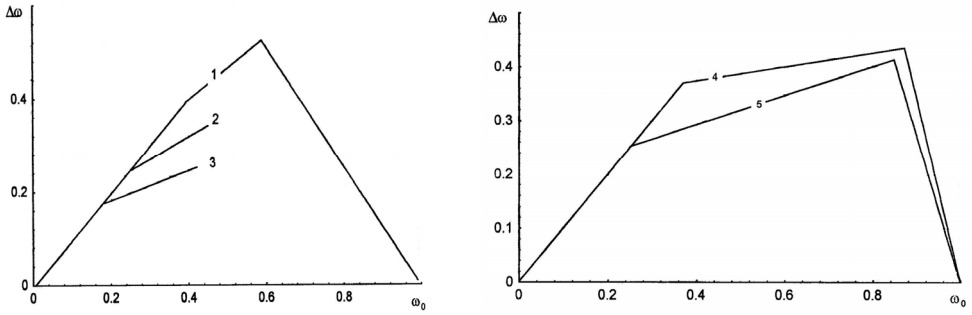

Figure 3: Diagrams of damage healing of some metal alloys: titanium alloys containing different amount of *Al* and *Mn* (1 – *0.8%Al + 0.8%Mn*; 2 – *1.5%Al +1%Mn*; 3 – *3.5%Al + 1.5%Mn*); 4 - low-alloyed *Cr*; 5 – *Cr + 35%Fe*.

A decrease of damage due to a recrystallization processes can be described by the equation

$$\omega = \left(\omega_{rv} - \omega_{rc}\right)\exp\left[-B\left(\frac{t - t_{rc}^0}{t_{rc} - t_{rc}^0}\right)^k\right] + \omega_{rc} \tag{9}$$

where t_{rc} is duration of the incubation period, ω_{rc} is the bottom limit level of healing of the damage due to the recrystallization.

Fig. 3 shows diagrams illustrating the degree of damage healing for some alloys in coordinates $(\omega_0, \Delta\omega)$. On value of the amount of $\Delta\omega$ one can estimate the completeness of the healing of micro-defects appearing in the pre-load stage. (Bear in mind, if $\Delta\omega = \omega_0$ the healing is complete, whereas if all the micro defects remain in the metal). Healability is different for different alloys. Recrystallization annealing leads to the complete healing of deformation damage if it is less than some value ω^*. When $\omega^* < \omega_0 < \omega^{**}$ there is partial damage healing, and a certain part of deformational defects remains in the metal. The researches executed by SEM technique, showed that at this stage defects are micro pores (Fig. 4a). When $\omega_0 < \omega^{**}$ the residual damage increases more intensively, micro pores coalesce, a pores and micro cracks is formed (Fig.4b). Investigations have shown that recrystallization annealing results in the healing of micro-discontinuities of sub-grain size (i.e. under 2-5 μm) by intensive surface diffusion of vacancies when they are crossed by the moving inter- grain boundary of the grain being recrystallized. Values of ω* and ω** is different for different alloys but are usually are in ranges $\omega^* =$ 0.2–0.5 and $\omega^{**} =$ 0.6-0.8.

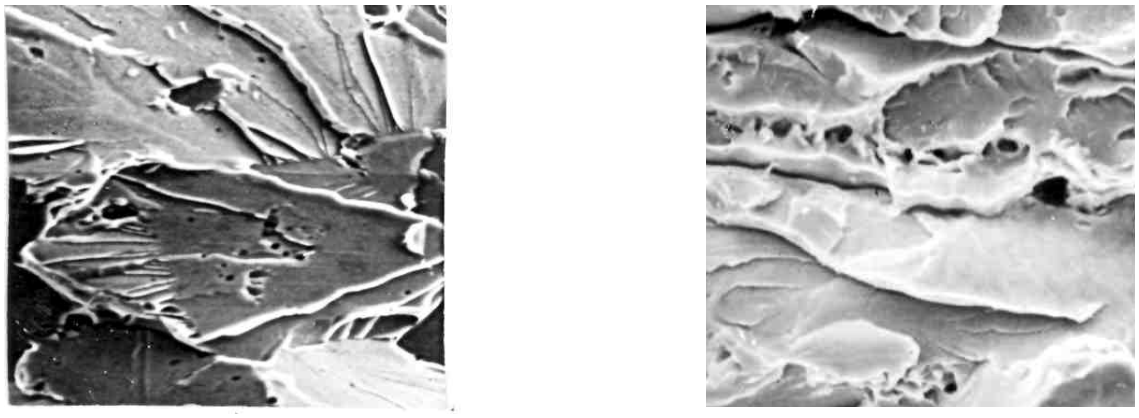

(a) (b)

Figure 4: Micro pores and crack which was formed of coalescence of micro pores (are shown by arrows). Material is deformed carbon steel 0.1%C after annealing (at 700°C, 1 hour). Values of the initial damage: *a* - $\omega_0 = 0.32$; *b* – $\omega_0 = 0.7$ (magnification x1000).

Calculation and analysis of damage accumulated in metal allow to optimize technology process of plastic treatment. One of number of practical examples may be given [16]. At the Pervouralsk Pipe-Making Plant (Russia) pipes of carbon steel 0.45%C for poles has been produced by cold rolling. Existing equipment did not allow to satisfy the demand for type product. To increase a volume of production it was offered to be produce at automated triple drawing line. One of major questions stated for engineers was a question of damage of pipes during drawing because the manufacturing line design did not suppose the intermediary annealing. Theoretical calculations allowed to choose an optimal drawing parameters, when the level of residual damage was not dangerous (Fig.5). The experimental investigations of the relative changes of density $\Delta\rho/\rho_0$ and then industrial tests of theoretical results show a validity of prediction.

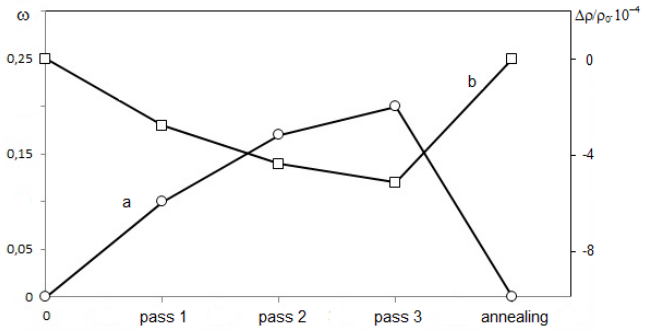

Figure 5: Changes of damage ω (a) and density $\Delta\rho/\rho_0$ (b) under drawing and annealing of 0.45%C carbon steel pipes.

CONCLUSIONS

In this work the equations of damage healing during recovery and recrystallization are in categories of damage mechanics are formulated. Diagrams of damage healing for some metal alloys are defined. It is shown that recrystallization annealing leads to the complete healing of deformation damage ω if it is less than some value ω^*. When $\omega^* < \omega_0 < \omega^{**}$ there is partial damage healing, and a certain part of deformational defects remains in the metal. The example of use of investigation results for optimization of industrial technology of pipes drawing is presented.

ACKNOWLEDGEMENTS

✓ This work has been executed according to plan of the project number 12-T-1-1010 of the UB RAS Research Program and was supported by a grant from the Russian Foundation for Basic Research, contract number 11-08-12083.

✓ The author expresses gratitude to the professor V.L. Kolmogorov for initiation of this research and discussion of its results.

REFERENCES

[1] V.G. Burdukovsky, V.L. Kolmogorov, B.A. Migachev, J. Mater. Process. Technol., 55 (1995) 292.
[2] L.M. Kachanov, Docladi Academii Nauk SSSR, Otdelenie Tekhnicheskih Nauk 8 (1958) 67 – 65 (in Russian).
[3] L.Kachanov, Introduction to Continium Damage Mechanics, Martinus Nijhoff Publishers, Dordrecht, (1986) 135.
[4] V.L. Kolmogorov, Metallurgiya (1970) 232 (in Russian).
[5] A.A. Bogatov, O.I. Mizhiritsky, S.V. Smirnov, Metallurgiya (1984) 144 (in Russian).
[6] J. Lemaitre, A Course on Damage Mechanics, Springer, Berlin (1987).
[7] V.L. Kolmogorov, In: Materials Processing Defects, S.K. Gosh, M. Predeleanu (Eds.), Elsevier, Amsterdam (1995) 87
[8] V.L. Kolmogorov, Wear 194 (1996) 71.
[9] A.G. Atkins, In: An Anniversary Volume in Honour of George R. Irvin's 90th Birthday, H.P. Rossmanith. A.A. Balkema (Eds.), Brookfield, Rotterdam (1997) 327.
[10] M. Oyane, Bulletin of JSME, 15, 90 (1972) 37.
[11] Z.J. Luo, W.H. Ji, N.C. Guo et alii, Journal of Material Processing Technology 30 (1992) 31.
[12] S.V. Smirnov, Key Engineering Materials, 528 (2013) 61.
[13] V.L. Kolmogorov, S.V. Smirnov, Journal of the Materials Processing Technology, 74 (1998) 83.
[14] A.A. Bogatov, V.L. Kolmogorov, S.V. Smirnov, Izvestiya VUZov, Chernaya Metallurgiya, 12 (1978) 43 (in Russian)
[15] S.V. Smirnov, T.V. Domilovskaya, A. A. Bogatov, In: Materials Processing Defects, S.K. Gosh, M. Predeleanu (Eds.), Elsevier, Amsterdam, (1997) 71.

Fatigue crack propagation in turbine disks of EI698 superalloy

A.A. Shanyavskiy
State Centre for Civil Aviation Flights Safety, Airport Sheremetievo-1, PO Box 54, Moscow region, Chimkinskiy State, 141426, Russia
shananta@mailfrom.ru

ABSTRACT. In-service fatigue cracking of turbine disks of EI698 superalloy is discussed based on crack growth analyses. In the bolt joint for disks to shaft connecting there is high level of stress-state, which directed to earlier in-disks fatigue crack origination in low-cycle-fatigue regime. Fracture surface pattern such as fatigue striations were used for their spacing measurement and crack growth duration estimating. Developed disk tests on a special bench by the equivalent program to in-service cyclic loads have allowed discovering one-to-one correlation between fatigue striation spacing and crack increment in one flight. Number of fatigue striations and beach-marks calculations permitted to estimate crack growth period for the different stages of in-service disks cracking. Equivalent stress level for in-service cracked disks was calculated and compared with stress-level in-tested disks under stress equivalent program to in-service operated cyclic loads. Based on this result non-destructive inspection intervals were discussed and recommended for in-service disks in dependence on number of their flights at the moment of developed inspection to exclude in-flight disks fast fracture.

KEYWORDS. Nickel-based superalloy; Crack initiation; Crystallographic facet; Fatigue striations; Crack growth period; Stress equivalent; Non-destructive inspection.

INTRODUCTION

Aircraft structures in-service fatigue cracking can be appeared under wide range of cyclic loads combinations [1-4]. Because of difference in structures loading conditions from one flight to another it can be effective to use material reaction for describing damage in-time accumulation in each of them [5]. This reaction on the external loading can be considered as material property pre-venting crack occurring and growth. Discussed property has not only mechanical but physical sense, and in the case of aircraft structure fatigue cracking, when Mode I crack opening is dominant, the discussed process can be described, for instance, applicably to durability, based on bifurcation diagram [6,7], Fig.1.

The bifurcation diagram allows describing fatigued metals behavior based on uniform synergetical methodological principle applicably to systems which evolution occurs far from the equilibrium position. Stated the synergetics concept allows to connect among themselves all experimentally demonstrated data on research of metals fatigue at different scale levels and to explain increase and decrease of dispersion of fatigue durability in process of increase of cyclic stress level at achievement of critical stress levels. Such manner of metal fatigue behavior consideration is lawful, even if in process of evolution metal undergoes only one unstable condition and consequently has only one bifurcation area between two boundary conditions when it is not loaded (one border) and when it is completely failed (the second border).

Because of complicated external cyclic loading and environment deterioration, material re-action there has to be considered based on the stress equivalent value which has difference in dependence on a structure and its stress-state [8]. In the case of through or semi-elliptically-shaped cracks, which usually takes place on the first stage of structure cracking one can see simply equation for principle stresses σ_1, σ_2, their ratio $\lambda = \sigma_2 / \sigma_1$, and value of σ_e in the form [9]:

$$\sigma_e = \sigma_1(1 + A_1\lambda + A_2\lambda^2) \quad (1)$$

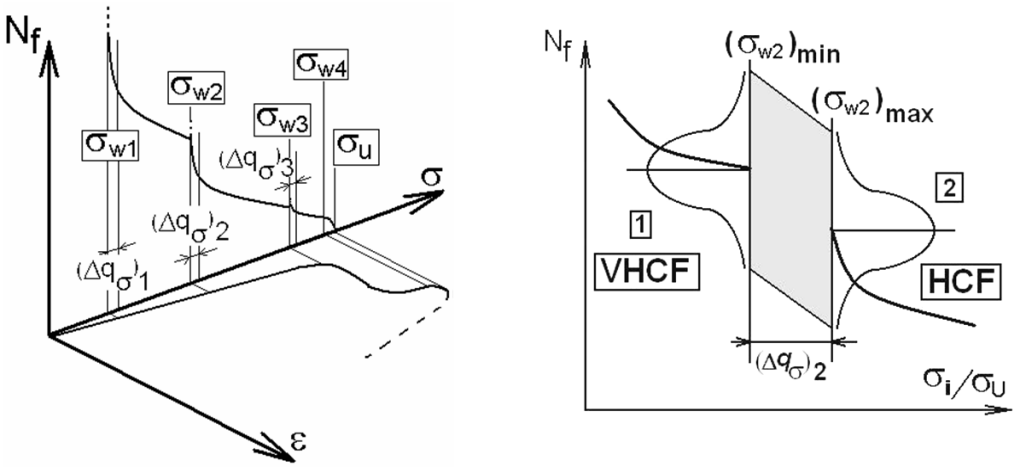

Figure 1: The bifurcation (a) diagram of metals fatigue has constructed according to the tension diagram and (b) schema of probability of metals cracking variation for the bifurcation area ($\Delta q_{\sigma 2}$). Bifurcation areas are specified at transitions from nano-(σ_{w1}-σ_{w2}) to meso-(σ_{w2}-σ_{w3}), and macro-(σ_{w3}-σ_{w4}) scale level of metals fracture.

Parameters A_1, A_2 depended on the material-type and can be determined in specimen biaxial tests [9].

Applicably to in-service aircrafts, in the case of Low-Cycle- (LCF) and High-Cycle-Fatigue (HCF), material reaction can be discovered after crack occurring when fracture surface will be analyzed in electron microscope [4]. That is why, if there were not estimated in-tests parameters of Eq.1, fractographic analyses of cracked aircraft structures can be used for estimating σ_e-value because fatigue striations and ΔK_{eff} or K_e - equivalent value has unified correlation in term of material reaction independently on the in-service unknown external loading condition [4-6].

Possessing aviation gas-turbine engines (GTE) with higher in-service parameters and reduced weight required heavier thermal and mechanical tension of the engine parts, including the turbine disks. Gas-turbine engines of some types have the turbine disks designed in such a way (existence of the central hole, arrangement of the fastening holes in the stressed part of the hub) that the disk material of nickel-based superalloy EI698 experiences elastic-plastic loading in stress-concentration zones by the holes. There is clear material biaxial stress-state in areas of crack origination and propagation with different λ-ratio for different bolt joint stressing from one exemplar of turbine disk to another.

Besides, the working temperatures are quite moderate in the fastening-hole regions. Hence, creep effects do not contribute much here and so the low-cycle fatigue in these regions is mostly responsible for the disks lifetime.

Under LCF conditions, the crack-growth period occupies most of a material lifetime [4]. Therefore, stronger thermal-and-mechanical tension of the disk material together with possible material defects introduced in manufacturing and in periodic servicing of the engine reasons the damage-tolerance approach to the disk service.

In service, fatigue cracks were found to grow in Stage-III disks of NK8-2u engine, Tu-154B aircraft; the cracks grew in the sites of high stress concentration by the holes used to fasten disks to the engine shaft. Complicated stressed state was calculated with finite-element method for those disk sites where linear stressed state was expected to exist according to the traditional calculation techniques [10, 11]. Solutions based on the generalized concept of plane-stress state in a series of sections neglect tangential stresses and, partly, a three-dimensional stressed state of the disk rim, including its labyrinth-seal portion. Erroneous estimations of the real stressed state are even more likely when applied to the stress-concentration sites by the holes for bolted joints of a turbine disk and shaft. In service, it is by those holes that fatigue cracks arise to then propagate towards the hub and shaft. The actual stressed state differed from the calculated one: according to calculation, the greatest stress intensity would correspond to the section normal to the plane actual crack growth.

Stage-III turbine disks of two NK8-2u engines (labeled arbitrarily as P-1 and P-2) broke in service. One of the in-service failed turbine disks has shown in Fig. 2. Both disks broke in a similar way during a starting run along the takeoff runway. Hence, a reasonable guess was that the same cause brought these similar-stage turbine disks about the failure.

Moreover, when having the engines serviced after different operation times, numerous fatigue cracks were discovered in the bolt-joint holes of the disks. Therefore, disks with different numbers of cracks in the holes were selected after different operation times, aimed at the analysis into the trends of the crack initiation and propagation.

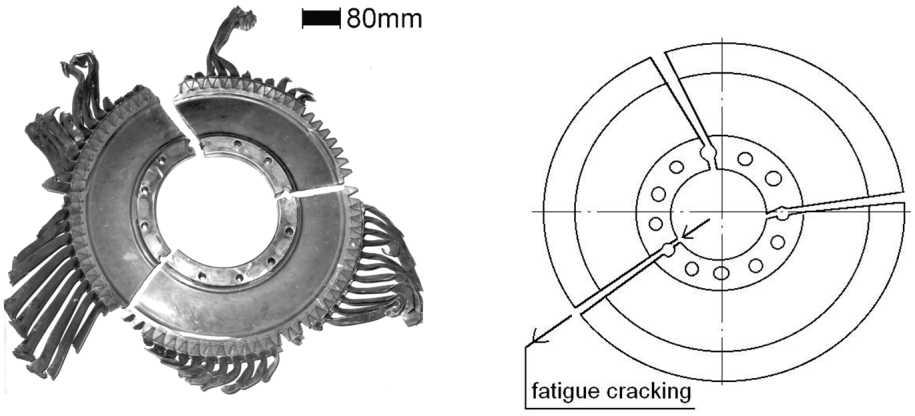

(a) (b)

Figure 2: (a) General view of the Stage-III turbine disk of a NK8-2u engine; (b) Scheme of the disk cracking sequence. Arrows indicate the disk section in that initial fatigue crack propagated.

INVESTIGATION PROCEDURE

Material

It was well-known superalloy EI698 is strengthened primarily by precipitation of a gamma prime phase (γ'), Fig. 3. The grain size was measured using the line intercept method on optical micrographs. The distribution of grain size has shown that the mean grain size, excluding the presence of annealing twins, is about 38 μm. Large grains on the order of two to three times of the average grain size and large grain clusters exist in the microstructure.

The disk material—EI698 superalloy—was tested using standard test specimens. The latter were made from the disks, broken in service, and subjected to shirt-term tensile tests and impact-toughness tests at 20°C and to creep-rupture tests at 750°C with 420 MPa applied stress (smooth specimens), 650°C, 720 MPa applied stress (smooth specimens) and 650°C, 850 MPa applied stress (notched specimens with a 0.15-mm curvature radius of the notch tip). The specimens were cut out of the under-rim part of a disk along a chord direction and out of the hub part.

At 20°C both disks exhibited mechanical properties that satisfied all standard requirements to the new disks. Ultimate tension stress, Yield stress and elongation were respectively not less than 1150 MPa, 720 MPa and 19 %.

The time to fracture shown by the smooth and notched specimens tested for creep-rupture strength appeared well above the smallest standard one (not below 50 hours), i.e., was indicative of a quite good high-temperature strength of the disk material.

Metallographic investigation of both investigated disks in area of crack origination has shown material structure in accordance with certificate for manufactured turbine disks (see Fig. 3) without any evidence of faults.

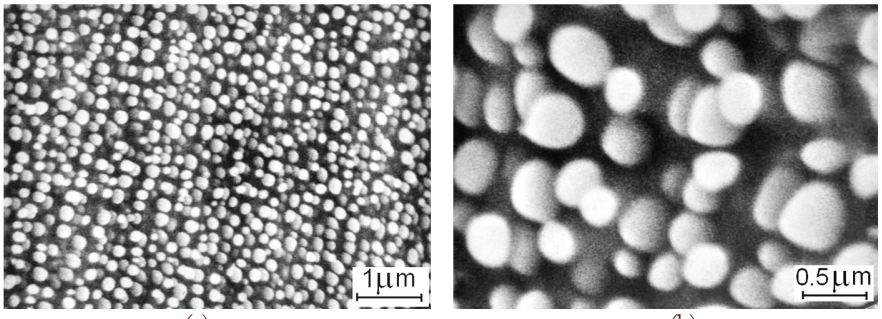

(a) (b)

Figure 3: Typical microstructure of EI698 with gamma prime phase (γ') under (a), (b) different magnification in electron microscope.

Non-destructive inspection data

In-service, after the failure discovering of two turbine disks, there was performed non-destructive inspection of all operated turbine disks. In many cases there were discovered cracks being different in size for different disks. Disks with

cracks were removed and some of them used in the present investigation. The disks with cracks that were selected for their fracture surfaces investigation and failed disks are described in Tab. 1.

Test procedure

Two of in-service cracked disks with small cracks were not subjected to crack opening and selected for their testing on the special bench-test. It was reproduced in-service acting stress-state with maximum stress level in accordance with maximum disks rotation speed in flight. During fatigue tests, in disks crack propagation was registered by the non-destructive day-penetrate periodical inspections.

№№	Time since new, flights/hours	n_1	n_2	c_i, mm	Comments
1	1329/3097	11	18	0.2–1.05	In-service discovered crack
2	1335/3658	8	9	1.5	- " -
3	1421/3962	11	8	0.05–1.65	- " -
4	1499/3733	1	8	2.0	- " -
5	1690/5780	11	2	0.6	- " -
6	2049/4688	4	13	0.1–0.5	- " -
7	3121/6609	12	9	1.2	- " -
8	2048/5994 + 561/2000 bench runs	8	1	4.0	In-service discovered crack; bench tests added
9	3079/5990 + 36 programmed runs	12	12	2.8	- " -
10	2619/6345	-	-	-	Broken in service
11	2696/5382	-	-	-	Broken in service

Table 1: In-service operation time of NK8-2u engines, numbers n_1 of the holes (see schema of the Fig.1) with cracks and n_2 of cracks in holes and crack size as measured by the hole-surfaces.

In one disks (P-3), it was realized block of 42 cyclic loads, reflecting in-service operated stress range during engine working, with constant stress amplitude and R-ratio near 0.4 between two neighbored disks cycling with one cycle at R=0. There were reproduced 50 blocks in disks fatigue tests. Maximum of stress level was reproduced for in-flight operated engine.

In another disk (P-4), it was used engine with reproducing for disk in-service loading by the cyclically-equivalent-program (CEP). This program used for estimating design service goal for in-service disks [12, 13].

Fractographic analyses

All selected disks were subjected to fractographic investigation on the scanning electron microscope EVO40 of the Karl Zeiss Company. Fracture surface patterns were used to reproduce in-service crack propagation in number of flights based on fatigue striations or beach mark number in accordance with developed earlier methodology [4, 6].

INVESTIGATION RESULTS

General trends of crack growth revealed by the broken disks

P-1 disk broke in service by cracking in three radial sections arranged at 120° angles to one another (see Fig. 2). These sections passed holes through that the disk was bolted to the engine shaft. In P-2 disk these angles were 150°, 120°, and 90°. Having matched the disk fracture surfaces, we saw the fracture to first initiate in one radial

section of a disk. As the crack propagated, plastic deformation of the disk occurred to cause a 35-mm crack-opening displacement, next to which final fracture occurred over the two different radial sections.
Finding the material to fit assigned mechanical properties indicated that the LCF cracks developed in the discs stressed as high as to exceed their working capacity. Therefore, the problem arose to make use of the actual durability with the still impossible failure of the disk due to the growth of LCF cracks. In fact, this was the problem of running engines with the disks tolerably damaged. We solved successfully this problem owing to the complex investigations that included quantitative fractography as a way of estimating the growth period of fatigue cracks.
We examined visually the fracture surface of the opened cracks to find them initiated in the disk-hub body at the surface of one or several fastening holes on the central-hole side. The cracks propagated along the disk radius toward the central disk hole, Fig. 4. Once a crack grew through, it began to grow toward the disk rim with a danger of disk fracture along its radius. The fractures colored golden formed between the fasting holes, used to bolt the disk to the turbine shaft, and the central disk hole. The fracture morphology indicated that the crack grew transgranularly, typical of superalloys fatigue cracking. Each of the disks had most strongly oxidized zones, arranged closer to the end of the hub. This zone was indicative of quite a long propagation period of the initially non-through semi-elliptic crack (see Fig. 4b).
The web of the disks, broken in service, showed signs of transgranular cracking of a cyclic nature over the region 63 to 65 mm long between the bolt-joint hole and the rim. These cycles left behind a sequence of fracture zones oxidized to different degrees. Elliptic fatigue lines so-called beach marks (BM) bordered these four zones (see Fig. 4c). Similar trends were revealed by the fracture surface of Stage-I high-pressure-compressor disk, made of titanium alloy VT3-1, in a D-30 engine: here zones of different roughness formed in the disk web [12]. A distance between two neighboring zones (each identified with BM) of different roughness answered to crack propagation during one flight. So in the above turbine-disk case, we considered the whole pattern of crack-propagation from the bolt-joint hole to disk rim as formed during five flights, with the last executive start of the engine in that number.
In both turbine disks, the two remaining fractures were of a mixed type (intergranular plus transgranular) with the signs of macroscopic plastic deformation all over the fracture boundaries; such a fracture pattern is typical of superalloys subjected to short-term static loading.
An important finding was that, in both disks, each of the short-term fractures revealed a portion of fatigue cracking, which, similar to the general long-term fatigue fracture, began by a bolt-joint hole. It was indicative of a multiple fatigue cracking from those holes in both of the in-service failed disks. Those initial portions of fracture were also transgranular and oxidized to golden-gray color. Their semi-elliptic boundary with the area of final shirt-term fracture was distinct, typical of the case that an abrupt increase of applied load occurred as soon as the general fatigue crack grew to its critical size. The general fatigue cracks grew to the dimensions of $2c = 6.5$ and $2c = 1.2$ mm at the disk hole surface and $a = 3.0$ and $a=0.3$ mm in depth direction for the P-1 and P-2 disks, respectively.
The crack grew to sequentially form four fracture zones of respectively changed dominating fracture mechanism that was indicated by the difference in fracture surface patterns.
Zone I (see Fig. 4) reveals gradual growth of the crack from the disk hole, predominantly by forming fatigue striations, Fig. 5. The striation spacing increases along the minor ellipse axis, toward disk-body depth. The smallest striation spacing was 0.5 and 0.3 μm for discs P-1 and P-2, respectively. Both values of spacing indicate to low-cycle fatigue conditions of the crack initiation, i.e., to a stress level as high as or higher than the yield strength of the material. A special feature is that the striation spacing increased linearly with crack growth to achieve 1.2 μm by the crack-penetration depth of about 1.2 mm, where the second fracture zone began in both broken disks. In the open fractures, striation spacing amounted to 0.7 and 1.2 μm for the greatest crack depths of 0.3 and 1.2 mm, respectively. All cracks revealed similar laws of increasing the striation spacing to obviously indicate that both disks experienced an about equally high level of stressed state around the holes.
Designing disks in terms of durability takes into account effect of protractedly holding them mechanically loaded when starting and shutting down the engine. With such holding under LCF-conditions, thermally activated plastic deformation and fracture increase the probability that slowly-going damage of grain boundaries and subboundaries by grain-boundary sliding and vacancy fluxes comes to a completion. Consequently, fracture becomes a mixed type (transgranular plus intergranular) of predominantly intergranular.
The fracture surface revealed fatigue striations to confirm that, with a moderate thermal tension of the disks, the intergranular mode of fracture was suppressed by the transgranular mode and slip. Transgranular slip brings about vigorous cracking of the material and, thereby, hinders from the formation of fatigue striations. Consequently, fatigue striations coexist with cracked regions of the fracture surface.
Zone II of further crack propagation (see Fig. 5) predominantly reveal fracture facets with the steps of intensive transgranular slip and hardly visible dimpled regions. Besides, the dimples look quire shallow. Such an abrupt transition to

Stage II of crack growth occurs as soon as the fatigue-striation mechanism is suppressed while transgranular slip and grain-boundary sliding become dominating. This is evidence that the fast transgranular slip does not bring about dominating grain-boundary damage of the material.

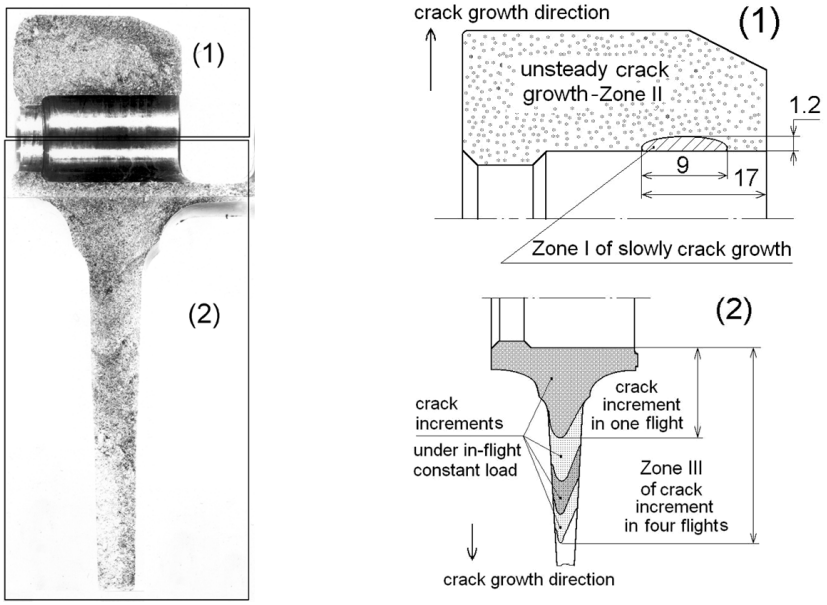

Figure 4: Fracture (general view) in one of the Stage-III turbine discs (NK8-2u engine) has broken in service; (1) and (2) the sequence (schematic) of the crack propagation in a disk.

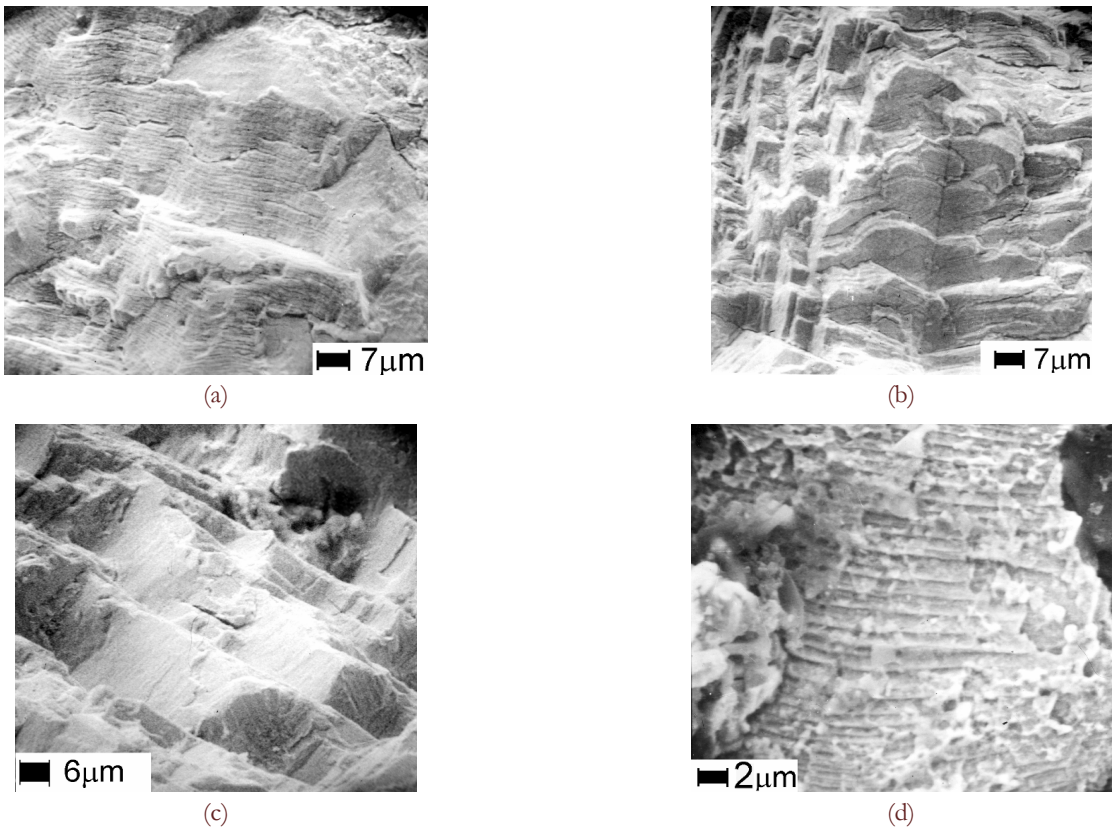

(a) (b) (c) (d)

Figure 5: Fracture morphologies of a in-service fatigued turbine disk (a–c) at the stages of (a) early steady and (b, c) accelerated growth of a fatigue crack and (d) by slow in-flight cracking under repeated static loading (see also Fig. 3).

If the threshold value of stress-intensity factor $(K_{max})_h$ is achieved, holding a material mechanically loaded will change a situation at the crack tip as far as the material is sensitive to the loading waveform. Now the plastic zone does not hinder the crack growth in the material held under a constant applied load. The crack grows slowly with progressing mixed transgranular and intergranular slip (see Figs. 5b, 5c). In so doing, the transgranular slip still dominates, indicating that the any serious effect of temperature, known by vigorous formation of grain-boundary voids, does not show itself. Transgranular slip develops until the material ductility is exhausted and, consequently, decohesion on the slip plane occurs the moment that the fracture surface forms. Such a pattern should be associated with the case of a highly stressed material in that transgranular slip occurs easier and, since the material is heated, is not blocked by the grain boundaries. As the slip is finished, cleavage on this slip plane occurs.

The crack propagates from a bolt-joint hole toward the central disk hole in a field of centrifugal forces, which determines the level of long-term static loading of the material. As the crack length increases fast by pure-shear under a constant applied load, we believe that the crack growth is controlled by a slowly increasing stress-intensity factor. These crack-propagation conditions, creative of quite extensive Zone II, are overcritical: the crack propagates fast (by tens or hundreds microns per one flight). Such a behavior of fatigue crack (propagating from the bolt-joint hole toward the engine shaft) conforms to the disk calculations for strength.

Zone III demonstrates a pattern of mixed transgranular fracture. This followed from transgranular slip and static ductile cracking (see Fig. 5d). The visible fracture surface reveals shallow dimples, indicative of low-energy fracture caused by static shear. The grain-body strength becomes virtually exhausted due to preceding vigorous transgranular slip. Consequently, formation of pores is limited as long as the free surface of fracture forms by decohesion on the slip planes. Decohesion appears a dominating way of fracture. Concurrently, local regions experience low-ductility fracture by forming degenerated dimples. Such a pattern is representative of transgranular formation and coalescence of pores, typical of a material held under a permanently applied load, Fig. 6. During a flight long as tens of minutes, a crack can propagate by tens of millimeters. Indeed, Zone-III fractures of the broken disk web reveal five sequentially repeated regions of a changed intensity of the fracture oxidation. These regions correspond to the repeated cycles of heating and cooling of the engine (having it launched and shat down, respectively). The boundaries between the regions conform to the crack-tip profiles the moment that the temperature-and-loading conditions were altered. Each region has extension over 5 mm along the crack path.

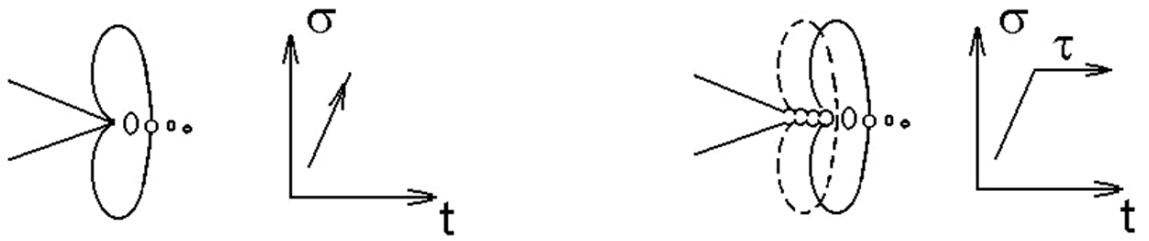

(a) (b)

Figure 6: The propagation sequence (schematic) of a fatigue crack under (a) increasing or (b) constant applied load with a result that a dimpled fracture is formed [15].

Zone IV represents the final-fracture area of the disks. It reveals a dimpled-type fracture adjacent to the grain boundaries and characteristic of this alloy when going through short-term fracture under temperature-and-loading conditions reaching its fracture toughness.

Thus, in service, a crack in the disks can pass the propagation Zones III and IV during a small number of flights. The crack propagates here by transgranular slip caused by a constant load applied at the maximum revolutions per minute of the engine. Therefore, the general crack-growth period, primarily contributing to the disk durability, relates to Zone I of the fracture. In Zone I, which extends to 1.0...1.2 mm in depth, steady crack growth occurs according to the fatigue-striation mechanism. Besides, the value striation spacing greater than 0.3 μm corresponds to the low-cycle range of fatigue fracture.

The regularities of damage caused by cracks in the disks

We carefully analyzed the above data on the broken disks to compare them with the crack-growth patterns brought to light by disks servicing (see Tab. 1). Therefore, we opened all of the detected cracks and examined them fractographically.

All of these fractures exhibited fatigue striations with the striation spacing not less than 0.34 μm by the edge of the hole, Fig. 7. The crack-growth rate was noticed to increase along the minor axis *a* (in-depth of a disk hole). This acceleration appeared the smaller the greater operation time to agree with the idea that the periods of a crack initiation and propagation change in the same proportion with a stress level and stressed state of the structure element [4]. In all examined cases, the value of striation spacing grew linearly long the minor axis of the semi-elliptic crack (see Fig. 7). Such a trend is typical of a structure-element behavior in a biaxial stressed state under LCF conditions with a constant strain range [16].

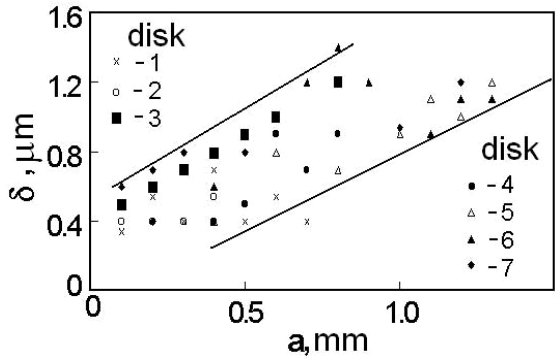

Figure 7: The changing trend of the value δ of fatigue-striation spacing along the crack-growth direction (minor axis ***a*** of the crack front shape) for the group of examined disks (disk data are given in Tab. 1).

Nos. 3 and 4 disks were close to the broken disks as concerns their operation times, and the opened fractures revealed the cracking depths of 1.8 and 2.0 mm, respectively. Deep as 1.2 mm, the value of striation spacing was 1.2 μm (close to that in the broken disks) and the disks experienced a change of fracture mechanisms: now the facet-type-pattern fracture morphology dominated born by transgranular slip. This just was Zone II, revealed by the fracture of the broken disks. In all the other examined fractures the crack did not reach its critical depth of 1.3 mm, i.e., transition to Zone II of crack growth did not occur.

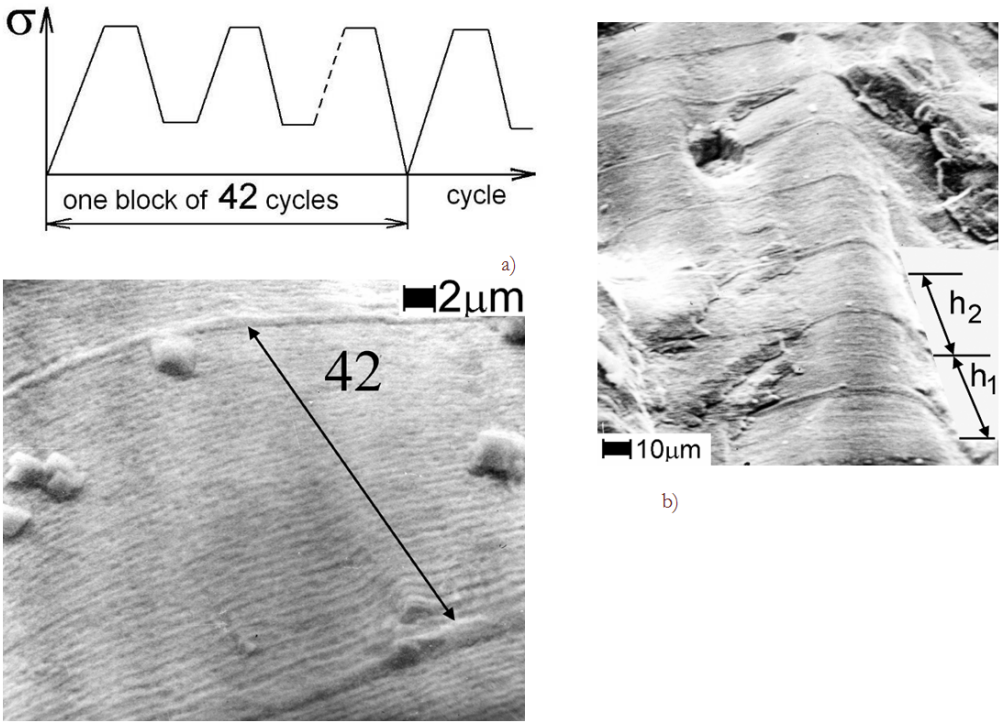

Figure 8: (a) Block of loading waveform (schematic) of a Stage III turbine disk applied when bench-testing an NK8-2u engine and (b, c) fatigue-striation blocks, h_i, illustrating the fracture response of the disk loaded in the engine.

Crack growth in tested disks

The tests of the disk P-3 were done according to a special routine by imitating blocks of 42 one-flight loading cycles, each block ended with a complete cutoff of the engine. The greatest and least numbers of engine revolutions corresponded to the end of take-off and reduced-speed regimes, respectively. On the tests, we opened the cracks to examine their growth behavior fractographically and have found 42 fatigue striations to be formed by 42 one-flight loading cycles (one test block, Fig. 8). The blocks of 42 striations, with the striation spacing nearly the same over a block area, were separated by a step (or a line) from one another. Each step formed to mark a complete cutoff of the engine. These findings confirmed that, in Zone I of crack growth (within 1.3-mm crack depth), each fatigue striation is indicative of a crack increment caused by a start-and-shut-down cycle of the engine, i.e., by a single flight of the aircraft.

We analyzed the crack-growth trends in the P-4 disk tested by ECP loading in the engine to discover that the disk-fracture morphology differed significantly from that peculiar the real in-service conditions. In the tests, the crack in Zone I was grown to 8-mm depth, Fig. 9; at this depth, the value of fatigue-striation spacing achieved nearly 2 μm. This is significantly greater than the critical value typical of changing for Zone II for in-service fractures. And, compared with the latter, striation spacing grew significantly faster with the crack depth.

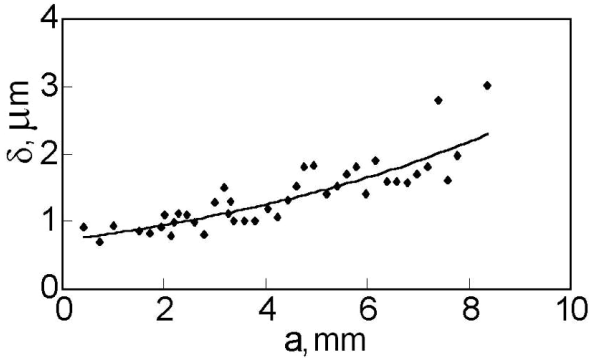

Figure 9: Striation spacing value δ against the minor axis, a, of semi-elliptically crack appeared in the turbine disk bench-tested by equivalent cyclic loading in an NK8-2u engine.

DISCUSSION

The number of loading cycles calculated from the number of fatigue striations showed agreement with the in-service operating time, Tab. 2. A larger operating time gave a greater number of fatigue striations. Hence, expecting fatigue striations to form during a start-and-shut-down cycle of the engine, a number of the fatigue striations must be characteristic of the growth period of a fatigue crack, measured as the number of flights of an aircraft.

Disk No.	1*	2*	3	4	5*	6*	7	8
N_f (flights)	1329	1335	1421	1499	1690	2041	2600	3121
N_p, striations	180	620	1000	860	760	710	1500	1360

Table 2: Operating times N_f of the disks since new and a calculated number N_p of fatigue striations for the cracks detected in service (*In disks-No 1, 2, and 5, 6 cracks did not reach their critical depth).

The data on crack-growth period show significant scatter, which should be related to a difference in stress levels between the disk-hole sites. For instance, only one crack was detected in No. 4 disc, its depth, though, as large as 2.0 mm. Yet other disks, of different operating time, exhibited four to twelve cracked holes. The holes may differ in the distance from the butt-end of the hub to the fracture origin site (1.5 to 13 mm), which also confirms the case of difference in the stress level between the disk holes.

Having analyzed the growth trends of fatigue cracks in the disks made it possible to estimate the stressing extent and, based on an acquired relationship between the numbers of fatigue striations and start-and-shut-down cycles of the engine, establish the due inspection frequency of the disks. By calculations, the number of fatigue striations was found to never

exceed the number of flights of an aircraft and, in some discs, respond to over 50% operating time (assuming one striation formed by one start-and-shut-down cycle of the engine (see Tab. 2).
Validity of using the above-mentioned relationship was evaluated based on the test results obtained for P-3 disk installed in an engine (see Fig.8). Having quantitatively estimated the fractographic parameters of fatigue fracture of turbine disks bench tested by ECP loading in an engine, we established that a single fatigue striation with a respective crack increment formed per each one-flight cycle under the takeoff conditions.
The stresses applied to the disk during ECP were significantly lower in such a bench test regime than in service. Using the fracture-mechanics approach, we compared the stressed states of the disks in the bench tests and in service.
For the discussed case of semi-elliptic crack a well-known formula of K_e equivalent stress-intensity factor is applicable [17]:

$$K_e = \left(\sigma_e \sqrt{\pi a}\right) / \left[\Phi\left(c / a\right)\right] \tag{2}$$

In Eq.2, $\Phi(c/a)$ is the elliptic integral of the secondary type, whose value depends on the ratio (c/a) of semi-elliptic-crack axes in any crack-growth direction.
In our case, term "equivalent" means that fractographic estimation of stresses based on fatigue striations value related to material reaction on its complicated stress-state. This reaction is equivalent in stress level with opened propagated crack by Mode I.
The Eq.2 can be applied correctly to the crack starting from a distance of 1 mm or greater from the in-hole surface of the disk: at that distance, effect of the surface-stress concentration is negligibly for crack-growth over the length in 1 mm. However, the calculated equivalent stress is totally expressive of all the strengthening-and-weakening effects of prominent plastic deformation typical of even the very first loading cycle of low-cycle fatigue. We should stress on that the cracks to be in-service detected belong to a small kind as concerns a crack length (within 1 mm) and the growth behavior of fatigue-striation spacing (linearly dependent of the crack length). For such cracks, using the concepts of strain-range or J-integral would be of greater accuracy and meaning than the concept of stress because of well-developed plastic deformation.
Nevertheless, when estimating a relationship between the characteristics of material behavior in service and in bench tests, the concept of equivalent stress remains still proper. Indeed, irrelevant to the way of loading, a value of striation spacing always corresponds to just a respective unique value of stress-intensity factor, completely determined by a respective equivalent stress [4, 6].
The disk material exhibits maximum stress intensity factor $(K_e)_{\max}$ = 70 MPa m$^{1/2}$ at the moment that the growth behavior of a fatigue crack changes from steady to unsteady, the value of fatigue-striation spacing being close to 1.2 μm. One can see that both from the Paris' curve in term of crack growth rate and fracture morphology of the material. We calculated elliptic integrals for the boundaries between Zone-I and Zone-II fractures of the broken P-1 and P-2 disks and for the line of 1.2 μm striation spacing in one of the opened cracks which were also discovered in P-1 disk; the integrals appeared 1.0158, 1.0325, and 1.09, respectively. With the cracks dimensions and the respective above-calculated values substituted to Eq.1, we calculated σ_e as 1130, 1320, and 1180 MPa. The calculations could be done owing to fractographic examination of those broken disks and artificially opened fatigue crack. Thus estimated equivalent stresses approximate to those acquired from the finite-element analysis of a complex stressed state of a disk with the shear stresses taken into account [11]. The above stress figures appear to exceed more than twice the stress level commonly acceptable for the disks. Accordingly, the disks bolted to the shaft through the holes in this particular way must be of a low expected durability.
We compared how much the disks were loaded in the bench-tests and in service. In so doing, we assumed that the stress-intensity factors are the same for the same values of fatigue-striation spacing irrespective of the loading prehistory of the disks because there were not discovered difference in material properties for all investigated disks. The stress- and strain-intensity factors were both discussed as representative of a stress pattern whether in bench-tests or service. From a comparative analysis, one can have a characteristic indicating how much the disks were stressed relative to one another. Hence, we can write,

$$\left(K_e\right)_0 = \left(K_e\right)_t \quad \text{for } \delta = 1.2 \text{ mm} \tag{3}$$

or

$$\left(\sigma_e\right)_0 / \left(\sigma_e\right)_t = \left(a_t / a_0\right)^{1/2} / \left(\Phi_0 / \Phi_t\right) \tag{4}$$

Here, in Eqs.3 and 4, subscripts "0" and "t" indicate to the cracking conditions in service and bench-tests, respectively.
In the bench-tested disk, the 1.2 μm spacing of fatigue striations corresponded to the crack depth and width of 3.5 and 8.0 mm, respectively, which was significantly greater than in the in-service disks. For this crack geometry, 1.19 is the value of elliptic integral. With the crack-geometry parameters substituted in equation (3), we have

$$\left(\sigma_e\right)_0 / \left(\sigma_e\right)_t = \left(3.5 / 1.2\right)^{1/2} / \left(1.016 / 1.19\right) = 1.46 \quad (5)$$

According to our calculations, the bench tests in an engine stress the disk to a level nearly as low as 0.75 of the level typical of real service. Assume that the disk durability reduces exponentially with increasing stress level for the exponent greater than two. In such a case, using the bench-test data in the durability simulation, we twice as much overestimates the expected operating time of the disk in service.
The above calculations all related to the early fracture zone, in which fatigue striations formed. Moreover, one can see from the formation pattern of fatigue striations that the in-service loading of the disk occurred under constant-strain-amplitude conditions. This was also evident from the finding that unsteady crack growth covered quite a long distance. Zones II and III of crack growth occupy significant portions of this area. The above data indicated that the stress level of the disk should be substantially reduced.
To establish the greatest tolerable period of disc service between two sequential inspections (solve the question of inspection frequency), we should have estimated the growth period of a crack throughout these two zones. We did such an estimation based on the knowledge of the laws of fatigue cracking. In so doing, we assumed that

- ✓ the crack growth accelerated steadily throughout Zone II of the fracture as long as it was controlled by a constant strain amplitude (like in Zone I of the fracture) and
- ✓ the distance between two nearest boundaries, separating two regions of different oxidation tints and marking the crack-tip positions, corresponds to a crack increment during one flight: indeed, not less than five typical tints changed regularly in Zone III of the disk-web fracture.

Within a distance 20-mm in depth from the hole-bolt-surface (Zone-II), fracture immediately adjacent to the central hole (to pass the engine shaft) of the disk. The greatest interboundary distance approximated 1.5 mm for a single-tint region. With the above assumptions, crack-growth rate measured within a one-flight 1.2-mm crack path, and a relationship obtained earlier [4], the estimation looked as

$$N_{p2} = lg\left(1.5 / 1.2 x 10^{-3}\right) / lg\left(1 + 1.5 / 18.8\right) = 110 \text{ cycles} \quad (6)$$

Thus calculated a figure indicates that the crack might grow for less than 1000 flights in any of the above fracture zones (mind the Tab. 2 data). The crack-growth period may exceed 50% total durability of a part under the low-cycle fatigue conditions. Hence, according to the above calculations, we should expect fatigue cracks to appear in many disks that passed more than 2000 flights. Besides, quite a number of those cracks should have shown dimensions beyond the steady-growth limit. To confirm this view, we inspected once all the disks that passed more than 2700 flights. We did it *insitu* with the eddy-current method, the rear bearing of the disk removed.
Of those disks, 40% turned out to reveal fatigue cracks. The applied method is low sensitive compared with, e.g., a dye-penetrate one. In addition, accessing into the holes was difficult. Therefore, we could be quite certain that the real portion of the discs with service-induced cracks (including small ones) is significantly greater. Based on this once-only inspection, a limiting operating time of 2700 flights was introduced into practice.
Accordingly, the disk design was modified as concerned the way of fastening a disk to the engine shaft. With the new design, stress concentration was reduced to result in a nearly thirty-fold increased durability of the disk. The discs that passed more than 2700 flights were first to be replaced by the newly designed disks.
The replacement activity of the old- by new-type discs required time. Hence, the service safety was to be ensured with the old-type disks still in service. While the new-type disks were being gradually put in use instead of the old ones, the problem was temporarily solved with the *damage-tolerance approach* applied. In so doing, a recurrent inspection of the disks by the eddy-current method was put into practice to examine the area between the hub and web as frequent as

- ✓ after each 50 flights for the operating time not longer than 2000 to 2400 flights;
- ✓ after 20 flights for the operating time of 2400 to 2500 flights;
- ✓ after four (plus two) flights for the operating time of 2500 to 2600 flights; and
- ✓ after two (plus two) flights for the operating time of 2600 to 2700 flights.

These periodicities were recommended based on the fractographic data and because the desired inspecting area of a disk (crosspieces between the holes for a bolt and for the engine shaft) was difficult to access in the discussed structure. With the rare disk-bearing structure not moved, the fillet area between the disk hub and web was only accessible for inspecting.

In the web, a crack-growth period did not exceed five flights. Yet it achieved 110 flights in the above-mentioned crosspieces. Assuming a once overseen crack likely, the above-mentioned inspection frequencies were introduced.
The recommended inspection sequence was introduced up to the disk-shaft joint has been redesigned. The disk to shaft joining was organized by the inner diameter of the discussed disk hub. The reconstructed disk joint to shaft has shown airworthiness for aircrafts with this type of engine without fatigue in-service disks cracking in recommended design service goal.

CONCLUSION

1. In-service turbine disks fatigue cracking of EI437B superalloy in aero-engine NK8-2u of the III stage was considered and LCF regime of their failure was demonstrated.
2. Unified description of fatigue crack growth in metals was applied to stress equivalent σ_e value estimation based on fatigue striations measurement in fracture surfaces. It was shown that in-service stress σ_e -level is very high that directed to earlier crack origination by the disk hole-surfaces in bolt-joint than it was designed.
3. Crack growth period for in-service cracked disks was estimated based on fatigue striation spacing measurements. It was discovered one-to-one relation between fatigue striation spacing and crack increment in one flight.
4. Based on crack growth period estimation results, it was recommended in-service non-destructive disks inspection with different intervals in dependence of operating time in service at the moment of developed tests.

REFERENCE

[1] Fractography in Failure Analysis. ASTM STP 645, ASTM, Philadelphia, (1978).
[2] Failure Analysis and Prevention: Metals Handbook, ASM. Handbook Commit., U.S., 11 (1986).
[3] L. Varkoly, J. Zuidema, B. Varkolyova, M. Chalupova, Fatigue failures of materials. TU Delf, Netherlands, (1998) 235.
[4] A. A. Shanyavskiy, Tolerance in-service fatigue cracking of aircraft structures. Synergetics in engineering applications. Ufa, Russia, (2003).
[5] A. A. Shanyavskiy, In: PROBAMAT- 21st Century: Probabilities and Materials, Ed. K. Franzisconys, Kluwer Academic Publisher, Netherlands, (1998) 11.
[6] A. A. Shanyavskiy, In: New results in fatigue and fracture, Eds: W. Kasprzak, E. Macha, V. Panasyuk, M.K. Schaper, Mechanika, Opole-Zakopane, Poland; 1 (300) (2005) 277.
[7] A. A. Shanyavskiy, Procedia Engineering, 2(1) (2010) 241.
[8] A. Carpinteri, A. Spagnoli, S. Vantadori, Fatigue Fract Engng Mater Struct, 26 (2003) 515.
[9] A. A. Shanyavskiy, Fatigue Fract Engng Mater Struct, 19 (1996) 1445.
[10] I. V. Demyanushko, I. A. Birger, Mashinostroenie, Moscow, Russia, (1978).
[11] I. V. Demyanushko, Yu. M. Temes, Problems of Strength, 4 (1981) 49.
[12] A. A. Shanyavskiy, A. I. Losev, M. D. Banov, Fatigue Fract. Engng Mater. Struct., 18 (1998) 539.
[13] V. I. Astafiev, D. G. Fedorchenko, L. N. Tzypkaikin, In: Sixth Intern. Fatigue Conf., Fatigue'96, Berlin, 6-10 May, 1 (1996) 499.
[14] V. I. Zeitlin, D. G. Fedorchenko, Problems of Strength, 2 (1983) 13.
[15] G.J. Lloyd, Fatigue at High temperature, Applied Science Publishers, London, New York, (1983) 187.
[16] Y. Murakami, In: Low Cycle Fatigue, Eds. H. D. Solomon, G. R. Halford, L. R. Kaisand, P. Leis, ASTM STP 942, ASTM, Philadelphia, (1986) 1048.
[17] Y. Murakami (Ed.) Stress Intensity Factors Handbook, Pergamon Press, Oxford (1987).

NOMENCLATURE

a	minor semi-axis of elliptical fatigue crack
c	major semi-axis of elliptical fatigue crack
da/dN	crack-growth rate in the depth direction
dc/dN	fatigue-crack-growth rate at the specimen surface
K_I	Mode I stress intensity factor

K_{max}	maximum Mode I stress intensity factor
$(K_{max})_h$	threshold value of stress-intensity factor to start of hold-time influencing fatigue cracking
K_e	equivalent Mode I stress intensity factor
$(K_e)_{max}$	maximum value of K_e for steady crack growth
ΔK_{eff}	effective stress intensity factor in Mode I crack opening
N_f	lifetime to failure (durability)
N_p	fatigue crack growth period
Δq_i	range of stress in bifurcation i-area
R	stress ratio
δ	fatigue striation spacing
λ	biaxial stress ratio (σ_1/σ_2)
$\sigma_{0.2}$	0.2% offset yield strength
σ_1	tensile stress opening fatigue crack
σ_2	tensile or compressive stress acting in a direction perpendicular to the σ_1-direction
σ_{wi}	mean stress for bifurcation i-area
σ_u	Ultimate tensile stress

Special Issue: Russian Fracture Mechanics School

Development of a formalism of movable cellular automaton method for numerical modeling of fracture of heterogeneous elastic-plastic materials

S. Psakhie, E. Shilko, A. Smolin, S. Astafurov, V. Ovcharenko
Institute of strength physics and materials science SB RAS, Tomsk, Russia
astaf@ispms.tsc.ru

ABSTRACT. A general approach to realization of models of elasticity, plasticity and fracture of heterogeneous materials within the framework of particle-based numerical methods is proposed in the paper. It is based on building many-body forces of particle interaction, which provide response of particle ensemble correctly conforming to the response (including elastic-plastic behavior and fracture) of simulated solids. Implementation of proposed approach within particle-based methods is demonstrated by the example of the movable cellular automaton (MCA) method, which integrates the possibilities of particle-based discrete element method (DEM) and cellular automaton methods. Emergent advantages of the developed approach to formulation of many-body interaction are discussed. Main of them are its applicability to various realizations of the concept of discrete elements and a possibility to realize various rheological models (including elastic-plastic or visco-elastic-plastic) and models of fracture to study deformation and fracture of solid-phase materials and media. Capabilities of particle-based modeling of heterogeneous solids are demonstrated by the problem of simulation of deformation and fracture of particle-reinforced metal-ceramic composites.

KEYWORDS. Particle-based approach; Movable cellular automata; Discrete elements; Many-particle interaction; Elastic-plastic medium; Fracture; Metal-ceramic composites.

INTRODUCTION

A modern theoretical approach used for description of heterogeneous solid is based on one of two concepts of representations of the medium: continuum or discrete. These concepts were suggested as memorandums to Paris Academy of Sciences by Cauchy and Navier, correspondingly, in the early 19th century. Notwithstanding the fact that discrete concept reflected discrete structure of matter more correctly at different spatial scales, during the following one and the half century the continuum concept prevailed. This was due to the fact that this concept gives the advantage of analytical description. It is necessary to note, that most of computational techniques used to model the behavior of condensed media is based on the continuum concept. The best known within this class of methods are finite element and finite-difference methods [1, 2]. At the present time meshless algorithms for numerical solution of equations of continuum (particle-in-cell method [3], SPH [4, 5], SPAM [6, 7]) are widely developed and applied as well. Numerical methods belonging to continuum concept has been proven quite efficient in solving problems of deformation of complex heterogeneous media of various nature. However, there exists a wide range of problems in which loading of a medium involves multiple fracture and slip of fragments, intense mass transfer, including effects of mass mixing, etc. Examples of these problems are flow of granular and loose media (powders, sands, soils), compaction of powder mixtures, processes in the contact spots of friction pairs, etc. These problems are too difficult to solve by methods of the continuum concept.

A promising class of numerical methods that "genetically" fit for simulation of fracture of solids and mass mixing are particle-based methods. These methods are widely used to study mechanical or thermomechanical response of solid-phase and liquid-phase systems at various scales up to the atomic scale. Note that the term "particle methods" is currently understood as a collective term and is referred to quite diverse numerical techniques including methods based on the formalism of the discrete concept in mechanics of solids as well as meshless numerical methods of continuum concept. Moreover, nowadays some modern realizations of conventional numerical methods (such as particle-finite element method [8]) are also referred to as particle methods. The following consideration will concern "conventional" particle methods.

In the framework of "conventional" particle methods simulated material is considered as an ensemble of interacting particles (elements) having finite size. Evolution of an ensemble is defined by solution of the system of Newton-Euler motion equations:

$$\begin{cases} m_i \dfrac{d^2\vec{R}_i}{dt^2} = \vec{F}_i = \sum\limits_{j=1}^{N_i}\left(\vec{F}_n^{ij} + \vec{F}_t^{ij}\right) \\ \hat{J}_i \dfrac{d^2\vec{\theta}_i}{dt^2} = \sum\limits_{j=1}^{N_i}\vec{M}_{ij} \end{cases} \tag{1}$$

where $\vec{R}_i$ and $\vec{\theta}_i$ are radius-vector and rotation angle of the particle i; m_i and $\hat{J}_i$ are particle mass and moment of inertia; $\vec{F}_i$ is the total force applied to the particle i from the surroundings; $\vec{F}_n^{ij}$ and $\vec{F}_t^{ij}$ are forces of normal and tangential interaction of considered element i with neighbor j, $\vec{M}_{ij}$ is momentum of force, N_i is a number of neighbors. Conventionally only nearest neighbors of particle i are taken into account in (1). It is seen from (1) that "macroscopic" (integral) properties of ensemble of particles are defined by the structure and parameters of potential (potential forces) of element interaction.

It should be noted that the particle methods have their origin in the well-known molecular dynamics methods (MDM) [9] applied to study of the response of a medium at the atomic scale. At the same time, capabilities of atomic description of the behavior of the solid body on spatial and temporal scales that are of interest for engineering applications are severely limited. This led to the development of numerical methods for meso- and macroscopic description of a medium (particle methods) on the base of MDM. In the framework of these methods structural elements (particles) have finite size and hence interaction with the immediate surroundings only is taken into account.

The best known representative of conventional particle-based methods is the discrete element method (DEM) [10, 11]. Its basic foundation was independently proposed by P.A. Cundall (distinct element method [10]) and Greenspan (particle modeling [12]) at the end of 1970s. At the present time these two similar methods have been developed into a quantity of methods and models, which are referred to collectively as DEM.

A distinctive feature of DEM in comparison with other particle-based methods is the presence of predefined initial shape of elements. Element shape can change (reversible or irreversibly) as a consequence of loading. This feature determined preferential development of the formalism of DEM towards correct modeling of flow of loose or weakly bonded porous materials [13-17]. In the numerical description of such systems, an adequate accounting of geometric characteristics of discrete elements imitating particles of loose medium and peculiarities of contact interaction of elements is of crucial importance. In a general case particles of the simulated medium (discrete elements) are considered as super-quadrics [15] or polygons [18] rather than as disks or spheres (these shapes are used within the simplest models of loose material). Central forces $\vec{F}_n^{ij}$ therewith can generate torque, which is impossible in the interaction of disks or spheres. At the same time, far less attention is paid to the analysis of structural form of potential (or potential force) of element interaction in loose medium. Indeed, the vast majority of models of interaction between discrete elements is based on the use of approximation of pair-wise elastic or elastic-plastic interaction. Such simplification is related, in particular, with the need to model long-time evolution of an ensemble of a large number of elements (up to tens millions particles in 3D problems). It should be noted that the range of problems that would be correctly solved with use of the approximation of pair-wise interaction between elements is limited by description of deconsolidated (including decompacted) materials and media with a large enough percentage of free volume (particulate media). In such systems the influence of lateral spread of deformed elements can be neglected. Therefore, the main areas of application of models with pair-wise interaction of discrete elements of complex shape are the theoretical study of flow (including transportation), mixing, segregation and compaction of granular materials in industrial and laboratory plants as well as under natural conditions (modeling of landslides and avalanches).

At the same time, the success of DEM in description of mechanical processes in consolidated solids (metals, low porous ceramic materials and rocks) is less visible. Hereinafter the term "consolidated solid" means low porosity or pore-free material retaining its shape under unconfined conditions. The characteristic features of the interaction of discrete elements, whose ensemble models consolidated material, are taking into account the resistance of element pairs both to compression and tension as well as limitation of the value of shear resistance (F_t^{ij}) by adhesion/cohesion strength rather than by coefficient of friction. Particular form of discrete elements modeling fragments of consolidated material or medium does not play a fundamental role. Conventionally the disk (in 2D problems) or spherical (in 3D problems) form of the element is used. At the same time the structural form of normal and tangential potential forces of discrete element interaction is of crucial importance for modeling consolidated materials.

In particular, the use of conventional models of pair-wise potential interaction can lead to a series of artificial manifestations (effects) of response of the ensemble of elements that are not inherent to modeled medium. Most important of them are:

- ✓ strongly pronounced dependence of macroscopic mechanical properties of ensemble of discrete elements on packing type (close, square, stochastic,…);
- ✓ problems in realization of desired ratio between macroscopic elastic moduli (shear and bulk moduli, Young modulus and Poisson ratio and so on), especially in case of regular packing;
- ✓ problems in correct simulation of irreversible strain accumulation in ductile materials, whose plasticity is provided by mechanisms of crystal lattice scale.

At present there are several methods of partial solutions of these problems. They are associated with generation of stochastic dense packing of nonuniform-sized elements [19], definition of particle interaction constants using lattice approximation of continuum [20] and so on. However, the capabilities of these solutions are strongly limited, because they do not remove the main limitation of the pair-wise approximation in description of element interaction, namely the neglect of the change of discrete element volume under loading. This problem may be solved with use of many-body interaction forces.

At present time different authors develop at least several approaches to description of the response of consolidated solids by ensemble of discrete elements with use of many-particle interaction models [20, 21]. However, the ability of these models at present is limited to description of elastic-brittle materials. Therefore the present paper is devoted to the development of a general approach to building many-body forces of discrete element interaction to simulate deformation and fracture of consolidated heterogeneous media with various rheological characteristics.

The proposed approach is realized within the framework of movable cellular automaton method (MCA) [22-25]. MCA method is a hybrid computational technique combining mathematical formalisms and capabilities of DEM [10, 11, 19] and conventional concept of cellular automata [26-28]. Originally MCA method was developed to study complex coupled processes in solids including deformation and fracture, phase transitions, chemical reactions and so on [22, 29]. In this case, to describe the mechanical interaction of elementary structural units (cellular automata) the basic postulates and relations of DEM are used. Therefore in modeling "pure" mechanical problems MCA method can be considered as an implementation of DEM, which has the following principal difference from other implementations. During the construction of the mathematical formalism of MCA method general structural forms of the central and tangential potential forces of interaction of movable cellular automata were derived. Central interaction between movable automata has many-body form, whereas tangential one has pair-wise form [24]. Thus, the interaction between movable cellular automata originally supposed to be many-particle. Note that conventional formalism of discrete elements does not have any supposition about the form of interaction potential/force.

In this paper consideration will be conducted by the example of two-dimensional problem statement, which provides the possibility of movement of three-dimensional objects in one plane only. Construction of many-particle interaction in the three-dimensional problem formulation is similar. Note also that the following approach and models are applicable not only for MCA method, but for a wide range of implementations of discrete element method. Therefore both terms (movable cellular automata and discrete elements) will be used in the text.

MAIN PARAMETERS OF INTERACTION OF DISCRETE ELEMENTS.

In the framework of proposed approach to modeling consolidated solids the description of the interaction of discrete elements (or movable cellular automata) is based on the use of two types of states of a pair of interacting elements. They are associated with presence (linked state) and absence (unlinked state) of chemical bond (or

cohesion/adhesion) between elements (Fig. 1). The feature of the central interaction of linked elements is the presence of resistance to both compression and tension. At the same time, the interaction of unlinked elements relates to the contact type and involves only the resistance to compression. Another difference of element interaction in linked and unlinked pairs is the fact that the magnitude of the tangential potential force is limited by the bonding strength in linked state, and by the dry friction force for contacting (unlinked) pairs. Thus, the ensemble of linked discrete elements simulates consolidated solid. In this case, discontinuities in such solid (damages, cracks, pores and so on) can be modeled by specifying unlinked pairs or by removing discrete elements.

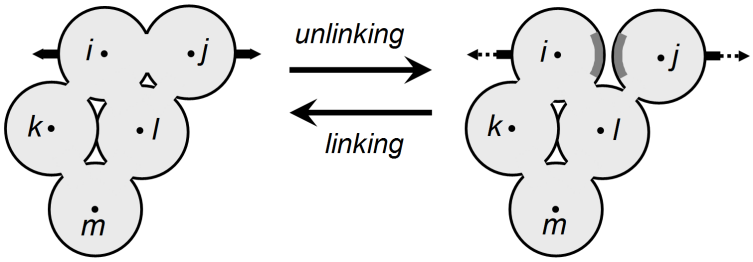

Figure 1: Schematic presentation of switching between *linked* (at the left) and *unlinked* (at the right) states of the pair of discrete elements *i* and *j*.

Switching between the *linked* and *unlinked* states of the pair is based on chosen criteria. Specific form of the criteria of direct (*linked→unlinked*) and reverse switch is defined by the nature of the materials modeled by discrete elements. In general it can be noted that switching criteria are functions of spatial and force parameters of the mechanical interaction between the elements. More details on this aspect of the interaction between discrete elements are discussed in Section 4.
In framework of the conventional models (1) the mechanical interaction between particles is divided into normal or central (along the line connecting the centers of mass of elements) and tangential constituents. Each of these components is controlled by the corresponding spatial parameters.
Normal interaction is determined by the value of element-element overlap h_{ij}:

$$h_{ij} = r_{ij} - r_{ij}^0 = r_{ij} - \left(d_i/2 + d_j/2\right) \tag{2}$$

where r_{ij} is the current distance between the centers of mass of the elements i and j, r_{ij}^0 is the original distance (in undeformed state), d_i and d_j are the sizes of elements. *Linked* pair of discrete elements can resists both to compression and tension, therefore the value of h_{ij} could be positive (tension of the pair) or negative (compression). In general, the discrete elements i and j can be characterized by different material properties, so that the contribution of each of them to h_{ij} may be different. In this regard, the concept of the distance between the center of mass of the element and the central point of plane of interaction (or, using the traditional terminology, the contact point) is introduced to the model:

$$r_{ij} = q_{ij} + q_{ji} \tag{3}$$

where q_{ij} and q_{ji} are the corresponding distances (Fig.2). Initial values of q_{ij} and q_{ji} are $d_i/2$and $d_j/2$ correspondingly.

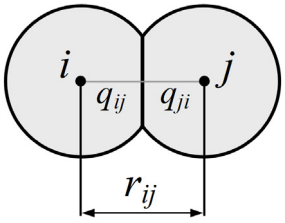

Figure 2: Parameters of spatial relation of the pair of discrete elements *i* and *j*: distance between mass centers (r_{ij}) and distances from mass centers of interacting elements to the center of plane of interaction (q_{ij} and q_{ji}).

For convenience hereinafter spatial parameters of central interaction of discrete elements will be considered in reduced units (deformations):

$$\Delta r_{ij} = \Delta\varepsilon_{ij}\left(d_i + d_j\right)/2 = \Delta q_{ij} + \Delta q_{ji} = \Delta\varepsilon_{i(j)}\, d_i/2 + \Delta\varepsilon_{j(i)}\, d_j/2\,, \tag{4}$$

where symbol Δ hereinafter indicates increment of corresponding parameter during one time step Δt, ε_{ij} is central strain of the pair *i-j*, variables $\varepsilon_{i(j)}$ and $\varepsilon_{j(i)}$ are central strains of discrete elements *i* and *j* in the pair (in the general case $\varepsilon_{i(j)} \neq \varepsilon_{j(i)}$).
Tangential interaction is determined by the relative shear displacement l_{ij}^{shear} of the elements in the pair. The value l_{ij}^{shear} is calculated in incremental fashion taking into account the rotation of elements [19, 22]:

$$\frac{\Delta l_{ij}^{shear}}{\Delta t} = V_{ij}^{shear} = V_{ij}^{tang} + \omega_i q_{ij} + \omega_j q_{ji}, \tag{5}$$

where V_{ij}^{tang} is the tangential component of the relative velocity vector $\vec{V}_{ij}$ for the elements *i* and *j* ($\vec{V}_{ij} = \vec{V}_j - \vec{V}_i$, $\vec{V}_i$ and $\vec{V}_j$ are velocity vectors of the centers of mass of the elements), ω_i and ω_j are angular velocities of the elements (in considered two-dimensional approximation they actually are signed scalars). Note that the accounting of angular velocities in (5) is required for tracking the rotation of the plane of interaction [19, 22].
As in the case of the central interaction, the contribution of the elements *i* and *j* in the shear deformation of the pair *i-j* can be different. By analogy with the central strains (4) the shear angles of the discrete elements *i* and *j* in the pair *i-j* are introduced:

$$\Delta l_{ij}^{shear} = V_{ij}^{shear} \Delta t = \Delta\gamma_{ij} r_{ij} = \Delta\gamma_{i(j)} q_{ij} + \Delta\gamma_{j(i)} q_{ji}, \tag{6}$$

where γ_{ij} is shear angle for the pair *i-j*, variables $\gamma_{i(j)}$ and $\gamma_{j(i)}$ are shear angles of discrete elements *i* and *j* in the pair (in the general case $\gamma_{i(j)} \neq \gamma_{j(i)}$).
Rotation of discrete elements can lead to "bending" of *linked* interacting pairs (Fig.3). This type of relative motion of surfaces of elements *i* and *j* is not taken into account by expression (5). Nevertheless such type of relative motion of "anchor surfaces" must be accompanied by appearance of special moment of resistance force. So, the special torque $\vec{K}^{gear}$ directed against pair bending (Fig.3) and having opposite signs for two elements of the pair is introduced:

$$\vec{K}_{ij}^{gear} = -\frac{q_{ij}}{q_{ji}} \vec{K}_{ji}^{gear} \tag{7}$$

Value of the torque $K_{ij}^{gear} = \left|\vec{K}_{ij}^{gear}\right|$ is defined by bending angle γ_{ij}^{gear}, which is calculated by analogy with γ_{ij}^{shear}:

$$r_{ij} \frac{\Delta\gamma_{ij}^{gear}}{\Delta t} = V_{ij}^{gear} = \omega_i q_{ij} - \omega_j q_{ji} \tag{8}$$

By analogy with the central (4) and shear (6) strains the bending angles of the discrete elements *i* and *j* in the pair *i-j* are introduced:

$$r_{ij} \Delta\gamma_{ij}^{gear} = V_{ij}^{gear} \Delta t = \Delta\gamma_{i(j)}^{gear} q_{ij} - \Delta\gamma_{j(i)}^{gear} q_{ji} \tag{9}$$

where $\Delta\gamma_{i(j)}^{gear}$ and $\Delta\gamma_{j(i)}^{gear}$ are bending angles of discrete elements *i* and *j* in the pair (in the general case $\left|\gamma_{i(j)}^{gear}\right| \neq \left|\gamma_{j(i)}^{gear}\right|$). As follows from the definition of torque K_{ij}^{gear}, bending angles $\gamma_{i(j)}^{gear}$ and $\gamma_{j(i)}^{gear}$ have opposite signs (in contrast to shear angles), as reflected in the expression (9).

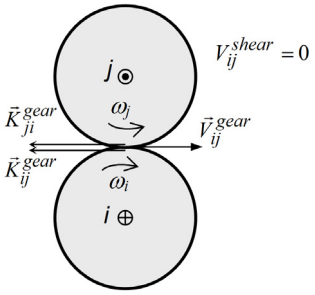

Figure 3: An example of bending of the pair of *linked* elements *i* and *j* for the simple case: $\omega_i = -\omega_j$, $q_{ij} = q_{ji}$ and $V_{ij}^{tang} = 0$.

Note that in the "conventional" models of the interaction of discrete elements do not take into account "bending" of the pair of discrete elements. This is perfectly valid in describing the contact interaction of *unlinked* elements. However, when considering *linked* pairs, accounting of this effect may be crucial.

It follows from (5), (6) and (9) that strains of elements *i* and *j* in the pair *i-j* differ from each other. The rule of strain distribution in the pair is inseparably linked with the expression for element interaction forces and will be discussed in the following Section.

By analogy with strains the forces of central (F_n^{ij}) and tangential (F_τ^{ij}) interaction of discrete elements *i* and *j* will be considered in reduced (specific) units:

$$\begin{cases} F_n^{ij} = \sigma_{ij} S_{ij} \\ F_t^{ij} = \tau_{ij} S_{ij} \end{cases} \tag{10}$$

where σ_{ij} and τ_{ij} are normal and shear stresses (specific forces) correspondingly, S_{ij} is an area of the plane of interaction of elements (contact area).

Note that the definition of S_{ij} is different for the description of consolidated and granular materials by ensemble of discrete elements. Thus, in the case of granular material the initial value of S_{ij} in the undeformed state (S_{ij}^0) is defined by shape of the elements *i* and *j* and by their mutual orientation. For example, $S_{ij}^0 = 0$ for the elements having a disk (2D case) or spherical (3D case) shape. With increase of compression the value of contact area grows up as a function *of* h_{ij}: $S_{ij} = S\left(h_{ij}\right)$, $h_{ij} < 0$. This kind of dependence is determined by the geometrical characteristics of both elements and their mutual orientation. At the same time, under the simulation of consolidated material the parameter S_{ij}^0 is obviously finite and determined by the ratio of sizes of the elements *i* and *j* and by features of the local packing of discrete elements in the neighborhood of the pair *i-j*. As a rule, the S_{ij}^0 is defined to minimize the volume of voids in simulated solid (note that in bonded-particle model [19] this is realized through introduction of the special interfacial zone between two bonded (*linked*) elements and by assigning its geometrical characteristics). Peculiarities of the procedure of assigning the initial area of plane of element interaction lead to the fact that in most models of consolidated solids a simplified form of discrete elements is used (disks or spheres).

In two-dimensional approximation discrete elements are considered as disks with diameters d_i in the plane of motion and the same value of height *h* for all of them. Note that in the case of a regular packing of elements with the same size $d_i=d$ the value S_{ij}^0 is determined by type of packing. For example, for a close packing $S_{ij}^0 = dh/\sqrt{3}$, for a square package $S_{ij}^0 = dh$ (Fig.4).

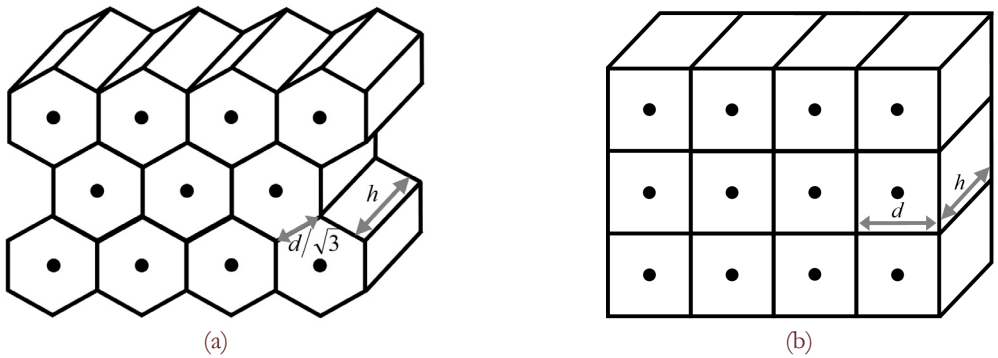

(a) (b)

Figure 4: Examples of regular packing of elements in 2D problem statement: close packing (a) and square packing (b).

Change of S_{ij} during deformation of the pair of discrete elements *i* and *j* is determined by approximations of applied model of element interaction. In particular, at small values of pair strain $\varepsilon_{ij} < 10^{-2}$ (typical strain range for brittle materials) the value of S_{ij} can rely constant ($S_{ij} = S_{ij}^0$).However, at larger pair strains the value of S_{ij} has to be considered as a function of the deformation process in the pair *i-j*.

GENERAL FORMALISM OF PROPOSED APPROACH TO BUILDING MANY-PARTICLE INTERACTION OF DISCRETE ELEMENTS

Authors propose a general approach to building many-body forces of discrete element interaction to simulate deformation and fracture of consolidated heterogeneous materials. The structural form of these forces is borrowed from the form of interatomic forces calculated on the basis of embedded-atom method. In the framework of embedded-atom model [30] the general expression for potential energy of atom i contains a pair interaction potential ϕ as a function of distance r_{ij} between atoms i and j and a "density-dependent" embedding function F (here it depends on electron charge density $\bar{\rho}_i$):

$$E_i(\mathrm{R}) = \sum_{j \neq i} \varphi\left(r_{ij}\right) + \sum_i F\left(\bar{\rho}_i\right), \tag{11}$$

where $\bar{\rho}_i = \sum_{j \neq i} \rho_j\left(r_{ij}\right)$ is a sum of contributions of neighbors j to local value of density at the location of atom i.

By analogy with this expression the following general form of notation of the expression for the force $\vec{F}_i$ acting on discrete element i from surroundings is proposed [23, 31]:

$$m_i \frac{d^2 \vec{\mathrm{R}}_i}{dt^2} = \vec{F}_i = \sum_{j=1}^{N_i} \vec{F}_{pair}^{ij} + \vec{F}_\Omega^i \tag{12}$$

This force is written as a superposition of pair-wise constituents $\vec{F}_{pair}^{ij}$ depending on spatial position/displacement of element i with respect to nearest neighbor j and of volume-dependent constituent $\vec{F}_\Omega^i$ connected with combined influence of nearest surroundings of the element.

When simulating locally isotropic materials/media with various rheologies the volume-dependent contribution $\vec{F}_\Omega^i$ can be expressed in terms of pressure P_i in the volume of discrete element i as follows [23]:

$$\vec{F}_\Omega^i = -A_i \sum_{j=1}^{N_i} P_i S_{ij} \vec{n}_{ij}\ , \tag{13}$$

where S_{ij} is square of area of interaction (contact) of elements i and j, $\vec{n}_{ij}$ is a unit vector directed along the line between mass centres of considered elements, A_i is a material parameter.

In such a formulation the right part of the expression (12) can be reduced to the sum of forces of interaction in pairs of elements and divided into central ($\vec{F}_n^{ij}$) and tangential ($\vec{F}_t^{ij}$) constituents:

$$\vec{F}_i = \sum_{j=1}^{N_i}\left(\vec{F}_{pair}^{ij} - A_i P_i S_{ij} \vec{n}_{ij}\right) = \sum_{j=1}^{N_i}\left[\left(F_{pair,n}^{ij}\left(h_{ij}\right) - A_i P_i S_{ij}\right)\vec{n}_{ij} + F_{pair,t}^{ij}\left(l_{is}^{shear}\right)\vec{t}_{ij}\right] = \sum_{j=1}^{N_i}\left(\vec{F}_n^{ij} + \vec{F}_t^{ij}\right), \tag{14}$$

where $F_{pair,n}^{ij}$ and $F_{pair,t}^{ij}$ are central and tangential components of pair-wise interaction force that depend on the values of element-element overlap h_{ij} and relative shear displacement l_{ij}^{shear}, $\vec{t}_{ij}$ is a unit vector which is oriented perpendicular to the line joining the centers of mass of elements i and j. In terms of specific interaction forces σ_{ij} and τ_{ij} the expression (14) can be rewritten in the following form:

$$\begin{cases} \sigma_{ij} = \sigma_{ij}^{pair}\left(\varepsilon_{ij}\right) - A_i P_i \\ \tau_{ij} = \tau_{ij}^{pair}\left(\gamma_{ij}\right) \end{cases} \tag{15}$$

where σ_{ij}^{pair} and τ_{ij}^{pair} are specific values of pair-wise components of interaction force. In fact σ_{ij} and τ_{ij} have the meaning of specific forces of response of the element/automaton i to the impact of the neighbour j. Taking into account the need to implement Newton's third law for interacting pairs of discrete elements ($\sigma_{ij}=\sigma_{ji}$ and $\tau_{ij}=\tau_{ji}$) the expression (15) has to satisfy the following equality:

$$\begin{cases} \sigma_{ij} = \sigma_{ij}^{pair}\left(\varepsilon_{ij}\right) - A_i P_i \equiv \sigma_{ji} = \sigma_{ji}^{pair}\left(\varepsilon_{ij}\right) - A_j P_j \\ \tau_{ij} = \tau_{ij}^{pair}\left(\gamma_{ij}\right) \equiv \tau_{ji} = \tau_{ji}^{pair}\left(\gamma_{ij}\right) \end{cases} \qquad (15')$$

The equality (15′) provides the basis for calculation of contributions of elements i and j ($\varepsilon_{i(j)}$ and $\varepsilon_{j(i)}$, $\gamma_{i(j)}$ and $\gamma_{j(i)}$) in the total pair strains ε_{ij} and γ_{ij}.

Note that although the right part of the expression (14) formally confirms to notation of element interaction in conventional DE models (1) [16,19,32], their fundamental distinction consists in many-body form of central interaction of discrete elements in the proposed model.

It is seen from (14)-(15) that an important problem in building many-particle interaction is definition of local value of pressure (P_i) in the volume of discrete element. Authors propose to use an approach to calculation of pressure P_i (or, what is the same – of mean stress) in the volume of the element *i* that is based on the computation of components of average stress tensor in the volume of the element [19, 33]. In terms of central (F_n^{ij}) and tangential (F_t^{ij}) interaction forces the component $\bar{\sigma}_{\alpha\beta}^i$ of average stress tensor in the volume of element *i* can be written as follows [19, 24, 25]:

$$\bar{\sigma}_{\alpha\beta}^i = \frac{1}{\Omega_i}\sum_{j=1}^{N_i} S_{ij} q_{ij} \left(\vec{n}_{ij}\right)_\alpha \left[\sigma_{ij}\left(\vec{n}_{ij}\right)_\beta + \tau_{ij}\left(\vec{t}_{ij}\right)_\beta\right], \qquad (16)$$

where $\alpha,\beta = x,y,z$ (XYZ is a laboratory system of coordinates), Ω_i is a current value of the volume of element *i*, $\left(\vec{n}_{ij}\right)_\alpha$ and $\left(\vec{t}_{ij}\right)_\alpha$ are projections of unit-normal and unit-tangential vectors onto the X-axis of lab coordinates.

In considered two-dimensional problem statement this expression can be rewritten as follows:

$$\begin{aligned} \bar{\sigma}_{\alpha\beta}^i &= \frac{1}{\Omega_i}\sum_{j=1}^{N_i} q_{ij}\left[F_n^{ij}\cos\theta_{ij,\alpha}\cos\theta_{ij,\beta} \pm F_t^{ij}\cos\theta_{ij,\alpha}\sin\theta_{ij,\beta}\right] = \\ &= \frac{1}{\Omega_i}\sum_{j=1}^{N_i} q_{ij} S_{ij}\left[\sigma_{ij}\cos\theta_{ij,\alpha}\cos\theta_{ij,\beta} \pm \tau_{ij}\cos\theta_{ij,\alpha}\sin\theta_{ij,\beta}\right] \end{aligned}, \qquad (16')$$

where $\alpha,\beta = x,y$ (*XY* is a plane of motion), $\theta_{ij,\alpha}$ is an angle between the line connecting mass centres of interacting elements *i* and *j* and axis α of laboratory system of coordinates (Fig.5), sign «±» implies use «+» in case of $\beta = x$ and use «–» in case of $\beta = y$. Components $\bar{\sigma}_{x\chi}^i$ and $\bar{\sigma}_{y\chi}^i$ are identically zero. Definition of $\bar{\sigma}_{\chi\chi}^i$ depends on constitutive equations of considered medium. Note that values of $\bar{\sigma}_{xy}^i$ and $\bar{\sigma}_{yx}^i$ coincide only in static equilibrium state of ensemble of discrete elements, while they can slightly differ at the stage of establishing static equilibrium. Therefore their mean value ($\left(\bar{\sigma}_{xy}^i + \bar{\sigma}_{yx}^i\right)/2$) is used in the proposed model (hereinafter it is called as $\bar{\sigma}_{xy}^i$).

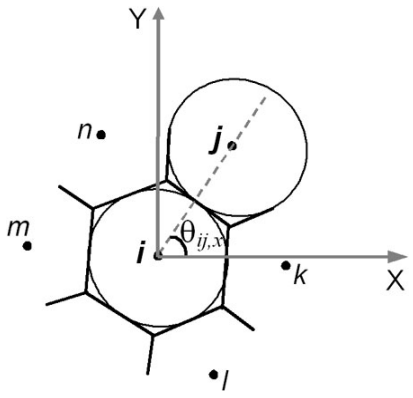

Figure 5: An example of definition of angle $\theta_{ij,\alpha}$ between line connecting mass centers of discrete elements in the pair *i-j* and α-axis of laboratory system of coordinates (α=*X* is considered here). The center of coordinate system is translated to the mass center of the element *i*.

Calculated in this way the stress tensor components can be used to determine the pressure in the volume of discrete element:

$$P_i = -\bar{\sigma}^i_{mean} = -\frac{\bar{\sigma}^i_{xx} + \bar{\sigma}^i_{yy} + \bar{\sigma}^i_{zz}}{3} \tag{17}$$

Note that calculated values of average stress tensor components can be used to determine other tensor invariants as well, for example stress intensity:

$$\bar{\sigma}^i_{\text{int}} = \frac{1}{\sqrt{2}}\sqrt{\left(\bar{\sigma}^i_{xx} - \bar{\sigma}^i_{yy}\right)^2 + \left(\bar{\sigma}^i_{yy} - \bar{\sigma}^i_{zz}\right)^2 + \left(\bar{\sigma}^i_{zz} - \bar{\sigma}^i_{xx}\right)^2 + 6\left[\left(\bar{\sigma}^i_{xy}\right)^2 + \left(\bar{\sigma}^i_{yz}\right)^2 + \left(\bar{\sigma}^i_{xz}\right)^2\right]} \tag{18}$$

It follows from (1), (14)-(16) that the central problem in the framework of proposed approach to building many-body interaction of discrete elements (or movable cellular automata) is to determine expressions for σ_{ij} and τ_{ij}, which provide necessary rheological characteristics of mechanical response of ensemble of elements. Analysis of relationships (1), (14)-(16) leads to the conclusion that expressions for interaction forces could be directly reformulated from constitutive equations of considered medium (equations of state).
Below is a derivation of such expressions for locally isotropic elastic-plastic materials.

DISCRETE ELEMENT INTERACTION FOR MODELING CONSOLIDATED ELASTIC-PLASTIC MEDIUM

Linearly elastic medium

Stress-strain state of isotropic linearly elastic medium is described on the basis of generalized Hooke's law. The following notation of this law will be used in the paper:

$$\begin{cases} \sigma_{\alpha\alpha} = 2G\varepsilon_{\alpha\alpha} + (1 - 2G/K)\sigma_{mean} \\ \tau_{\alpha\beta} = G\gamma_{\alpha\beta} \end{cases} \tag{19}$$

where $\alpha,\beta = x,y,z$; $\sigma_{\alpha\alpha}$ and $\varepsilon_{\alpha\alpha}$ are diagonal components of stress and strain tensors; $\tau_{\alpha\beta}$ and $\gamma_{\alpha\beta}$ are off-diagonal components; $\sigma_{mean} = \left(\sigma_{xx} + \sigma_{yy} + \sigma_{zz}\right)/3$ is mean stress; K is bulk modulus; G is shear modulus.

It can be seen that the form and the matter of expressions (19) for diagonal and off-diagonal stress tensor components are analogous to expressions (15) describing normal and tangential interaction of discrete elements. This leads to the simple idea to write down expressions for *force response* of automaton i to the impact of the neighbor j by means of direct reformulation of Hooke's law relationships:

$$\begin{cases} \sigma_{ij} = 2G_i\varepsilon_{i(j)} + \left(1 - 2G_i/K_i\right)\bar{\sigma}^i_{mean} \\ \tau_{ij} = 2G_i\gamma_{i(j)} \end{cases} \tag{20}$$

where G_i and K_i are shear and bulk elastic moduli of material filling the element i, $\varepsilon_{i(j)}$ and $\gamma_{i(j)}$ are central strain and shear angle of element i in the pair i-j (see Section 2), mean stress $\bar{\sigma}^i_{mean}$ is calculated using (17).
It is necessary to note that double shear modulus ($2G_i$) is used in the second expression of (20) instead of G in (19). This feature is concerned with the fact that relative tangential displacement of discrete elements leads to their rotation. Initiated rotation of the elements decreases twice the value of relative shear displacement in interacting pairs. So, to match "macroscopic" (integral) shear modulus of ensemble of discrete elements simulating consolidated solid with corresponding shear modulus G double value of shear modulus ($2G_i$) is used in the second expression of (20).
Proposed relationships (20) for forces of element response to the impact of the neighbor j are not arbitrary. It is easy to verify that substituting proposed expressions (20) for respond force in (16) automatically provides implementation of the Hooke's law for components of average stress ($\bar{\sigma}^i_{\alpha\beta}$) tensor in the volume of element i. Detail description is presented in Appendix A.
Proposed relationships (20) make it possible to calculate central and tangential interaction of discrete elements, whose ensemble simulates isotropic elastic medium. Taking into account the need to implement Newton's third law for

interacting pairs of discrete elements (15') and the need to distribute relative displacement of elements in the pair the expressions for specific interaction forces can be written as follows:

$$\begin{cases} \sigma_{ij}^{cur} = \sigma_{ij}^{pre} + \Delta\sigma_{ij} = \sigma_{ij}^{pre} + 2G_i\Delta\varepsilon_{i(j)} + \left(1 - \dfrac{2G_i}{K_i}\right)\Delta\bar{\sigma}_{mean}^{i} = \\ = \sigma_{ji}^{cur} = \sigma_{ji}^{pre} + \Delta\sigma_{ji} = \sigma_{ji}^{pre} + 2G_j\Delta\varepsilon_{j(i)} + \left(1 - \dfrac{2G_j}{K_j}\right)\Delta\bar{\sigma}_{mean}^{j} \\ \Delta r_{ij} = \Delta\varepsilon_{i(j)} d_i/2 + \Delta\varepsilon_{j(i)} d_j/2 \end{cases} \quad (21)$$

and

$$\begin{cases} \tau_{ij}^{cur} = \tau_{ij}^{pre} + \Delta\tau_{ij} = \tau_{ij}^{pre} + 2G_i\Delta\gamma_{i(j)} = \tau_{ji}^{cur} = \tau_{ji}^{pre} + \Delta\tau_{ji} = \tau_{ji}^{pre} + 2G_j\Delta\gamma_{j(i)} \\ V_{shear}^{ij}\Delta t = \Delta\gamma_{i(j)} d_i/2 + \Delta\gamma_{j(i)} d_j/2 \end{cases} \quad (22)$$

Here, relations for calculating the central and tangential interaction forces are written in incremental fashion (in hypoelastic form); "*cur*" and "*pre*" upper indexes mark values of specific reaction forces at the current step of integrating the equations of motion of discrete elements (or cellular automata); mean stress increments $\Delta\bar{\sigma}_{mean}^{i}$ and $\Delta\bar{\sigma}_{mean}^{j}$ are taken from previous time step or determined with use of predictor-corrector modification of a numerical scheme. Equations (21)-(22) are first solved for strain increments $\Delta\varepsilon_{i(j)}$, $\Delta\varepsilon_{j(i)}$, $\Delta\gamma_{i(j)}$ and $\Delta\gamma_{j(i)}$. Found values of strain increments are then substituted in (21)-(22) to calculate current values of specific forces σ_{ij}^{cur} and τ_{ij}^{cur}.

The above relations have a general (three-dimensional) form. In considered two-dimensional problem statement the approximations of plane stress (σ_{zz}=0) or plane strain (ε_{zz}=0) state are used. In the model under consideration, this means that the average stress tensor components $\bar{\sigma}_{xz}^{i}$ and $\bar{\sigma}_{yz}^{i}$ are equal to zero. A component $\bar{\sigma}_{zz}^{i}$ is calculated as follows:

$$\begin{cases} \bar{\sigma}_{zz}^{i} = \nu_i\left(\bar{\sigma}_{xx}^{i} + \bar{\sigma}_{yy}^{i}\right),\ \bar{\varepsilon}_{zz}^{i} = 0 & \textit{Plane strain} \\ \bar{\sigma}_{zz}^{i} = 0,\ \Delta\bar{\varepsilon}_{zz}^{i} = \left(\left(2G_i - K_i\right)/\left(2G_iK_i\right)\right)\Delta\bar{\sigma}_{mean}^{i} & \textit{Plane stress} \end{cases} \quad (23)$$

where ν_i is a Poisson ratio.

Resistance of the pair *i-j* to bending (Fig.3) is not included in the expressions (21)-(22). So, the form of the dependence $K_{ij}^{gear}\left(\gamma_{ij}^{gear}\right)$ has to be assigned extra. In the present model this is done by analogy with (22):

$$\begin{cases} \Delta\gamma_{i(j)}^{gear} = -\dfrac{G_i}{G_j}\Delta\gamma_{j(i)}^{gear} = \dfrac{-V_{ij}^{gear}\Delta t}{q_{ij} + \dfrac{G_i}{G_j}q_{ji}} \\ \Delta K_{ij}^{gear} = -\dfrac{q_{ij}}{q_{ji}}\Delta K_{ji}^{gear} = -q_{ij}S_{ij}G_i\Delta\gamma_{gear}^{i(j)} \end{cases} \quad (24)$$

Testing of the proposed model of element interaction by the example of elastic wave propagation through ensemble of *linked* elements showed that use of shear modulus *G* as an elastic modulus of resistance to bending in (24) provides the best agreement of simulation results with analytical solutions and results of simulation by finite difference method.

Relations (21)-(24) make it possible to simulate fragments of a locally isotropic linear elastic medium by an ensemble of *linked* discrete elements (or movable cellular automata).

Elastic-plastic medium

An important advantage of the proposed approach to building many-body interaction of discrete elements is a capability to realize various models of elasticity and plasticity within the framework of DEM/MCA. In particular, a model of plastic flow (incremental plasticity) with von Mises criterion of plasticity was implemented to simulate deformation of locally isotropic elastic-plastic medium.

For this purpose, radial return algorithm of Wilkins [2] was adopted to particle-based approach. Conventionally, this algorithm is formulated in terms of the stress deviator $\hat{D}_\sigma$ (Fig.6):

$$\hat{D}'_\sigma = \hat{D}_\sigma M \tag{25}$$

where

$$\hat{D}_\sigma = \begin{vmatrix} \sigma_{xx} - \sigma_{mean} & \tau_{yx} & \tau_{zx} \\ \tau_{xy} & \sigma_{yy} - \sigma_{mean} & \tau_{zy} \\ \tau_{xz} & \tau_{yz} & \sigma_{zz} - \sigma_{mean} \end{vmatrix}$$

M is a coefficient of stress drop (stress scaling), $\hat{D}_\sigma$ is a stress deviator after solution of elastic problem at the current time step, $\hat{D}'_\sigma$ is a scaled stress deviator.

Being written in terms of stress, for components of average stress tensor in the volume of discrete element i the algorithm of Wilkins can be presented in the following form:

$$\left(\bar{\sigma}^i_{\alpha\beta}\right)' = \left(\bar{\sigma}^i_{\alpha\beta} - \delta_{\alpha\beta}\bar{\sigma}^i_{mean}\right) M_i + \delta_{\alpha\beta}\bar{\sigma}^i_{mean} \tag{26}$$

where $\alpha,\beta = x,y,z$; $\left(\bar{\sigma}^i_{\alpha\beta}\right)'$ are scaled (returned) components of average stress tensor; $\bar{\sigma}^i_{\alpha\beta}$ are stress tensor components, which result from solution of elastic problem (21)-(23) at the current time step; $M_i = \sigma^i_{pl} \big/ \bar{\sigma}^i_{\text{int}}$ is current value of the coefficient M for discrete element i; σ^i_{pl} is current radius of von Mises yield surface for the element i; $\bar{\sigma}^i_{\text{int}}$ is calculated with use of expression (18) after solving elastic problem at the current time step; $\delta_{\alpha\beta}$ is the Kronecker delta.

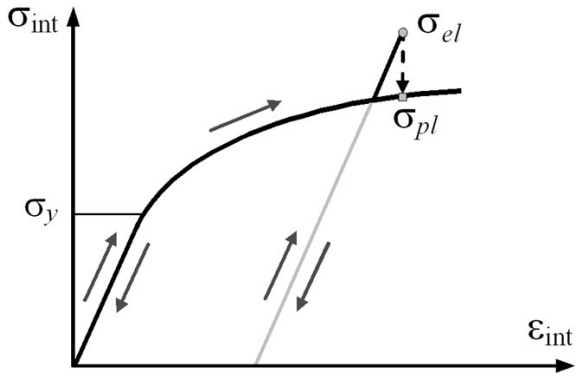

Figure 6: Schematic representation of functioning of radial return algorithm of Wilkins. Here σ_{el} is stress intensity after elastic problem solution at the current time step, σ_{pl} is a current value of yield stress (taking into account hardening), σ_y is an "initial" value of yield stress.

The main problem in realization of the algorithm of Wilkins within the framework of DEM/MCA is formulation of correcting relations for element interaction forces that provide implementation of necessary conditions of the algorithm [2]. By analogy with the elastic problem the expressions for scaling specific central and tangential forces of response of the element i to the impact of the neighbor j were derived by direct reformulation of relations (26) for average stress:

$$\begin{cases} \sigma'_{ij} = \left(\sigma_{ij} - \bar{\sigma}^i_{mean}\right) M_i + \bar{\sigma}^i_{mean} \\ \tau'_{ij} = \tau_{ij} M_i \end{cases} \tag{27}$$

where σ'_{ij} and τ'_{ij} are scaled values of specific reaction forces.

As is shown in Appendix B, substitution of (27) in expression (16) for average stress tensor automatically provides reduction of its components to yield surface for the element i. This gives possibility to correctly simulate plastic deformation in the volume of discrete elements.

Note that independent use of the expressions (27) for interacting elements i and j can lead to unequal values of respond

forces ($\sigma'_{ij} \neq \sigma'_{ji}$ and $\tau'_{ij} \neq \tau'_{ji}$) in the pair *i-j*. In view of the need for implementation of Newton's third law, the current values of element interaction forces in (10) are calculated on the basis of the following proportion:

$$\begin{cases} \sigma_{ij} = \dfrac{\sigma'_{ij} q_{ji} + \sigma'_{ji} q_{ij}}{r_{ij}} \\ \tau_{ij} = \dfrac{\tau'_{ij} q_{ji} + \tau'_{ji} q_{ij}}{r_{ij}} \end{cases} \tag{28}$$

In considered two-dimensional problem statement scaling of specific forces σ_{ij} and τ_{ij} and stress $\bar{\sigma}^i_{zz}$ has peculiarities for approximations of plane strain and plane stress state. In the first case these variables are scaled using the expressions (26) for $\bar{\sigma}^i_{zz}$ and (27) for specific forces. In the second case the special iterative procedure proposed by Wilkins [34] is adopted to particle-based approach (see Appendix C).

By analogy with the case of elastic problem, law of scaling of resistance of the pair *i-j* to bending has to be defined extra. In the present model this was done by analogy with scaling of shear resistance force τ_{ij}:

$$\begin{cases} \left(K^{gear}_{ij}\right)' = K^{gear}_{ij} M_i \\ \left(K^{gear}_{ji}\right)' = K^{gear}_{ji} M_j \\ K^{gear}_{ij} = \dfrac{\left(K^{gear}_{ij}\right)' q_{ji} - \left(K^{gear}_{ji}\right)' \left(q^2_{ij} / q_{ji}\right)}{r_{ij}} \end{cases} \tag{29}$$

Rheological properties of material of discrete element *i* are defined through assigning constitutive relation $\bar{\sigma}^i_{\text{int}} = \Phi\left(\bar{\varepsilon}^i_{\text{int}}\right)$ (when applied to movable cellular automaton, it is called as "mechanical response function of automaton/element" [22-25]). Current value of $\bar{\varepsilon}^i_{\text{int}}$ could be calculated incrementally using known values of $\bar{\sigma}^i_{\text{int}}$ after solution of elastic problem at the considered time step (*n*+1) and at the end the previous time step *n*:

$$\left(\bar{\varepsilon}^i_{\text{int}}\right)_{n+1} = \left(\bar{\varepsilon}^i_{\text{int}}\right)_n + \frac{\left(\bar{\sigma}^i_{\text{int}}\right)_{n+1} - \left(\bar{\sigma}^i_{\text{int}}\right)^{final}_n}{3G_i} \tag{30}$$

where $\left(\bar{\sigma}^i_{\text{int}}\right)_{n+1}$ is stress intensity value, which results from solution of elastic problem at the current time step (*n*+1); $\left(\bar{\sigma}^i_{\text{int}}\right)^{final}_n$ is stress intensity value at the end of the previous time step *n* (after realization of stress return procedure if necessary). Note, that following the idea of Wilkins' algorithm the value of $\left(\bar{\varepsilon}^i_{\text{int}}\right)_{n+1}$ remains unchanged throughout the stress return procedure (this is applied both to central and shear strains of discrete elements *i* and *j* in the pair *i-j*).

Calculation of current values of element volume and square of area of interaction of the pair

In addition to forces σ_{ij}, and τ_{ij}, acting on the surface of discrete element *i*, important constituents of the expression (16) for the components of average stress tensor are element volume Ω_i and squares of areas of interaction of the element with neighbours S_{ij}. The current values of these variables can be found using the average strain tensor components $\bar{\varepsilon}^i_{\alpha\beta}$ in the volume of the discrete element *i*. The values of components $\bar{\varepsilon}^i_{\alpha\beta}$ can be found directly in terms of pair strains $\varepsilon_{i(j)}$ and $\gamma_{i(j)}$ of element (see Appendix A) or through the components of the average stress tensor $\bar{\sigma}^i_{\alpha\beta}$. In the last case, the specific relations between $\bar{\varepsilon}^i_{\alpha\beta}$ with $\bar{\sigma}^i_{\alpha\beta}$ are determined by considered rheological model of the medium. In the framework of above described two-dimensional model of elastic-plastic interaction of discrete elements with von Mises criterion of plasticity these relations should be presented in hypoelastic form:

$$\begin{cases} \Delta\bar{\varepsilon}^i_{xx} = \dfrac{\Delta\bar{\sigma}^i_{xx}}{2G_i} + \dfrac{2G_i - K_i}{2G_iK_i}\Delta\bar{\sigma}^i_{mean} \\ \Delta\bar{\varepsilon}^i_{yy} = \dfrac{\Delta\bar{\sigma}^i_{yy}}{2G_i} + \dfrac{2G_i - K_i}{2G_iK_i}\Delta\bar{\sigma}^i_{mean} \\ \Delta\bar{\varepsilon}^i_{xy} = \dfrac{\Delta\bar{\sigma}^i_{xy}}{2G_i} \\ \Delta\bar{\varepsilon}^i_{xz} = \Delta\bar{\varepsilon}^i_{yz} = 0 \end{cases} \tag{31a}$$

$$\begin{cases} \Delta\bar{\varepsilon}^i_{zz} = 0 & \textit{Plane strain} \\ \Delta\bar{\varepsilon}^i_{zz} = \dfrac{2G_i - K_i}{2G_iK_i}\Delta\bar{\sigma}^i_{mean} & \textit{Plane stress} \end{cases} \tag{31b}$$

Here $\Delta\bar{\sigma}^i_{\alpha\beta}$ are stress increments calculated after solving the elastic task at the current time step.

Calculated values $\bar{\varepsilon}^i_{\alpha\beta}$ are used to define current volume of the discrete element *i*:

$$\Omega_i = \Omega_i^0\left(1+\bar{\varepsilon}^i_{xx}\right)\left(1+\bar{\varepsilon}^i_{yy}\right)\left(1+\bar{\varepsilon}^i_{zz}\right) \tag{32}$$

where Ω_i^0 is "initial" volume of the element (in undeformed state).

Determination of current value of S_{ij} is more complicated problem due to possible significant element shape distortion under large loads. The following approximation to estimate the value of S_{ij} is suggested. It is based on definition of local values of strain tensor components at the area of interaction (contact area) of considered pair of discrete elements *i* and *j* (hereinafter denote this tensor as $\varepsilon^{ij}_{\alpha\beta}$) by linear interpolation of corresponding components of average strain tensors ($\bar{\varepsilon}^i_{\alpha\beta}$ and $\bar{\varepsilon}^j_{\alpha\beta}$) to the central point of this area:

$$\varepsilon^{ij}_{\alpha\beta} = \frac{\bar{\varepsilon}^i_{\alpha\beta}q_{ji} + \bar{\varepsilon}^j_{\alpha\beta}q_{ij}}{r_{ij}} \tag{33}$$

Components of $\varepsilon^{ij}_{\alpha\beta}$ tensor are transformed from the laboratory system of coordinates to the instantaneous local coordinate system $X'Y'$ of the considered pair (Fig.7): $\varepsilon^{ij}_{\alpha\beta} \rightarrow \varepsilon^{ij}_{\alpha'\beta'}$. Components $\varepsilon^{ij}_{x'x'}$ and ε^{ij}_{zz} thus defined in local coordinate system are used for calculation of the current value of square of the area of pair interaction:

$$S_{ij} = S_{ij}^0\left(1+\varepsilon^{ij}_{x'x'}\right)\left(1+\varepsilon^{ij}_{zz}\right) \tag{34}$$

Here S_{ij}^0 is the initial value of square corresponding to the pair of undeformed elements *i* and *j*.

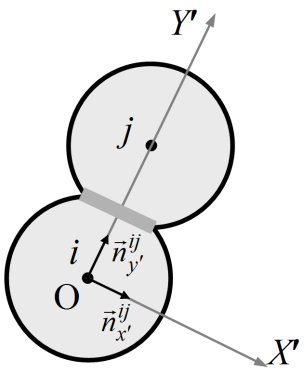

Figure 7: Instantaneous coordinate system X′Y′ associated with the current spatial orientation of the pair *i-j*.

Organization of the step of numerical integration of motion equations

Thus, numerical algorithm realizing the proposed model of elastic-plastic interaction of discrete element (or movable cellular automaton) i with neighbours j includes the following main stages:

i. Calculation of σ_{ij}, τ_{ij} and K_{ij}^{gear} at the current time step (n+1) in elastic approximation according to Eqs. (21)-(24). Calculation of corresponding values of $\bar{\sigma}_{xx}^{i}$, $\bar{\sigma}_{yy}^{i}$, $\bar{\sigma}_{xy}^{i}$, $\bar{\sigma}_{zz}^{i}$ or $\bar{s}_{zz}^{i}$, $\bar{\sigma}_{mean}^{i}$, $\bar{\sigma}_{\text{int}}^{i}$ and $\bar{\varepsilon}_{\text{int}}^{i}$ with use of expressions (16)-(18), (23), (30).

ii. Calculation of current values of $\bar{\varepsilon}_{xx}^{i}$, $\bar{\varepsilon}_{yy}^{i}$, $\bar{\varepsilon}_{xy}^{i}$, $\bar{\varepsilon}_{zz}^{i}$ and $\bar{\varepsilon}_{\text{int}}^{i}$ with use of expressions (31).

iii. Examination of exceeding the yield surface by element i stress state controlling parameter $\bar{\sigma}_{\text{int}}^{i}$. Calculation of the coefficient M_i if necessary.

iv. Carrying out the procedure of stress returning to yield surface for element i with use of expressions (26)-(27),(29), i.e. calculation of σ_{ij}', τ_{ij}' and $\left(K_{ij}^{gear}\right)'$. Calculation of scaled values of average stress tensor components and invariants.

v. Calculation of forces and torques of element interaction.

vi. Calculation of new values of automaton volume Ω_i and squares of areas of pair interaction S_{ij} with use of expressions (32)-(34)

vii. Integration of Newton-Euler equations of motion of discrete elements (or movable cellular automata).

The equations of motion (1) of discrete elements are numerically integrated with the use of the explicit integration scheme (for example, with use of well-known velocity Verlet algorithm) [35] modified by introducing a predictor cycles for estimation of $\bar{\sigma}_{\alpha\beta}^{i}$ at the current step. The need of the numerical scheme modification is caused by the fact that specific forces of the central interaction of discrete elements σ_{ij} at the current time step are computed using mean stress $\bar{\sigma}_{mean}^{i}$ (21). At the same time these forces are used to define mean stress according to (16). To solve this problem of numerical integration the predictor cycles are used for the calculation of the elastic task. At the initial predictor cycle increment of mean stress is calculated from the previous time step: $\Delta\bar{\sigma}_{mean}^{i}=\left(\bar{\sigma}_{mean}^{i}\right)_{n}^{final}-\left(\bar{\sigma}_{mean}^{i}\right)_{n-1}^{final}$. Value of $\Delta\bar{\sigma}_{mean}^{i}$ such calculated is used in (21) to get estimated values of σ_{ij} and corresponding estimated value of $\left(\bar{\sigma}_{mean}^{i}\right)_{n+1}^{pred}$ at the current step. The obtained value is used for the calculation of $\Delta\bar{\sigma}_{mean}^{i}=\left(\bar{\sigma}_{mean}^{i}\right)_{n+1}^{pred}-\left(\bar{\sigma}_{mean}^{i}\right)_{n}^{final}$ at the next predictor cycle. The number of predictor cycles is defined by assigned tolerance of mean stress change during one cycle (normally the solution converges very fast and 2 predictor cycles are enough).

MODELING FRACTURE AND "HEALING" WITH PARTICLE-BASED FORMALISM

One of the main advantages of particle-based methods in mechanics is the feasibility of direct simulation of fracture (including multiple fracture) of material and bonding of fragments through changing the state of a pair of particles ("linked" pair ↔ "unlinked" pair, Fig. 1). The criterion for pair state switching is normally the ultimate value of interaction force or the ultimate value of relative displacement [19]. The developed approach to the description of interaction of movable cellular automata (or discrete elements) in the many-particle approximation makes it possible to apply various multiparametric "force" fracture criteria (Huber-Mises, Drucker-Prager, etc) as element-element bond fracture criteria.

The model to calculate debonding of the pair (linked→unlinked transition)

It's well known that crack formation is a fundamentally brittle and extremely localized phenomenon. Fracture is connected with rupture of interatomic bonds and spatial diversity of atomic layers. That is realized under the influence of local, rather than the average stress. Thus, the used criterion of pair bond breakage between linked elements i and j must be expressed in terms of local variables of the interaction of elements, in particular, through the forces σ_{ij} and τ_{ij} acting in a pair.

In this regard, the following approach to implement parametric fracture criteria as criteria of pair bond breaking (*linked→unlinked* transition of the state of the pair) is suggested. In the framework of classical formalism of discrete elements pair bond breakage occurs on the surface of their interface (at the area of interaction of the pair, in other words,

at the contact area). Therefore applied "force" failure criterion (for example, the criterion of Drucker-Prager) must be calculated at the area of interaction of elements using the local stress tensor components identified at this area. By analogy with strain tensor $\varepsilon_{\alpha\beta}^{ij}$ (see Section *Calculation of current values of element volume and square of area of interaction of the pair*) this local tensor will be denoted as $\sigma_{\alpha\beta}^{ij}$. In the local coordinate system $X'Y'$ of the pair *i-j* (Fig.7) components $\sigma_{y'y'}^{ij}$ and $\sigma_{x'y'}^{ij}$ of this stress tensor are numerically equal to specific forces of central (σ_{ij}) and tangential (τ_{ij}) interaction of the elements (these forces are applied to the contact area S_{ij}):

$$\begin{cases} \sigma_{y'y'}^{ij} \equiv \sigma_{ij} \\ \sigma_{x'y'}^{ij} \equiv \tau_{ij} \end{cases} \tag{35a}$$

Other components ($\sigma_{x'x'}^{ij}$ and $\sigma_{z'z'}^{ij}$) of the local stress tensor can be determined on the basis of linear interpolation of corresponding values for elements *i* and *j* ($\bar{\sigma}_{x'x'}^{i}$ and $\bar{\sigma}_{x'x'}^{j}$, $\bar{\sigma}_{z'z'}^{i}$ and $\bar{\sigma}_{z'z'}^{j}$) to the area of interaction:

$$\begin{cases} \sigma_{x'x'}^{ij} = \dfrac{\bar{\sigma}_{x'x'}^{i} q_{ji} + \bar{\sigma}_{x'x'}^{j} q_{ij}}{r_{ij}} \\ \sigma_{zz}^{ij} = \dfrac{\bar{\sigma}_{zz}^{i} q_{ji} + \bar{\sigma}_{zz}^{j} q_{ij}}{r_{ij}} \end{cases} \tag{35b}$$

where $\bar{\sigma}_{\alpha'\beta'}^{i}$ and $\bar{\sigma}_{\alpha'\beta'}^{j}$ are components of average stress tensor in the volume of elements *i* and *j* in the local coordinate system $X'Y'$ of the pair (these stresses result from transformation of average stresses $\bar{\sigma}_{\alpha\beta}^{i}$ and $\bar{\sigma}_{\alpha\beta}^{j}$ to local coordinates). Components $\sigma_{\alpha'\beta'}^{ij}$, thus defined, can be used to calculate necessary invariants of stress tensor which then can be used to calculate current value of applied criterion of pair fracture. Below the examples of bond breaking conditions for the pair *i-j* with use of Huber-Mises-Hencky and Drucker-Prager criteria are shown:

$$\begin{cases} \sigma_{\text{int}}^{ij} > \sigma_c \\ \sigma_{\text{int}}^{ij} 0.5(a+1) + \sigma_{mean}^{ij} 1.5(a-1) > \sigma_c \end{cases} \tag{36}$$

where σ_c is the corresponding threshold value for considered pair (value characterizing strength of cohesion/adhesion), $a = \sigma_c / \sigma_t$ is a ratio of compressive strength (σ_c) of the pair bond to tensile strength (σ_t), σ_{int}^{ij} and σ_{mean}^{ij} are corresponding invariants of stress tensor $\sigma_{\alpha'\beta'}^{ij}$. Variables σ_{int}^{ij} and σ_{mean}^{ij} are calculated by analogy with (17)-(18).

When using the explicit scheme of integration of motion equations (1) the value of time step Δt is limited above by a quantity associated with the time of propagation of the sound through the volume of element:

$$\Delta t_{\max} = \lambda \frac{d}{V_{elast}} \tag{37}$$

where V_{elast} is velocity of the longitudinal elastic wave in the material, $0<\lambda<1$ – dimensionless coefficient (normally $\lambda=1/5\div1/4$). In conventional DEM-based models breakage of bond in pairs of discrete elements is carried out for one time step Δt. It this case the local value of the crack growth rate (defined as the ratio of the linear size of the area of pair interaction to Δt) is higher than sound velocity in the material. Obviously, such a model of bond breakage is an idealized because virtually suggests that the spatial separation of atomic layers occurs uniformly over the whole surface of interaction of elements. In modern models of fracture mechanics it is supposed that fracture has a discrete character, that is, the crack length increases by "quanta". In different models these quanta of length are called as "fracture quantum" [36, 37] or "process zone" [38, 39]. Thus, in conventional DEM-based models of fracture it is implicitly assumed that the linear dimension of the surface of interaction of elements is equal to the step of crack growth. At the same time, the value of "fracture quantum" is a material parameter and its scale normally is nanometers or fractions of nanometer [39, 40]. In the most tasks the size of discrete elements is significantly larger than this value. Therefore, in most cases, the model of bond breaking in pair of discrete elements within one integration step Δt means the overestimation of the rate of physical process of fracture of the material modeled by the pair of linked discrete elements.

In accordance with the foregoing, the following approach to a more accurate description of the dynamics of crack growth is suggested. In this approach, it is assumed that breaking of the bond (*linked→unlinked* transition of the state of the pair) is a time-space distributed process. This process is technically expressed through change of the dimensionless coefficient k_{link}^{ij} $(0 \le k_{link}^{ij} \le 1)$. This coefficient has the meaning of the portion of linked part of the contact area S_{ij}. In this case the square of linked part of the contact area in the pair *i-j* is $S_{link}^{ij} = S_{ij} k_{link}^{ij}$, while $S_{unlink}^{ij} = S_{ij}\left(1 - k_{link}^{ij}\right)$ is the square of unlinked part of this area. Thus, in this approach, the dynamics of bond breaking in a pair of elements is expressed by the dependence $k_{link}^{ij}(t)$, where k_{link}^{ij} decreases from initial value 1 (totally linked pair) to final value 0 (totally unlinked pair).

Depending on the size of the discrete elements and features of the internal structure of fragment of the material, which is simulated by the discrete element (in particular, the presence of pores, damages, block structure) the stable or unstable crack growing model can be applied to describe the breakage of bond in the pair.

In the first model, the process of fracture develops in accordance with predefined dependence $\frac{dk_{link}^{ij}}{d\varepsilon_{\text{int}}^{ij}} = f\left(\varepsilon_{\text{int}}^{ij}, k_{link}^{ij}, \dot{\varepsilon}_{\text{int}}^{ij} \ldots\right) < 0$, where $\varepsilon_{\text{int}}^{ij}$ is a pair strain intensity (value $\varepsilon_{\text{int}}^{ij}$ can be calculated, for example, using the components of the tensor $\varepsilon_{\alpha\beta}^{ij}$ defined by analogy with $\sigma_{\alpha\beta}^{ij}$). In the simplest case this dependence can be considered as a constant: $dk_{link}^{ij} / d\varepsilon_{\text{int}}^{ij} = const < 0$. Note also that the additional conditions for decrease of k_{link}^{ij} (i.e. conditions of crack advance through the area of pair interaction) at the current time step are:

i. Exceeding the fracture criterion threshold at this step.

ii. $d\varepsilon_{\text{int}}^{ij} > 0$.

Dependence $dk_{link}^{ij} / d\varepsilon_{\text{int}}^{ij}$ has to be assigned for each pair of materials filling linked elements.

In the second model (the approximation of unstable crack growth) it is assumed that if the fracture criterion threshold is exceeded, a crack begins to grow spontaneously according to some specified law $\frac{dk_{link}^{ij}}{dt} = f\left(t, k_{link}^{ij} \ldots\right) < 0$, where t is time.

In the simplest case this dependence can be considered as a constant ($dk_{link}^{ij} / dt = const < 0$), that means that crack advances through pair interaction area with constant velocity V_{crack}. The value of V_{crack} is a predefined (model) parameter, which reflects the features of rheology of the interface between the materials filling interacting elements. In particular, for brittle materials V_{crack} can be set to be equal to transverse sound velocity, while for ductile materials its value, obviously, should be significantly smaller. Note that the model of unstable crack growth has to be used together with requirement of exceeding the fracture criterion threshold at each time step during crack advance through the area of pair interaction. Model parameter V_{crack} has to be assigned for each pair of materials filling linked elements.

Possibility of unlinked to linked transition

Chemical bonding of contacting *unlinked* automata is imitated by *unlinked→linked* transition of the pair state (this transition is interpreted as formation of new chemical bond or recovery of previously broken one). Note that such transition describes "healing" of *partially linked* pairs of elements $(0 < k_{link}^{ij} < 1)$ as well. Physical mechanisms of "integration" (linking) of independent material fragments into a consolidated piece could be different and include cohesion (or adhesion) of smooth and pure enough contacting surfaces under compression, "welding" of contacting surfaces under the condition of compression and intensive friction, interpenetration ("mixing") of surface layers of contacting material fragments as a result of strong compression and intensive shear (torsion) under constraining side boundary conditions, healing of nano- and microscopic damages and cracks and so on. Therefore specific form of bonding/linking criterion is defined by physical peculiarities of contact interaction of automata as well as by chemical composition and structural features of interacting surfaces.

Due to a surface roughness the process of "integration" of surface layers of contacting automata is gradual. The degree of "integration" of surface layers increases with increasing the values of variables of loading (normal load, shear load, plastic work of deformation). To take into account these features, the following model of linking/bonding of unlinked and contacting automata is suggested. The change of degree of "integration" of surface layers of totally or partially unlinked elements *i* and *j* is taken into account by means of change of the value of previously introduced coefficient k_{link}^{ij} (see Section *The model to calculate debonding of the pair (linked→unlinked transition)*). In the framework of this model the criterion of pair linking takes the form of dependence of k_{link}^{ij} on the variables of loading. The following simple and physically based

criteria are proposed:

1. Linear dependence of k_{link}^{ij} on specific normal force σ_{ij}:

$$\begin{cases} \Delta k_{link}^{ij} = \dfrac{\left(-\Delta\sigma_{ij}\right)}{\sigma_{\max}-\sigma_{\min}}, & if\ \left(-\sigma_{ij}\right)>\sigma_{\min},\ \left(-\Delta\sigma_{ij}\right)>0,\ \left(-\sigma_{ij}\right)>\left(-\sigma_{peak}^{ij}\right) \\ \Delta k_{link}^{ij} = 0 & otherwise \end{cases} \tag{38}$$

where σ_{ij} is a current value of specific central force in the pair *i-j*; $\Delta\sigma_{ij}$ is an increment of specific central force during one time step Δt; $\sigma_{\min}$ is the minimum (threshold) value of normal pressure in the pair (negative specific normal force) for linking; $\sigma_{\max}$ ($\sigma_{\max}>\sigma_{\min}$) is another parameter having the dimension of specific force and regulating the slope of the dependence $k_{link}^{ij}\left(\sigma_{ij}\right)$; σ_{peak}^{ij} is a maximum value of specific normal force previously achieved from the moment of linking beginning.

2. Linear dependence of k_{link}^{ij} on plastic work of deformation W_{ij} taking into account specific normal force σ_{ij}:

$$\begin{cases} \Delta k_{link}^{ij} = \dfrac{\Delta W_{ij}}{W_{\sigma}}, & if\ \left(-\sigma_{ij}\right)>\sigma_{\min},\ \Delta W_{ij}<W_{\sigma} \\ \Delta k_{link}^{ij} = 1, & if\ \left(-\sigma_{ij}\right)>\sigma_{\min},\ \Delta W_{ij}\geq W_{\sigma} \\ \Delta k_{link}^{ij} = 0 & otherwise \end{cases} \tag{39}$$

where W_{σ} is normalizing parameter depending on specific normal force σ_{ij}:

$$W_{\sigma} = \frac{\left(-\sigma_{ij}\right)-\sigma_{\min}}{\sigma_{\max}-\sigma_{\min}}\left(W_{\sigma_{\max}}-W_{\sigma_{\min}}\right)+W_{\sigma_{\min}} \tag{40}$$

Here ΔW_{ij} is an increment of plastic work of deformation of the pair *i-j* during one time step Δt; $W_{\sigma_{\min}}$ is the value of plastic work to make pair totally linked at threshold normal pressure $\sigma_{\min}$; $W_{\sigma_{\max}}$ is the value of plastic work to make pair totally linked at normal pressure $\sigma_{\max}$ (normally $W_{\sigma_{\max}}<W_{\sigma_{\min}}$). Plastic work in (39) has to be considered in specific units (per unit of volume). Parameters $\sigma_{\min}$, $\sigma_{\max}$, $W_{\sigma_{\min}}$ and $W_{\sigma_{\max}}$ in criteria (39)-(40) are assigned (user-defined) values, which have to be determined for each pair of materials filling elements *i* and *j*.

One of the problems with the use of the criterion (39) is the calculation of ΔW_{ij}. As a first approximation it can be considered as the sum of increments of plastic work of deformation of both interacting elements/automata:

$$\Delta W_{ij} = \Delta W_i + \Delta W_j \tag{41}$$

A specific expression to calculate increment of plastic work of deformation of the element is determined by the applied model of plasticity. In the case of the above model of plasticity with von Mises criterion the value of ΔW_i can be calculated as follows:

$$\Delta W_i = \Delta A_i^{total} - \Delta A_i^{elast} = \frac{0.5\left[\left(\bar{\sigma}_{\text{int}}^{i}\right)_{n+1}+\left(\bar{\sigma}_{\text{int}}^{i}\right)_{n}\right]}{\left(\bar{\varepsilon}_{\text{int}}^{i}\right)_{n+1}-\left(\bar{\varepsilon}_{\text{int}}^{i}\right)_{n}} - \frac{1}{2}\left(\frac{\left(\bar{\sigma}_{\text{int}}^{i}\right)_{n+1}^{2}}{3G_i}-\frac{\left(\bar{\sigma}_{\text{int}}^{i}\right)_{n}^{2}}{3G_i}\right) \tag{42}$$

where ΔA_i^{total} and ΔA_i^{elast} are increments of total work of deformation and its elastic part correspondingly, *n* is a number of time step.

In a general case criterion of pair linking has more complex form as it takes into account combined influence of central force, plastic work and other parameters of pair interaction including strain rate and/or relaxation times.

Note that during time-distributed process of pair linking the condition of bond breaking in a pair can be achieved. Therefore, under certain conditions, local processes of linking and unlinking can proceed in parallel (*unlinked↔linked* transition).

MCA-BASED STUDY OF FEATURES OF DEFORMATION AND FRACTURE OF METAL-CERAMIC COMPOSITES

Capabilities and advantages of the developed approach to the construction of many-body potentials/forces of interaction between particles (discrete elements or movable cellular automata) and implemented rheological models make it possible to study the response (including fracture) of heterogeneous materials and media of different nature. An important area of application of particle-based numerical modeling is investigation of the influence of the features of internal structure on the mechanical properties and fracture pattern in composite materials. This will be demonstrated by the example of MCA-based modeling of particle-reinforced metal-ceramic composite.

Metal-ceramic composites are advanced representatives of the class of dispersion-reinforced materials, which have enhanced values of mechanical and service characteristics, such as strength, stiffness-to-weight ratio, crack growth resistance, wear resistance, fracture energy, ratio of thermal conductivity to thermal expansion coefficient, thermal stability and so on. This makes them very attractive for a wide application in various industries as materials for extreme operating conditions [41-43]. At the present time working parts of machines and mechanisms operating under conditions of shock loading, abrasion, high temperatures and corrosive environments are made mostly of metal-ceramic composites on the basis of very hard and refractory compounds (carbides, nitrides, carbonitrides) with metallic binder (nickel and iron alloys are mainly used) [41,42,44-46]. This class of materials is fabricated from powder mixtures of the compounds using powder metallurgy methods [41,42,47]. Mechanical and physical properties of the sintered metal-ceramic composite are determined, in addition to phase composition, by a number of structural factors. Some of them are conventionally observed: volume fraction, dispersion (including the size distribution), geometry and faultiness of reinforcing particles, structural-phase state of the metallic binder et al. [41,42,48,49]. It should be noted that one of the key elements of the internal structure of the metal-ceramic composites are the interfaces between particles of refractory compounds and a metallic binder. The change in technological peculiarities of metal-ceramic composite fabrication (in particular, applying additional heat treatment of the composite) can vary the geometry (width) of interfaces as well as their structural and, consequently, the mechanical properties [50].

The analytical models and numerical simulation are of great importance for studying the mechanical properties of composite materials and their connection with geometric and mechanical properties of inclusion/matrix interfaces. As a rule, the analytical models to study the effect of the properties of interfaces on the macroscopical mechanical properties of dispersion-reinforced composites are valid for elastic or viscoelastic approximations and a regular packing of very hard inclusions having a simple geometry. In this connection the predominant attention in solving such problems is given to the numerical simulation of deformation and fracture of composites taking into account their mesoscopical internal structure. Finite element and finite difference methods are most extensively used numerical techniques for this purpose [48,51-53]. With the application of these numerical methods the influence of various structural factors (geometry, volume fraction, size and spatial distribution of reinforcing particles) on the elastic and strength properties, deformation capacity and fracture toughness of dispersion-reinforced composites was investigated [48,52,54]. At the same time, the influence of strength properties and the width of interphase boundaries interfaces on the mechanical characteristics of metal-ceramic composites is still under discussion. Thus in this paper, particle-based MCA method has been applied to study the influence of these factors on strength, ultimate strain and fracture energy of the composite under dynamic loading. A TiC-particle-reinforced Ni-Cr matrix composite (50 vol.% TiC) has been chosen as a model system classified as the metal-ceramic composite materials in which the particles are much stiffer than the binder.

Mesoscopical model of metal-ceramic composite

The TiC-particle-reinforced Ni-Cr matrix composite (50 vol.% TiC) was used as a prototype to create a numerical model of metal-ceramic sintered composite. A typical microstructure of Ni-Cr/TiC composite is shown in Fig. 8a. As can be seen from Fig. 8a, carbide component consists of particles with quite complex geometrical shapes. The mean size of reinforcing particles D_{mean} is 2.7±1.2 μm, maximal particle size D_{max} is 7.6 μm, Fig. 8b. It is necessary to note that thermally activated diffusion processes during the course of sintering result in the formation of a transition zone (the region of variable chemical composition) at the ceramic/metal interfaces. The characteristic width (H_{ij}) of the transition zone in considered composite is a few micrometers. Note that local profile of distribution of chemical elements is defined by the features of a local microstructure (including the distance to neighbouring TiC particle, shape of particle surface and so on). Thus, the metal-ceramic composite contains three main structural components: a metallic binder (Ni-Cr), integrated high-strength brittle inclusions (TiC) of mesoscopical scale (1-10 μm in diameter) and transition zone "particle-binder" (the region of variable chemical composition), whose width can reach several micrometers.

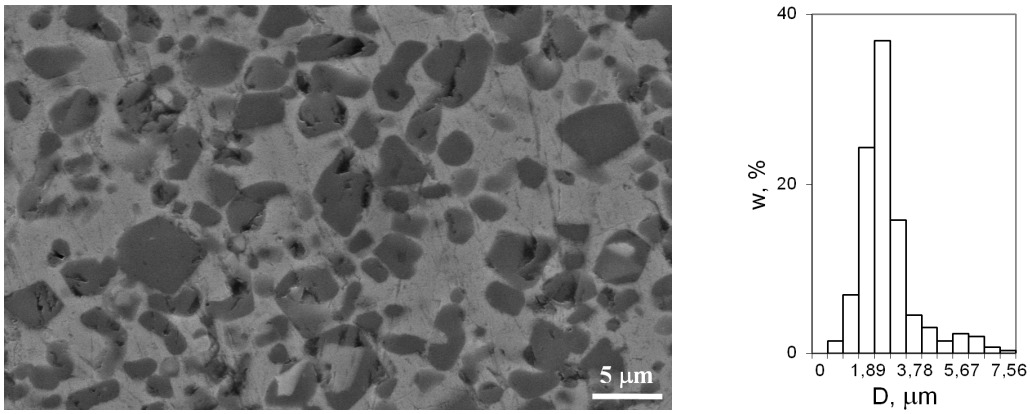

(a) (b)

Figure 8: (a) Typical microstructure of TiC-particle-reinforced Ni-Cr matrix composite (50 vol.% TiC); (b) size distribution of carbide particles (D_{mean} = 2.7±1.2 μm).

Mentioned above main features of the mesoscopical structure in metal-ceramic composite formed the basis for a two-dimensional structural model developed in the framework of the numerical MCA method. Each of constituents is modelled by ensemble of movable cellular automata (discrete elements) with appropriate rheological parameters (thus the cellular automaton simulates a domain/fragment of an inclusion, a binder, or an interface zone). The size d of a cellular automaton is an assigned parameter of the model. In the presented model a requirement for the value of d was accepted to be a few times higher than the characteristic size of grains of the binder. In that case mathematical models of elasticity and plasticity of isotropic media can be correctly applied to describe the deformation of the material fragment with characteristic size corresponding to the automaton size d. The maximal value of the dimensional parameter d of the model determines a specification of TiC particle shape in detail. "Optimum" definition range of the value d (the size of the discrete element) is 0.1-0.3 μm for the considered metal-ceramic composite (typical grain size of the metallic matrix in this composite does not exceed 0.1 μm).

As an example of MCA-based structural model, Fig. 9 shows the structure of an idealized metal-ceramic composite with TiC particles having a nearly spherical shape and the average size D_{TiC} of 3 μm (the size of movable cellular automaton in this case is d=0.3 μm). In this example the approximation of "monosize" distribution of TiC particles is used (sizes of the inclusions are uniformly distributed about the mean value D_{TiC}; the amplitude of deviation from the mean value of the particle size is $0.1 \cdot D_{TiC}$). The volume fraction of carbide particles in the model composite is 45%, which is close to the corresponding value (50%) in the real composite. The spatial distribution of TiC inclusions in the shown idealized composite is slightly inhomogeneous (i.e. no pronounced clustering of particles), the characteristic distance between the surfaces of neighboring particles is about 1.5 micrometers that is 50% of D_{TiC}.

Depending on features of internal structure of real composite and on the level of detail of the model there are two ways to account spatial (including width) and physical-mechanical characteristics of the transition layer between reinforcing particles and a metallic binder:

1. The model of a "narrow" transition zone. In this model, it is assumed that the width of the interface is much smaller than the size of movable cellular automaton d. Capabilities of the model are limited by specifying certain values of strength parameters (adhesive strength) in pairs of movable cellular automata, one of which simulates a segment of the inclusion surface and the second one represents an adjoining (adjacent) segment of the binder. Such approach does not take into account geometric characteristics of the transition zone, the presence of a concentration gradient of the chemical elements, and hence the existence of a gradient in mechanical properties. The defining characteristics of a "narrow" interphase boundary are its strength properties. An assigned value of adhesive strength for the pair of dissimilar cellular automata corresponds to the effective strength of interphase boundary. Note that described model does not account for the features of the rheology of the transition layer and can be used effectively in the case where the width of this layer does not exceed the assigned size of movable cellular automaton d.
2. The model of a "wide" transition zone. In this model, it is assumed that the width of the interface is comparable or greater than the size of the movable cellular automaton d. Here particle/binder interface is regarded as an area of variable composition of chemical elements (Ti, Ni, Cr, C) and modeled by several layers of cellular automata. Physical and mechanical characteristics of these "transition" automata vary with a distance from particle surface into the volume of binder for a given law (in accordance with local chemical composition). Relations between a local content of

chemical elements and the corresponding rheological properties of "transition" cellular automata must be determined on the basis of experimental data. The proposed model can be efficiently used in numerical simulation of composites in the case of the width of the transition zone higher than the assigned size *d* of a cellular automaton.

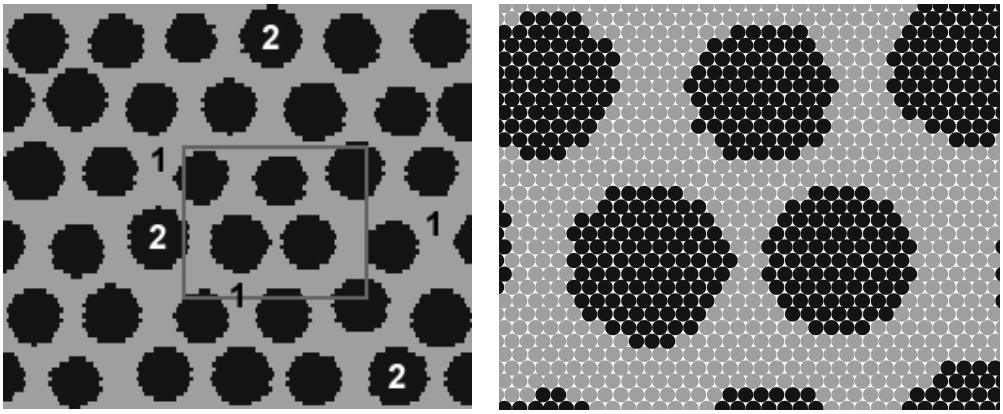

Figure 9: Structural model of metal-ceramic composite: (a) general view and (b) enlarged area inside of grey rectangle in (a). Main constituents of the structure are: nickel-chromium plastic binder (1) and high-strength brittle TiC particles (2).

To implement the explicit way to account the transition zone between particles and a binder in the numerical model of composite the special algorithm was developed. This algorithm uses information about a change in characteristic particle size during composite fabrication and resulting profile of distribution of chemical elements (for example, Ti) in formed transition layer. The output of the algorithm is a set of data about physical (density, concentration of chemical elements) and mechanical characteristics of movable cellular automata belonging to transition zone. These properties correspond to material at an appropriate distance from the surface of the inclusion. Example of a model metal-ceramic composite with explicit consideration of transition zone between particles (TiC) and the binder (Ni-Cr) is shown in Fig. 10.

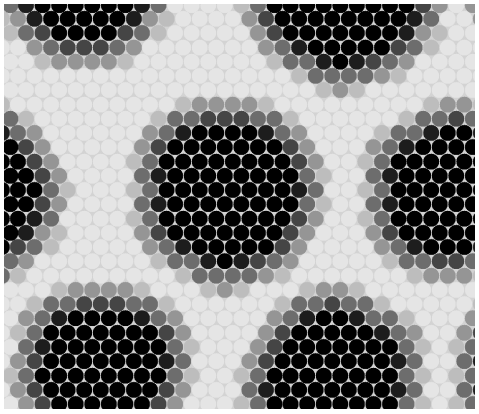

Figure 10: The internal structure of a model metal-ceramic composite with a "wide" transition zone (~0.8 μm in the present example) between TiC particles (shown in black) and the Ni-Cr binder (shown in light gray). Shades of gray color of varying intensity mark areas of the transition zone with appropriate content of TiC.

The main problem when using an explicit way of modeling the transition zone at particle/binder interface is the determination of rheological parameters and strength of transition areas (layers) that are at different distances from the particle surface. These parameters are difficult to determine in experiment. Therefore in the present study a simple (phase mixture) model was used to determine the mechanical properties of cellular automata that simulate transition zone. It is based on the assumption that the transition zone has a structure similar to the solid solution of titanium and carbon in the metallic binder. Their content in the binder decreases with increasing distance from the particle surface. In this model the rheological and strength parameters of transition zone are determined by linear interpolation of corresponding values for titanium carbide and (Ni-Cr) binder (that is proportional to the local concentration of titanium and carbon):

$$P_{trans} = P_{TiC}C_{TiC} + P_{NiCr}C_{NiCr} \quad (43)$$

where P is a considered parameter (Young modulus, Poisson ratio, yield stress, tensile or compressive strength and so on), C is a local concentration of corresponding constituent of the composite ($C_{TiC} + C_{NiCr} = 1$).

The components of metal-ceramic composites have very different rheological properties (high-strength brittle particles of refractory compound and elastic-plastic metallic binder). To simulate the processes of deformation and fracture of such complex systems by MCA method the developed two-dimensional model of elastic-plastic interaction of cellular automata is used. An incremental theory of plasticity of isotropic medium with von Mises plasticity criterion and the plane stress approximation are used to model deformation of metallic binder on the mesoscopical scale. Elastic constants of the material and the diagram of uniaxial loading are used as input parameters for the model of interaction of cellular automata. These parameters determine mechanical response function of movable cellular automaton.

To simulate the elastic-plastic metallic binder of the composite the parameters of mechanical response of movable cellular automaton conforming to the mechanical properties of nickel-chromium alloy were chosen. The response function of automaton modeling (Ni-Cr) is a "σ–ε" diagram with a linear hardening (curve 1 in Fig. 11). This diagram was obtained by approximation of the experimental diagrams for uniaxially compressed macroscopical samples of the alloy. Mechanical properties of automata simulating a high-strength brittle inclusion correspond to idealized properties of real particles of titanium carbide in ceramic phase (linear-elastic behavior up to failure, curve 2 in Fig. 11).

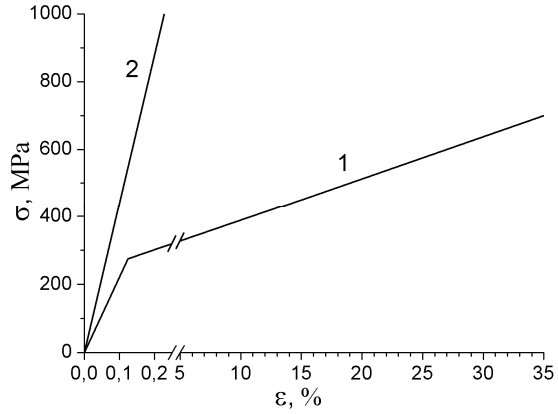

Figure 11: Mechanical response function of movable cellular automata for modelling (Ni-Cr)-alloy (1) and titanium carbide TiC (2).

An important role in building the mechanical model of composites belongs to determining the strength criterion (fracture criterion) for the system components (TiC and Ni-Cr) and the parameters of the chosen criterion. It is well-known that fracture is a fundamentally brittle and extremely localized phenomenon. Since the physical mechanisms of fracture are concerned with break of interatomic bonds and spatial separation of atomic layers, the criterion for material failure, in contrast to the criterion of plasticity, cannot be determined solely by the shear stresses and should take into account the effect of hydrostatic pressure. Therefore a two-parameter criterion of Drucker-Prager (36) was applied as one for interelement bond failure (fracture criterion) in the proposed model.

It is necessary to note that for each of the composite components there are reliable published data about only one of the parameters of the criterion (36). Tabulated data are the values of the compressive strength (σ_c^{TiC}) for TiC and tensile strength (σ_t^{NiCr}) for (Ni-Cr)-alloy. Values of the second parameters (σ_c^{NiCr} and σ_t^{TiC}) are unknown or estimated very roughly and uncertainly. Therefore, estimates of these missing parameters of fracture criterion were used in the model:

1. (Ni-Cr)-alloy: σ_t^{NiCr} =700 MPa (tabulated value), σ_c^{NiCr} =2100 MPa (estimated value), $a_{NiCr} = \sigma_c^{NiCr} / \sigma_t^{NiCr} = 3$.
2. TiC: σ_c^{TiC} =10000 MPa (tabulated value for ceramic phase), σ_t^{TiC} =2000 MPa (the tensile strength was estimated under the assumption of the absence of significant defects in TiC particles), $a_{TiC} = \sigma_c^{TiC} / \sigma_t^{TiC} = 5$.

As discussed above, the service characteristics of metal-ceramic composite (as well as of other composite materials) are largely provided by the adhesion of the binder to the reinforcing refractory inclusions. Depending on applied approach to the description of interphase boundaries the parameters of adhesive strength of dissimilar cellular automata (e.g., automata modeling TiC and Ni-Cr) were assigned in different ways:

1. When using the model of "narrow" interphase boundaries, the parameters σ_t^{bound} and a_{bound} are the only characteristics

of the model interface. In the simulations carried out, the parameter σ_t^{bound} was considered as a variable (assigned) value and varied within the limits between $0.5\sigma_t^{NiCr}$ (imitation of weak interfaces) and $2.5\sigma_t^{NiCr}$ (extremely strong interfaces). The parameter a_{bound} in the criterion (36) was assumed to be 3 in all calculations.

2. When using the model of "wide" interphase boundaries, the values of strength parameters σ_t and σ_c for the transition layer with certain local concentrations of components (C_{TiC} and C_{NiCr}) were determined on the basis of phase mixture model using the relation (1). For a pair of dissimilar cellular automata (characterized by different values of C_{TiC}) parameters σ_c and σ_t of bond fracture criterion (36) were defined as the minimal values corresponding to the strength characteristics of the areas modeled by these automata. For example, for a pair of dissimilar automata characterized by concentrations of TiC $C_{TiC}=1$ (automaton with pure TiC properties) and $C_{TiC}=0$ (automaton with pure (Ni-Cr)-alloy properties) the value of tensile strength for the pair σ_t is equal to σ_t^{NiCr}: $\sigma_t=\sigma_t^{NiCr}$ =700 MPa. Compressive strength for this pair is determined in a similar way: $\sigma_c=\sigma_c^{NiCr}$ =2100 MPa.

Simulation results

A three-point bending test of the model samples of metal-ceramic composite TiC-(Ni-Cr) was simulated. Since the main research task was to analyze the changes in "macroscopical" response of the composite due to variation of the characteristics of interphase boundaries, the complex geometry of the mesoscopical TiC particles and features of particle size and spatial distributions were not taken into account. A composite with an idealized internal structure shown in Fig. 9 (the model of "narrow" interfaces) was considered. Note that TiC particles in real metal-ceramic composite may contain damages and microcracks. To eliminate the influence of this factor on the simulation results it was assumed that TiC particles in the model sample have a "monolithic" internal structure and do not contain significant defects. All interphase boundaries were assumed to be free of flaws as well.

The structure of the model set-up is shown in Fig. 12. Dynamic loading by 20 μm cylindrical mandrel with constant velocity V_{load} was applied to the sample of 24×130 μm in size. The values of loading velocity ranged from 0.2 m/s to 1 m/s. The value of the maximal resistance of the sample to bending and the corresponding displacement of the mandrel, the dynamics and pattern of the sample fracture as well as the fracture energy characterized by an area under the loading diagram were analyzed.

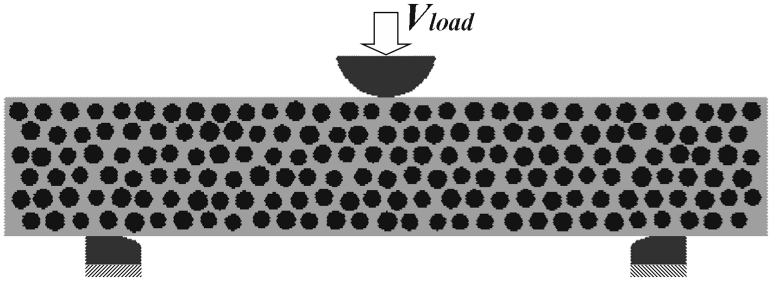

Figure 12: Scheme of the simulation of three-point bending test of the model composite sample.

The simulation results showed that the change in interface strength (σ_t^{bound}) leads to a purposeful change in the integral characteristics of the composite response of 2-10 times. Fig. 13a shows diagrams of dynamic loading of simulated composite sample with different values of adhesive strength of the metallic binder to carbide particles (loading velocity in these calculations was V_{load} = 0.4 m/s). The diagrams are plotted in the terms "normalized stress σ/σ_t^{NiCr} versus bending angle α". Here stress σ is defined as a force of composite resistance to mandrel indentation referred to the area of the upper surface of the mandrel. The bending angle α is calculated as is shown in Fig. 13b. It is established that increasing the strength of "narrow" interphase boundaries leads to a twofold growth in strength of the composite and makes the value of the limit strain (strain corresponding to peak resistance) higher by an order of magnitude. Note that the falling (supercritical) part of the loading curves is associated with the initiation and development of main crack in the sample.

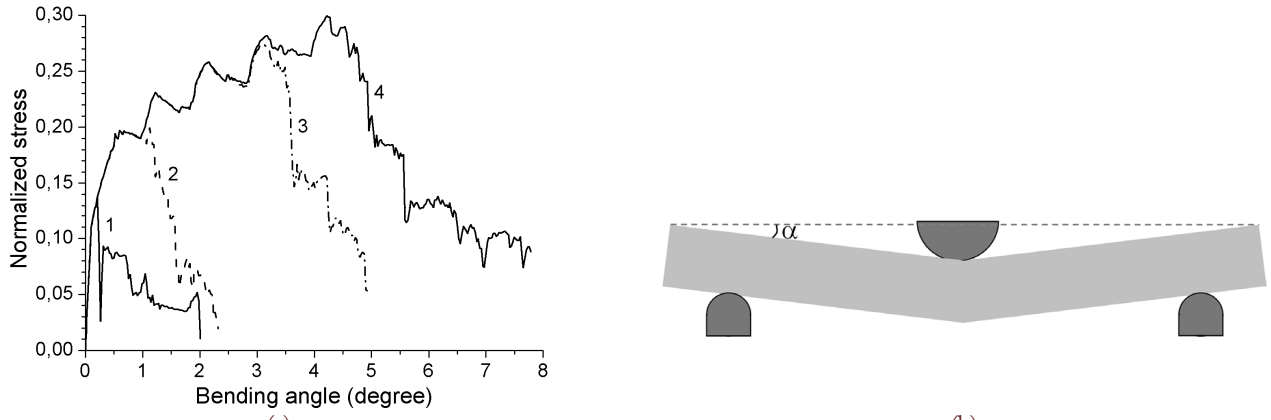

(a) (b)

Figure 13: (a) The load-displacement diagrams for the model samples of metal-ceramic composite with different strength (σ_t^{bound}) of "narrow" interphase boundaries under three-point bending test (diagrams are expressed in terms of normalized stress σ/σ_t^{NiCr} and bending angle α): $0.5\sigma_t^{NiCr}$ (1), $1.0\sigma_t^{NiCr}$ (2), $1.5\sigma_t^{NiCr}$ (3), $2.0\sigma_t^{NiCr}$ (4); (b) scheme for definition of bending angle α. Results presented hereinafter correspond to the loading velocity of V_{load} = 0.4 m/s.

The change of integral parameters of the composite response with increase in strength of interphase boundaries (σ_t^{bound}) has a pronounced non-linear character. Fig. 14a shows dependence of the sample strength (maximal value of σ) on the value of σ_t^{bound}. This dependence can be divided into three main sections. The first one (section I in the Fig. 14a) corresponds to low values of interface strength ($\sigma_t^{bound} < \sigma_t^{NiCr}$) and is characterized by small values of integral strength of the composite. In the second (transition) section ($\sigma_t^{NiCr} < \sigma_t^{bound} < 2.0\sigma_t^{NiCr}$) there is a considerable increase in the strength of the composite. In the third section corresponding to composites with high strength of interfaces ($\sigma_t^{bound} > 2.0\sigma_t^{NiCr}$), the value of composite strength reaches the saturation. The described stages are pronounced in the curve of interface strength depending on fracture energy (Fig. 14b). It can be seen that the fracture energy of composites with high-strength interphase boundaries increases by an order of magnitude in comparison with composites containing low-strength interfacial boundaries.

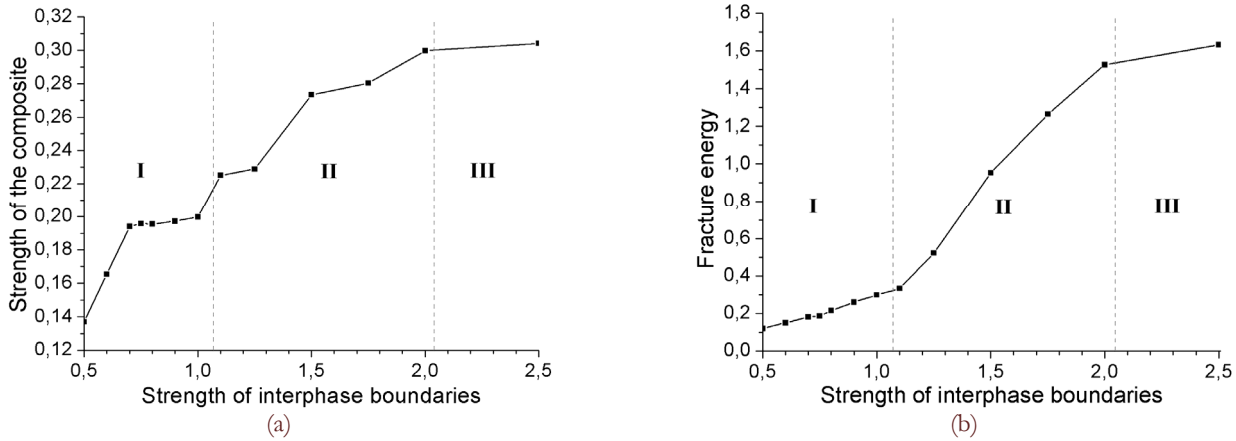

(a) (b)

Figure 14: Strength (a) and fracture energy (b) in model metal-ceramic composite depending on interphase boundary strength σ_t^{bound}. Values of interphase boundary strength and "macroscopical" composite strength are normalized by tensile strength of the binder σ_t^{NiCr}. Fracture energy was calculated as an area under the loading diagram expressed in the units "normalized stress – bending angle" (Fig. 13a).

The analysis of simulation results showed that staging of the change in integral parameters of the composite response with increase in strength of interphase boundaries (σ_t^{bound}) is associated with a change in the nature of fracture. Fig. 15 shows

the main stages of fracture in composites with different values of the strength of interphase boundaries. In the case of low values of interface strength σ_t^{bound} (smaller than the strength of metallic binder σ_t^{NiCr}), from the early stages of loading (at small applied strain) TiC particles are detached (debonded) from the binder producing the extended splitted sites on the interphase boundaries, which are under tensile stresses (see top row in Fig.15). Increase in the applied strain joints these separate sites due to cracks passing through the binder. For high values of σ_t^{bound}, under approaching of the strength of reinforcing particles the crack is nucleated, and it grows through the matrix bypassing the interphase boundaries, while interface zones remain virtually undamaged (see bottom row in Fig.15). In the "intermediate" range of interface strength (σ_t^{bound} is equal to or a bit higher than the value of binder strength) the character of composite failure changes from an "interfacial" type to a "binder" one. It is clear that crack initiation in the plastic binder takes place under high applied strains, and crack growth is rather slow. As a consequence, fracture energy of composites with high-strength interfacial boundaries increases by an order of magnitude compared to composites with low-strength interfaces (Fig.14b). Thus, the strength of interfaces between reinforcing inclusions and plastic binder is a critical factor, which determines a number of service characteristics in metal-ceramic composites, such as strength, critical strain, crack growth resistance and others.

The strength of the interface is an integral parameter whose value is determined by a number of features of internal structure and geometry of the given boundary. One of the key factors determining the strength of metal-ceramic composites is the width of the transition zone (zone of variable chemical composition) H_{ij}, which determines gradients of concentration of chemical elements and of local mechanical properties. As shown in [52, 55], shear stresses at the interfaces between elastic-brittle reinforcing particles and plastic matrices may exceed stresses in the matrix up to 5-10 times. This is due to a significant difference in the rheological characteristics of the interacting components of the composite. It is clear that high stress concentration determines a rapid debonding of particles from the binder in case of weak interphase boundaries (top row in Fig.15). At the same time, wide transition zones at the interface can reduce the magnitude of the gradient of mechanical properties and, thus, decrease the stress gradient. That "smearing" of stress concentrator can lead to a substantial increase in the strength and deformation characteristics of the interfaces. This effect can be demonstrated by the given simulation results on three-point bending test of the metal-ceramic composite with "wide" interphase boundaries. A composite with the interphase boundary of 0.8 μm wide was considered (the structure of the transition zone is shown in Fig. 10). Rheological and strength characteristics of movable cellular automata modelling the transition zone areas were determined on the basis of phase mixture model (43) using linear interpolation of corresponding values (parameters) for the titanium carbide and (Ni-Cr)-alloy. Fig. 16 shows the load-displacement diagrams for three-point bending test of the model sample of considered metal-ceramic composite (curve 1) and composites with "narrow" interphase boundaries (curves 2 and 3). It can be seen that a sufficiently wide transition zones provide high values of strength, ultimate strain and fracture energy of the material. The values of these parameters are close to the maximum corresponding to the metal-ceramic composites with high-strength "narrow" boundaries (Fig. 14). Note that for the composite with wide interfaces, fracture occurs by means of initiation and propagation of cracks in the binder. As a rule, the crack envelopes the transition zones in this case. The foregoing shows that the broad interphase boundaries with a gradual change in mechanical properties possess high values of the effective strength and have a significant influence on integral ("macroscopical") mechanical properties of metal-ceramic composite.

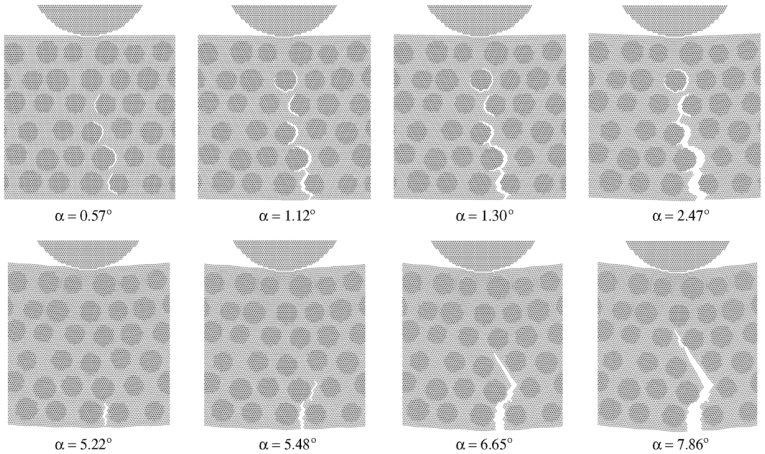

Figure 15: Dynamics of fracture in metal-ceramic composite specimens characterized by different values of the strength of interface boundaries σ_t^{bound}: $0.7\sigma_t^{NiCr}$ (top row); $2.5\sigma_t^{NiCr}$ (bottom row). Here α is bending angle.

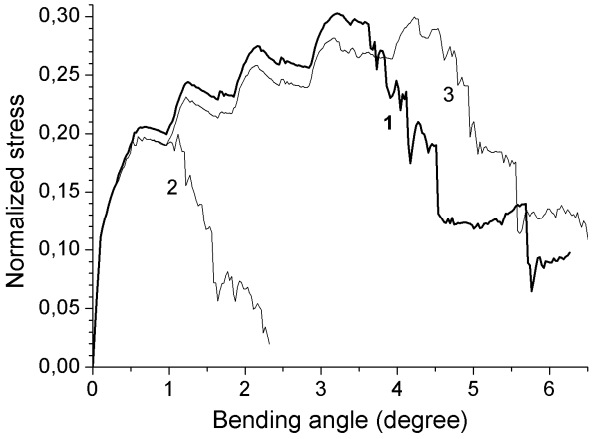

Figure 16: The load-displacement diagrams for three-point bending test of model samples of metal-ceramic composite with "wide" (curve 1) and "narrow" (curves 2 and 3) interphase boundaries (V_{load} = 0.4 m/s). Curves 2 and 3 correspond to composites with different values of strength (σ_t^{bound}) of "narrow" interfaces: $1.0\sigma_t^{NiCr}$ (2); $2.0\sigma_t^{NiCr}$ (3).

As follows from analysis of stress distribution in model composites, high effective strength of wide interphase boundaries is a result of a significant expansion of the area of internal stress decreasing from high values in the reinforcing particles (which are stress concentrators in the composite [55]) to significantly lower values in the plastic binder (Fig. 17). This leads to two-three-fold decrease in the value of stress gradients for wide interphase boundaries as compared to "narrow" interfaces. As a consequence of a smoother distribution of internal stresses, the integral ("macroscopical") deformation and strength characteristics of metal-ceramic composite significantly increase, and fracture mechanism changes from damages and crack formation at the interfaces to the crack propagation in the plastic binder.

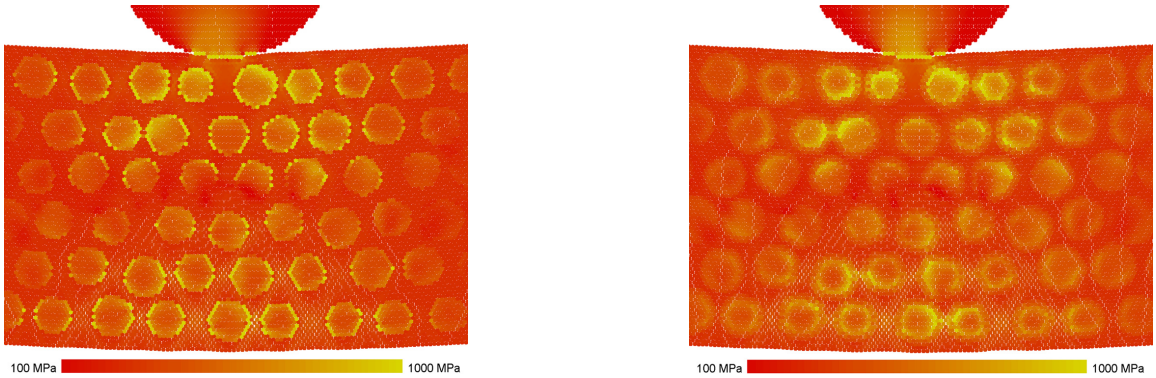

(a) (b)

Figure 17: Stress intensity distribution in the central part of the samples of metal-ceramic composite with "narrow" (a) and "wide" (b) interphase boundaries. Three-point bending test. Stress distributions correspond to the bending angle $\alpha = 3.5°$

Analysis of simulation results indicate that increase of the width of transition zone at the interphase boundaries in metal-ceramic composites can provide an increase in the integral parameters of mechanical response of materials (strength, ultimate strain and fracture energy). Fig. 18 shows dependencies of the sample strength (Fig. 18a) and fracture energy (Fig. 18b) in model metal-ceramic composite depending on width of transition zone. It is seen that presence of even narrow mesoscale transition zone (~0.3 μm) between the TiC particles and (Ni-Cr)-alloy increases specimen strength and the fracture energy in 1.5 and 5 times respectively. A further widening of the interface leads to decrease of the rate of increase of integral parameters of the composite response. And when the value of H_{if} becomes comparable to the average distance between TiC particles (H_{if} >1 μm) changing of strength and fracture energy of the composite becomes insignificant.

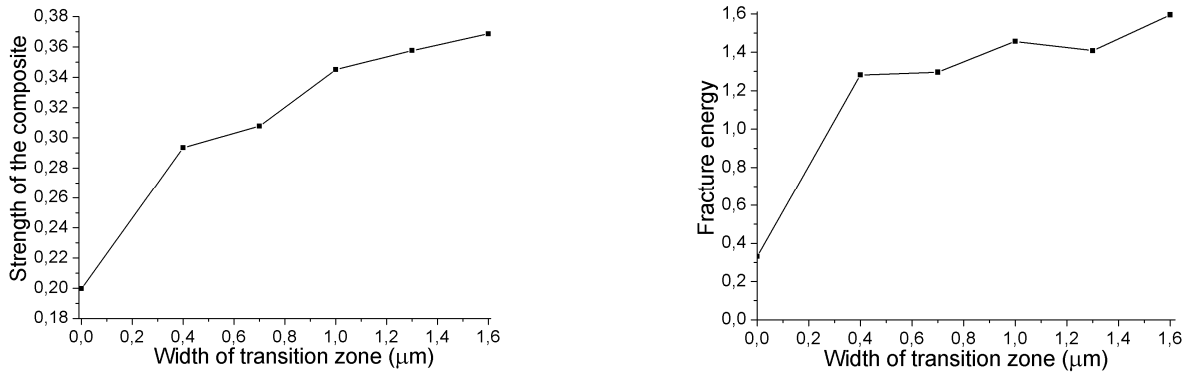

(a) (b)

Figure 18: Strength (a) and fracture energy (b) in model metal-ceramic composite depending on width of transition zone. Value of composite strength is normalized by tensile strength of the binder σ_t^{NiCr}.

CONCLUSIONS

The group of particle-based numerical methods belonging to the concept of discrete elements (DE) is an extensively used and efficient tool to study complex processes of deformation and fracture of heterogeneous solids under complex loading conditions. The main advantage of these methods compared to conventional numerical methods in continuum mechanics (FEM, FDM and other) is a capability of direct modeling of numerous fracture accompanied by sliding and repacking of fragments, dilatancy of the medium and so on. Nevertheless, until recently, capabilities of this methods were limited by description of brittle and granular materials and media.

A new approach which makes possible fundamental extension of the application field of DE-based methods to elastic-plastic and visco-elastic-plastic solids is proposed in the paper. This approach is based on the idea about building associations between the components of stress/strain tensor of the local volume and the inter-element forces/displacements. The proposed associating allows one to rewrite relations of the applied model of plasticity (which are conventionally written in terms of stress/strain tensor components) in terms of forces and displacements or their increments. In particular, implementation of plastic flow theory with von Mises yield criterion within the discrete element concept is described. The movable cellular automaton (MCA) method [22-24] combining formalisms of cellular automaton methods and discrete element method was used as a numerical technique to implement this model of plasticity. Note that the developed approach provides potential possibility to realize various models of elastoplasticity or viscoelastoplasticity (including Dricker-Prager, Nikolaevskiy and other dilatant plasticity models) in the framework of "conventional" particle methods. Furthermore, it allows one to get isotropic (independent of the packing of elements) deformation pattern even on regularly packed particle ensembles, that is a fundamental problem in conventional formalism using pair-wise interaction potentials.

Another important advantage of the developed formalism of discrete element interaction is a possibility to directly apply complex multiparametric fracture criteria (Drucker-Prager, Mohr-Coulomb, etc) as criteria of interelement bond breakage. The use of these criteria is very important for correct modeling of fracture of complex heterogeneous materials of various nature.

To demonstrate the capabilities of the approach some aspects of the problem of modeling of deformation and fracture of metal-ceramic composites are considered. On this example the prospects of application of particle-based numerical methods (in particular, of movable cellular automaton method) to study the influence of the features of internal structure of heterogeneous materials on their mechanical properties (strength, fracture toughness, etc) and fracture pattern are shown.

At the present time described models of interaction of movable cellular automata belonging to the concept of discrete elements are approved and widely used to study fracture-related problems at different scales from nanoscopic to macroscopic one, whose investigation by conventional numerical methods of continuum mechanics is difficult. The problems of this type include physical and mechanical processes in contact patches of technical and natural frictional pairs [24,56-58], multiple (quasi-viscous) fracture of porous ceramics or composite coatings [25,59,60], dynamics of damage accumulation and dilatancy in active fault zones [61,62] and so on.

ACKNOWLEDGMENTS

The investigation has been carried out within the SB RAS Program III.23.1 for Basic Research and at partial financial support of the Project No. 5 of the Belarus NAS and SB RAS Program for Joint Basic Research and the Project No. 2.12.2 of the Program No.12 of the Department of Energy, Mechanical engineering, Mechanics and Processes Control of RAS.

REFERENCES

[1] O.C. Zienkiewicz, R.L. Taylor, The finite element method set. Elsevier, (2005).
[2] M.L. Wilkins, Computer simulation of dynamic phenomena. Berlin Heidelberg: Springer-Verlag, (1999).
[3] M.W. Evans and F.H. Harlow, The particle-in-cell method for hydrodynamic calculations. Los Alamos Scientific Laboratory Report No. LA-2139, (1957).
[4] J.J. Monaghan, Reports on progress in physics, 68(8) (2005) 1703.
[5] G.R. Liu and M.B. Liu, Smoothed Particle Hydrodynamics: a meshfree particle method. Singapore: World Scientific, (2003).
[6] W.G. Hoover, C.G. Hoover, Computing in Science and Engineering, 3(2) (2001) 78.
[7] W.G. Hoover, C.G. Hoover, American Journal of Physics, 76(4-5) (2008) 481.
[8] E. Onate, S.R. Idelson, F. Del Pin, R. Aubry, International Journal of Computational Methods, 1(2) (2004) 267.
[9] M. Rieth, Nano-engineering in science and technology. Singapore: World Scientific, (2003).
[10] P.A. Cundall, O.D.L. Strack, Geotechnique 29(1) (1979) 47.
[11] L. Jing, O. Stephansson, Fundamentals of discrete element method for rock engineering: theory and applications. Elsevier, (2007).
[12] D. Greenspan, Computer-oriented mathematical physics. University of Texas at Arlington: Pergamon Press, (1981).
[13] P.W. Cleary, M.D. Sinnott, R.D. Morrison, Minerals Engineering, 22(14) (2009) 1218.
[14] P.W. Cleary, M.D. Sinnott, R.D. Morrison, Minerals Engineering, 22(14) (2009) 1230.
[15] J.E. Hilton, L.R. Mason, P.W. Cleary, Chemical engineering Science, 65(5) (2010) 1584.
[16] L. Sibille, F. Nicot, F.V. Donze, F. Darve, International Journal for Numerical and Analytical Methods in Geomechanics, 31(3) (2007) 457.
[17] N. Cho, C.D. Martin, D.C. Sego, International Journal of Rock Mechanics and Mining Sciences, 45(8) (2008) 1335.
[18] G. Saussine, C. Cholet, P.E. Gautier, F. Dubois, C. Bohatier, J.J. Moreau, Computer Methods in Applied Mechanics and Engineering, 195(19-22) (2006) 2841.
[19] D.O. Potyondy, P.A. Cundall, International Journal of Rock Mechanics and Mining Sciences, 41(8) (2004) 1329.
[20] G. Wang, A. Al-Ostaz, A.H.-D. Cheng, P.R. Mantena, Computational Materials Science, 44(4) (2009) 1126.
[21] V.L. Popov, S.G. Psakhie, Physical Mesomechanics, 4(1) (2001), 15.
[22] S.G. Psakhie, Y. Horie, S.Yu. Korostelev, A.Yu. Smolin, A.I. Dmitriev, E.V. Shilko, S.V. Alekseev, Russian Physics Journal 38 (1995) 1157.
[23] S.G. Psakhie, Y. Horie, G.P. Ostermeyer, S.Yu. Korostelev, A.Yu. Smolin, E.V. Shilko, A.I. Dmitriev, S. Blatnik, M. Spegel, S. Zavsek, Theoretical and Applied Fracture Mechanics, 37 (2001) 311.
[24] S.G. Psakhie, Y. Horie, E.V. Shilko, A.Yu. Smolin, A.I. Dmitriev, S.V. Astafurov, International Journal of Terraspace Science and Engineering, 3(1) (2011) 93.
[25] S.G. Psakhie, E.V. Shilko, A.Yu. Smolin, A.V. Dimaki, A.I. Dmitriev, Ig.S. Konovalenko, S.V. Astafurov, S. Zavsek, Physical Mesomechanics, 14 (2011) 224.
[26] A.S. Mikhailov, Foundations of Synergetics I. Distributed Active Systems. Berlin: Springer, (1994).
[27] D. Basanta, P.J. Bentley, M.A. Miodownik, E.A. Holm, Lecture Notes in Computer Science, 2610 (2003) 77.
[28] A.V. Dimaki, E.V. Shilko, S.G. Psakhie, Combustion, Explosion, and Shock waves, 41(2) (2005) 151.
[29] S.G. Psakhie, E.V. Shilko, A.Yu. Smolin, A.I. Dmitriev, S.Yu. Korostelev, Proceedings of US-Russian Workshop "Shock Induced Chemical Processing" (1996) 21.
[30] M.S. Dawa, S.M. Foilesa, M.I. Baskes, Materials Science Reports, 9, (1993) 251.
[31] S.G. Psakhie, M.A. Chertov, E.V. Shilko, Physical Mesosmechanics, 3(3) (2000) 89.
[32] L. Jing, O. Stephansson, Fundamentals of discrete element method for rock engineering: theory and applications. Elsevier, (2007).

[33] A. Love, A Treatise on the mathematical theory of elasticity. Cambridge: Cambridge University Press, (1927).
[34] M.L. Wilkins, M.W. Gutman, Plane stress calculations with a two dimensional elastic-plastic computer program. Preprint UCRL-77251, University of California, Lawrence Livermore Laboratory, (1976).
[35] M. Rieth, Nano-engineering in science and technology. Singapore: World Scientific, (2003).
[36] H. Neuber, Theory of notch stresses. Berlin: Springer, (1958).
[37] V.V. Novozhilov, Journal of Applied Mathematics and Mechanics-USSR, 33 (1969) 212.
[38] M.P. Wnuk, A. Yavari, Engineering Fracture Mechanics 75 (2008) 1127.
[39] M.P. Wnuk, A. Yavari, Engineering Fracture Mechanics 76 (2009) 548.
[40] M. Elices, G.V. Guinea, J. Gomez, J. Planas, Engineering Fracture Mechanics, 69 (2002) 137.
[41] N. Chawla, K.K. Chawla, Metal matrix composites, Springer, New York, (2006).
[42] S. Suresh, A. Mortensen, A. Needleman, Fundamentals of metal-matrix composites, Butterworth-Heinemann, Stoneham, MA, (1993).
[43] K.U. Kainer, In: K.U. Kainer (Ed.), Metal Matrix Composites. Custom-made materials for Automotive and Aerospace Engineering, Wiley-VCH Verlag, Weinheim, (2006).
[44] A. Pramanik, L.C. Zhang, J.A. Arsecularante, International Journal of Machine Tools and Manufacture, 46 (2006) 1795.
[45] V.E. Ovcharenko, Baohai Yu, S.G. Psahie, Journal of Materials Science and Technology, 21 (2005) 427.
[46] Baohai Yu, V.E. Ovcharenko, S.G. Psakhie, O.V. Lapshin, Journal of Materials Science and Technology, 22 (2006) 511.
[47] P.A. Vityaz, L.I. Grechikhin, Physical Mesomechanics, 7 (5-6) (2004) 51.
[48] A. Ayyar, N. Chawla, Composites Science and Technology, 66 (2006) 1980.
[49] S.N. Kulkov, Physical Mesomechanics, 9 (1-2) (2006) 73.
[50] W.F. Caley, B. Paton, D.P. Bishop, G.J. Kipouros, Journal of Materials Science, 38 (2003) 1755.
[51] K.N. Tran, Y. Ding, J.A. Gear, ANZIAM Journal, 51 (2010) C16.
[52] Yu.V. Sokolkin, V.E. Vil'deman, A.V. Zaitsev, I.N. Rochev, Mechanics of Composite Materials, 34 (1998) 171.
[53] T. Christman, A. Needleman, S. Nutt, S. Suresh, Materials Science and Engineering A, 107 (1989) 49.
[54] L. Mishnaevsky, M. Dong, S. Honle, S. Schmauder, Computational Materials Science, 16 (1999) 133.
[55] N. Chawla, K.K. Chawla, Journal of Materials Science, 41 (2006) 913.
[56] W. Österle, A.I. Dmitriev, Wear, 271(9-10) (2011) 2198.
[57] A.I. Dmitriev, W. Österle, H. Kloss, Nanosystems: Physics, Chemistry, Mathematics, 2(2) (2011) 58.
[58] S.G. Psakhie, V.L. Popov, E.V. Shilko, A.Yu. Smolin, A.I. Dmitriev, Physical Mesomechanics, 12(5-6) (2009) 221.
[59] S.G. Psakhie, D.D. Moiseyenko, A.Yu. Smolin, E.V. Shilko, A.I. Dmitriev, S.Yu. Korostelev, E.M. Tatarintsev, Computational Materials Science, 16 (1999) 333.
[60] Ig.S. Konovalenko, A.Yu. Smolin, S.Yu. Korostelev, S.G. Psakhie, Technical Physics, 54(5) (2009) 758.
[61] S.G. Psakhie, V.V. Ruzhich, E.V. Shilko, V.L. Popov, S.V. Astafurov, Tribology International, 40(6) (2007) 995.
[62] S.V. Astafurov, E.V. Shilko, S.G. Psakhie, Physical Mesomechanics, 13(3-4) (2010) 164.

APPENDIX A

Let's assume that under consideration of isotropic linearly elastic medium the expressions for specific forces of normal (central) and shear (tangential) response of discrete element *i* to mechanical action by neighbouring element *j* are defined on the basis of reformulation of Hooke's law for diagonal and off-diagonal components of stress tensor (19):

$$\begin{cases} \sigma_{ij} = 2G_i\varepsilon_{i(j)} + \left(1 - {}^{2G_i}\!/_{K_i}\right)\bar{\sigma}^i_{mean} \\ \tau_{ij} = 2G_i\gamma_{i(j)} \end{cases} \qquad \text{(A1)}$$

Explanation of meaning of variables in (A1) can be found in Sections 2-4 (*Main parameters of interaction of discrete elements - Discrete element interaction for modeling consolidated elastic-plastic medium*).
The proposed expressions (A1) are correct as they provide fulfillment of Hooke's law (19) for average stress and strain tensors in the volume of discrete element *i*. Actually, substitution of relations (A1) in the expression (16′) for $\alpha=\beta=x$ leads to the following relationship:

$$\bar{\sigma}^i_{xx} = \frac{1}{\Omega_i}\left[\sum_{j=1}^{N_i} S_{ij} q_{ij} \sigma_{ij} \cos^2\theta_{ij,x} + \sum_{j=1}^{N_i} S_{ij} q_{ij} \tau_{ij} \cos\theta_{ij,x} \sin\theta_{ij,x}\right] =$$
$$= 2G_i \frac{1}{\Omega_i}\left[\sum_{j=1}^{N_i} S_{ij} q_{ij} \varepsilon_{i(j)} \cos^2\theta_{ij,x} + \sum_{j=1}^{N_i} S_{ij} q_{ij} \gamma_{i(j)} \cos\theta_{ij,x} \sin\theta_{ij,x}\right] + \quad \text{(A2)}$$
$$+\left(1 - \frac{2G_i}{K_i}\right)\bar{\sigma}^i_{mean} \frac{1}{\Omega_i}\sum_{j=1}^{N_i} S_{ij} q_{ij} \cos^2\theta_{ij,x}$$

To understand the meaning of the first contribution in (A2)

$$2G_i \frac{1}{\Omega_i}\left[\begin{array}{l}\sum_{j=1}^{N_i} S_{ij} q_{ij} \varepsilon_{i(j)} \cos^2\theta_{ij,x} + \\ + \sum_{j=1}^{N_i} S_{ij} q_{ij} \gamma_{i(j)} \cos\theta_{ij,x} \sin\theta_{ij,x}\end{array}\right]$$

the notion of average strain tensor in the volume of discrete element i has to be introduced. Considering relative normal and shear displacements of interacting elements i and j as components of the vector of relative displacement the expression for average strains $\bar{\varepsilon}^i_{\alpha\beta}$ in the volume of element i can be formally written by analogy with $\bar{\sigma}^i_{\alpha\beta}$. In considered two-dimensional problem statement it has the following form:

$$\bar{\varepsilon}^i_{\alpha\beta} = \frac{1}{\Omega_i}\sum_{j=1}^{N_i} q_{ij} S_{ij}\left[\varepsilon_{i(j)} \cos\theta_{ij,\alpha} \cos\theta_{ij,\beta} \pm \gamma_{i(j)} \cos\theta_{ij,\alpha} \sin\theta_{ij,\beta}\right] \quad \text{(A3)}$$

According to (A3) the first contribution in the right part of (A2) has the meaning of corresponding average strain tensor component:

$$\frac{1}{\Omega_i}\sum_{j=1}^{N_i} q_{ij} S_{ij}\left[\varepsilon_{i(j)} \cos^2\theta_{ij,x} + \gamma_{i(j)} \cos\theta_{ij,x} \sin\theta_{ij,x}\right] = \bar{\varepsilon}^i_{xx}. \quad \text{(A4)}$$

To understand the meaning of the sum

$$\frac{1}{\Omega_i}\sum_{j=1}^{N_i} S_{ij} q_{ij} \cos^2\theta_{ij,x}$$

in the second contribution in (A2) the procedure of homogenization of unit second-rank tensor

$$\hat{e} = \begin{vmatrix} 1 & 0 & 0 \\ 0 & 1 & 0 \\ 0 & 0 & 1 \end{vmatrix}$$

has to be considered. General expression for average value $\bar{e}^i_{\alpha\beta}$ of unit tensor component $e^i_{\alpha\beta}$ in the volume of discrete element i ($e^i_{\alpha\beta} \equiv \bar{e}^i_{\alpha\beta}$) has the form:

$$\bar{e}^i_{\alpha\beta} = \frac{1}{\Omega_i}\int_{\Omega_i} e_{\alpha\beta} d\Omega = \frac{1}{\Omega_i}\int_{\Omega_i} e_{\gamma\beta} \frac{\partial r_\alpha}{\partial r_\gamma} d\Omega, \quad \text{(A5)}$$

where the identity

$$e_{\alpha\beta} = \delta_{\alpha\gamma} e_{\gamma\beta} = \frac{\partial r_\alpha}{\partial r_\gamma} e_{\gamma\beta}$$

was applied (the Kronecker delta $\delta_{\alpha\gamma}$ and the Einstein summation convention are employed here); r_α is projection of a

radius-vector to corresponding axis of laboratory system of coordinates. The volume integral in (A5) can be rewritten as a surface integral by applying the Gauss divergence theorem:

$$\overline{e}^{i}_{\alpha\beta} = \frac{1}{\Omega_i}\int\limits_{\Omega_i} e_{\gamma\beta}\frac{\partial r_\alpha}{\partial r_\gamma}d\Omega = \frac{1}{\Omega_i}\int\limits_{\Omega_i} x_\alpha e_{\gamma\beta} n_\gamma d\Omega = \frac{1}{\Omega_i}\int\limits_{S_i} x_\alpha n_\beta dS\,, \tag{A6}$$

where S_i is the surface of element i; n_β is the unit outward normal to infinitesimal surface area dS. The element i is loaded by forces acting at discrete interaction surfaces S_{ij} (10). So, its total surface S_i can be represented as a set of S_{ij}, and surface integral can be replaced by the following sum:

$$\overline{e}^{i}_{\alpha\beta} = \frac{1}{\Omega_i}\int\limits_{S_i} x_\alpha n_\beta dS = \frac{1}{\Omega_i}\sum_{j=1}^{N_i} S_{ij} q_{ij} \cos\theta_{ij,\alpha}\cos\theta_{ij,\beta}\,, \tag{A7}$$

where $\theta_{ij,\alpha}$ is defined as shown in the Fig.5; N_i is total number of interaction surfaces ($\sum_{j=1}^{N_i} S_{ij} = S_i$). In accordance with (A7) the sum in the second contribution in the right part of (A2) is:

$$\frac{1}{\Omega_i}\sum_{j=1}^{N_i} S_{ij} q_{ij} \cos^2\theta_{ij,x} = \overline{e}^{i}_{xx} \equiv e^{i}_{xx} = 1\,. \tag{A8}$$

So, the expression (A2) can be rewritten in the form:

$$\overline{\sigma}^{i}_{xx} = 2G_i\overline{\varepsilon}^{i}_{xx} + \left(1-\frac{2G_i}{K_i}\right)\overline{\sigma}^{i}_{mean} \equiv \overline{\sigma}^{i}_{xx} \tag{A9}$$

which is Hooke's law for average stress and strain tensor components $\overline{\sigma}^{i}_{xx}$ and $\overline{\varepsilon}^{i}_{xx}$.
Corresponding expressions for other components of average stress tensor can be derived in analogous fashion:

$$\begin{aligned}
\overline{\sigma}^{i}_{yy} &= \frac{1}{\Omega_i}\left[\sum_{j=1}^{N_i} S_{ij} q_{ij}\sigma_{ij}\sin^2\theta_{ij,x} - \sum_{j=1}^{N_i} S_{ij} q_{ij}\tau_{ij}\cos\theta_{ij,x}\sin\theta_{ij,x}\right] = \\
&= 2G_i\frac{1}{\Omega_i}\left[\sum_{j=1}^{N_i} S_{ij} q_{ij}\varepsilon_{i(j)}\sin^2\theta_{ij,x} - \sum_{j=1}^{N_i} S_{ij} q_{ij}\gamma_{i(j)}\cos\theta_{ij,x}\sin\theta_{ij,x}\right] + \\
&+\left(1-\frac{2G_i}{K_i}\right)\overline{\sigma}^{i}_{mean}\frac{1}{\Omega_i}\sum_{j=1}^{N_i} S_{ij} q_{ij}\sin^2\theta_{ij,x} = 2G_i\overline{\varepsilon}^{i}_{yy} + \left(1-\frac{2G_i}{K_i}\right)\overline{\sigma}^{i}_{mean} \equiv \overline{\sigma}^{i}_{yy}
\end{aligned} \tag{A10}$$

$$\begin{aligned}
\overline{\sigma}^{i}_{xy} &= \frac{1}{\Omega_i}\left[\sum_{j=1}^{N_i} S_{ij} q_{ij}\left[\sigma_{ij}\cos\theta_{ij,x}\sin\theta_{ij,x}\right] - \sum_{j=1}^{N_i} S_{ij} q_{ij}\left[\tau_{ij}\cos^2\theta_{ij,x}\right]\right] = \\
&= 2G_i\frac{1}{\Omega_i}\left[\sum_{j=1}^{N_i} S_{ij} q_{ij}\left[\varepsilon_{i(j)}\cos\theta_{ij,x}\sin\theta_{ij,x}\right] - \sum_{j=1}^{N_i} S_{ij} q_{ij}\left[\gamma_{i(j)}\cos^2\theta_{ij,x}\right]\right] + \\
&+\left(1-\frac{2G_i}{K_i}\right)\overline{\sigma}^{i}_{mean}\frac{1}{\Omega_i}\sum_{j=1}^{N_i} S_{ij} q_{ij}\cos\theta_{ij,x}\sin\theta_{ij,x} = \\
&= 2G_i\overline{\varepsilon}^{i}_{xy} + \overline{e}^{i}_{xy}\left(1-\frac{2G_i}{K_i}\right)\overline{\sigma}^{i}_{mean} = 2G_i\overline{\varepsilon}^{i}_{xy} \equiv \overline{\sigma}^{i}_{xy}
\end{aligned} \tag{A11}$$

Relations (A9)-(A11) are derived on the basis of assumption that total surface S_i of the element i is "occupied" by interacting neighbours j. However, if a part of surface S_i of automaton/element i is free (i.e. neighbouring elements j "occupy" only part of S_i), corresponding unoccupied surfaces S_{ik} can be formally considered as surfaces of interaction with virtual neighbours having zero stiffness. In that case specific forces at unoccupied surfaces S_{ik} has to be assigned as zero: $\sigma_{ij}=\tau_{ij}=0$ (this doesn't hold true for corresponding pair strains: $\varepsilon_{i(j)}\neq 0$ and $\gamma_{i(j)}\neq 0$). Therefore equalities (A9)-(A11) are correct for discrete elements with partially free surface as well. In accordance with above mentioned the number of real

neighbors of element i (N_i^{real}) can be used in expression (16)-(16′) when calculating average stress tensor components. At the same time a total number of neighbours (including virtual ones) have to be used in expression (A3).
Thus, average stress and strain tensor components are connected by Hooke's law when expressions (A1) are used for assigning central (normal) and tangential (shear) response of particle to mechanical impact of neighbours. This result confirms correctness of the proposed approach to description of interaction of discrete elements (or movable cellular automata) simulating locally isotropic linearly elastic medium.

APPENDIX B

Proposed expressions

$$\begin{cases} \sigma'_{ij} = \left(\sigma_{ij} - \bar{\sigma}^i_{mean}\right) M_i + \bar{\sigma}^i_{mean} \\ \tau'_{ij} = \tau_{ij} M_i \end{cases} \tag{B1}$$

for scaling specific central and tangential forces of response of the element/automaton i to the impact of the neighbor j provide a fulfillment of radial return algorithm of Wilkins (25)-(26) for average stresses in the volume of the element i. Actually, substitution of relations (B1) in the expression (16′) for $\alpha=\beta=x$ leads to the following equation:

$$\begin{aligned} \left(\bar{\sigma}^i_{xx}\right)' &= \frac{1}{\Omega_i}\left[\sum_{j=1}^{N_i} S_{ij} q_{ij} \sigma'_{ij} \cos^2\theta_{ij,x} + \sum_{j=1}^{N_i} S_{ij} q_{ij} \tau'_{ij} \cos\theta_{ij,x} \sin\theta_{ij,x}\right] = \\ &= M_i \frac{1}{\Omega_i}\left[\sum_{j=1}^{N_i} S_{ij} q_{ij} \sigma_{ij} \cos^2\theta_{ij,x} + \sum_{j=1}^{N_i} S_{ij} q_{ij} \tau_{ij} \cos\theta_{ij,x} \sin\theta_{ij,x}\right] + \\ &+ \left(1 - M_i\right) \bar{\sigma}^i_{mean} \frac{1}{\Omega_i} \sum_{j=1}^{N_i} S_{ij} q_{ij} \cos^2\theta_{ij,x} \end{aligned} \tag{B2}$$

According to (16′) the sum

$$\frac{1}{\Omega_i}\left[\sum_{j=1}^{N_i} S_{ij} q_{ij} \sigma_{ij} \cos^2\theta_{ij,x} + \sum_{j=1}^{N_i} S_{ij} q_{ij} \tau_{ij} \cos\theta_{ij,x} \sin\theta_{ij,x}\right]$$

in the first contribution in the right part of (B2) has a meaning of corresponding average stress tensor component before stress returning procedure ("elastic" stress $\bar{\sigma}^i_{xx}$).
In accordance with (A7)-(A8) the second sum

$$\frac{1}{\Omega_i} \sum_{j=1}^{N_i} S_{ij} q_{ij} \cos^2\theta_{ij,x}$$

in the right part of (B2) is a diagonal component $\bar{e}^i_{xx}=1$ of unit second-rank tensor.
Therefore, the expression (B2) can be rewritten in the form:

$$\begin{aligned} \left(\bar{\sigma}^i_{xx}\right)' &= M_i \bar{\sigma}^i_{xx} + \left(1 - M_i\right) \bar{\sigma}^i_{mean} \bar{e}^i_{xx} = \\ &= \left(\bar{\sigma}^i_{xx} - \bar{\sigma}^i_{mean}\right) M_i + \bar{\sigma}^i_{mean} \end{aligned} \tag{B3}$$

which coincides with expression (26) for the case $\alpha=\beta=x$.

Corresponding expressions for other components of average stress tensor can be derived in analogous fashion:

$$\begin{aligned} \left(\bar{\sigma}^i_{yy}\right)' &= M_i \bar{\sigma}^i_{yy} + \left(1 - M_i\right) \bar{\sigma}^i_{mean} \bar{e}^i_{yy} = \\ &= \left(\bar{\sigma}^i_{yy} - \bar{\sigma}^i_{mean}\right) M_i + \bar{\sigma}^i_{mean} \end{aligned} \tag{B4}$$

$$\left(\bar{\sigma}^i_{xy}\right)' = M_i\bar{\sigma}^i_{xy} + \left(1-M_i\right)\bar{\sigma}^i_{mean}\bar{e}^i_{xy} = \bar{\sigma}^i_{xy}M_i \tag{B5}$$

It is clear that use of expressions (B1) along with (26) provides for rigorous satisfaction of the necessary conditions

$$\left(\bar{\sigma}^i_{mean}\right)' = \bar{\sigma}^i_{mean}$$

and

$$\left(\bar{\sigma}^i_{\text{int}}\right)' = M_i\bar{\sigma}^i_{\text{int}}$$

of the algorithm of Wilkins.

Thus, the proposed method (expressions (B1) and (26)) of scaling (return) of specific forces in pairs of discrete elements (or movable cellular automata) rigorously match radial return algorithm by Wilkins. This makes possible correct simulation of plastic deformation of consolidated solids under mechanical loading by the ensemble of discrete elements.

APPENDIX C

Algorithm of Wilkins for scaling local stresses in plane stress approximation (two-dimensional problem statement) is more complex than in general 3D problem or in plane strain state approximation. It is realized by iterative method [34]. When using a single iteration only, the procedure of scaling of stress tensor components can be represented as the following sequence of operations done at each step of integration of motion equations.

1. At the current time step (n+1) elastic problem is solved in incremental fashion. New values of stresses $\sigma_{\alpha\beta}$ and strains $\varepsilon_{\alpha\beta}$ are results of this solution. Calculated stresses can be further adjusted while strain values are "frozen".
2. New values of invariants of stress/strain tensor are calculated. Yield condition is checked. If the local stress state (point in the stress space) is inside the limit surface ($\sigma_{\text{int}} < \sigma_{pl}$), the procedure finishes. If the condition of crossing the yield surface is met, the value of stress scaling coefficient M is calculated. On of the features of stress scaling in plane stress state approximation is that the value of parameter M is a solution of the fourth-order polynomial equation [34]:

$$\left[\left(\sigma_{xx}-\sigma_{yy}\right)^2 + 4\tau_{xy}^2\right]\left(1+b-M\right)^2M^2 + 3b^2s_{zz}^2\left(2-M\right)^2M^2 - \\ -\frac{4}{3}\sigma_{pl}^2\left(2-M\right)^2\left(1+b-M\right)^2 = 0 \tag{C1}$$

   Here s_{zz} is a Z-component of deviatoric stress tensor ($\sigma_{zz}=0$, $s_{zz}=-\sigma_{mean}$); $b=\left(1+4G/K\right)$ is a material elastic constant. In general, this equation has several different roots with different signs. The physical situation corresponds to the positive root that is less than 1 and closest to 1. General analytical solution of (C1) does not exist and therefore Wilkins proposed to use Newton's iteration method with $M=\sigma_{pl}/\sigma_{\text{int}}$ as an initial value for iterative procedure.
3. Calculated coefficient M is then used to calculate irreversible (plastic) increment of Z-component of strain tensor ($\Delta\varepsilon_{zz}^{pl}$):

$$\Delta\varepsilon_{zz}^{pl} = \frac{s_{zz}}{2G}\frac{b\left(1-M\right)}{bM+\left(1-M\right)} \tag{C2}$$

   Note that the variable s_{zz} in (C1)-(C2) corresponds to the solution of elastic problem at the current time step.
4. Found parameters M and $\Delta\varepsilon_{zz}^{pl}$ are then used for scaling of s_{zz} and stress tensor components σ_{xx}, σ_{yy}, τ_{xy}:

$$\begin{cases} s'_{zz} = s_{zz} - \Delta\varepsilon_{zz}^{pl}\dfrac{2G}{b} \\ \sigma'_{xx} = \left(\sigma_{xx}+s_{zz}\right)M - s'_{zz} - \dfrac{s_{zz}}{2}\left(1-M\right) + \Delta\varepsilon_{zz}^{pl}\dfrac{G}{b} \\ \sigma'_{yy} = \left(\sigma_{yy}+s_{zz}\right)M - s'_{zz} - \dfrac{s_{zz}}{2}\left(1-M\right) + \Delta\varepsilon_{zz}^{pl}\dfrac{G}{b} \\ \tau'_{xy} = \tau_{xy}M \end{cases}. \tag{C3}$$

Here upper stroke marks scaled values of stresses. Note that original expressions in [34] bind scaling of diagonal stresses to correction (adjustment) of the values of plastic increments of strain tensor and volume change during the time step: $\sigma'_{\alpha\alpha} = f\left(\Delta\varepsilon^{pl}_{\alpha\alpha}, \Delta\Omega/\Omega\right)$. Expressions (C3) are obtained by simple mathematical transformation of original relationships into the notation in terms of stresses: $\sigma'_{\alpha\alpha} = f\left(\Delta\varepsilon^{pl}_{\alpha\alpha}, \sigma_{\alpha\alpha}, s_{\alpha\alpha}, s'_{\alpha\alpha}\right)$.

5. The total increment of Z-component of strain tensor (ε_{zz}) is calculated:

$$\Delta\varepsilon_{zz} = \Delta\varepsilon^{el}_{zz} + \Delta\varepsilon^{pl}_{zz} = \frac{s'_{zz} - \left(s_{zz}\right)_n}{2G} + \frac{\sigma'_{mean} - \left(\sigma_{mean}\right)_n}{K} + \Delta\varepsilon^{pl}_{zz} \tag{C4}$$

where $\Delta\varepsilon^{el}_{zz}$ is elastic component of strain increment, σ'_{mean} is mean stress value after stress scaling procedure (note that in contrast to 3D problem the procedure of stress correction in plane stress approximation is not accompanied by the persistence of mean stress because its value after the solution of elastic problem is overestimated [34]), index "*n*" indicates the value of corresponding variable referred to the end of the previous time step *n*.

Implementation of this procedure within the framework of discrete element concept is concerned with scaling of element response forces σ_{ij} and τ_{ij} to satisfy the expressions (C3) for average stress tensor components in the volume of the element *i*. By the analogy with elastic problem the expressions for correction of σ_{ij} and τ_{ij} are obtained by direct reformulation of relationships for $\sigma_{\alpha\alpha}$ and $\tau_{\alpha\beta}$ in (C3):

$$\begin{cases} \sigma'_{ij} = \left(\sigma_{ij} + \overline{s}^i_{zz}\right) M_i - \left(\overline{s}^i_{zz}\right)' - \dfrac{\overline{s}^i_{zz}}{2}\left(1 - M_i\right) + \Delta\overline{\varepsilon}^{i,pl}_{zz}\dfrac{G_i}{b_i} \\ \tau'_{ij} = \tau_{ij} M_i \end{cases} \tag{C5}$$

where $\Delta\overline{\varepsilon}^{i,pl}_{zz}$ is irreversible (plastic) increment of Z-component of average strain tensor in the volume of the element *i*. It is easy to demonstrate that scaling of element/automaton response forces σ_{ij} and τ_{ij} in accordance with (C5) rigorously satisfies the expressions (C3) for $\overline{\sigma}^i_{xx}$, $\overline{\sigma}^i_{yy}$ and $\overline{\tau}^i_{xy}$.

Note that in the case of multiple iterations of the procedure of stress/force scaling the relationships used have more cumbersome form [34], however their matter is the same.

Fractal statistics of brittle fragmentation

M. Davydova, S. Uvarov

Institute of Continuous Media Mechanics Ural Branch Russian Academy of Sciences, 1, Ac. Korolev str., 614013 Perm, Russia.
davydova@icmm.ru; usv@icmm.ru

ABSTRACT. The study of fragmentation statistics of brittle materials that includes four types of experiments is presented. Data processing of the fragmentation of glass plates under quasi-static loading and the fragmentation of quartz cylindrical rods under dynamic loading shows that the size distribution of fragments (spatial quantity) is fractal and can be described by a power law. The original experimental technique allows us to measure, apart from the spatial quantity, the temporal quantity - the size of time interval between the impulses of the light reflected from the newly created surfaces. The analysis of distributions of spatial (fragment size) and temporal (time interval) quantities provides evidence of obeying scaling laws, which suggests the possibility of self-organized criticality in fragmentation.

KEYWORDS. Fragmentation of brittle materials; Fractal statistics; Self-organized criticality.

INTRODUCTION

Fragmentation is the process of breaking a solid into separate fragments caused by multiple fractures. Such phenomenon can be observed in both engineering and natural objects over a wide range of spatial and temporal scales. An investigation of fragmentation statistics generally includes the determination of the cumulative distribution of fragment sizes or masses, i.e., the number of fragments $N(m)$ with a size or mass larger than S or m, respectively. The distribution type depends on loading conditions, material characteristics and sample geometries. Many types of distribution functions have been observed experimentally: log-normal, power-law, Mott, exponential, Weibull, and combined exponential and power-law [1 - 8]. Summarizing the results of experimental data processing, we can classify all these distribution functions into two groups: exponential and power law. The assumption that the exponential distribution is typical of the fragmentation of ductile materials and the power-law distribution characterizes brittle fragmentation has been discussed by Grady [7]. Donald Turcotte [8] has pursued the fragmentation of brittle materials as a fractal process resulting in the power law distribution function $N \sim x^{-d}$, where N is the number of fragments, x is the linear dimension of fragments, and d is the fractal dimension. The fractal character of the distribution function in a wide range of fragment sizes allows Oddershede et al. [3] to suppose that the fragmentation exhibits self-organized criticality (SOC). In their seminal paper Per Bak, Chao Tang and Kurt Wiesenfeld [9] present a new concept of SOC; numerical simulation allows them to describe the behavior of a sand pile (example of a self-organized critical system) and to conclude:

- ✓ distribution of life times of avalanches obeys a power law;
- ✓ distribution of avalanche sizes follows a power law as well.

In other words, to prove that the system exhibits SOC, it is necessary to establish the existence of a power law for temporal and spatial quantities. The purpose of this experimental study is to demonstrate that the fragmentation process exhibits SOC. To this end, we need to determine the distribution of temporal and spatial variables. It has been shown that for the fragmentation of glass plates under quasi-static loading there exists scaling in the crack pattern formed during fragmentation and fragment size distribution are also described by the power law. The experiments on quartz cylindrical

rods under dynamic loading were carried out to test the effect of sample size and variation in loading type. It was found out that the type of distribution function did not change, it remained a power law. The fragment size distribution was determined using a standard sieve analysis technique and electronic balance. In order to investigate temporal scaling, an original method was proposed. The main idea was to measure the kinetic of the appearance of the fracture surface. For a loaded glass sample illuminated with the light source, the newly formed fracture surface produced light impulses, which were registered by Photo Multiplayer Tube connected to the oscilloscope. The temporal variable was the interval between impulses, or in other words, the time between the fracture events. The statistical data processing shows that the distribution of time intervals obeys the power law. In the case of analyzing data corresponding to the initial time of the process the distribution of time interval is governed by the exponential law. The explanation of the fact that fracture kinetics at the initial stage is characterized by another distribution function requires additional investigation.

FRAGMENTATION OF THE GLASS PLATES UNDERQUASI-STATIC LOADING

Quasi-static testing was performed in the experiments with glass plates loaded in a "sandwich" to save the glass fragmentation pictures (Fig. 1a). Using the original software, the images were transformed into schematic pictures corresponding to the fragmentation patterns (Fig. 1b). This allowed us to determine the size and number of fragments and the total length of cracks. We consider two types of scaling. The first type is based on the relation

$$L(r) \sim r^D \tag{1}$$

where $L(r)$ is the total crack length in the boxes of a size $r \times r$ centred at the point B (Fig. 1b), and D is the fractal dimension. The second type is the traditional definition of the cumulative distribution of fragment sizes, in other words, the calculation of the number of fragments $N(S)$ with a size larger than S.

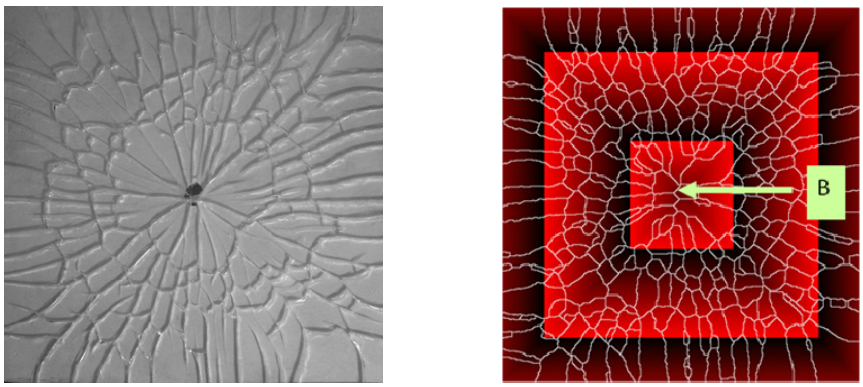

(a) (b)

Figure 1: a) Photo of typical fragmentation patterns. b) Schematic pictures of the fragmentation patterns used to determine the size and number of fragments and the total length of cracks.

The use of expression (1) was discussed by Sornette et al. [10]. However, it should be noted that the fracture pattern [10] does not have a distinct central point. At the same time, the examined fragmentation patterns have a central point, and their configuration is similar to that created with the model of diffusion-limited aggregation (DLA) [11] or the model of dielectric breakdown (DB) [12]. Relation (1) can be used to define the fractal dimension for both these models. In the case of the DB model, $L(r)$ is the total length of the discharge branches within the circle of radius r For the DLA model, $L(r)$ is the number of particles. By analogy with the DLA and DB models, to determine the fractal dimension of the fragmentation patterns, we use relation (1), where $L(r)$ is the total length of cracks in the boxes of a size $r \times r$ centred at the point B (Fig. 1b). The minimal number of the boxes used for calculation of the fractal dimension is 200. The scaling law obtained using the relation for the crack length (1) is presented in Fig. 2a. The processing of the fragment sizes shows that the relation between the fragment area and number is also fitted by a power law (Fig. 2b).

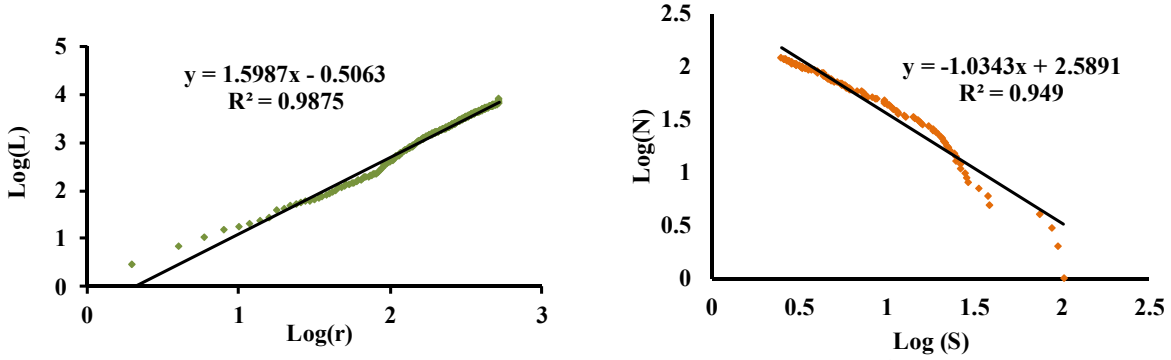

(a) (b)

Figure 2: a) Scaling law obtained using the relation for crack length (1). b) Cumulative distribution of the fragment size in a log-log plot.

There are two types of energy-dependent fragmentation patterns leading to a breakup (Fig. 3). Fig. 3a presents a fragmentation pattern that illustrates the fracture accompanied by radial crack formation. The right fragmentation pattern (Fig. 3b) has two zones corresponding to two different fracture mechanisms. The central zone has a radial crack only. In the second zone, the crack branching process is observed. Suppose that different fracture mechanisms characterize different fractal dimensions, we have

$$L(S) \sim S^D \tag{2}$$

where $L(S)$ is the total crack length inside the square frame with a thickness h (Fig. 3a), S is the frame area, and D is the fractal dimension. Calculation the fractal dimension using expression (2) shows that for the left fragmentation pattern (Fig. 3a) the data is fitted by a single line, whereas for the right pattern the log-log representation of $L(S)$ changes a slope, and the power-law exponent D decreases. A change in the fracture mechanism (from radial crack-to-crack branching) correlates with the qualitative changes in the fractal dimension.

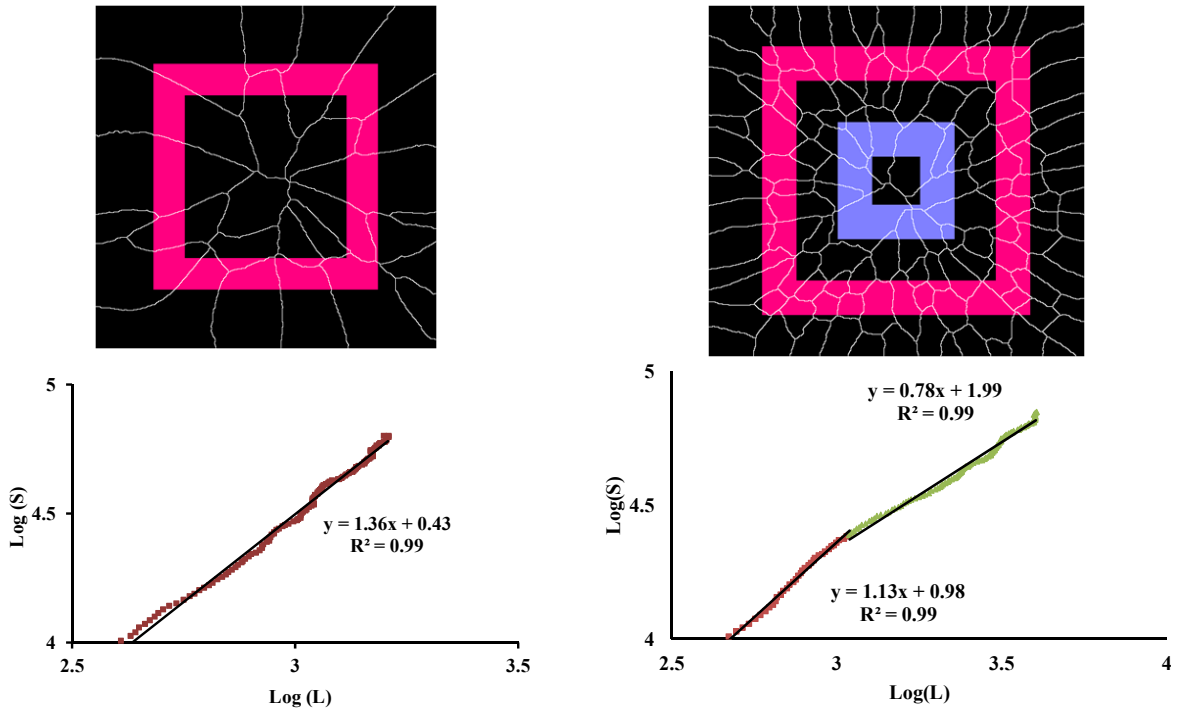

(a) (b)

Figure 3: a) Fragmentation pattern and fractal dimension definition for the fracture accompanied by radial crack formation. b) Fragmentation pattern and fractal dimension definition for the fracture accompanied by a change in the fracture mechanism.

FRAGMENTATION OF QUARTZ RODS UNDER DYNAMIC LOADING

Spatial Scaling

The fragmentation statistics was studied in recovery dynamic experiments with loaded quartz cylindrical rods using a ballistic set-up, which consisted of a gas gun with bore diameter of 19.3 mm, a velocity registration system and a base where the specimen was placed (Fig. 4). The sectional glass rod was composed of a buffer and the main part covered by an elastic shell. The buffer was used for realization of uniaxial loading produced by a cylindrical projectile of mass 13.9 g accelerated up to the velocities of 6-20 m/s. The mass of the fragments passing through the sieves was obtained by weighting the fragments using an electronic balance HR-202i (accuracy 10^{-4} g). The mass of the fragments corresponding to the maximum of the probability density function m_{max} varied in the range from $2*10^{-4}$g to $6*10^{-4}$ g (Fig. 5a). The cumulative fragment size distribution, i.e. the number of fragments $N(m)$ with a mass greater than a specified value m, was fitted by the power law (Fig. 5b).

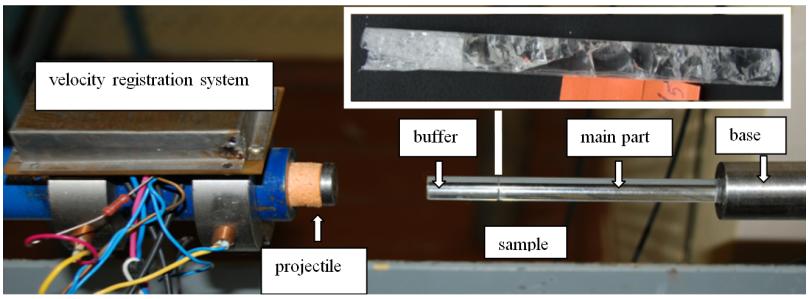

Figure 4: Ballistic set-up. An example of the fragmentation pattern is given in the upper right-hand corner.

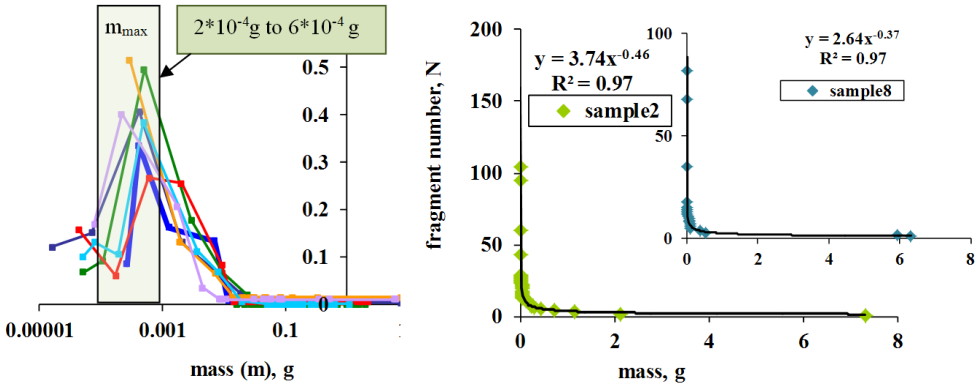

Figure 5: a) Probability density function (different colors correspond to different samples). b) Cumulative fragment size distribution.

In order to avoid the possible influence of the reflected wave on the fragmentation scenario, the ballistic set-up was modified. The sample was placed into a steel cylinder filled with plastic foam (Fig. 6). The sectional glass rod was composed of the buffer, the main part and the outer part. The presence of the last part allowed us to catch the reflected wave.

The fragmentation statistics was analyzed by varying the sample size and load intensity (projectile velocity). The results of experiments have indicated that the variation in the sample size and loading conditions does not lead to the change in the type of probability density and cumulative mass distribution functions. We have analyzed the dependence of m_{max} on the projectile energy (Fig. 7). The markers indicate the fragmentation under different loading conditions: circles correspond to the fragmentation due to interaction between the direct and reflected compression waves (Fig. 4); triangles correspond to fragmentation under the action of a compression wave (Fig. 6); boxes correspond to fragmentation induced by a direct compression wave and its reverberation in rod (Fig. 9). At low energy of the projectile, a more considerable scattering was found for m_{max}. This actually means that for low energy we have two or three sieves with a comparable number of fragments, and for high energy - only one sieve with a predominant number of fragments.

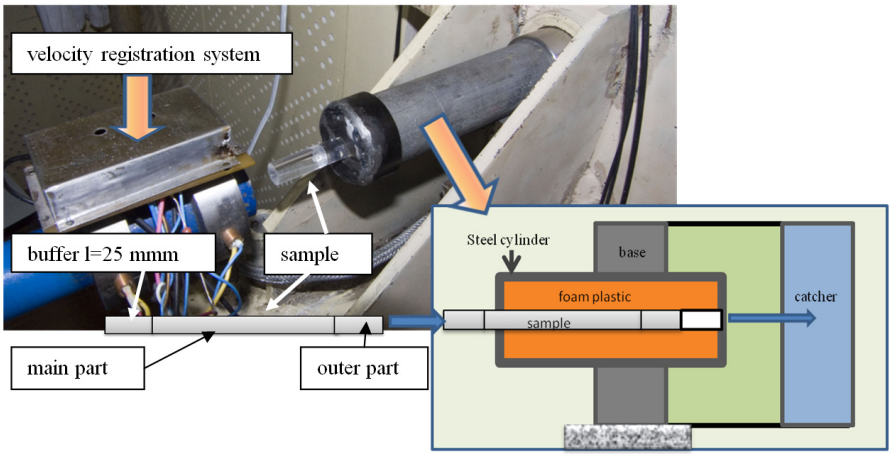

Figure 6: Ballistic set-up and scheme of steel cylinder with a sample.

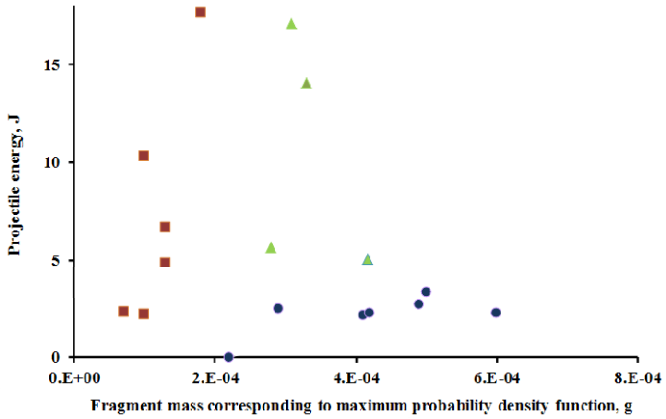

Figure 7: The dependence of fragment mass corresponding to maximum probability density function on the projectile energy.

Thus, the cumulative distributions illustrating the relation between the numbers of fragments and their linear dimension are represented as a log-log plot (Fig. 8). The linear dimension is defined as a cube root of mass or a square root of area. The distribution is fractal by nature with a power law in the form $N(>r)=Cr^{-D}$, where N is the number of fragments with a characteristic linear dimension greater than r. The fractal dimension D varies from 1.6 to 2.0 for a plate and from 1.1 to 1.7 for a rod.

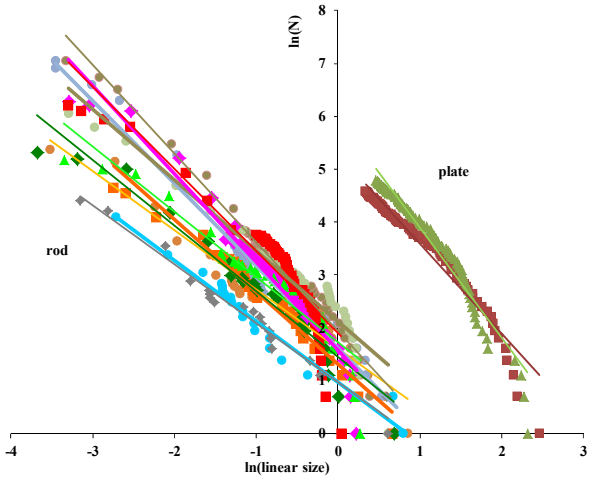

Figure 8: Double logarithmic plot of the cumulative distribution function for a plate and a rod (different colors correspond to different samples).

Temporal Scaling

As shown in the section Introduction, to confirm the fact that the fragmentation exhibits SOC, we need to establish the existence of a power law for temporal and spatial quantities. The evidence of the spatial scaling for the fragmentation of brittle materials under different loading conditions was given in two previous sections. For measurement of temporal scale we developed an experimental device to determine the time interval between the impulses of the light reflected from the newly created fracture surfaces. In our investigation (fragmentation of quartz rods under dynamic loading), SOC means that there exist:

- ✓ power law distribution of fragment size;
- ✓ power law distribution of time interval between the impulses of the light reflected from newly created surfaces.

To obtain the fragment size distribution, the technique described in the previous experiments was used, which made it possible to get the distribution obeying the scaling law.

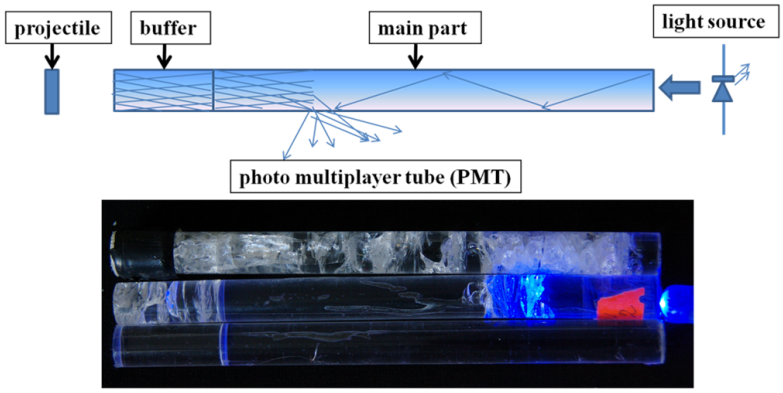

Figure 9: Scheme of the experiment for measuring the distribution time interval between the impulses of the light reflected from the fracture surfaces. The photo of the sample illuminated with the light source.

The scheme given in Fig. 9 illustrates the experimental technique used to measure the distribution of time quantities. The sample is illuminated with the light source. The intensity of the light reflected from the fracture surfaces is registered by the Photo Multiplayer Tube connected with the oscilloscope (oscilloscope sample rate is 1 GHz).

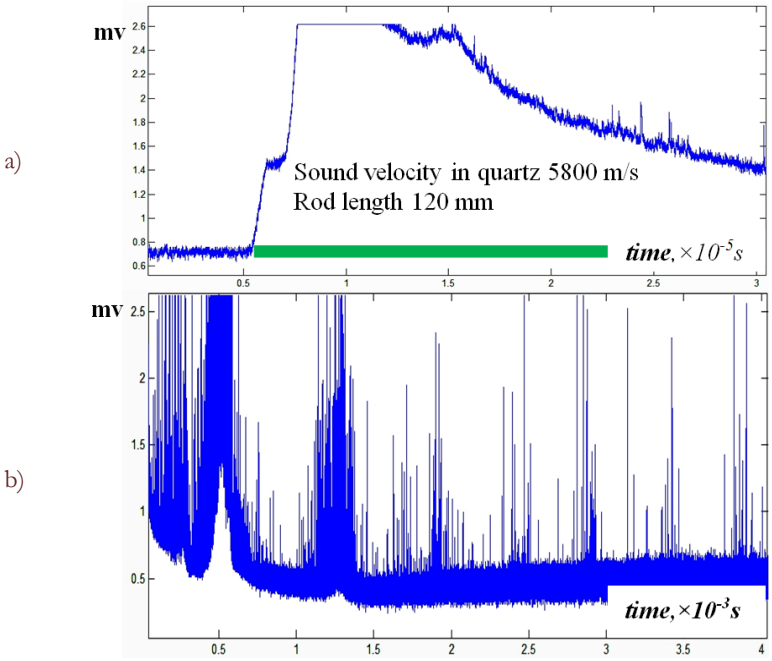

Figure 10: Signal from the oscilloscope corresponding to the intensity of the light reflected from the newly created surfaces.

The registered signal corresponds to the change in the scattered light intensity on the interface between the fractured and unfractured parts of the sample. The appearance of the new surfaces produces the impulses with a sharp front. Fig. 10 shows the signal from the oscilloscope. The bottom plot (Fig. 10b) is the total signal, and the upper plot (Fig. 10a) corresponds to the initial stage of the process. These two plots have different time scales. The green bar indicates the propagation time of the compression wave. The time during which the signal is registered is greater (6 *ms*) than the time of compression wave propagation (20 μs).
The first step of data processing is signal filtration. The definition of the size of time interval between the impulses of light reflected from the fracture surfaces is presented in Fig. 11. The second step involves measuring the distance between the green bars showing a sharp rise in impulse. We consider only the impulses which cross the red line. All the impulses below the red line are noise.

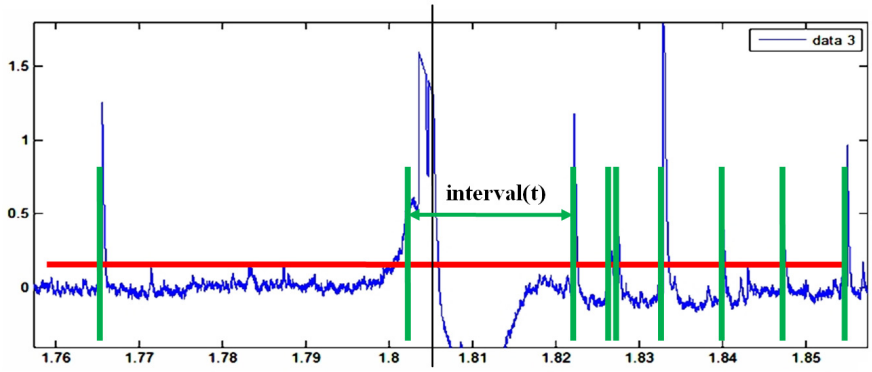

Figure 11: Determination of the size of time interval between the impulses of the light reflected from the facture surfaces.

The cumulative distribution function of the time interval in the double logarithmic plot (Fig. 12) is fitted by the straight line (total number of points 1073). At small sizes (77 points – 7.1761 % of the total number of points), the curve deviates from the straight line because the size of time interval is comparable with the oscilloscope sample rate (1 GHz). The falloff at the largest interval sizes (16 points – 1. 5% of the total number of points) is due to finite-size effects. In this case the time interval is comparable with the process time. The central part is the line covering 91.3% of the total number of points.

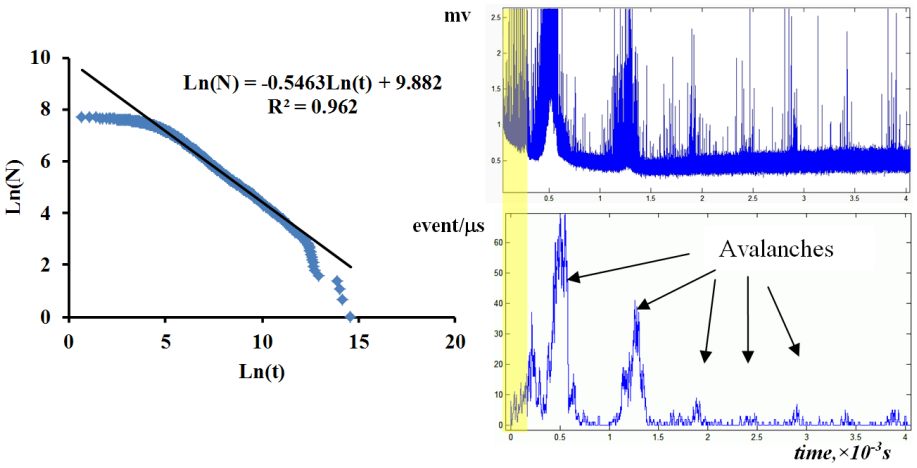

(a) (b)

Figure 12: a) Cumulative distribution function of time interval in the double logarithmic plot. b) The signal from the oscilloscope and the frequency of impulse appearance.

The process of light reflection looks like the process of avalanche spreading (Fig. 12b). The lower plot represents the event frequency. The events are distributed in blocks. We have analyzed the time interval distribution in avalanches and found that the distribution at the initial stage (marked in yellow in Fig. 12b) cannot be described by the power law.

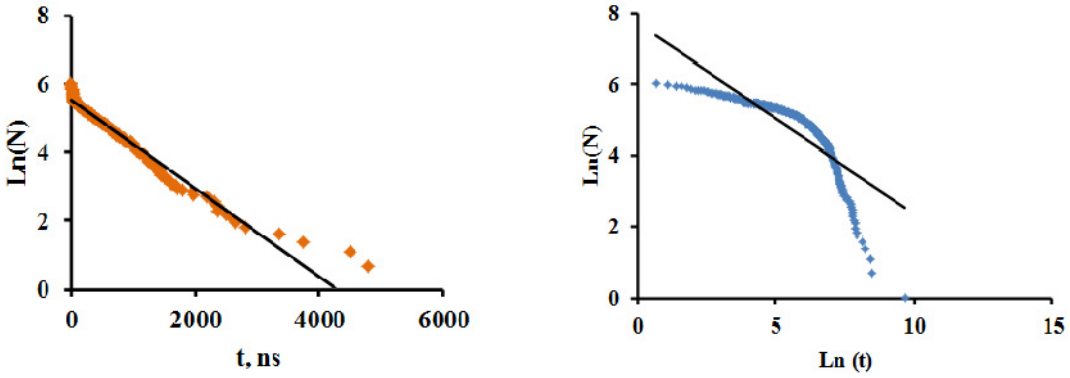

(a) (b)

Figure 13: a) Cumulative distribution function of time interval for initial stage in a double logarithmic plot. b) Cumulative distribution function of time interval for initial stage in a coordinate system *LN (N)* –time *t*.

The left plot in Fig. 13 illustrates the distribution at the initial stage in double logarithmic coordinates. In the right plot in Fig. 13, only the vertical coordinate is logarithmic. The time interval distribution is subjected to the exponential law. An exponential functional form requires a characteristic length scale which can be defined as

$$X_{ch} = tV \tag{3}$$

where X_{ch} is the characteristic size, t is the x-coordinate of point C (t= *457 ns*), and V = 5800 *m/s* is the sound velocity in quartz. We suppose that this length scale $X_{ch} = 2.6 \times 10^{-6}$ *m* correlates with the characteristic length scale of structure heterogeneity of quartz (Fig. 14). This problem will be the object of our future research. The initial stage statistics does not change the total statistics, because only 10% of the points belong to the initial stage.

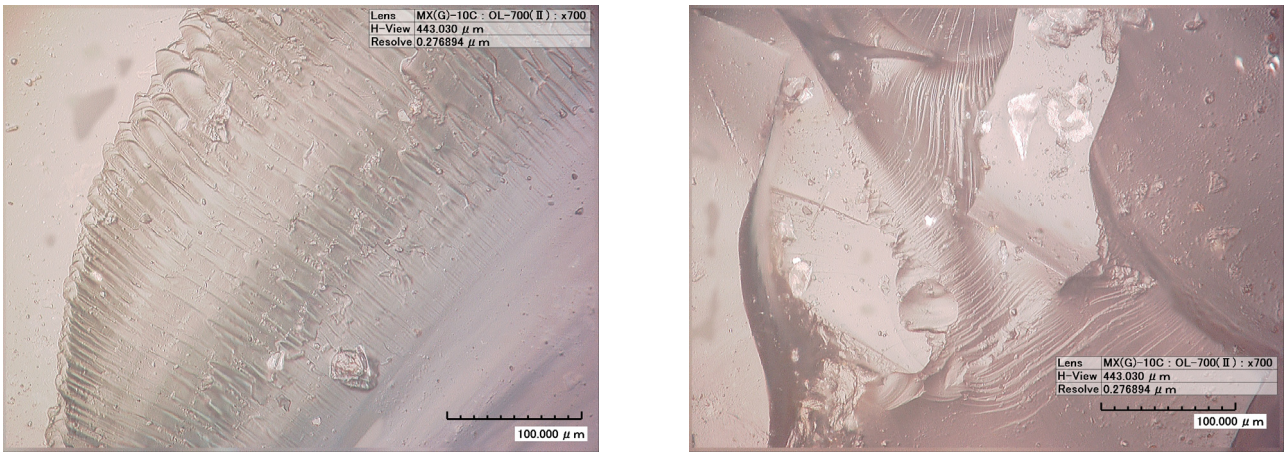

(a) (b)

Figure 14: Fracture surface of quartz. Optical microscopy.

CONCLUSION

Experimental investigations have been carried out to examine the fragmentation of brittle materials under quasi-static and dynamic loading conditions. Based on the obtained results, we can conclude:

- ✓ fragmentation patterns of glass plates are fractal;
- ✓ variation in the fracture mechanism of plates correlates with the changes in the fractal dimension;
- ✓ fragment size distribution for the observed type of fragmentation is fractal and satisfies the relation $N(>r) = Cr^{-D}$
- ✓ fragment size distributions and time interval distributions show evidence of obeying scaling laws, which suggests the possibility of self-organized criticality in fragmentation.

ACKNOWLEDGMENTS

We are very grateful to Vladimir Leont'ev for help in performing experiments. The author would like to acknowledge the Russian Foundation for Basic Research (grant RFBR 11-01-96010, grant RFBR 11-01-00712).

REFERENCES

[1] D. E. Grady, M. E. Kipp, J.Appl. Phys., 58(3) (1985) 1210.
[2] T. Kadono, Phys. Rev. Letters., 78(8) (1997) 1444.
[3] L. Oddershede, P. Dimon, J. Bohr, Phys. Rev. Letters., 71(19) (1993) 3107.
[4] V. V. Sil'vestrov, Combustion, Explosion, and Shock Waves, 40(2) (2004) 225.
[5] J. Weiss, Engineering Fracture Mechanics, 68 (2001) 1975.
[6] E. S. C. Ching, S. L. Lui, X. Ke-Qing, Physica A, 287 (2000) 83.
[7] D. E. Grady, International Journal of Fracture, 153(1-2) (2010) 85.
[8] D. L. Turcotte, Fractals and chaos in geology and geophysics. Cambridge University Press, UK (1997).
[9] P. Bak, C. Tang, K. Wiesenfeld, Phys. Rev. Lett., 59(4) (1987) 381.
[10] A. Sornette, P. Davy, D. Sornette, Phys. Rev. Letters, 65(18) (1990) 2266.
[11] L. Niemeyer, L. Pietronero, H. J. Wiesmann, Phys. Rev. Letters, 52(N12) (1984) 1033.
[12] T.A. Witten, L.M. Sander, Phys. Rev. Letters, 47 (19) (1981) 1400.

Optimization of fractional composition of the excipient in the elastomeric covering for asphalt highways

E. M. Nurullaev, A. S. Ermilov

Perm National Research Polytechnic University. 614990 Perm, Komsomol prospect, 29.

ABSTRACT. The computational method of optimum fractional composition of a dispersible filler of polymeric composite on the basis of three-dimensionally linked elastomer is developed according to non-linear programming. The coefficient of dynamic viscosity of polymeric suspension or the initial module of a viscoelasticity of the join solidification low-molecular rubbers with the final functional groups, filled by many fractional dioxide of silicon are considered as criteria of optimization. Influence of the limiting volume filling on energy of mechanical destruction was investigated. The elastomeric material is offered for use as a covering of asphalt highways in the form of a frost-proof waterproofing layer, which allowing multiply to increase operating properties.

KEYWORDS. Viscosity; Mechanical destruction; Elastomeric composites with a dispersed filler; Rheology; Rubber; Polymeric binder; Asphalt highways.

INTRODUCTION

Fractional composition of a dispersed filler is essential for formation of rheological behavior of suspensions on the basis of fluid and viscid polymeric binding and mechanical characteristics of three-dimensionally linked filled elastomers. At the same time the major parameter of composition is effective extent of volume filling – φ / φ_m, herein φ – volume proportion of solids of an filler, φ_m – the limiting extent of volume filling depending on a form of particles and their distribution by the size, and also from physical and chemical interaction on border "a filler - a binder". Value φ_m can be defined by the viscometric method [1] or calculated by a combinatorial and multiplicative method [2].

Coefficient of dynamic viscosity η and the initial module of a viscoelasticity $\mathrm{E} = \frac{\mathrm{d}\sigma}{\mathrm{d}\alpha}, (with\ \alpha = 1)$ are connected by a ratio (1):

$$\eta_r = \frac{\eta_f}{\eta_o} = E_r = \frac{E_f}{E_o} = \left(1 + 1.25\frac{\varphi / \varphi_m}{1 - \varphi / \varphi_m}\right)^2 \qquad (1)$$

herein the "f" and "o" indexes fall into to the filled and free conditions of the polymeric binding.

Energy (work) of destruction was estimated in the form of the envelope by curve of destruction [4] dependences of the conditional ultimate break tension σ_b (tension divided by the initial section of the sample) from break deformation ε_b, bound to degree of the relative elongation by ratio $\alpha_b = 1 + \varepsilon_b / 100\%$. The line envelopes of around points of a break of exemplars and constructed in logarithmic scale $(\log\sigma_b - \log\varepsilon_b)$, corresponds to energy of mechanical destruction in the form of the area of the chart of stretching in Cartesian coordinates:

$$A_b = \int_1^{\sigma_b} \sigma(\alpha) d\alpha \qquad (2)$$

herein structural and mechanical dependence of the conditional tension σ from elongations extent α on condition of lack by abruption of particles of an filler from elastomeric binder, (for example, covering for asphalt), is proved by us earlier [5]:

$$\sigma(\alpha) = \nu_{ch} \varphi_r^{1/3} R T_\infty \left\{ 1 + 29 \exp\left[-0.225 \cdot 10^{-3} \left(T - T_\infty \right)^2 \right] \right\} \alpha^{-1} a_{\dot{\alpha}}^{-1} \left(1 + 1.25 \frac{\varphi / \varphi_m}{1 - \varphi / \varphi_m} \right)^2 \left(\alpha - \alpha^{-2} \right) \qquad (3)$$

herein:

$\nu_{ch} = \rho / \bar{M}_c$: molar concentration of transversal chemical bonds in a polymeric basis a binder (ρ – polymer density, $\bar{M}_c$ – an average statistical molecular mass);

φ_r : volume ratio of polymer in binder, containing softener;

R : universal gas constant;

T_∞ : equilibrium temperature at which concentration of transversal "physical" (intermolecular) communications ν_{ph} is negligible;

T : test temperature of an exemplar;

T_g : temperature of a structural glass transition of the polymeric binding;

$a_{\dot{\alpha}}$: coefficient of high-speed mixing ($a_{\dot{\alpha}} = 1$, $\dot{\alpha} = 1.4 \cdot 10^{-3} s^{-1}$ -standart for applications);

ϕ : volume ratio of a dispersible filler;

φ_m : the limiting extent of volume filling of the elastomers, depending on a form and fractional composition of particles, and also from physical and chemical interaction on border "a filler - a binder".

Value φ_m can be defined by the viscometric method [1] or calculated by a combinatorial and multiplicative method [2].

Value α_b in the Eq. (2), as well as ε_b , searched with the help of Eq. (4):

$$\alpha_b^f = \alpha_b^o (1 - \sqrt[3]{\varphi / \varphi_m}) + \sqrt[3]{\varphi / \varphi_m}; \quad \varepsilon_b^f = \varepsilon_b^o (1 - \sqrt[3]{\varphi / \varphi_m}) \qquad (4)$$

herein the "f" and "o" indexes fall into to the filled and free conditions of an elastomer.

Breaking deformation of a elastomeric binder ε_b^o , defining by efficiency concentration of cross-links ($\nu_{eff} = \nu_{ch} + \nu_{ph}$), was set experimentally [5].

Research objective were development of a method of optimization of fractional composition of a dispersed filler for creation of a frost-proof waterproof elastomeric materials for covering for asphalt highways located in zones with sharply continental climate in form of rolled.

THEORETICAL STUDY

The problem of optimization of fractional composition of dispersible components of a polymeric material (for the given weight average particle sizes of fractions) taking into account realization of a condition of an optimality on other production characteristics can be formulated in the form of the formulation of a non-linear programming:

$$\varphi_m(\vec{\varphi}, \vec{q}, \vec{d}) \Rightarrow \max; \quad \eta_r \Rightarrow \min; \quad E_r \Rightarrow \min$$

$$\varphi_j^{opt} = \varphi_{j1} + \varphi_{j2} + \varphi_{j3} + ... + \varphi_{jm_j} = \sum_{v=1}^{m_j} \varphi_{jv}$$

$$0 \le \varphi_{jv}^{\min} \le \varphi_{jv} \le \varphi_{jv}^{\max} \le 1, \; v = 1, \; 2, \; 3, \; ..., \; m_j \quad \text{with} \; \forall_j \in I_n$$

$$\varphi_j^{opt} = \frac{x_j^{opt} / \gamma_j}{\sum_{j \in I_n} x_j^{opt} / \gamma_j}$$

herein

$\vec{\varphi}$, $\vec{q}$, $\vec{d}$: vectors of volume fractions, sponginess and particle sizes of fractions of dispersible components as a part of a polymeric material respectively;

φ_j^{opt} : optimum volume fractions of fraction an filler in structure;

φ_{jv} : volume fraction

v : fraction by j -type an filler in structure;

m_j : number of j-type fractions of a dispersed component;

$\varphi_{jv}^{\min}$, $\varphi_{jv}^{\max}$: respectively the lower and upper bounds for volume fractions of fractions of solid components in structure;

x_j^{opt} : optimum for the corresponding block of characteristics, for example, mechanical, mass concentration of firm disperse components in polymeric composition;

γ_j : density of disperse components;

I_n : a set of the indexes belonging to types of a filler, entering into a compounding of a polymeric material.

In view of complexity, the task includes restrictions such as equalities, will be transformed to a problem of nonlinear programming with restrictions such as inequalities. The quantity of independent optimized variables is equal $n = (m_j) - m$, herein

m : number of types of solid components by a polymeric material.

Thus normalizing ratio in case of the solution of a task is carried out automatically.

$$\sum_{j \in I_n} \sum_{v=1}^{m_j} \varphi_{jv} = \sum_{j \in I_n} \varphi_j^{opt} = 1$$

Further the vector of optimum volume fractions of fractions of filler in composition is defined:

$$\vec{\varphi}^{opt} = (\varphi_{jv}^{opt};\ \forall_j \in I_n); \quad v = 1,\ 2,\ 3,\ ...,\ m_j$$

herein

φ_{jv}^{opt} : an optimum volume fraction

v : fraction by j -type a filler.

Transition to optimum mass concentration of the relevant fractions of firm components

$$\vec{x}_j^{opt} = (\vec{x}_{jv}^{opt};\ \forall_j \in I_n;\ v = 1,\ 2,\ 3,\ ...,\ m_j)$$

is carried out on a formula: $x_{jv}^{opt} = (\phi_{jv}^{opt} \gamma_j) / (\phi_j^{opt} / \gamma_j) \cdot P$

herein $P = \sum_{j \in I_n} \sum_{v=1}^{m_j} x_{jv}^{opt} = \sum_{j \in I_n} x_j^{opt}$ is the sum of mass concentration (shares) of solid components by a polymeric compositing.

EXPERIMENTAL STUDY

Characteristics used a fraction of silica as a dispersed filler for slurry on based low-molecular rubbers (oligomers) with final epoxy groups polydienurethanepoxide (trademark PDI-3B) and carboxyl groups polybutadiencarbocsilate (trademark SKD-CTR) are shown in Tab. 1.

Surface by response of function in the projection in the chart Gibbs "composition-property" (Fig. 1), which we obtained by the developed computer program [3], demonstrates the calculated dependence of value $\eta_r = \eta_f / \eta_o$ the investigated polymer slurry from the volume ratio of the three fractions of silica, differing characteristics in accordance with Tab. 1. Constant volume fraction of filler is 0.75. In all cases, the calculation of the limit of bulk fill φ_m, through the coefficients of the porosity of various mixtures of fractions implemented with help by the coefficients of the porosity of individual fractions identified viscometric method [1]. At the same time physical and chemical factors influencing the limiting filling

of a polymeric binder takes into account "automatically", according to the physical nature of viscosimetric method. It can be seen that the minimum value of the relative coefficient dynamic viscosity η_r is provided an optimal ratio of volume fractions of fractions (rounded): 600μ 30μ 1μ = 0.5: 0.3: 0.2. It shows also the experimental values η_r.

Characteristics	1 (small)	2 (medium)	3 (large)
Porosity (volume fraction of pores)	0.450	0.384	0.379
Void ratio (the ratio of the volume fractions of pores and particles)	0.818	0.623	0.610
Weight average particle size, μ	1	30	600

Table 1: Characteristics fractions of silica.

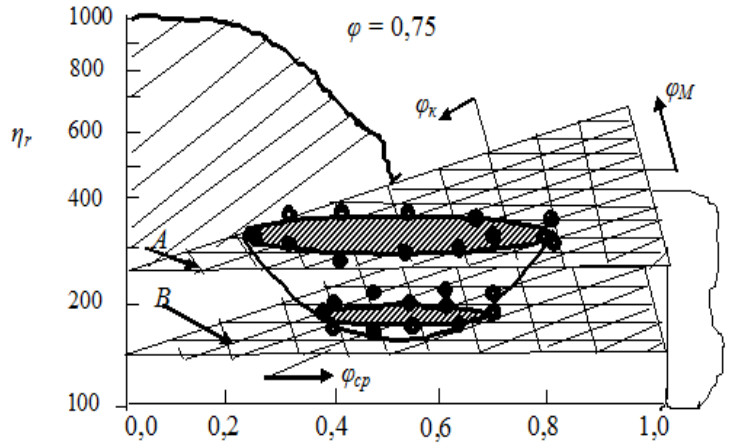

Figure 1: The calculated and experimental dependences of the relative dynamic viscosity polymer slurry based by polydinurethanepoxide (PDI-3B) and polybutadiencarboxilate (SKD-CTR) from volumetric ratios of 3 fractions of silica: A, B - levels calculated iso-viscosity, round icons - experimental data.

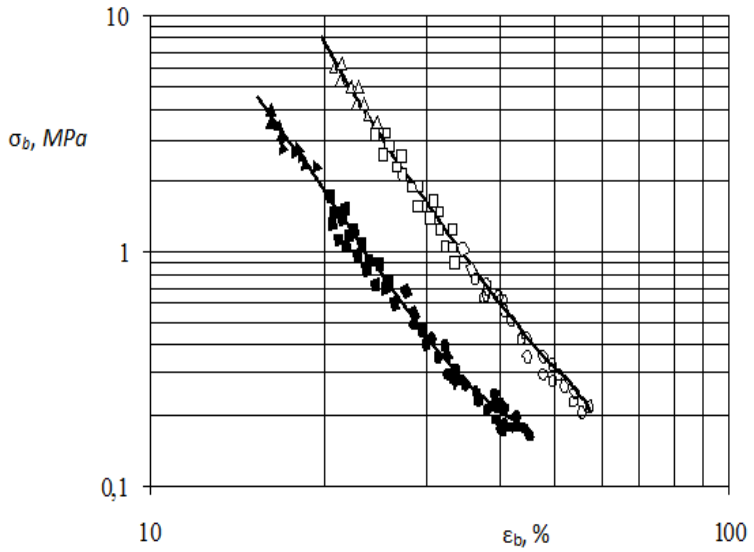

Figure 2: Envelopes by points of destruction [σ_b (MPa) = f [εb (%)] (in logarithmic scale) of the samples elastomer filled bifraction (black symbols) silica three fraction (white symbols) of silica:

○ a sample of T = 323 K ● the standard T = 323 K
□ a sample of T = 223 K ■ the standard T = 293 K
△ a sample of T = 293 K ▲ the standard T = 223 K

Experimental study of prescription's parameter φ / φ_m filled elastomer at strain-strength characteristics, expressed in the form of envelopes by destruction was carried out using silica the following fractional composition:

1 - initial test sample - (240: 5) μ = (20: 80)%

2 - prototype - (240: 5: 1) μ = (40: 40: 20%).

As the polymer binder used stoichiometric mixture (1: 2 moles) of low molecular weight rubber trademarks PDI-3B and SKD-CTR, three-dimensionally cross-linked three-functional aromatic epoxy resin trademark EET-1 (1 mol). Specific surface area of contact "filler-binder" in both cases remained constant.

Indication in Fig. 2 (with the normal motion from the lower to the upper right) shows that at a fixed value of the volume fraction of silica $\varphi = 0.712$ modified effective volumetric filling φ / φ_m from 0.712 / 0.752 = 0.946 to 0.712 / 0.816 = 0.72 leads to an increase in the energy by mechanical destruction by elastomeric composite 1.5 - 1.7 times. Reducing the maximum degree of volume filling from 0.946 to 0.872 promotes increase "return" of the polymeric binder in the growth of energy mechanical destruction elastomer composite in accordance with the mathematical relationship (2, 3, 4). [5].

Thus, the use by optimal multifractional filler for constant chemical composition of the composition allows for increase significantly in service life of the studied composite material which offered as frost-resistant waterproof covering (oil-fired sub-layer) for asphalt highways located in areas with sharply continental climate.

Use as frost-resistant waterproofing covering which filled three-dimensional cross-linked elastomer, provides an elastically deformability surface of the road-load transport in the temperature range of 223 K ... 323 K (-50 ... +50 ° C); this prevents the massive destruction of asphalt at alternating temperatures and operating loads at the expense of phase transitions' water-ice-water ", which accompanied by a volume expansion of ice when water freezes in the initial cracks of asphalt.

The following is an example of the engineering realization of recommended material.

- ✓ The composition contains: A polymer binder (in the ratio 1: 2) polydienurethanepoxide with final epoxy groups (PDI-3B) and polybutadiencarbocsilate with a terminal carboxyl groups (SKD-KTR) (13.5 wt.%),
- ✓ Natural macro crystalline quartz (57.4 wt.%); Fumed silica grade "Aerosil-380" (24.6 wt.%),
- ✓ Processing aids: thixotropic amplifier of elastomer and pigment - technical carbon (3.0 wt.%), three-dimensional cross-linking agent - epoxy gum brand EET-1 (1.45 wt.%), three-dimensional crosslinking catalyst - acetolacetonate Fe (0,05 wt.%).
- ✓ Blending components conducted at 55 - 60 ° C in a continuous mixer such as "SND-75", followed by formation of canvas width 3.0 meters and a thickness of 0.012 m (12 mm). Three-dimensional cross-linking the polymer base material was conducted out in a continuous drum-vulcanizer at a temperature 170 - 180 ° C with a residence time in the apparatus 7-5 minutes respectively. received and rolled from rolls (25 meters long each) on the asphalt, smearing by liquid bitumen (oil), waterproof canvas with a relative speed of uniaxial tension $1.4 \cdot 10^{-3}$ s^{-1} had the following mechanical characteristics specified in Tab. 2. In the same part of the recommended composition based on a three-dimensional cross-linked elastomer filled three-fraction silica.

Such a roll material on intermediate "glue" layer of liquid bitumen (oil), is to protect the asphalt canvas based on bituminous binder, becoming brittle in the cold, from the ravages of a pair of "water - ice" These characteristics indicate on increased frost-resistant developed coating of asphalt highways and you can use it in a wide temperature range for 20 ... 30 years.

Composition	Volume fractions	Mechanical properties					
		323 *K*		293 *K*		223 *K*	
		σ_b, *MPa*	ε_b, %	σ_b, *MPa*	ε_b, %	σ_b, *MPa*	ε_b, %
Polimeric binder: Rubber SKD-CTR; Rubber PDI-3B; Epoxy EET-1	0.288	0.25	55	1.20	32	6.00	22
Filler: Silica (240:5:1) μ = (40:40:20)%	0.712						

Table 2: Mechanical characteristics of composition.

CONCLUSIONS

Based on non-linear programming was developed mathematical optimization method of fractional composition of the disperse filler, which significantly affects the coefficient of dynamic viscosity of the suspension and the energy of mechanical destruction three dimensional cross-linked elastomeric composite. Also was proposed formulation of the polymer compositions based on low molecular rubbers with final functional groups, filled with silica optimal fractional composition, allowing increase the service life of asphalt highways. In relation of frost-resistance and waterproofing of the created coating based of the filled elastomer, engineering example shows the practical effectiveness of the proposed method to increase the service life of asphalt highways.

REFERENCES

[1] A. S. Ermilov, K. Zyryanov, Plant Laboratory. Diagnostic materials, 67(9) (2001) 62.
[2] A. S. Ermilov, A. M. Fedoseev, J. of Applied Chemistry, 77(7) (2004) 1218.
[3] Certificate number 2012613349 RF. software identify and optimize the packing density of solid dispersed polymer composite fillers materials (rheology). / Ermilov A. S, Nurullaev E. M., Duregin K. A. - Priority from 09.04.2012.
[4] T. L. Smith, J. Appl. Phys., 35 (1964) 27.
[5] A. S. Ermilov, E. M. Nurullaev, Mechanic composite materials, 48(3) (2012) 359.

Multiscale approach to description of deformation and fracture of brittle media with hierarchical porous structure on the basis of movable cellular automaton method

Ig. S. Konovalenko
Institute of Strength Physics and Materials Science SB RAS, 2/4 Akademicheskii pr., Tomsk, 634021, Russia
igkon@ispms.tsc.ru

A. Yu. Smolin, S. G. Psakhie
Institute of Strength Physics and Materials Science SB RAS, 2/4 Akademicheskii pr., Tomsk, 634021, Russia
Tomsk State University, 36 Lenin pr., Tomsk, 634050, Russia

ABSTRACT. An approach to multiscale description of deformation and fracture of brittle porous materials on the basis of movable cellular automaton method was proposed. The material characterized by pore size distribution function having two maxima was considered. The core of the proposed approach consists in finding the automaton effective response function by means of direct numerical simulation of representative volume of the porous material. A hierarchical two-scale model of mechanical behavior of ceramics under compression and shear loading was developed. Zirconia based ceramics with pore size greater than the average grain size was considered. At the first scale of the model only small pores (corresponding to the first maximum of the pore size distribution function) were taking into account explicitly (by removing automata from the initial structure). The representative volume and effective elastic properties of the porous material at this scale were evaluated. At the second scale of the model, big pores were taking into account explicitly, the parameters of the matrix corresponded to the ones determined at the first scale. Simulation results showed that the proposed multiscale model allows qualitatively and quantitatively correct describing of deformation and fracture of brittle material with hierarchical porous structure.

KEYWORDS. Deformation and fracture; Brittle materials; Porous ceramics; 2D modeling; Particle-based approach, Movable cellular automaton method.

INTRODUCTION

It is well known that real porous materials are characterized by hierarchical pore structure and complex mechanical behavior, including fracture [1-3]. To study and describe these materials the information about the relationship of their structure and mechanical properties at various scales is needed. One of the ways of getting this information is numerical simulation. In the framework of one-scale approach direct taking into account all peculiarities of structure and mechanical behavior of a material at each scale seems to be impossible. Therefore the goal of this paper is development of the multiscale approach, represented in [4], and construction of the corresponding hierarchical model for describing deformation and fracture of nanostructured porous ceramics under compression and shear on the basis of movable cellular automaton method (MCA). Detailed description of the MCA method can be found in paper [5] published in this issue of the journal. Note, that this method have been chosen because it has successfully proved itself in studying

mechanical behavior of brittle porous materials from initiation of the first damages till cracks propagation and complete failure [6-9]. The calculations were carried out for a model material having mechanical properties of nanocrystalline $ZrO_2(Y_2O_3)$ (yttria-stabilized zirconia) with the average pore size greater than the average grain size and two maxima in its pore size distribution function [2, 3].

The hierarchical model of the material with properties of the ceramics under consideration was constructed in several stages. At the first stage, the response of the ceramic material at the microscale (20÷250 μm) was simulated with explicit taking into account the porous structure of the material under various types of mechanical loading and the representative volume of this scale was determined. The result of the first stage was determination of the response function parameters of macroscale movable automata, corresponding to representative volume of the microscale. At the second stage, similar calculations were carried out at the macroscale with explicit taking into account of the porous structure of this scale. Data on the porous structure of lower scale were allowed for in the effective automata response functions defined at the first stage. At the final third stage, qualitative and quantitative verification of the developed model at the macroscale was made including comparison of simulation and experimental data.

DETERMINING THE REPRESENTATIVE VOLUME OF THE MICROSCALE AND THE MACROSCALE EFFECTIVE RESPONSE FUNCTION

At the microscale of the proposed model, the representative volume is determined by analyzing the convergence of elastic and strength characteristics of porous model specimens with an increase in their dimension. Modeling of six groups of porous ceramics specimens under uniaxial compression and simple shear was performed. All the specimens in each group had the same dimension, but different pore distribution in space. Each group was consisted of six plane square specimens. Specimens under consideration had dimension (square side) of 20, 60, 100, 150, 200 and 250 μm according to the groups. It was supposed that all pores in the ceramics under investigation, as well as the model material, were equiaxed. The pore size of the model material, according to the maximum of the ceramics pore size distribution function, was equal to 3 μm [2, 3]. Diameter of the movable cellular automata, according to the average grain size, was equal to 1 μm [2, 3]. The pore structure of the specimens was specified by randomly removing individual automata and their six nearest neighbors. The total porosity for all the specimens was equal to 7% [2, 3]. Typical initial structure of one of the model specimens is shown in Fig. 1.

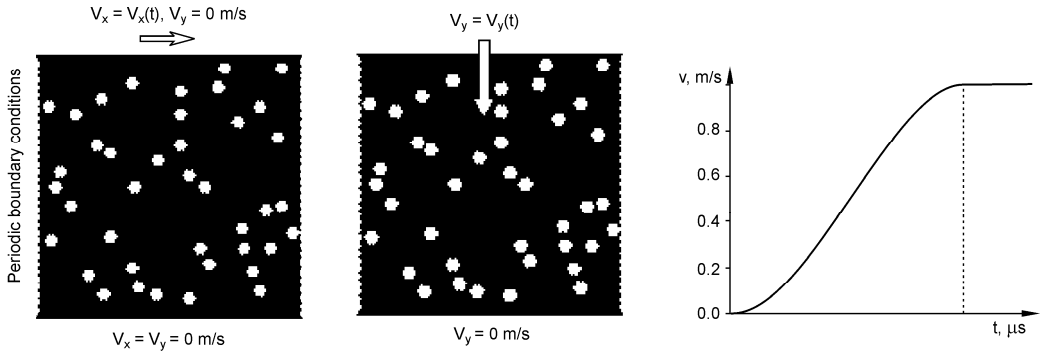

Figure 1: Initial structure of a model specimen with a size of h = 60 μm and scheme of loading for shear (a) and uniaxial compression (b); the plot of velocity vs time for the upper automaton layer of the specimen (c).

The shear loading was simulated by setting up one and the same horizontal velocity to all automata in the upper layer with automata of the lower layer being rigidly fixed (Fig. 1,a,c). At the initial stage, the velocity of automata of the upper layer was increased by the sinusoidal law from 0 to 1 m/s and then was assumed to be constant. This scheme ensured a quasi-steady regime of loading and allowed dynamic effects to be eliminated until the first damage appeared. Duration of the loading velocity increase depended on the size of the specimen and was determined by preliminary calculations. All the samples had periodic boundary conditions in the direction of shear loading. The uniaxial compression loading was simulated by setting up one and the same velocity in vertical direction (up to 1 m/s) to all automata in the upper layer (Fig. 1,b,c). The vertical velocity of automata in the lower layer were set to zero. Displacements in horizontal direction were allowed for automata in the both lower and upper layers. The lateral surfaces of the specimen were free. The problem was solved under plane strain conditions. The response function of automata corresponded to the loading

diagram for nanocrystalline $ZrO_2(Y_2O_3)$ with total porosity of 2% and an average pore size to be equal about the grain size [2, 3]. Shear modulus G and Poisson ratio ν of the movable cellular automaton were equal to 59.2 GPa and 0.3 correspondingly. Inter-automaton bond rupture criterion used in calculations was formulated as a threshold value for intensity of shear stresses [10].

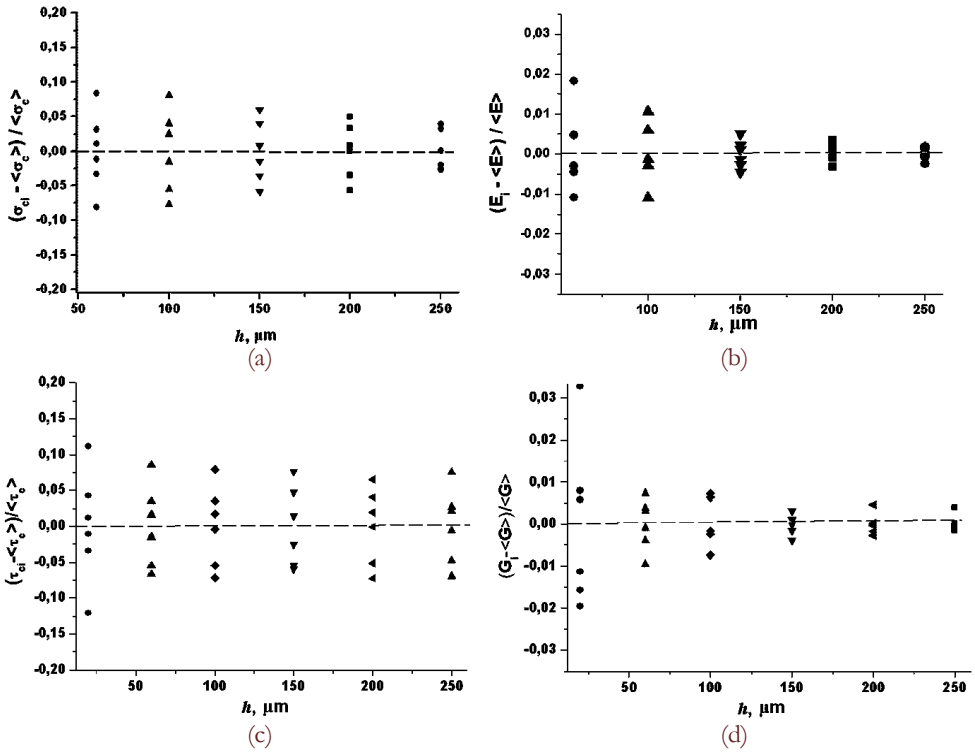

Figure 2: Relative deviation of compression modulus E_{eff}, shear modulus G_{eff}, compression strength σ_c and shear strength τ_c of the model specimens from the corresponding mean values $<E_{eff}>$, $<G_{eff}>$, $<\sigma_c>$, $<\tau_c>$ under uniaxial compression (a, b) and shear (c, d).

Convergence analysis of mechanical properties for the porous model specimens with increase of their size was performed in terms of estimated deviation of effective elastic and strength properties of the specimens (modulus of compression E_{eff}, shear modulus G_{eff}, compression strength σ_c and shear strength τ_c obtained from simulated loading diagram) from the corresponding mean values in the groups $<E_{eff}>$, $<G_{eff}>$, $<\sigma_c>$ and $<\tau_c>$. The specimen size for which the deviation did not exceed 3% for E_{eff}, G_{eff} and 15% for σ_c, τ_c was accepted as the size of representative volume. The results of simulation (Fig. 2) showed nonlinear convergence of strength and elastic properties of the model specimens. For the model specimens with the side of 150 μm relative deviations of E_{eff} , G_{eff}, σ_c and τ_c from the corresponding group average values were 0.51, 0.38, 6.0 and 7.6% correspondingly. These values did not exceed the prescribed limits. Thus, it proved that the porous specimens with dimension of 150 μm are representative volumes of the model material under consideration. The values of $<E_{eff}>$ and $<\sigma_c>$ were taken as the parameters of response function of automata at macroscopic scale. Slight deviations of these values (−9.5 % and 36.0 %) from ones evaluated experimentally are related with two-dimensional formulation of the problem and incomplete correspondence of the model pore morphology with the one of real ceramics. Therefore the corresponding characteristics of response function were corrected by means of the correction ratio. The conversion from the elastic modulus determined from the loading diagram under plane strain conditions E_{PSS} to the Young's modulus was based on the ratio $E = E_{PSS}(1-\nu^2)$ [11].

SIMULATIONS AT MACROSCALE

At macroscale the calculations were carried out for nine square porous specimens with the dimension of 22.5 mm. According to the representative volume determined at the previous stage the diameter of movable cellular automata at this scale was equal to 150 μm. The information about structure and strength properties of the

material was transferred from micro- to macroscale by means of the response function with the parameter values corresponding to the loading diagrams of the representative volume of the material at microscale. The response function of automata was chosen to be a linear one and characterized by two parameters: the maximal value of specific resistance force (corresponded to strength limit) and the elastic parameter (corresponded to Young's modulus). The values of these parameters determined at the first stage were found to be equal to 846 MPa and 112 GPa correspondingly. Explicit setting up of pore structure of the material at macroscale scale, loading conditions and assumption about stress state were similar with that of the first stage. According to the pore size distribution function the explicit porosity of the macroscale specimens was equal to 28% and the pore size was equal to 450 μm [2, 3].

VERIFICATION OF THE MODEL

Let us assume the model to be successfully verified (i.e. the model represents the main features of the ceramics under investigation) if the simulation results satisfy the following criteria: 1) the loading diagram of the modeled specimen is linear in elastic region and contains horizontal section corresponding to quasi-ductile fracture for porosity greater than 20 %; 2) qualitative correspondence of the fracture patterns of the modeled specimens to real ceramics; 3) strength properties of the modeled specimens belong to a certain value interval found from experimental data.

The loading diagrams which are typical for all the model specimens in case of different types of mechanical loading are presented in Fig. 3. On these diagrams one can see several parts. The first linear part, corresponding to elastic deformation of the specimen, is typical for brittle materials with any value of porosity. The next part is still ascending but insignificantly, it also contains multiple stress "oscillations" (only under uniaxial compression, Fig. 3, a). This part corresponds to repetitive processes of damage generation, local cracking and subsequent elastic deformation of the material all over the entire specimen. The last part of the diagram is descending. It corresponds to macrocrack propagation as well as generation of separate multiple damages. In shear loading (Fig. 3, b) one can see another ascending sections of the curve with breakdowns and subsequent drop-down on the plotted diagram after the above mentioned parts. Under constrained deformation conditions, it is to these portions of the diagram that the development of a system of macrocracks in the specimen corresponds, and the first descending portion corresponds to nonrecurring generation of damages throughout the entire specimen and their development without the formation of a system of macrocracks.

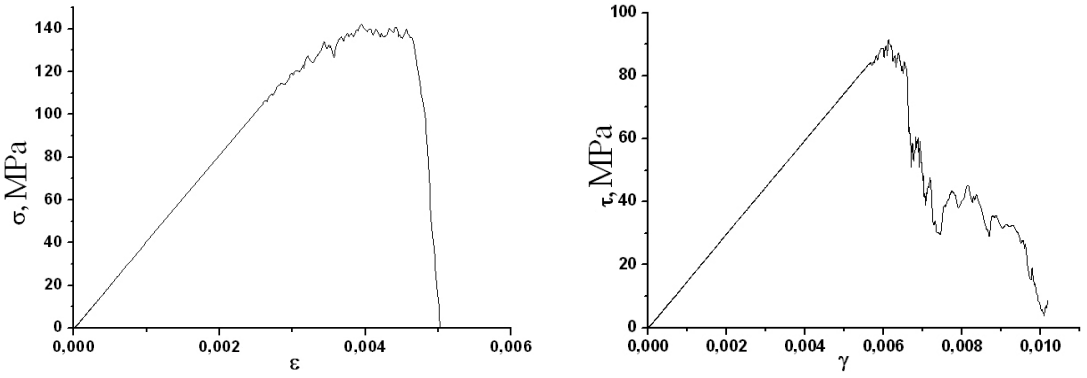

(a) (b)

Figure 3: Loading diagrams of the model specimen with dimension of 22.5 mm under uniaxial compression (a) and shear loading (b).

It should be noted, that the horizontal plateau on the compression diagram of the brittle specimens (Fig. 3, a) reveals their quasi-ductile fracture, which occurs only when porosity of the specimen is greater than 20% [9]. The extent to which these properties show up is proportional to the length of the given portion (plateau) and is different for different model specimens. A decrease in the length of this diagram portion points to the proximity of fracture to brittle fracture. It would appear reasonable that both the transition to quasi-ductile fracture and the extent to which it develops are determined by certain critical local porosity of the specimens. The critical local porosity is associated, in particular, with the total specimen porosity and with the pore shape and size. It is worthy of note that quasi-ductile fracture in this case is completely determined by the geometric factor, because the model takes into account neither phase transitions, nor rearrangement of the material lattice.

Typical loading diagrams of brittle porous solids under shear and uniaxial compression are presented in Fig. 4 [2, 9]. Comparison of the diagrams in Fig. 3 with corresponding diagrams of brittle porous solids in shear and uniaxial compression [2, 9] shows their good qualitative agreement. Thus, the first macroscale criterion of model verification, which is in the loading diagram correlation, is fulfilled.

Typical fracture pattern of the model specimens, represented as inter-automaton bond net at the time of first macrocrack propagation, are shown in Fig. 5. Under uniaxial compression the specimen failure occurred due to generating therein the asymmetrical system of macrocracks with complex propagation path. In addition, generation of multiple separated fracture regions took place near the macrocracks.

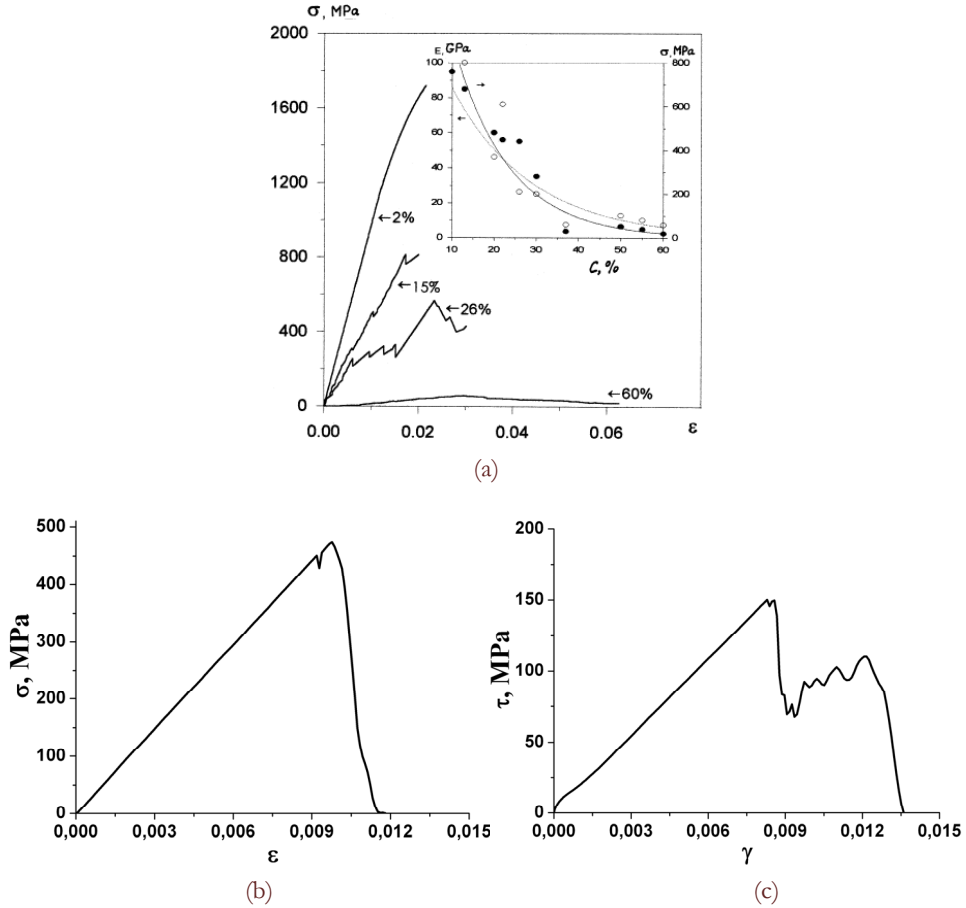

(a) (b) (c)

Figure 4: Experimental loading diagrams of ZrO_2 ceramic specimen with different value of porosity under uniaxial compression (a) [2] and corresponding diagrams obtained from numerical simulation (b and c) [9].

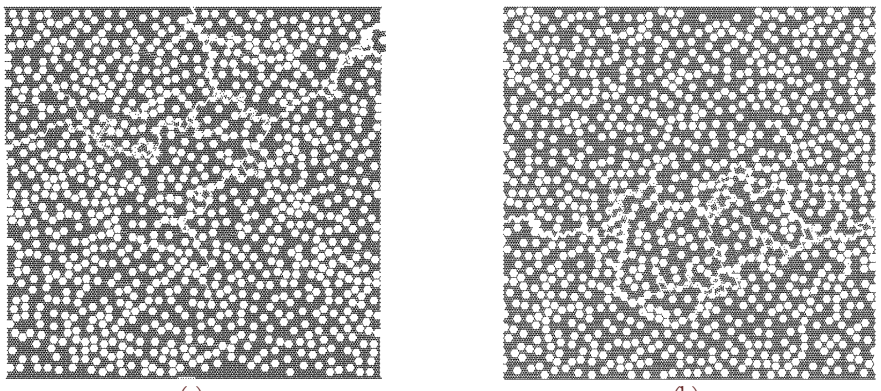

(a) (b)

Figure 5: Fracture patterns of the model specimen with the porosity of 28 % at the moment of the first macrocrack propagation under uniaxial compression (a) and shear loading (b).

In the case of quasi-ductile fracture (Fig. 3, a) damage generation and crack growth occurred locally, in several regions of the sample, characterized by the highest value of local porosity (and the least thickness of web between isolated pores). Until a certain moment, some cracks were not merged into main crack, the stage of its growth were somehow elongated. It led to extensive local cracking of the material without losing the integrity of the sample and, consequently, to a substantial dissipation of elastic energy and decreasing of the effective elastic properties of the material (of the whole specimen). Thus, the second criterion of the constructed model verification is fulfilled.
To verify the third criterion of the model verification the average value of the effective elastic modulus ($<E_{eff}>$) and maximum specific resistance force to loading under uniaxial compression were calculated. Then they were compared with the corresponding values found from real experiments. It was shown that the deviation of $<\sigma_{s\_eff}>$ and $<E_{eff}>$ for the model samples from the experimental data did not exceed 30 % and 12 %, respectively. It is a rather good accuracy for simulating highly porous media in plane approximation. This indicates to a good quantitative agreement of the calculations and the experiment and means that the third criterion of the model verification is fulfilled.
Thus, a two-scale model of porous ceramics with bimodal pore size distribution function was constructed herein based on a multiscale approach to numerical simulation and validated against available experimental data.

CONCLUSIONS

A multiscale approach to numerical simulation of porous materials is developed on the basis of movable cellular automaton method. The hierarchical two-scale model constructed using the proposed approach can adequately describe deformation and fracture of the porous zirconia ceramics under mechanical loading. Since the proposed approach is sufficiently general, then, if it is necessary, a heterogeneous material containing more than two structural scales can be also simulated on the basis of this approach.

ACKNOWLEDGEMENTS

This study was supported by the Russian Foundation for Basic Research, project No. 12-08-00379-a.

REFERENCES

[1] Global Roadmap for Ceramics: Proceedings of 2nd International congress on ceramics (ICC2). Alida Belosi and Gian Nicola Babini (Eds.). Institute of Science and Technology for Ceramics, National Research Council, Verona (Italy), (2008).
[2] S.P. Buyakova, Han Wei, Li Dunmy et al., Tech. Phys. Lett., 25(9) (1999) 695.
[3] S.N. Kulkov, S.P. Buyakova, V.I. Maslovskii, Vestnik TGU, 13 (2003) 34 [in Russian]
[4] Ig.S. Konovalenko, A.Yu. Smolin, S.G. Psakhie, Phys. Mesomech., 13(1–2) (2010) 47.
[5] S. Psakhie, E. Shilko, A. Smolin, S. Astafurov, V. Ovcharenko, Frattura ed Integrità Strutturale, 24 (2013) 26.
[6] Ig.S. Konovalenko, A.Yu. Smolin, In: Proc. of the XXXVI Summer School "Advanced problems in mechanics (APM' 2008)" D. A. Indeitsev, A. M. Krivtsov (Eds.), Institute for problems in mechanical engineering, St. Petersburg, (2008) 352.
[7] A.Yu. Smolin, Ig.S. Konovalenko, S.N. Kul'kov, S.G. Psakhie, Tech. Phys. Lett., 32(9) (2006) 738.
[8] A.Yu. Smolin, Ig.S. Konovalenko, S.N. Kulkov, S.G. Psakhie, Izv. vuzov Fizika, 49(3) (2006) 70 [in Russian].
[9] Ig.S. Konovalenko, Theoretical Study of Deformation and Fracture of Porous Materials for Medicine and Biomechanical Structures, Cand. Degree Thesis (Phys&Math), IFPM SO RAN, Tomsk, (2007) [in Russian].
[10] L.M. Kachanov, The Foundations of Fracture Mechanics, Nauka, Moscow, (1974) [in Russian]
[11] L.I. Sedov, A Course in Continuum Mechanics, Wolters-Noordhoff, Groningen, (1971).

A study of the stored energy in titanium under deformation and failure using infrared data

A.Yu. Fedorova, M.V. Bannikov, O.A. Plekhov

Institute of Continuous Media Mechanics of the Ural Branch of the Russian Academy of Sciences, 614013, Ac. Koroleva Street, 1, Perm, Russia

poa@icmm.ru

ABSTRACT. The work is devoted to the experimental study of heat dissipation caused by plastic deformation and failure processes taking place in a titanium alloy Ti-4.2Al-1.6Mn. To investigate the spatial and time evolution of temperature, a set of experiments has been carried out on plane titanium smooth specimens and specimens with pre-grown centered fatigue cracks. The original mathematical algorithm for experimental data processing has been applied to obtain the rate of heat dissipation generated by plastic deformation and stored energy. It is shown that the stored energy is accumulated in titanium specimens undergoing fatigue tests, and at the time of damage to fracture transition it is equal to zero.

KEYWORDS. Heat dissipation; Infrared thermography; Stored energy.

INTRODUCTION

It is well known that real metals have a complex structure, which is a hierarchy of different scale levels [1, 2]. Under deformation, the structural evolution is observed at all scale levels and leads to irreversible deformation and failure that is accompanied by energy accumulation and dissipation. Investigation of thermodynamics of deformation and failure is a key issue in solid mechanics. These studies allow one to develop a universal material failure criterion for estimating different stress-strain states (including multi-axial ones) and loading histories.

The experimental and theoretical study of the energy balance during deformation is based on an extensive bibliography. The importance of this problem was originally shown by J. H. Lambert in 1779 in his work concerning the energy similarity of mechanical and thermal failure processes of solids. The essence of this similarity is that the mechanical failure of metals can occur when the relative deformation in at least one direction reaches a value equal to the linear thermal expansion at the melting point. A substantial contribution to the development of these ideas was made by V.S. Ivanova, who proposed the structure-energy theory of metal fracture [3]. A detailed analysis of thermodynamic effects produced by cyclic deformation and failure in metals was carried out by V.T. Troshchenko and V.V. Fedorov. A review of strength energy criteria was given in [4, 5].

To analyze the thermodynamic characteristics of deformation processes in solids, it is necessary to take into account the fact that the plastic deformation work is converted into two parts: heat energy caused by the movement and annihilation of defects at various structural levels, and hidden (stored) energy of plastic deformation accumulated in the elastic fields of defects. The energy is dissipated in the surrounding environment by conduction, convection and radiation and also stored in the material as thermal energy that increases due to the self-heating effect.

The main difficulty encountered in the analysis of deformation and failure processes is a choice of thermodynamic parameters required to determine the exhaustion degree of material deformability. In work [5] published in 1979, it was experimentally shown that an endurance limit can be determined by using almost any thermodynamic characteristics of the process: inelastic deformation per one load cycle, irreversibly consumed energy per one load cycle, self-heating

temperature, energy dissipation rate, and energy storage rate. For a more rapid determination of the endurance limits of metals, the author proposed two types of tests: a slowly increasing load (stress) amplitude test and a block amplitude test (used more often today). In the beginning of 1970th, V. Fedorov developed an original experimental setup that permitted him to control the heat dissipation and to measure the temperature of the specimen under cyclic loading.
The analysis of the experimental studies carried out in USSR in 1970-1980 has led us to the conclusion that the obtained parameters are indirect and thus cannot be used as a basis for the development of the universal material failure criteria.
For example, it is experimentally shown [5] that the thermal energy dissipated during the cyclic deformation of specimens made from 40X, 2X10, 25, 45 steels (Russian marking) may have very different values [5]. Conversely, the value of the stored energy during deformation is independent of loading conditions and correlates, at the time of failure, with the value of enthalpy of the material in a liquid state at melting temperature.
With the advent of infrared cameras it became possible to significantly simplify the schemes of experiments and to accelerate the determination of fatigue limits of materials [6-8]. Infrared thermography allows one to measure, in real time, the temperature of materials under deformation and to calculate the thermal energy of specimens and the rate of heat dissipation.
Investigation of the energy accumulation process in metals at different loading conditions was carried out over the entire 20th century. The review of experimental works devoted to the methods of studying the stored energy in the material under deformation and the peculiarities of this process for different materials and load conditions is available in [9]. Currently, it has been convincingly shown that the ratio of the energy storage rate to the plastic work rate can reach a value of 0.3-0.4 at the initial stages of plastic deformation process [10, 11].
The aforementioned experimental results indicate the importance of further development of methods for investigation of the thermodynamic parameters of the deformation process. At present, infrared thermography is one of the most promising techniques for thermodynamic measurements; it requires no changes in the standard schemes of mechanical testing.
One of the main problems facing scientists today is the development and realization of mathematical methods for experimental data processing, including noise filtering for temperature measurements based on infrared radiation data, elimination of external effects during the experiments (reflection of infrared waves from the metal specimen surface, relative motion of a specimen, etc.), and calculation of heat losses in the course of the experiment. The major goal of such experimental data processing is to provide a solution to the inverse problem and to evaluate the heat source evolution caused by the structure evolution in the material. A comparison of these data with the results of mechanical tests will enable one to determine the value of stored energy and to propose a local material failure criterion. This criterion can be applied for calculation of the stored energy value and determination of the moment at which this parameter is equal to zero, that is, the time of local material failure. In the present paper, the proposed criterion is used in the analysis of stress field and energy dissipation at the fatigue crack tip.

MATERIALS AND CONDITIONS OF EXPERIMENT

The experimental study of temperature evolution at the fatigue crack tip was carried out on the two types of the plane specimens of titanium alloy. The chemical composition of the material is presented in Tab. 1. Experiments were made on smooth specimens and specimens weakened by holes to initiate fatigue cracks in the center of the specimen. The specimens were manufactured from a titanium sheet 3 mm thick. The mechanical properties of the materials were determined based on the original experiment. Mechanical tests were carried out using a 100 kN servo-hydraulic machine Bi-00-100. The mechanical properties and fatigue loading conditions are presented in Tab. 2. The geometry of specimens is shown in Fig. 1.

Al	Zr	Si	Fe	O	H	N	C	Mn
3.68	0.3	0.12	0.3	0.15	0.012	0.05	0.1	1.16

Table 1: The chemical composition of titanium alloy(%).

Modulus of elasticity	Yield stress	Ultimate stress	Fatigue limit	Fracture toughness	P_{min}	P_{max}	Stress ratio
64 GPa	800 MPa	900 MPa	460 MPa	75.6 MPa$\sqrt{m}$	-18.7 MPa	367 MPa	-0.051

Table 2: The mechanical properties of Ti-4.2Al-1.6Mn and fatigue loading conditions.

The test conditions comply with the conditions of the experiment described in detail in [12]. Investigation of the heat source evolution was carried out on the smooth specimens during a quasi-static tensile test. Crack propagation was studied at loading frequency of 5 Hz and 10 Hz. The temperature evolution was recorded by an infrared camera FLIR SC 5000. The spectral range of the camera is 3-5 mm. The maximum frame size is 320×256 pixels; the spatial resolution is 10^{-4} meters. The temperature sensitivity is from 25 mK to 300 K.

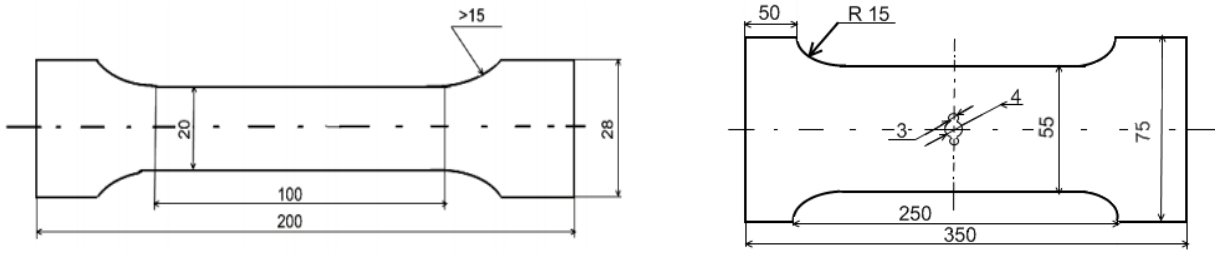

(a) (b)

Figure 1: Geometry of specimen (a – smooth specimen, b – specimen with a hole). All sizes are in millimeters.

EXPERIMENTAL DATA PROCESSING AND STORED ENERGY DETERMINATION

Post experimental data processing

At the beginning of the data processing procedure, the first frame was subtracted from the film to eliminate the influence of infrared camera lens radiation on the temperature field. To increase data accuracy and to eliminate the influence of random temperature fluctuations, the spatially fixed temperature signal of the smooth specimen was processed using the two-dimensional discrete Fourier transform with a standard Gaussian kernel [13]. The result of such data processing used to calculate the heat source field is illustrated in Fig. 2.

The relative motion of the specimen with cracks and the infrared camera lens observed in cyclic tests causes the problem of motion compensation, which should be overcome to obtain the correct temperature data at the given point on the specimen surface. To compensate this relative motion, the algorithm described in detail in [13] was used. The main idea of the algorithm consists in finding a marker zone on the examined surface and searching for this area on the surface in each time step. Further, the displacement of every point on the surface is calculated for each time step. The data processing yielded the temperature increment field (Fig. 3), which was used to determine the heat source field.

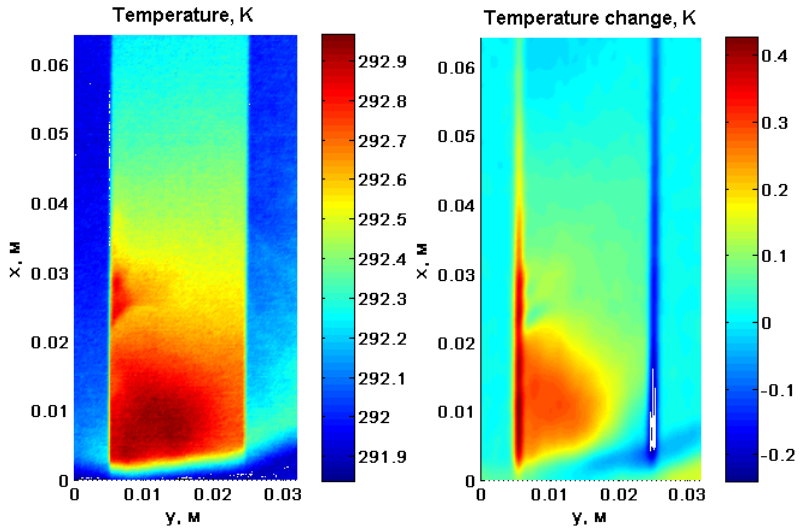

(a) (b)

Figure 2: Infrared image of the smooth specimen before data processing (a) and the obtained temperature change field (b).

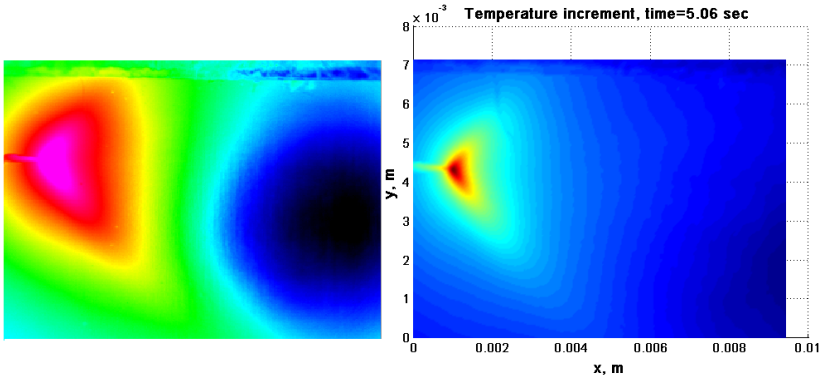

(a) (b)

Figure 3: Infrared image of the specimen with crack before data processing (a) and the obtained temperature increment field (b).

Calculation of stored energy under quasistatic loading

To calculate the specific power of heat source, we have used the finite difference scheme of equation (1) for heat source evolution

$$s = \rho c\left(\dot{T} + \frac{T}{\tau}\right) - k\Delta T \qquad (1)$$

where T is the temperature, ϱ is the density (4550 kg/m³), c is the heat capacity (600 J/(kg·K)), k is the heat conductivity (6.5 W/(m·K)), s is the unknown specific power of heat source (W/m³), and τ is the constant corresponding to the heat loss due to heat exchange with the surroundings (103 J/(m³·K)).

The power of heat source at time close to fracture is shown in Fig. 4. The plastic zone is localized on the surface of the smooth specimen (Fig. 4a). Fig. 4b presents the last moments before fracture of the specimen with crack; one can observe strong plastic deformation at the crack tip, and the plastic zone has the form of a "butterfly".

Here we also use the assumption [14, 15] that some of the irreversible plastic work contributes to heat generation, while the rest is stored as the energy of crystal defects accompanying plastic deformation, traditionally known as the stored energy of cold work.

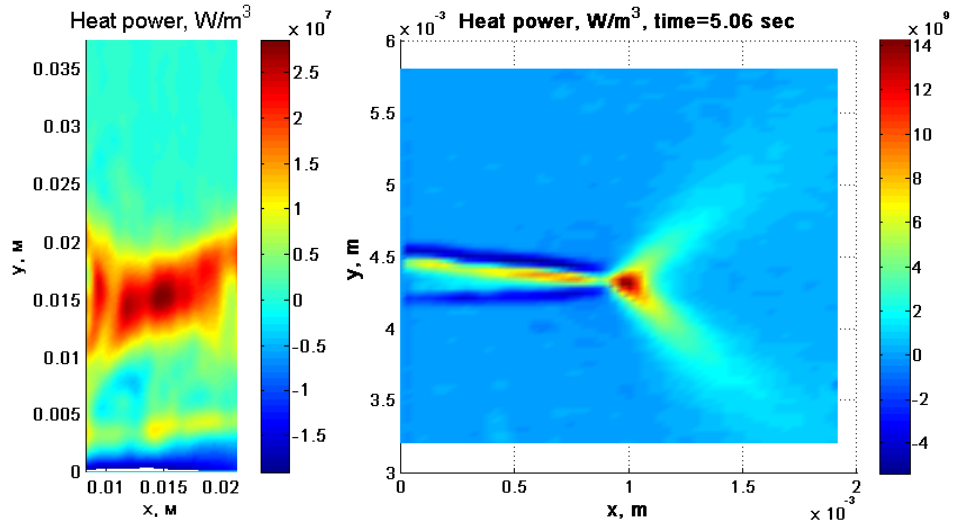

(a) (b)

Figure 4: Experimental data for the heat power field near the crack tip at the beginning of unstable crack propagation.

For plane specimens without crack the plastic work under quasi-static tensile loading is calculated using the experimental data obtained for the applied force $F(t)$ and the deformation velocity V:

$$W_p^{quasi}(t) = F(t)V \tag{2}$$

The power of heat source is integrated over the plastic localization zone, and the heat dissipation energy is defined by the equation

$$Q^{quasi}(t) = \int_{x1}^{x2}\int_{y1}^{y2} s(x,y,t)dxdy \tag{3}$$

where x_1, x_2, y_1, y_2 are the rectangular coordinates of the plastic deformation zone.
The stored energy is determined as a difference between the plastic work and the heat dissipation energy. The results of calculation are presented in Fig. 5.

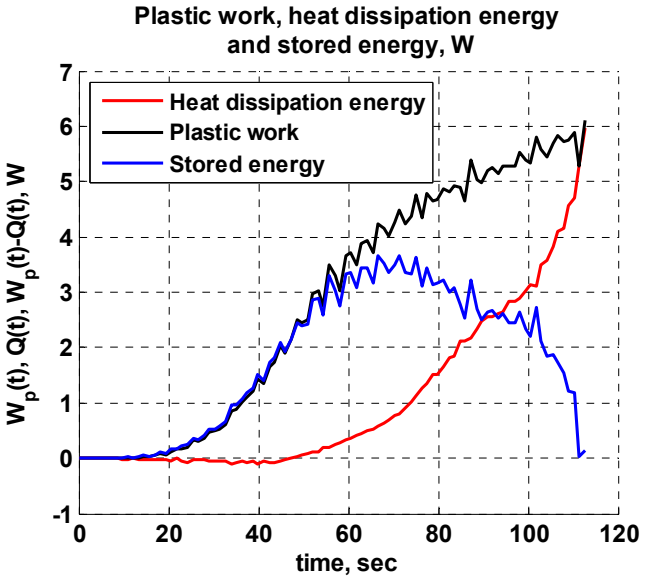

Figure 5: Time dependence of plastic work, heat dissipation energy and stored energy calculated for the smooth specimen.

By analyzing the data presented in Fig. 5, we can conclude that the stored energy rate tends to zero at the time of failure. This supports the results [5] indicating that the stored energy is a thermodynamic parameter, which can adequately describe the damage evolution in metals under deformation.

Calculation of stored energy at fatigue crack tip

To define the plastic work at the fatigue crack tip, we have used the solution for stress distribution at the crack tip obtained by Hutchinson, Rice and Rosengren (HRR-solution). The specific plastic work in the direction of crack propagation can be written as [16]:

$$w_p(r,\theta,t) = \int_0^{\varepsilon_p} \sigma d\varepsilon = \frac{n}{n+1}\frac{J(t)\sigma_e^{n+1}(\theta,n)}{I_n r} \tag{4}$$

where n is the hardening coefficient (in our case, n=4), I_n is the function of the hardening coefficient, r and θ are the polar coordinates of the point near the crack tip (x=$r$cosθ, y=$r$sinθ), σ_e is the tabulation function, and $J(t)$ is the energy J-integral that is the function of applied cycling loading and crack length. The time dependence of the J-integral is plotted in Fig. 6.
The stored energy is obtained as a difference between the accumulated plastic work and the accumulated heat dissipation energy calculated in the area near the crack tip at all time moments of the experiment. Thus, we have

$$W_p(x,y,t) = \int_0^{t_i} w_p(x,y,t)dt \tag{5}$$

$$Q(x,y,t) = \int_0^{t_i} s(x,y,t)dt \tag{6}$$

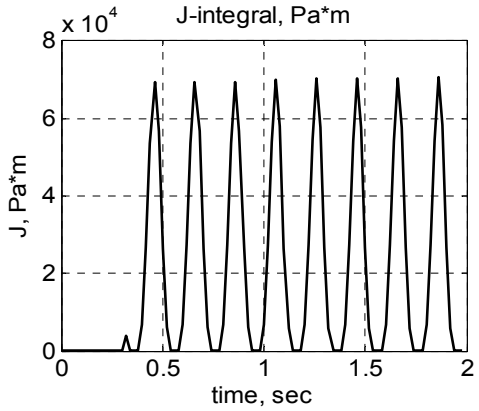

Figure 6: Time dependence of the energy J-integral under cycling loading.

The time dependence of accumulated plastic work, dissipative energy and stored energy calculated for the moving fatigue crack tip is shown in Fig. 7. To calculate the parameters presented in Fig. 7, the maximum of the temperature field near the crack tip was registered at each step of the experiment, and in equations (4)-(6) the origin of coordinates was displaced to a new position at each time moment. By comparing the time evolution of plastic work and dissipative energy, the deformation process corresponding to the transition from the stable state to the unstable state of crack propagation can be divided into three parts.

The first stage lasts for approximately 1.3 second; correlation between two curves is good. From 1.3 second to 5 seconds, the dissipation energy increases slowly compared to the plastic work. Over this period, the stored energy is monotonically accumulated in the deformed material and transformed into the potential energy of lattice distortion. At the last moments before fracture, the heat dissipation energy increases jumpwise and reaches the value of plastic work. At this time the rate of plastic work is less than the rate of heat dissipation energy. It can be assumed that the damage accumulation mechanism is changed, and the material approaches the fracture stage, where the role of macroscopic displacements is essential, and the energy dissipation increases significantly. We can suppose that the plastic work at this moment cannot be described by traditional HRR-solution (4), because this model does not agree with the effect of a jumpwise increase in the dissipation energy. So, the stored energy calculated at this moment should be corrected.

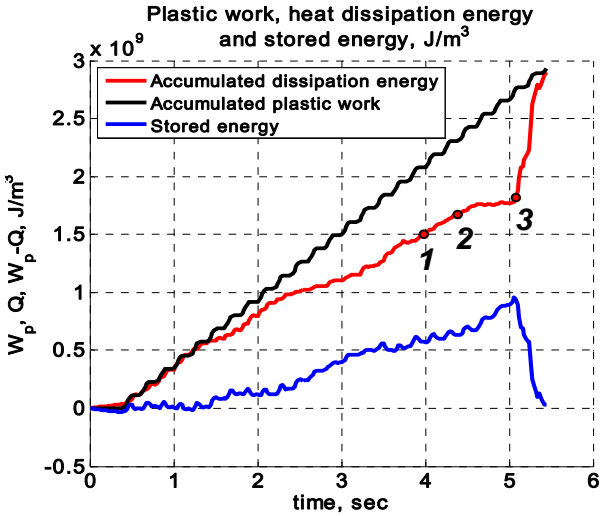

Figure 7: Time dependence of plastic work, heat dissipation energy and stored energy at the point near the crack tip (1, 2, 3 – time points for β-distribution in Fig. 8).

The data obtained for the examined material indicate that the stored energy reaches a critical value, after which the HRR solution is unable to describe the behavior of plastic work near the crack tip. We suppose that the stored energy observed at the last moment before fracture is equal to some constant that indicates the approaching material destruction.

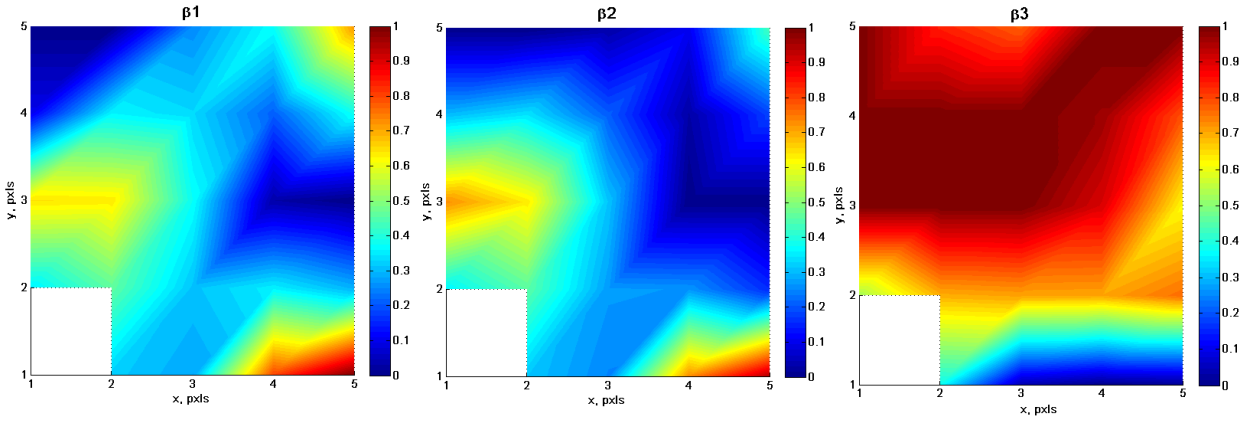

Figure 8: The first coordinate quarter of the space β-distribution at different time moments is shown in Fig. 7. The crack propagates along the *x*-axis.

We introduce the parameter β to evaluate the value of stored energy in metals:

$$\beta(x,y,t)=\frac{W_p(x,y,t)-Q(x,y,t)}{W_p(x,y,t)} \tag{7}$$

The space distribution of the parameter β at different time points is given in Fig. 8. A white pixel is the point of the crack tip where stresses are calculated based on the HRR-solution. Therefore, the plastic work has singularity at the crack tip. Pictures 1, 2 and 3 correspond to the points shown in Fig.7. It is seen that the dissipation energy increases depending on the plastic work, and the images of the space β -distribution are similar (pictures 1, 2). Picture 3 indicates that the β-distribution changes, that is, in front of the crack tip an area with zero β appears in the direction of crack propagation. Thus, the crack growth can be expected in the area of zero β.

The space distribution of the parameter β makes it possible to access the direction of crack motion and to predict its growth up to the specimen failure. This circumstance allows us to use the parameter β as a failure criterion that is based on the thermodynamic laws.

CONCLUSION

The infrared technique has been applied to investigate the effect of heat dissipation under quasi-static loading and its localization at the crack tip under cyclic loading. The original data processing algorithm developed earlier has allowed us to calculate the values of heat dissipation at the crack tip and to determine the area of plastic deformation localization on the surface of a smooth sample during the tensile test. A method has been developed for determining the stored energy and the parameter β, which could be used as a thermodynamic fracture criterion. The spatial and time distribution of the stored energy has been calculated using the infrared data. The damage parameter is taken as the ratio between the stored energy and the work of plastic deformation. For both the weakened and smooth samples, it has been found that the stored energy is accumulated in titanium specimens undergoing fatigue tests, and the value of stored energy is equal to zero when failure concentration reaches the critical value corresponding to specimen fracture. The obtained results yield information that can be used to develop engineering methods for analyzing the actual state of structures that undergo real loading.

ACKNOWLEDGEMENTS

This work was supported by the grant of the President of Russian Federation for support of young Russian scientists and leading scientific schools (MD-2684.2012.1) and RFBR (grant № 11-01-96005).

REFERENCES

[1] V. E. Panin, Yu.V. Grinyaev, V. V. Danilov et al, Structural levels of plastic deformation and fracture. Novosibirsk: Nauka, (1990) 255 (in Russian).
[2] V. V. Rybin, Severe plastic deformation and failure of metals. M.:Metalurgiya, (1986) 224 (in Russian).
[3] V. S. Ivanova, V. F. Terentiev, The nature of the fatigue of metals. Moscow «Metallurgy», (1975) 456 (In Russian)
[4] V.T. Troshchenko, Deformation and fracture of metals under high cyclic loading. Kiev: «Naukova Dumka», (1981) 344 (In Russian)
[5] V.V. Fedorov, Thermodynamic aspects of strength and fracture of solids. Tashkent: «FAN» Uz SSR, (1979) 168 (In Russian)
[6] G. Curti, G. La Rosa, M. Orlando, A. Risitano, In: 14th AIAS Italian National Conference, Catania, Italy, (1986) 211 (in Italian).
[7] G. La Rosa, A. Risitano, Int. Journal of F., 22 (2000) 65.
[8] M. P. Luong, Nuclear Engineering and Design, 158 (1995) 363.
[9] M. B. Bever, D. L. Holt, A. L. Tichener, Prog. Mat. Sci., 17 (1973) 1.
[10] W. Oliferuk, A. Korbel, W. Bochniak, Materials Science and Engineering A, 319-321 (2001) 250.
[11] O. Plekhov, N. Saintier, T. Palin-Luc, S. Uvarov, A. Naimark, Material Science and Engineering A, 462(1) (2007) 367.
[12] M. Bannikov, A. Terekhina, O. Plekhov, Vestnik Permskogo gosudarstvennogo tehnicheskogo universiteta. Mehanika, 2 (2011) 14. (In Russian).
[13] A.Yu. Fedorova, M.V. Bannikov, O.A. Plekhov, Fracture and Structural Integrity, 21 (2012) 46.
[14] J. Hodowany, G. Ravichandran, A.J. Rosakis, P.Rosakis, Exp Mech, 40(2) (2000) 113.
[15] O. Plekhov, S. Uvarov, O. Naimark, Strength of materials, 1(391) (2008) 101.
[16] Yu.G. Matvienko, V.G. Avramenko, Deformation and fracture of materials, 10 (2009) 2. (In Russian)

Research of the effectiveness of mechanical testing methods with analysis of features of destructions and temperature effects

A.V. Babushkin, D.S. Lobanov, A.V. Kozlova, I.D. Morev
Perm National Research Polytechnic University, 614990, Komsomolsky av., 29, Perm, Russia
bav651@yandex.ru

ABSTRACT. In this paper is carried out the comparative analysis of effectiveness of test methods of determination of stiffness and strength properties of highly filled unidirectional fiberglass (Direct "E" roving 0.7 - orthophthalic polyester resin 0.3) via tensile testing along the reinforcement and three-point bending testing at several bases. The necessity of deviation from standard procedures is substantiated. Deformation and failure features of the material under quasi-static loading, as well as at low and high temperatures, are shown.

KEYWORDS. Composite materials; Highly filled fiberglass; Test methods; Deformation and failure; High and low temperature.

INTRODUCTION

For designing and providing reliable operation of high loaded shell structures from layered-fiber cross-reinforced composites are relevant issues of an adequate definition of effective elastic and strength properties of the material. These issues are usually resolved with help of mathematical modeling or tests. In this case, the structural-phenomenological modeling should be also based on the test determination of properties and features of the mechanical behavior of structural components of the composite. For modeling of a cross-reinforced fiberglass are most relevant properties of texture layer - that is a unidirectional fiber composite. Determination of unidirectional fiber composite properties is usually based on ASTM D 3039. In the test research of composite materials in the product is convenient to use method of beam-specimens bending on different bases, as this method allows determine the longitudinal strength and elastic modulus, shear modulus and shear (interlayer) strength [1]. According to this method, the properties are determined by three-point bending testing on different bases of beam-specimens, which are cut in the appropriate direction of finished product. This approach allows take into account technological features of the material production into product. However, this method gives obviously lower results, as work conditions of relatively short reinforcing fibers in cut specimen and continuous fibers in the product are significantly different. Anyway, in both cases, the result is based on test data. In practice, the lower results at test are interpreted as a certain margin of safety in product designing. Naturally, questions of estimation of this stock value and the adequacy of various test methods for providing structural mathematical modeling on the one hand, and product design in the framework of phenomenological approaches - on the other, arise.

In this paper is held a comparative analysis of different methods of test determination of unidirectional fiberglass stiffness and strength properties, deformation and fracture characteristics of these materials under quasi-static loading and also at low and high temperatures.

MATERIALS AND CONDITIONS OF TEST

Uniaxial tensile testing of unidirectional fiberglass

Tests of unidirectional fiberglass (Direct "E" roving 0.7 - orthophthalic polyester resin 0.3) were carried out in the direction of reinforcement. This material has main feature, which is high (70%) content of the reinforcing component. Increase of fibers volume fraction increases material strength in the direction of the reinforcement and a sharp decrease in strength in the transverse direction. The desire to test at high and low temperatures imposes certain restrictions on the size of the specimen. These circumstances lead to restrictions on the usage of standard approaches and methods (ASTM D 3039 / D 3039M-08) for the material testing.
The grip in a form of sleeve has been designed and produced specifically for uniaxial tensile testing along the reinforcement. One of the device features is the lack of cross-compression in the gripping part of the specimen [2]. Unidirectional fiberglass specimen is made in a form of rod with a constant cross section. A specimen is holding in gripping area by adhesion, while it is being deformed and failed. Strength of this design is determined by the properties of the adhesive and the depth of the immersion. In this case, specimen length with the steel gripping sleeve is limited by working area of a temperature chamber. On the specimen gage length were applied labels for using non-contact extensometer Instron AVE, as shown in Fig. 1.

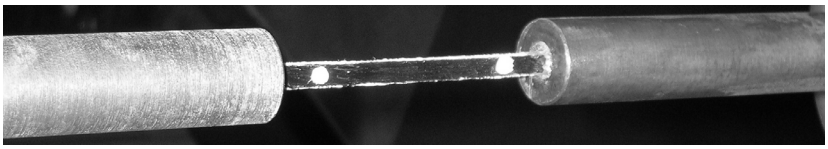

Figure 1: The appearance of highly filled fiberglass specimen for uniaxial tensile test with applied labels for using non-contact extensometer Instron AVE [2]

Tensile tests of unidirectional fiberglass along the reinforcement were held on a universal electromechanical system Instron 5882 with video extensometer Instron AVE. Climate chamber Instron 3119-407 was used at low and high temperatures tests. On Fig. 2 are shown testing system Instron 5882 (1), video extensometer (2) and a climatic chamber (3), and a specimen of the proposed construction in grips at tensile test at room temperature (22°C). The necessity of a non-contact extensometer is explained by fracture behavior of specimens, which are made from this material.

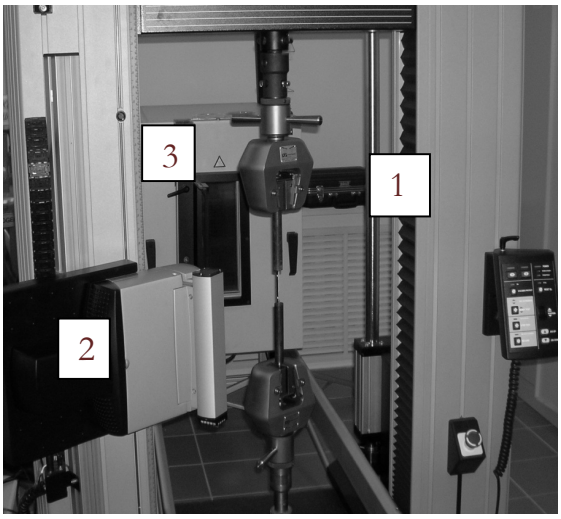

Figure 2: The appearance of the unidirectional fiberglass specimen in grips at tensile tests: Instron 5882 test set (1), video extensometer (2), climate chamber (3).

Twelve specimens were tested at room temperature. At low temperature were tested only 8 unidirectional fiberglass specimens: 4 specimens at 30°C, 4 specimens at 0°C. At high temperatures, were tested three specimens at each temperature of 40°C and 50°C. It should be noted, that the usage of sleeves and epoxy binder as an adhesive at high

temperatures sometimes leads to the failure, which happens in form of creep of rod out sleeves without fiber failure of the specimen. For providing the compactness of the general assembly and for determination of fiberglass stiffness and strength properties was made an attempt of using upgraded grip-sleeves, shown in Fig. 3. [2] The essence of this device is to have a tapered hole, through which was expected to create a uniform compliance (glue) cross-compression of rod specimen at tension test. However, this test circuit didn't always provide a positive result. So, ultimate tensile strength of fiberglass (Direct "E" roving 0.7 - orthophthalic polyester resin 0.3) at 50ºC in this test wasn't determined.

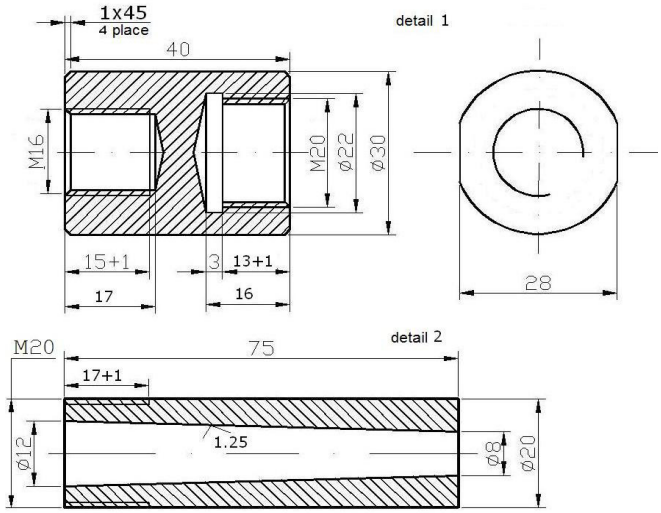

Figure 3: Scheme of device for unidirectional rod specimen testing at high temperatures [3]

Types of diagrams of unidirectional fiberglass (Direct "E" roving 0.7 - orthophthalic polyester resin 0.3) deformation in tensile test at various temperatures came out similar. On Fig. 4 is shown typical diagram of unidirectional fiberglass deformation in tensile test with usage of videoextensometer Instron AVE.

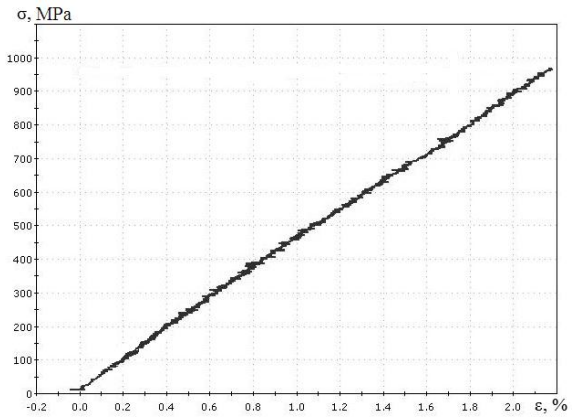

Figure 4: The appearance of typical diagram of unidirectional fiberglass Direct "E" roving 0.7 - orthophthalic polyester resin 0.3 deformation in tensile test.

Thus, as a result of specimen testing of highly filled unidirectional fiberglass on uniaxial tensile along the direction of reinforcing at room, low and high temperatures, have been identified elastic and strength characteristics of the material.

Three-point bending testing of unidirectional fiberglass

Main characteristics of unidirectional composite were also determined at bending tests. Tests were carried out by three-point bending method of beam specimens with various lengths between brackets. For calculation of mechanical characteristics were used mathematical tools for anisotropic materials [1]. Testing scheme is shown on the Fig. 5. In whole

testing technique is similar to ASTM D2344. At this case, fiberglass (Direct "E" roving 0.7 - orthophthalic polyester resin 0.3) specimens were cut along reinforcement in a form of beams with cross section 5x5 mm. Three specimens were tested on each of four bases: l_1 = 30 mm, l_2 = 50 mm, l_3 = 70 mm, l_4 = 100 mm. Specimen lengths respectively were defined like $L_i = l_i + l_i/5$. By the results of tests were made force-displacement diagrams. Mechanical characteristics calculations from test results of three specimens on one base were averaged.

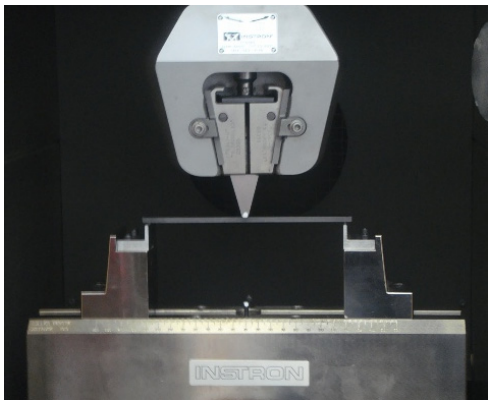

Figure 5: Bending test of unidirectional fiberglass (Direct "E" roving 0.7 - orthophthalic polyester resin 0.3).

THE PROCESSING OF THE EXPERIMENTAL DATA

From uniaxial tension test could be determined the ultimate tensile strength σ_b, elastic modulus E and Poisson's ratio ν. In this case, tensile strength and Young's modulus were determined [2]. Necessary stress and strain for these characteristics calculations were on gage length. Ultimate tensile strength was determined by formula

$$\sigma_b = \frac{P_{\max}}{F}$$

where $P_{\max}$ – maximum force at specimen deformation, F – initial cross section area of gage length. Longitudinal deformations were measured by non-contact videoextensometer Instron AVE and were calculated by formula

$$E = \frac{\Delta\sigma}{\Delta\varepsilon}$$

where $\Delta\sigma$ – increment of stress on linear region of deformation curve, $\Delta\varepsilon$ – corresponding increment of specimen linear deformation.

For calculation of elastic and strength characteristics at bending of fiberglass specimens was used improved theory [1]. In addition to the normal stress in the bent beam there are tangential stresses, influence of which on the strength and stiffness of isotropic composites is negligible. At bending tests of anisotropic beams, depended on the nature of the failure of specimen, can be determined flexural strength or strength at interlaminar shear. In practice, both normal and shear stresses are working in the specimen, so the determination of the properties of anisotropic composite materials at bending should take into account their mutual influence.

The adjusted formula for determination of maximum of normal stress σ_b at bending has the following form

$$\sigma_b = \sigma_f \left(1 + \frac{\chi^2}{15} - \frac{\chi^4}{525}\right)$$

and for determination of maximum of shear stress $\tau_b = \tau_f \left(1 - \frac{\chi^2}{60} + \frac{\chi^4}{12600}\right)$,

where $\sigma_f = \frac{3}{2} \cdot \frac{P_{\max} \cdot l_i}{bh^2}$ and $\tau_f = \frac{3}{4} \cdot \frac{P_{\max}}{bh}$, so $\chi = \frac{\pi h}{2l_i} \cdot \sqrt{\frac{E_f}{G}}$ – parameter of anisotropy, E_f – fictitious elastic modulus; G – interlayer shear modulus; b – specimen width, l_i –length between brackets at three-point bending.

For defying elastic modulus at three point bending of laminate composite material should be used refined dependencies, which consider influence of shear deformations and binding maximum flexure $\omega_{\max}$ of the beam in the middle of brackets with applied force P, true elastic modulus at bending E_f^t and interlayer shear modulus G:

$$\omega_{\max} = -\frac{P \cdot l_i^3}{48 E_f I}\left(1 + \alpha_k \left(\frac{h}{l_i}\right)^2 \frac{E_f}{G}\right) \tag{1}$$

where α_k – coefficient, which depends on cross section form of the beam (for rectangular $\alpha_k \cong 1.2$); $I = \frac{bh^3}{12}$ – moment of inertia of beam cross section. True elastic modulus at bending E_f^t is bonded with fictitious modulus $E_f = \frac{P \cdot l_i^3}{48 \cdot I \cdot \omega_{\max}}$ in the following ratio

$$\frac{1}{E_f} = \frac{1}{E_f^t} + \frac{1.2}{G} \cdot \left(\frac{h}{l_i}\right)^2 \tag{2}$$

The higher ratio of thickness of the specimen to its length $\frac{h}{l_i}$ and the higher degree of anisotropy of composite material, characterized by $\frac{E_f^t}{G}$, the more different true elastic modulus from fictitious.

With one test it is impossible to calculate elastic modulus by formula (1) as it has two unknowns E_f and G. So for their determination are tested several specimens with different ratios $\left(\frac{h}{l_i}\right)$ and then was diagram made, where on the horizontal axis was put off value $\left(\frac{h}{l_i}\right)^2$ and on the vertical axis $-\frac{1}{E_f}$. In this coordinates, relation (2) has to be represented as a straight line, which crosses the vertical axis at the point $\frac{1}{E_f^t}$ and slope of this line to the horizontal axis equal $\frac{1.2}{G}$. Then value of E_f^t and G are determined by method of least square.

DISCUSSION OF RESULTS

Tension test results of highly filled fiberglass specimens (Direct "E" roving 0.7 - orthophthalic polyester resin 0.3) are in the Tab. 1.

Temperature, °C	Tensile strength at break σ_b MPa	Young's modulus in tension E, GPa
-30	922.1	34.2
0	980.2	36.8
+22	987.1	47.8
+40	690.5	38.8
+50	-	37.4

Table 1: Unidirectional fiberglass (Direct "E" roving 0.7 - orthophthalic polyester resin 0.3) properties at tension test [3].

According to the table, highest values of the characteristics are at test at room temperature. When temperature is lower or higher, then room temperature, characteristic value decreases. Strength at 50°C couldn't be determined.
In the Tab. 2 there are three-point bending test results of highly filled fiberglass specimens (Direct "E" roving 0.7 - orthophthalic polyester resin 0.3). It should be noted, that this method allows getting more characteristics: to Young's modulus E and to longitudinal strength σ_b are added interlayer shear modulus G and shear strength τ_b. There were no problems with testing at various temperatures. However, this method is more sensitive to the quality of the test. In [1] there are range of parameters, which influence on results: slide from brackets, optimal ratio h/l, and edge effects. There are no clear tendencies of temperature effects. Value of normal strength is lower on 20-25%, then values which were got at tensile tests. Influence of shear components on comparable (E, σ_b) characteristics is clearly noticeable.

Temperature, °C	Properties			
	E, GPa	G, MPa	σ_b, MPa	τ_b, MPa
- 30	40.4	762	682	24
+ 22	30.7	924	674	32
+ 50	35.7	1142	489	38

Table 2: Unidirectional fiberglass (Direct "E" roving 0.7 - orthophthalic polyester resin 0.3) properties at bending tests

FEATURES OF FAILURE

All tested unidirectional fiberglass specimens at uniaxial tensile, regardless of the temperature, failed like it is shown on Fig. 6. This type of failure is typical for fiber exfoliation and complete matrix destruction. Obviously, is the presence of shear deformation, which was not taken into account at stress calculation. This kind of failure may be associated with the grip construction without crimping.

Figure 6: Failed unidirectional fiberglass (Direct "E" roving 0.7 - orthophthalic polyester resin 0.3) specimens after uniaxial tensile tests.

The same influence of specimen and grip construction was also noted in the paper [4] when was used NOL-method for getting characteristics of unidirectional fiberglass, Fig. 7, a. However, preliminary cyclic loading leaded to qualitative change in the type of failure (Fig. 7, b), whereas specimen and grip construction wasn't changed.

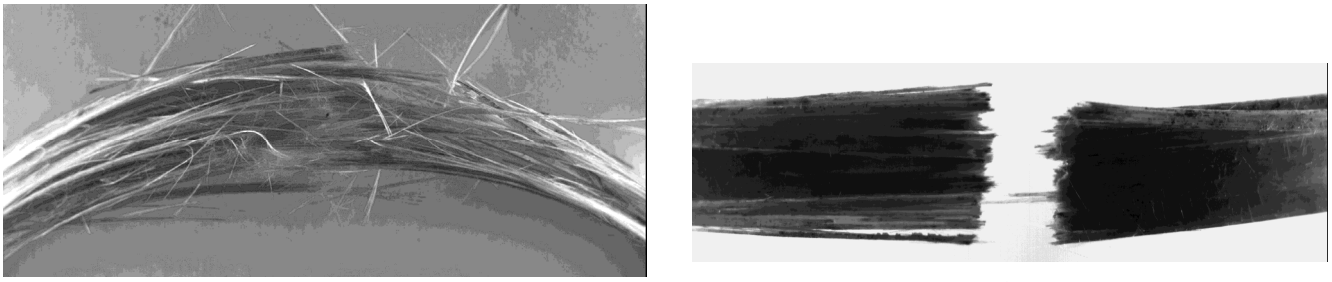

(a) (b)

Figure 7: RBN 1680-UP 2217 fiberglass failure at static deformation by rigid half-discs (a) and after cyclic loading (b).

On Fig. 8 are shown types of failure of beam specimens at three point bending tests on large (a) and small (b) bases. Clearly seen failure character: on long base – from normal stresses at tearing and crushing of fibers; on short base – mainly on in-plain shear, perpendicular to the plain of loading.

Figure 8: Failed unidirectional fiberglass (Direct "E" roving 0.7 - orthophthalic polyester resin 0.3) at three point bending tests on large (a) and small (b) bases.

Conclusion

Thus, the identified properties of unidirectional fiberglass in two ways: in the direction of the tensile reinforcement and in three-point bending at different bases. Tests were carried out at normal, high and low temperatures. Values of comparable properties are close, but obvious tendency of temperature effect at tensile tests doesn't confirm at bending tests. Strength of normal separation, measured at bending testing, is lower on 20-25% than strength, measured at tensile testing. Both test methods are forced to differ from standard methods. At tensile tests were used grips without lateral compression of specimen material or with uniform pliable compression, which is caused by wedge effect. Bending tests can determine more characteristics, are not critical to changes of temperature and use improved theory of bending. Type of failure of unidirectional fiberglass at tensile tests along reinforcement is similar to the usage of NOL-method in the absence of damage accumulation. This type of failure suggests a significant influence of shear deformations. At three point bending tests specimen failed traditionally: on long bases – mainly from normal stresses, on short – from tangent.

Acknowledgments

Research were carried out on equipment of the Center of Experimental Mechanics of Perm National Research Polytechnic University with financial support from grant RFBR № 12-08-31336.

References

[1] Y. M. Tarnopolsky, T. Y. Kintsis, Methods of static tests of reinforced plastics, Chemistry, Moscow (1981).
[2] A.V. Babushkin, V.E. Wildemann, D.S. Lobanov, Factory laboratory. Materials' diagnostics, 76(7) (2010) 57.
[3] D.S. Lobanov, A.V. Babushkin, In: Proc. of ECCM15: European Conference on Composite Materials, Venice, Italy, (2012), Paper ID: 1224. – ISBN 978-88-88785-33-2.
[4] A.V. Babushkin, A.V. Kozlova, Composites: Mechanics, Compositions, Applications. An International Journal, 2(3) (2011) 223.

Special Issue: Russian Fracture Mechanics School

Tests in tension-torsion conditions with descending sections of strain curve construction

M.P. Tretiakov, V.E. Vildeman
Center of Experimental Mechanics, Perm National Research Polytechnic University, Komsomolskiy Pr. 29, 614990, Perm, Russia
cem_tretyakov@mail.ru

ABSTRACT. The paper is devoted to theoretical and experimental investigation of materials behavior on postcritical deformation stage (strain softening). Tests results, which confirm theoretical justification of specimen configuration impact on the possibility of creating descending sections of strain curve, are given. It is shown that, with sufficient stiffness of loading system, equilibrium postcritical deformation of materials is possible. It is confirmed in uniaxial tension tests with unloading on postcritical deformation stage. Test results on tension with torsion of thin-walled tubular specimens in strain softening conditions are adduced.

KEYWORDS. Experimental mechanics; Postcritical deformation; Proportional tension with torsion.

INTRODUCTION

Dissipative processes of inelastic deformation, including the processes of structural failure and fracturing, reflect on the deformation curve as nonlinearity. At the final stage this leads to softening of materials and the appearance of a descending section on strain curve. Completeness of implementation of the load-carrying capacity of strength constructions is determined by the degree of postcritical deformation. When postcritical deformation stage is taken into account in adjusted computation, it allows a reserve of constructions load-carrying ability to be revealed. It makes possible to forecast the destruction moment more accurately [1, 2]. Questions of theoretical, experimental and numerical study of postcritical deformation mechanisms of materials attract attention of researches in connection with the questions of use of materials deformation reserves, the rise of load-carrying ability and survivability of materials, and the analysis of possibilities of failure processes management [1-9].

On the postcritical deformation stage the formation of macro-destruction conditions takes place. These conditions, unlike the traditional view that defines the use of force or deformation criteria are not definitely related to the stress-strain state at the point of deformed body. During the transition from the equilibrium stage of damage accumulation to non-equilibrium stage of destruction, interaction of the deformed body with the loading system plays the key role. As a result, based on loading conditions, each point on the descending section of stress-strain curve can correspond to the time of the loss of load-carrying ability as a result of transitioning from stable to non-equilibrium stage of the damage accumulation process. Thus, the rigid loading system may contribute to the "adaptation" of the object in the process of destruction due to local dissipation of elastic energy [1, 2]. However the force or deformation criteria can be considered with a view to transition of material to postcritical strain stage (similarly the condition of transition to plastic state). It is necessary to experimentation verify of criteria, particularly by test results in plane stress state under combined tension-torsion loading [11- 13].

It is known that it is necessary to use high-stiffness test systems for obtaining equilibrium curves of materials postcritical deformation. However, even with high-stiffness test machine, in some cases obtaining descending sections of strain curve is not possible. It may be associated with specimen geometry. In work [10] a deformable body Ω is considered with boundary Σ and contact type boundary conditions:

$$\left[\sigma_{ij}(\boldsymbol{r})n_j + R_{ij}(\boldsymbol{r})u_j(r)\right]|_{\Sigma_S} = S_i^0(\boldsymbol{r})$$

where R_{ij} are coefficients of loading system stiffness, $n_j(\boldsymbol{r})$ are direction cosines of normal vector to the surface of body Ω in the point with coordinate r . Defining relationship is written in the following form:

$$d\sigma_{ij} \equiv C'_{ijmn}(\varepsilon,\chi)d\varepsilon_{mn}$$

where χ is indicator reflecting the nature of the process (active loading ($\chi = 1$)or unloading). The condition of postcritical deformation stability in weakness zone Ω_0 is written as follows:

$$\int_{\Sigma} R_{ij}\delta u_j \delta u_i d\Sigma + \int_{\Omega-\Omega_0} C'_{ijmn}\delta\varepsilon_{mn}\delta\varepsilon_{ij}d\Omega > \int_{\Omega_0} D_{ijmn}\delta\varepsilon_{mn}\delta\varepsilon_{ij}d\Omega$$

where $D_{ijmn} \equiv -C'_{ijmn}(\varepsilon,\chi=1)$ are components of softening modulus tensor. The sign of postcritical deformation is formulated in the following form:

$$d\sigma_{ij}d\varepsilon_{ij} < 0$$

In a particular case of uniaxial deformation of a solid cylindrical specimen with length l and cross section square F and with weakness zone length l' and cross section square $F'<F$, the main volume of the specimen is part of the loading system with respect to the weakness zone. It has been shown that the necessary condition of reaching postcritical deformation stage in the weakness zone is:

$$Q_0 > Q_c + Q_M$$

where $Q_M = R_M^{-1}$ is compliance of test machine (R_M is stiffness of test machine), $Q_c = (l-l')/(EF)$ is compliance of bar (main volume), $Q_0 = l'/(DF')$ is compliance of the softening region ($D = -d\sigma/d\varepsilon$ is the current meaning of tangent softening modulus). Similarly for a thin-walled tubular specimen with length l and moment of inertia J_p, with weakness region with length l' and moment of inertia $J'_p\left(J'_p < J_p\right)$, it can be seen that the condition necessary for postcritical stage realization in the weakness region under torsion can be written in the following form:

$$L_0 > L_c + L_M$$

where $L_M = N_M^{-1}$ is the compliance of test machine on torsion (N_M is stiffness of test machine on torsion), $L_c = (l-l')/(GJ_p)$ is the compliance of the bar on torsion (main volume), $L_0 = l'/(D_G J'_p)$ is the compliance of the softening region on torsion ($D_G = -d\tau/d\gamma$ is the current meaning of tangent softening modulus on torsion).
The aim of the work is experimental examination of the impact of loading system stiffness (particularly geometrical parameters of specimens) on the construction of strain curve with descending sections, and construction of strain curves with postcritical deformation stages in uniaxial tension and proportional tension-torsion tests.

TESTS AND RESULTS

Test equipment

Tests were carried out on Instron 8850 biaxial servohydraulic test system (maximum load 100 kN, maximum torque 1000 Nm, cyclic tests with frequency up to 30 Hz). Strain in the test part of specimen in uniaxial tension tests was registered by Instron 2620-601 extensometer, and in proportional tension-torsion tests it was registered by Epsilon 3550-010M biaxial extensometer.

Tests with various loading system stiffness

Experimental investigation of the effect of stiffness of the loading system on the construction of strain curves with descending sections was performed in two test groups. In the first test group, solid cylindrical specimens with test part length of 10 mm, diameter of 6 mm with additional deformation parts of different lengths (length of 30 mm, 60 mm, diameter of 8 mm) were used. In this case the additional test parts increased the compliance of the loading system with respect to the weakened central part. In the second test group specimens with different diameters (5 mm, 10 mm, 13.5 mm) with the same ratio of test part length to diameter ($l_0/d=1$) were used. In this case, the change of the specimen's diameter changes the specimen's stiffness and consequently changes the ratio of specimen stiffness to test machine stiffness.

In Fig. 1 the results of two test groups of steel 20 (GOST 1050-88) are shown. The influence of the loading system stiffness is reflected by the presence of different points on the descending section of strain curve, which correspond to the loss of stability moment of the deformation process. Stress is calculated as ratio of load to initial cross-section square of the specimen, the strain is $\varepsilon_{ln} = \ln(1+\varepsilon)$, where ε is the ratio of extension by extensometer to initial gauge length.

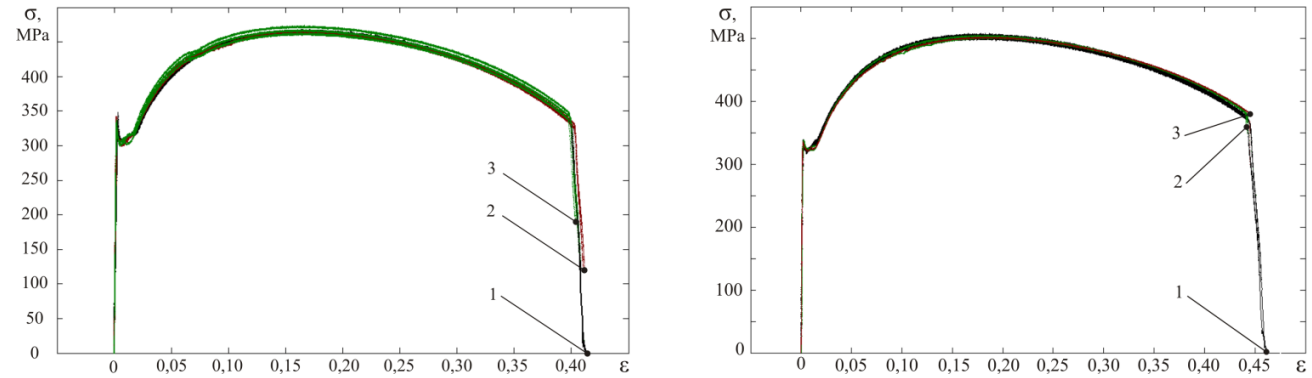

Figure 1: Strain curve of steel 20 and destruction moments: (a) is test results of specimens with additional elements (*1* is specimen without additional elements, *2* and *3* are specimens with additional elements, with total lengths of 30 mm and 60 mm), (b) is test results of specimens with different stiffness (*1, 2* and *3* are specimens with diameters 5.0 mm, 10.0 mm and 13.5 mm.

The possibility of equilibrium material deformation on softening stage is also confirmed by unloadings and repeat loadings. In Fig. 2 the strain curve of steel 20 at uniaxial tension with unloading on different stages of elastoplastic and postcritical deformation (*a*) and final section of softening with unloadings (*b*) are shown. Strain rate at tension and unloading was 0.02 min^{-1}.

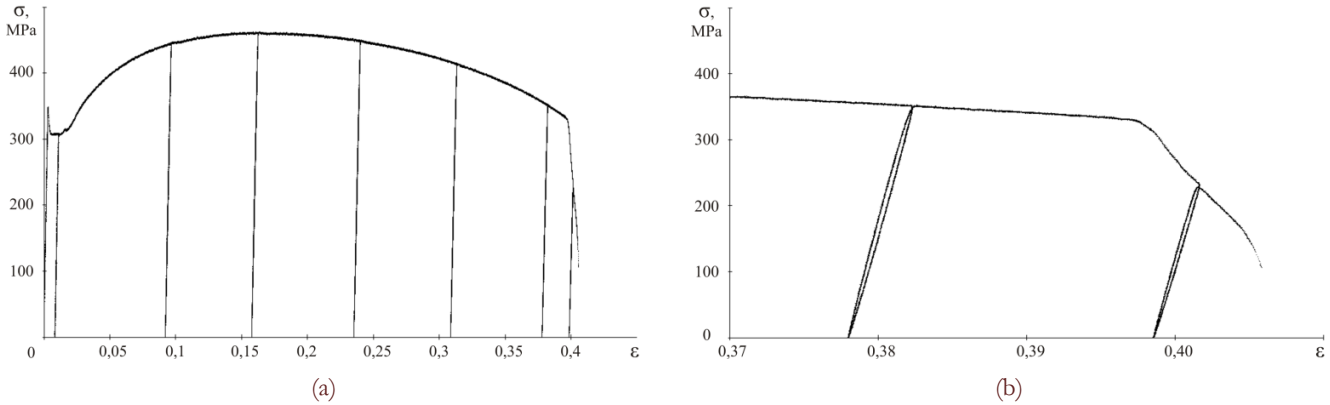

Figure 2: Strain curve of steel 20 at uniaxial tension: with unloading on different deformation stage (a), final section of strain curve (b).

Thus, to obtain equilibrium descending sections of the strain curve and complete curves (equilibrium drop of load to zero value), it is necessary to provide conditions of sufficient loading system stiffness with respect to test part of the specimen (high stiffness of the test machine, geometrical parameters of the specimen). With the above conditions, it is possible to

obtain strain curves with sections of softening both under uniaxial tension and under tension combined with torsion. From the perspective of creation and improvement of postcritical deformation mechanics models the important question is the behavior of materials at a softening stage in combined tension-torsion conditions.

Strain softening in tension-torsion tests

Proportional tension-torsion tests were implemented on thin-walled tubular specimens of steel 40X (GOST 4543-71) and 15X2ГМФ (TU 14-159-227-93 (RF Technical Requirements)) with reduced test part length. Shape and dimensions of specimens are shown in Fig. 3.

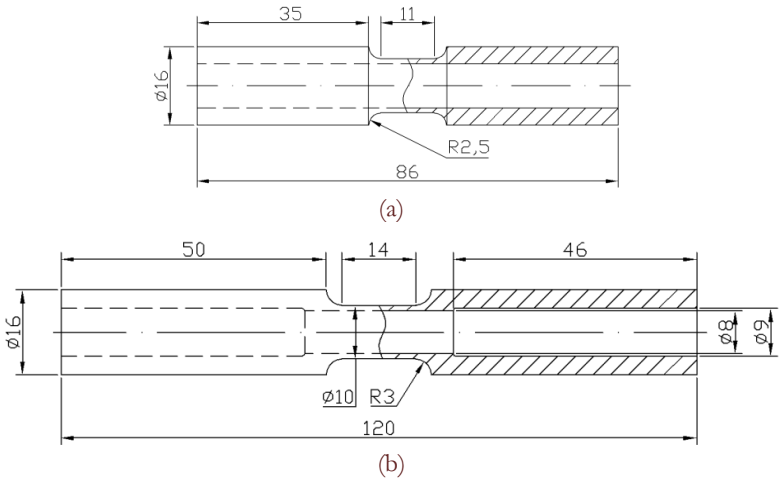

Figure 3: Shape and dimensions of thin-walled tubular specimens of steel 15X2ГМФ (a) and steel 40X (b).

Strain trajectories in deformation space correspond to straight lines. For steel 40X the ratio of axial strain to shear angle is 1.60 and 0.80, for steel 15X2ГМФ it is 0.57 and 0.30. The biaxial extensometer is intended for a small measurement range and it was used for correction of strain curves (by the linear section of the diagrams) which were obtained from the data of test system internal transducers. In Fig. 4 and Fig. 5 test results of steel 20 and 15X2ГМФ at proportional tension with torsion are shown.

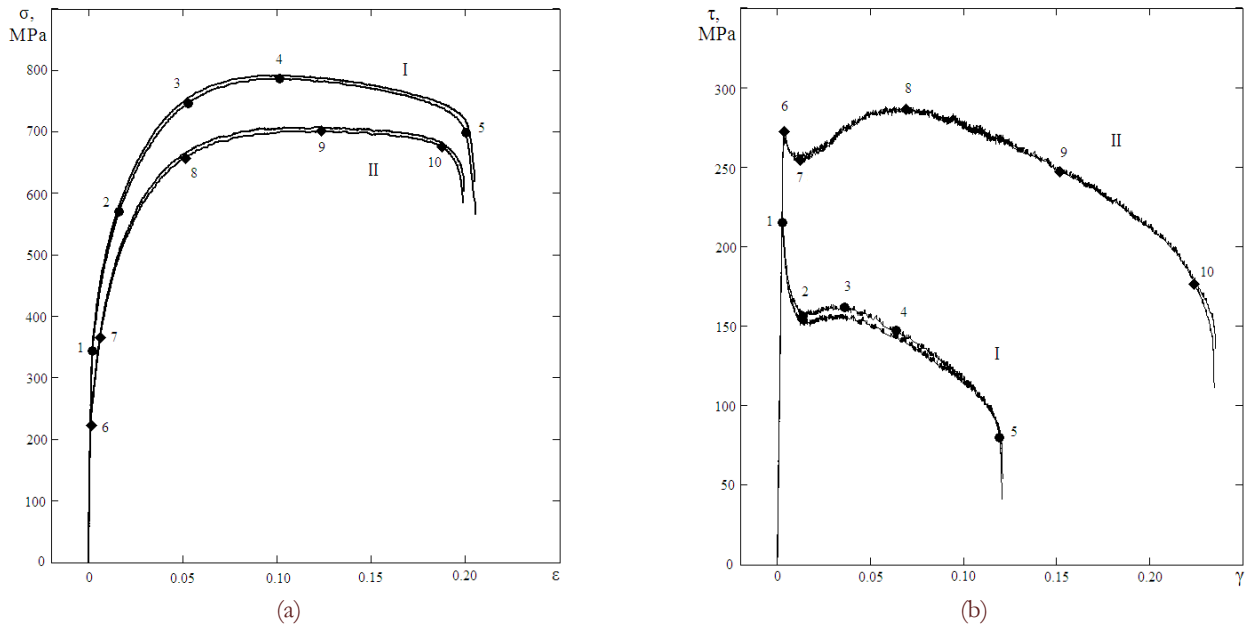

Figure 4: Test results of steel 40X at proportional tension-torsion with ratio ε/γ=1.60 (I) and ε/γ=0.80 (II) in coordinates "axial stress – axial strain" (a) and "shear stress – shear angle" (b).

Stress is calculated as ratio of load to initial cross-section square of the specimen, the strain is $\varepsilon = \Delta l / l_0$, shear stress is $\tau = M / (2\pi r^2 h)$, shear angle is $\gamma = r\varphi / l_0$. In Fig. 4 the strain curves are presented which were constructed at tests of two specimens for each strain trajectories. For steel 15Х2ГМФ stress curves for the two specimens for each strain trajectories were obtained, in Fig. 5 results for one specimen are shown.

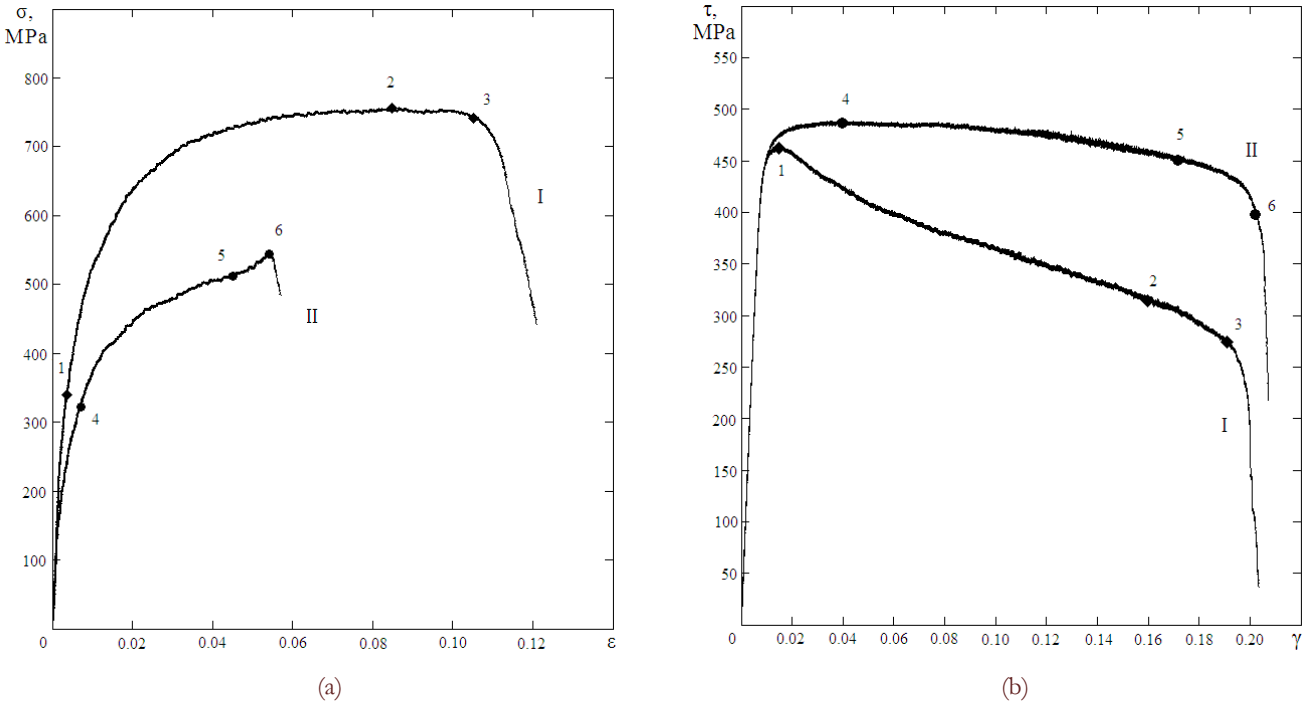

(a) (b)

Figure 5: Test results of steel 15Х2ГМФ at proportional tension-torsion with ratio ε/γ=0.57 (I) and ε/γ=0.30 (II) in coordinates "axial stress – axial strain" (a) and "shear stress – shear angle" (b).

The important question is which deformation moment corresponds to the start of the softening stage, i.e. the reduction of loads at constant increase of strains. In Fig. 4 and Fig. 5 curves are marked with points and numbered for the convenience of comparison of strain curves in coordinates "axial stress – axial strain" and "shear stress – shear angle". In the analysis of experimental data diagram sections corresponding to the hardening of material at tension axis and shear axis can be highlighted. This corresponds to sections 2-3 and 7-8 in Fig. 4 and sections from limits of elasticity to points 1 and 4 in Fig. 5. There is also the strain range in which the softening of material at tension axis and shear axis occurs (the sections 4-5 and 9-10 in Fig. 4 and the sections from points 2 and 6 to specimen destruction in Fig. 5). It is necessary to draw special attention to areas of strain curves corresponding the hardening of material in coordinates "axial stress – axial strain" with synchronic softening in coordinates "shear stress – shear angle". The above is shown in sections of strain curves 3-4 and 8-9 in Fig. 4 and sections 1-2 and 4-6 in Fig. 5.

CONCLUSIONS

In a result of this work, there is experimental confirmation of the influence of loading system stiffness with respect to test part of the specimen (geometrical parameters of the specimen) on realization of strain curve descending section at uniaxial tension. This is reflected in the presence of different points on the descending section which corresponds with the loss of deformation processes stability. The possibility of obtaining postcritical strain curves with sufficient stiffness of the loading system is confirmed by unloadings and repeated loadings at the softening stage under uniaxial tension.

The stress-strain curves of materials with softening sections at proportional tension with torsion of thin-walled tubular specimens are obtained at different trajectories of strain. It confirms the possibility of postcritical strain realization at different types of stress-strain state and allows us to obtain new data for creating models of softening medium mechanics.

REFERENCES

[1] V.E. Vildeman, Yu.V. Sokolkin, A.A. Tashkinov, Mechanics of inelastic deformation and fracture of composite materials, (1997) 288.
[2] V.E. Vildeman, Int. J. for Computational Civil and Structural Engineering, 4(2) (2008) 43.
[3] V.E. Vildeman, Yu.V. Sokolkin, A.A. Tashkinov, Mechanics of Composite Materials, 28(3) (1992) 214.
[4] Yu.V. Sokolkin, V.E. Vildeman, Mechanics of Composite Materials, 29(2) (1993) 120.
[5] V.V. Struganov, Vestnik SSTU, Physics-mathematics science, 30 (2004) 5.
[6] V.V. Struganov, Physical Mesomechanics, 7(S1-1) (2004) 169.
[7] Yu.V. Sokolkin, V.E. Vildeman, A.V. Zaitsev, I.N. Rochev, Mechanics of Composite Materials, 34(2) (1998) 171.
[8] A.V. Ilinykh, M.V. Radionova, V.E. Vildeman, Composites: Mechanics, Computations, Applications, 2(2) (2011) 95.
[9] V.E. Wildemann, A.V. Ilyinykh, Physical Mesomechanics, 10(4) (2007) 23.
[10] V.E. Wildemann, J. Appl. Maths Mechs, 62(2) (1998) 281.
[11] S. Nohut, A. Usbeck, H. Özcoban, D. Krause, G.A. Schneider, Journal of the European Ceramic Society, 30 (2010) 3339.
[12] A.A. Lebedev, B.I. Kovalchuk, F.F. Gignyak, V.P. Lamashevskii, Mechanical properties of structural materials under complex stress state, (2003) 540.
[13] N.M. Zarroug, R. Padmanabhan, B.J. MacDonald, P. Young, M.S.J. Hashmi, J. of Materials Processing Technology, 143–144 (2003) 807.

NOMENCLATURE

Ω	deformable body	Ω_0	weak zone of deformable body
Σ	boundary of deformable body	Σ_S	boundary part with force conditions
σ_{ij}	stress tensor components	ε_{ij}	strain tensor components
u_j	displacement vector components	R_{ij}	loading system stiffness tensor components
S_i^{ρ}	force vector components	χ	indicator of the process nature
C'_{ijmn}	components of tangent material modulus tensor	D_{ijmn}	components of softening modulus tensor
D	softening modulus under tension	D_G	softening modulus under shear
R_M	coefficient of test machine stiffness under tension	N_M	coefficient of test machine stiffness under torsion
$\boldsymbol{r}$	radius-vector	σ	axial stress
ε	axial strain	ε_{ln}	logarithmic axial strain
τ	shear stress	γ	shear angle
E	Young modulus	G	shear modulus
Q_0	compliance of the softening region	L_0	compliance of the softening region on torsion
Q_C	compliance of bar (main volume)	L_C	compliance of bar (main volume) on torsion
Q_M	compliance of test machine	L_M	compliance of test machine on torsion
l	current test part length	l'	length of specimen weak zone
l_0	initial test part length	M	torque
F	cross section square of specimen main zone	F'	cross section square of specimen weak zone
J_p	polar moment of inertia of main zone of thin-walled tubular specimen	J'_p	polar moment of inertia of weak zone of thin-walled tubular specimen
h	wall thickness of thin-walled tubular specimen	φ	torsion angle
r	middle radius of test part of thin-walled tubular specimen	d	test part diameter of solid cylindrical specimen

Special Issue: Russian Fracture Mechanics School

Study of the conditions of fracture at explosive compaction of powders

Andrey E. Buzyurkin, Evgeny I. Kraus
Khristianovich Institute of Theoretical and Applied Mechanics of Siberian Branch of RAS, 4/1 Instituskaya str., Novosibirsk, 630090, Russia
buzjura@itam.nsc.ru, kraus@itam.nsc.ru

Yaroslav L. Lukyanov
Lavrentyev Institute of Hydrodynamics of Siberian Branch of RAS, 15 Lavrentyev pr., Novosibirsk, 630090, Russia
lukyanov@hydro.nsc.ru

ABSTRACT. Joint theoretical and experimental investigations have allowed to realize an approach with use of mathematical and physical modeling of processes of a shock wave loading of powder materials.
In order to gain a better insight into the effect of loading conditions and, in particular, to study the effect of detonation velocity, explosive thickness, and explosion pressure on the properties of the final sample, we numerically solved the problem about powder compaction in the axisymmetric case.
The performed analysis shows that an increase in the decay time of the pressure applied to the sample due to an increase of the explosive thickness or the external loading causes no shrinkage of the destructed region at a fixed propagation velocity of the detonation wave. Simultaneously, a decrease in the propagation velocity of the detonation wave results in an appreciable shrinkage of this region.

KEYWORDS. Shock waves; Fracture; Powder.

INTRODUCTION

Methods of explosive loading of powder materials in conservation ampoules are applied in order to obtain new materials including composite ones with the unique physical and mechanical properties. In addition, these methods can be used to study phase transitions occurring in materials at high pressures and temperatures taking place behind shock waves, as well as for the synthesis of metastable phases.
In recent decades, significant development has been achieved in such a scientific and technical branch of materials science as powder metallurgy. This term is currently understood a whole complex of problems connected with the design of materials and products from metal and nonmetal powders. Interest in these problems is quite understandable since the opportunity to create new classes of materials with unique and controllable properties which can not be obtained by ordinary metallurgy methods has arisen.
A special place in the powder metallurgy is occupied by explosive compaction of powder materials. It is easy to explain the strong interest in the explosive compaction. It consists in the fact that virtually all the methods of composite materials' production from powder mixtures lead to a change in initial material properties due to high temperatures and relatively long duration of the process.

Since the powders being in the form of granules, fibers, needles and ribbons, possessing the necessary properties in the initial state, can not be used directly to produce semi-finished products or components, the methods of compaction of these materials perform two tasks at once. On the one hand the compaction changes the shape and size of the powders, and on the other hand it produces the material itself. From this point of view, the short exposure to high temperatures and pressures during explosive compaction allows, in general, to keep the original structure and properties of the components. At the same time, varying of the intensity and time exposure to high pressure and temperature in shock compression allows to modify, if necessary, the structure and properties of the compacts a controlled manner.

The loading of the powder materials in the conservation ampoules can be carried out by means of both plane and oblique shock waves. Each of the methods has its pros and cons. The explosive loading by oblique shock wave is characterized by high values of shear strain, in comparison with the plane impact, which leads to stronger bonds between the compacted particles. In addition, this scheme allows to obtain the compacts not only in the form of plates, but pipes, rods, cones, etc as well. One can also get the compacts of large sizes. The loading by plane shock waves allow to vary the pressure and temperature behind the shock front in a wider range and to reach much higher values of these parameters. At the same time, the method is more material-consuming and has limitations on the size of the loaded samples.

Investigation into the interaction between oblique shock waves in porous materials and powders is a topical problem in optimization of loading conditions for obtaining, from a given sample, a compacted material with spatially uniform physical and mechanical properties. In compacting a powder in the cylindrical scheme, an irregular interaction between shock waves occurs. The compacted powder displays substantial non-uniformity in particle displacements, resulting in inhomogeneity of powder characteristics and, in some cases, even in material failure.

In compacting porous material and powders, the strong bonding between particles is achieved through the combined pressure-shear loading. During the compacting, a substantial energy is released at the interfaces between powder particles, resulting in surface cleaning and material melting in narrow interfacial regions. As a result, pore collapsing, giving rise to strong bonding between particles, occurs. Below, this phenomenon is termed compaction.

V.F. Nesterenko proposed the following criterion for the formation of a strong compact:

$$P > 2H_V \tag{1}$$

where, according to [1], $H_V \approx 3Y_s$. Following [1], we can write criterion (1), deduced from experimental data, as

$$P > 6Y_s \tag{2}$$

In turn, R. Prummer [2] uses the following condition for obtaining a uniform, in its physical properties, cylindrical compact with no Mach reflection induced singularities at its center: $P \approx H_V$, where P is the detonation pressure. Comparing condition (1) with the condition $P \approx H_V$, Nesterenko [1] arrives at a conclusion that it is impossible in principle, without a central rod, to obtain a spatially uniform compact in the cylindrical loading scheme since the shock pressure required for obtaining a dense compact (2) will always lead to Mach reflection at the center of the sample.

Another important problem is preservation of the finish compact after loading. With the arrival of unloading waves, there arises a tensile stress that results in partial or complete destruction of the sample. We assume that the sample undergoes mechanical failure if the maximum tensile stress σ_{max} reaches a certain critical value σ_*. In line with the adopted hypothesis, the following condition for the sample failure should be assumed:

$$\sigma_{max} > \sigma_* \tag{3}$$

where σ_{max} is the highest stress among the principal stresses for the strained state under study and σ_* is the critical stress.

In the present work, the critical stress σ_* is estimated as

$$\sigma_* = (2/3)Y_s ln(1/m_1)$$

where m_1 is the residual porosity. Taking the finish-compact density to equal 99%, we obtain $m_1 = 0.01$ and $\sigma_* \approx 3Y_s$. For the principal stresses, we have:

$$\sigma_1 = \frac{\sigma_{xx} + \sigma_{yy}}{2} + \frac{1}{2}\sqrt{(\sigma_{xx} - \sigma_{yy})^2 + 4\sigma_{xy}^2}$$

$$\sigma_2 = \frac{\sigma_{xx} + \sigma_{yy}}{2} - \frac{1}{2}\sqrt{(\sigma_{xx} - \sigma_{yy})^2 + 4\sigma_{xy}^2}$$

$$\sigma_3 = \sigma_{\theta\theta}$$

EXPERIMENTAL STUDY OF THE COMPACT STRUCTURE

Experiments on the explosive compaction have been conducted by a cylindrical scheme without a central rod. The powder has consisted of particles of nearly spherical shape and with size of 145-310 μm (Fig. 1). Bulk density of the powder has been in all experiments for copper equal to -5.0 ± 0.05 g/cm^3, for aluminum -1.4 g/cm^3. The experimental arrangement is shown in Fig. 2.

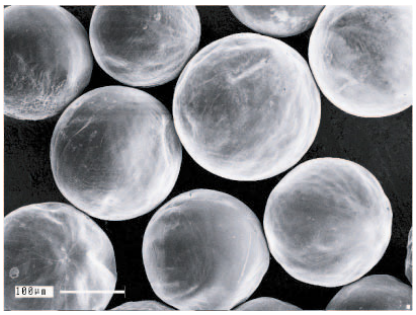

Figure1: Initial cooper powder.

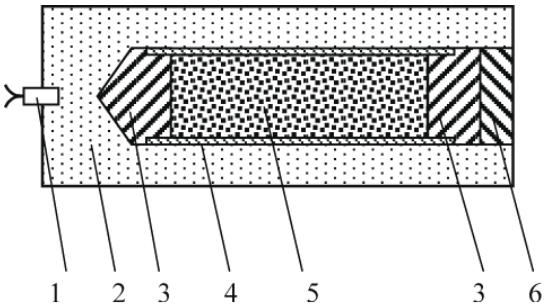

Figure 2: Scheme of explosive compaction: 1 – detonator, 2 – explosive charge, 3 – steel plugs, 4 – container (steel tube 12 mm in diameter), 5 – copper powder, 6 – momentum trap.

Explosive compaction occurs under the action of the detonation products of the contact explosive charges. For varying of the detonation velocity the charges were made from ammonite, RDX and mixture of ammonite with RDX in different proportions. The detonation velocity (D) was measured by electrical contact technique, and ranged from 3.19 to 5.26 km/s. Container wall was thin compared to the thickness of explosive layer and diameter of the powder sample. Structure of compacts cross-sections were studied using an optical microscope NEOPHOT.
In Fig. 3 the structures of the cross sections near the axis of the samples is shown for three different values of detonation velocity (3.19, 3.95 and 5.26 km/s) and at the same thickness of explosive charge – 5 mm.

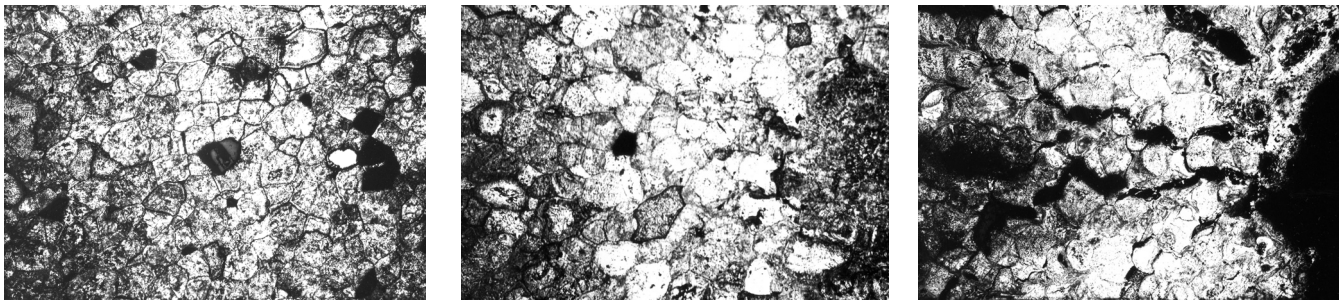

(a) (b) (c)

Figure 3: The structures of the cross sections of the samples for three different values of D and at the same thickness of explosive charge – 5 mm: a) D=3.19 km/s; b) D=3.95 km/s; c) D=5.26 km/s.

It can be noted that with the increase of the detonation velocity, and hence the shock pressure, a compacts structures change. At minimum value of D compact is homogeneous. Then, in the center due to the irregular reflection of the converging shock wave a zone of melt appear. And at D=5.26 km/s in the compact the radial cracks arise. A further increase in D can lead to the destruction of the container. To investigate the effect of the thickness of the explosive charge on the crack formation, an experiment was conducted in which the thickness of the charge was increased to 10 mm, and the detonation velocity was 5.17 km/s. The structure of this compact is shown in Fig. 4.

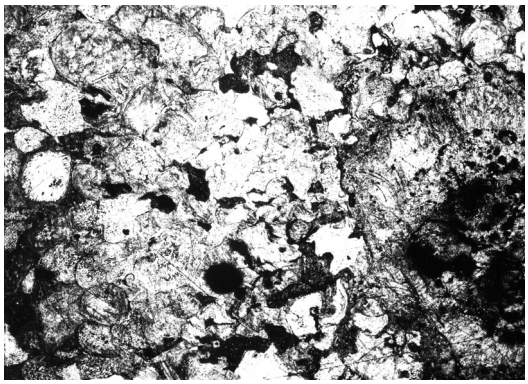

Figure 4: The structures of the cross section of the sample loaded at D=5.12 km/s and thickness of the explosive charge 10 mm.

Comparing structures from Fig. 3a and Fig. 4, it is visible, that in spite of approximately identical detonation regimes, in a compact in Fig. 4 cracks are absent.

NUMERICAL SIMULATION OF THE EXPLOSIVE LOADING

In order to gain a better insight into the effect of loading conditions and, in particular, to study the effect of detonation velocity, explosive thickness, and explosion pressure on the properties of the final sample, we numerically solved the problem about powder compaction in the axisymmetric case using conditions of above mentioned experiments.
The problem statement according to experimental scheme is clear from Fig. 5.

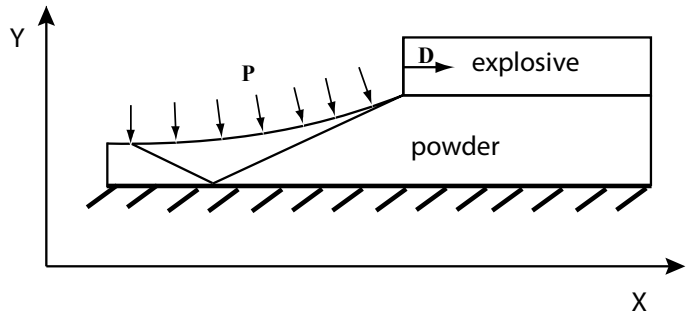

Figure 5: The problem statement.

We solved the full system of equations governing the deformation of a porous elastic-plastic material [3]. The action of the explosion products on the sample was modeled with a pressure applied to the upper border of the sample. The pressure was calculated by the approximation formula for the pressure upon unrestricted dispersion of detonation products [4]:

$$P(t) = P_H \exp(-(t - x/D)/t_1), \quad t_1 = \sqrt{\frac{3(\gamma_e + 1)}{4(\gamma_e - 1)}} \frac{\delta_e}{D}$$

Here δ_e is the explosive thickness and γ_e is the adiabatic exponent of the detonation products. Since the problem is symmetric, a half of the experimental assembly is considered.
The symmetry axis is the axis of the container with the powder. On the symmetry axis rigid wall boundary conditions are set. The right boundary is considered to be free of stress, and at the left boundary condition of a rigid wall is put. Computation of the contact boundaries is performed by using a symmetric algorithm [5]. The calculations are carried out by the M.L. Wilkins scheme [6]. The shock wave propagates from left to right. Geometric dimensions and values of the physical parameters correspond to the experimental data mentioned above. In this paper a few-parametric equation of state is applied [7], which has allowed to simulate shock-wave processes with a minimal number of physical parameters as the initial data.

$$E = E_x + c_{v,l}T + \frac{1}{2}c_{v,e0}T^2\left(\frac{V}{V_0}\right)^{2/3}$$

$$P = -\left(\frac{dE_x}{dV}\right) + \frac{\gamma_l c_{v,l}T}{V} + \frac{1}{3}\frac{c_{v,e0}T^2}{V}\left(\frac{V}{V_0}\right)^{2/3}$$

or, in terms of free energy

$$F(V,T) = E_x(V) + c_{v,l}T\ln\left(\frac{\theta(V)}{T}\right) - \frac{1}{2}c_{v,e0}T^2\left(\frac{V}{V_0}\right)^{2/3}$$

where P_x and E_x - pressure and specific internal energy of the zero isotherm, T - temperature, $c_v = c_{v,l} + c_{v,e}$ - heat capacity at constant volume, $\theta(V)$ - the Debye temperature.

The equation of state presented here is based on the dependence of the Gruneisen coefficient γ on the volume [8]

$$\gamma(V) = 2/3 - 2/(1 - aV_0/V)$$

$$a = 1 + 2/(\gamma_s - 2\beta) + 2P_{t,0}/K_s$$

where $\gamma_s = \beta K_s V_0 / c_v$, K_s - adiabatic bulk modulus, β -oefficient of thermal expansion, $P_{t,0}$ - heat pressure under the normal conditions.

To find the elastic curves a generalized model describing the Gruneisen coefficient $\gamma(V)$ is used:

$$\gamma(V) = -\left(\frac{2-t}{3}\right) - \frac{V}{2}\left[\frac{d^2\left(P_x V^{2t/3}\right)/dV^2}{d\left(P_x V^{2t/3}\right)/dV}\right]$$

at $t = 0$ the equation corresponds to the Landau and Slater theory [8, 9], at $t = 1$ it corresponds to the Dugdale and MacDonald hypothesis [10], and at $t = 2$ to the theory of free volume [11].

In the physics of shock waves a method of calculating the pressure at the Hugoniot adiabat of the porous material by pressure on the "reference" Hugoniot adiabat of monolithic material [12] is known:

$$P_{h,p} = \frac{P_h\left(1 + 0.5\gamma(V)\left(1 - V_0/V\right)\right)}{1 + 0.5\gamma(V)\left(1 - V_{00}/V\right)}$$

Here V is the specific volume of the Hugoniot adiabats, V_0 and V_{00} are specific volumes of monolithic and porous materials , respectively, at the normal initial conditions.

CALCULATION RESULTS AND DISCUSSION

Fig. 6, a and b shows the pressure isolines for the cases of planar and cylindrical symmetries with identical loading conditions. It is seen from Fig. 6 that, in the planar statement of the problem, a regular reflection of the incident shock wave takes place. In the case of the cylindrical loading scheme, the incident shock waves bends as it approaches the cylinder axis, and, under the same loading conditions, an irregular reflection occurs.

Fig. 7a shows the pressure profile near the symmetry axis for the cases of planar and cylindrical statements (solid and dashed curves, respectively). An appreciable pressure rise near the symmetry axis is observed in the case of cylindrical configuration compared to the planar problem due to the divergence of the shock wave to the axis.

Fig. 7b shows the profile of the longitudinal velocity u_x across the sample under loading behind the shock front. The solid and dashed lines show the data for the planar and axisymmetric problem statements, respectively. It is clearly seen that the velocity in the cylindrical case is much greater than in the planar variant.

As stated above, an important problem is preservation of finish compact, i.e., preventing its mechanical failure and obtaining a sample with uniform properties. Using criterion (3), we can find the interface between the solid and distructed materials. The regions of the compacted and porous materials for various explosive thicknesses for the external pressures

$P = 0.05$ Mbar and $P = 0.075$ Mbar are shown in Fig. 8, a and b, respectively. In these calculations, the detonation velocity was $D = 5$ km/s. The solid, dashed, and dot-and-dash lines outline the destruction regions for the explosive thicknesses $\delta_e = 2$ cm, $\delta_e = 3$ cm, and $\delta_e = 5$ cm, respectively. Region 1 is the compacted region, and Region 2, the destruction region. An analysis of these graphs shows that an increase in the explosive thickness and, hence, an increase of the loading decay time does not cause any substantial shrinkage of the destruction region.

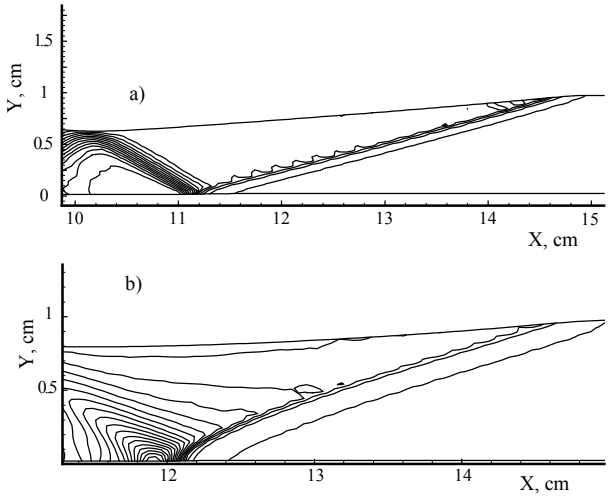

Figure 6: Pressure isolines: a) planar geometry; b) cylindrical configuration.

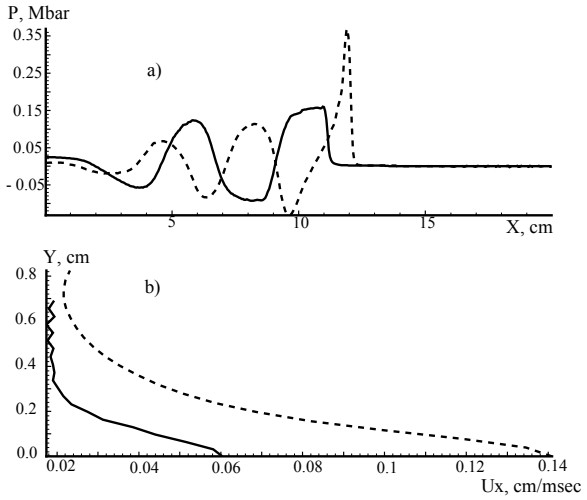

Figure 7: Pressure profile (a) and longitudinal-velocity profile $u_x(y)$ (b) for the planar and cylindrical geometries (solid and dashed lines, respectively).

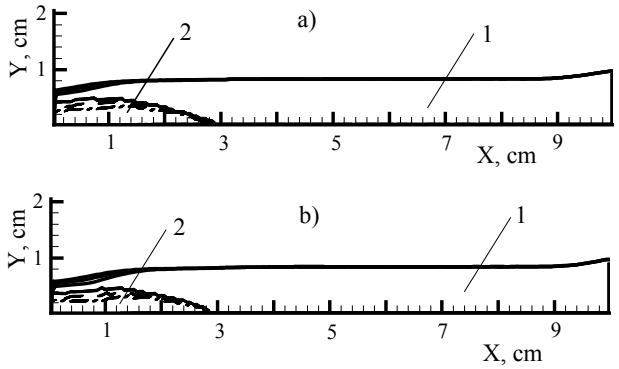

Figure 8: Compacted and destruction regions for various explosive thicknesses under external pressures $P = 0.05$ Mbar (a) and $P = 0.075$ Mbar (b). The detonation velocity is $D = 5$ km/s. The solid, dashed, and dot-and-dash lines refer to the explosive thicknesses $\delta_e = 2$ cm, $\delta_e = 3$ cm, and $\delta_e = 5$ cm, respectively. The compacted and destruction regions are indicated by 1 and 2.

It should be emphasized that this conclusion is valid for criterion (3). In derivation of (3), it was implicitly assumed that the interfacial melted zones are narrow, and the material in these zone rapidly solidifies as the particles in the bulk of the material undergo cooling. If this condition does not hold, then there can be a situation in which, by the moment of arrival of the unloading wave, the material in the interfacial zones still remains melted, which will prevent compaction. In this case, the dimensions of the destruction region will be dependent on the loading decay time and on the explosive thickness. The explosive thickness should be large enough to prevent shock wave damping in the powder and to enable complete pore collapsing in the sample. Fig. 9, a and b shows the density isolines for the explosive thickness $\delta_e = 0.5$ cm and the external pressure $P = 0.05$ Mbar. Parts a and b of Fig. 9 depict the data for the axisymmetric and planar problem statements. Damping of the incident shock wave is evident from the figure. This results in incomplete powder compaction; the latter is clear from Fig. 10, which shows the distribution of porosity m_1 across the sample. The solid and dashed lines in this figure correspond to the planar case and to the cylindrical configuration, respectively. An analysis of

these graphs shows that, in the axisymmetric case, due to the wave divergence to the axis, the pores undergo collapsing in a larger volume than in the planar variant.

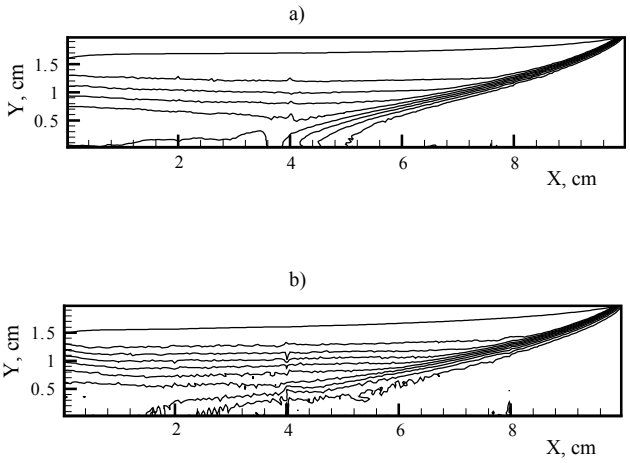

Figure 9: Density isolines for $\delta_e = 0.5$ cm: a) cylindrical configuration; b) planar statement.

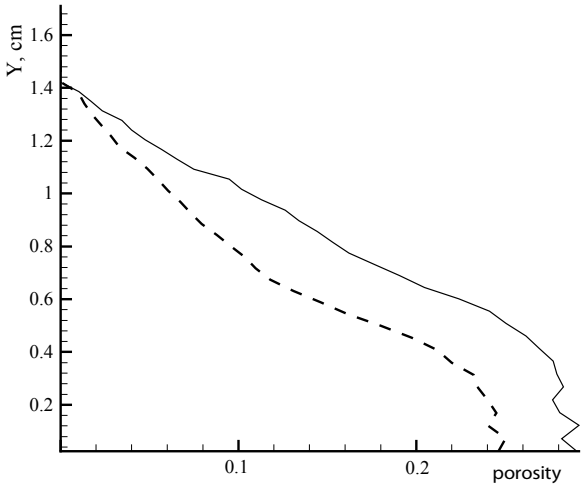

Figure 10: Porosity m_1 for $\delta_e = 0.5$ cm: solid line is planar statement; dashed line is cylindrical configuration.

A twofold increase in the explosive thickness makes the decay of the incidence shock wave less intensive. The density isolines for the explosive thickness $\delta_e = 1$ cm and the external pressure $P = 0.05$ Mbar are shown in Fig. 11, a and b. Parts a and b of this figure shows the calculation data for the axisymmetric and planar statements, respectively. It is clearly seen that in the case of cylindrical symmetry the shock wave bends near the axis, giving rise to an irregular reflection; in the planar configuration, a regular interaction occurs. Fig. 12, which depicts the distribution of porosity m_1 across the sample compacted in the cylindrical geometry (the dashed line in Fig. 12), is indicative of complete collapsing of pores over the entire thickness of the sample. In the planar case (see the dashed line in Fig. 12), the complete collapsing of pores is observed approximately over half the thickness of the sample, and the porosity near the symmetry axis is close to the initial one, m_1^0.

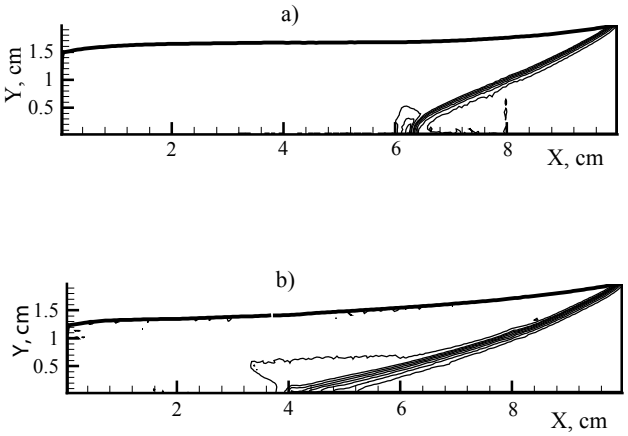

Figure 11: Density isolines for $\delta_e = 1$ cm: a) cylindrical configuration; b) planar configuration.

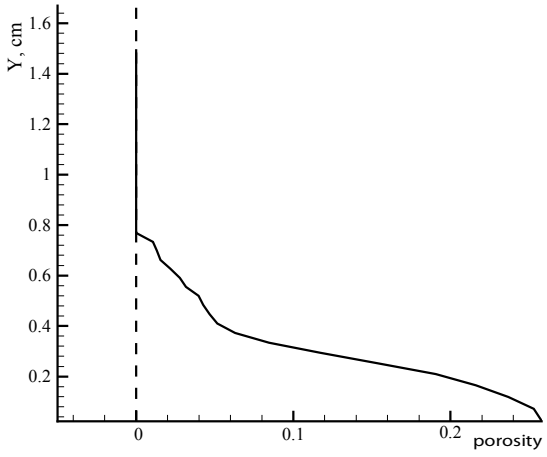

Figure 12: Porosity m_1 for $\delta_e = 1$ cm: solid line - planar statement; dashed line - cylindrical configuration.

The density isolines for the explosive thickness $\delta_e = 2$ cm are shown in Fig. 13, a and b. The external pressure was taken to be $P = 0.05$ Mbar. Parts a and b of this figure show the calculation data for the axisymmetric and planar statements. In the cylindrical case (see Fig. 13, a), an irregular reflection is clearly observed, whereas in the planar case (see Fig. 13, b) the

incident shock wave interacts with the rigid wall in the regular manner. In both cases, all pores in the sample collapse completely.

Further calculations were carried out for the explosive thicknesses $\delta_e = 2$ cm, $\delta_e = 3$ cm and $\delta_e = 5$ cm.

Fig. 14, a and b illustrates the effect of applied pressure on the thickness of the destruction region. In the calculations, the external pressures were $P = 0.05$ Mbar and $P = 0.075$ Mbar, respectively, and the detonation velocity in both cases was $D = 7$ km/s. The solid and dashed lines show the data for the explosive thicknesses $\delta_e = 3$ cm and $\delta_e = 5$ cm. Regions 1 and 2 are the compacted and destruction regions. As is seen from the figure, an increase in the external load causes no shrinkage of the destruction zone. Thus, it can be concluded that an increase in the decay time of the pressure applied to the sample resulting from an increase in the explosive thickness or in the value of the external load does not make the destruction zone shrink at a fixed propagation velocity of the detonation wave.

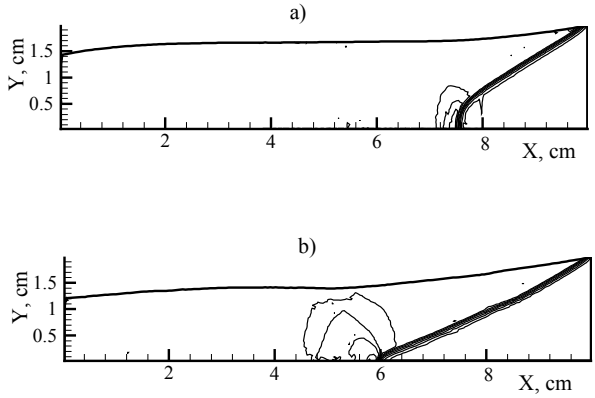

Figure 13: Density isolines for $\delta_e = 2$ cm: a) cylindrical configuration; b) planar statement.

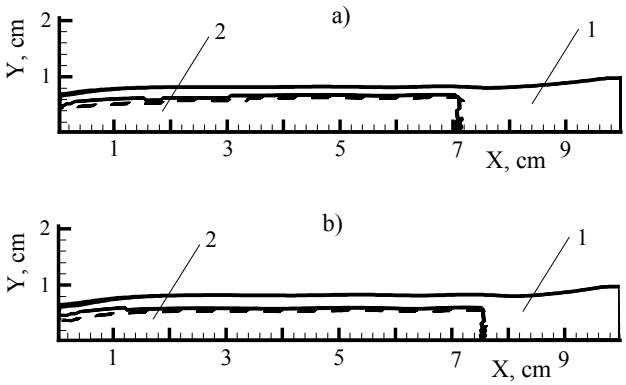

Figure 14: Compacted and destructed regions for two values of external pressure, $P = 0.05$ Mbar (a) and $P = 0.075$ Mbar (b). The detonation velocity is $D = 7$ km/s. The solid and dashed lines show the calculation data for the explosive thicknesses $\delta_e = 3$ cm and $\delta_e = 5$ cm.

As shown by above mentioned experiments an increase of the velocity of the detonation wave results in a considerable shrinkage of the destruction region. Fig. 15 show the compacted (1) and destructed (2) regions in the sample for the detonation velocities $D = 3$, 5, 7 km/s at a fixed explosive thickness $\delta_e = 5$ cm and at a fixed external pressure $P = 0.05$ Mbar. The solid, dashed, and dot-and-dash lines show the calculation data for the detonation velocities $D = 3$ km/s, $D = 5$ km/s, and $D = 7$ km/s.

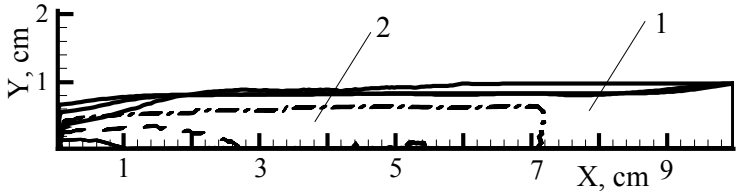

Figure 15: Compacted (1) and destructed (2) regions for three values of the detonation velocity. The solid, dashed, and dot-and-dash lines refer to $D = 3$ km/s, $D = 5$ km/s, and $D = 7$ km/s.

The isolines of pressure for the indicated loading parameters are shown in Fig. 16, a-c. It is seen from the graphs that, as the shock-wave propagation velocity increases, the angle of incidence decreases and the reflected shock causes material destruction (see Fig. 16, b and c). As the velocity of the detonation wave increases, the angle of incidence of the incident shock wave increases and, as it is seen from Fig. 16, a, at the velocity $D = 3$ km/s the incident shock wave is close to the normal shock and the amplitude of the reflection wave is almost zero.

Since in the case of cylindrical symmetry no regular reflection occurs, the final sample turns out to be inhomogeneous. Fig. 17 shows the distribution of the longitudinal velocity u_x (Fig. 17, a) and temperature T (fig. 16, b) across the sample

in the compacted region for the detonation velocity $D = 5$ km/s. An appreciable non-uniformity in the distribution of parameters is evident from the graphs. Near the axis, both the velocity and temperature are greater than in the region some distance away from it.

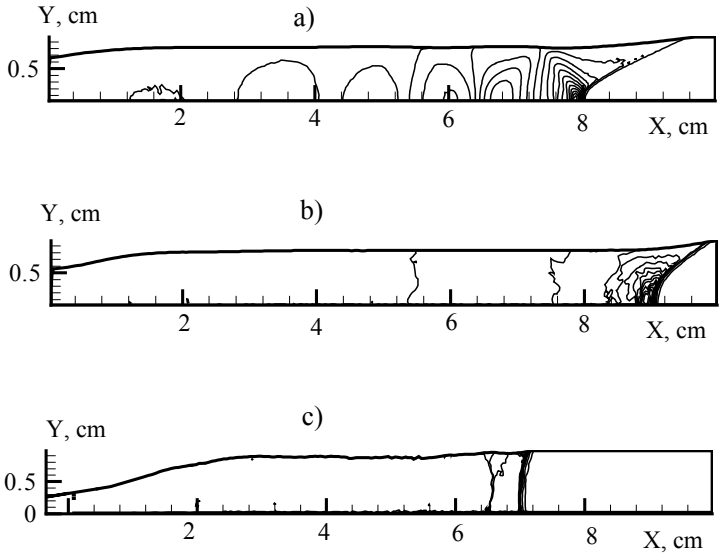

Figure 16: Pressure isolines: a) detonation velocity $D = 7$ km/s; b) detonation velocity $D = 5$ km/s; c) detonation velocity $D = 3$ km/s.

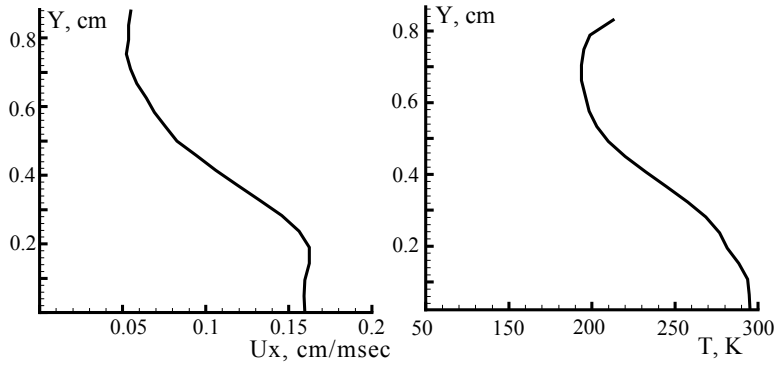

Figure 17: Predicted distributions of the longitudinal velocity u_x (a) and temperature T (b) across the compacted region of the sample for the detonation velocity $D = 5$ km/s.

Parts a and b of Fig. 18 show the distributions of the longitudinal velocity u_x and temperature T across the compacted region of the sample predicted for the detonation velocity $D = 3$ km/s. Here, under identical loading parameters, the final sample is quire homogeneous.

As a result, it becomes possible to obtain spatially uniform compacted samples. The necessary condition for this is sufficiently low detonation velocity, equal, for the aluminum powder, to 0.3 cm/$m$sec. Here, on the one hand, compaction condition (1) should be fulfilled and, on the other, the uniformity of loading parameters across the sample should be ensured.

Thus, the compaction of powders with low detonation velocities results in a considerable shrinkage of destruction zones in finish samples and in spatial uniformity of material parameters in their compacted parts.

The performed analysis shows that an increase in the decay time of the pressure applied to the sample due to an increase of the explosive thickness or the external loading causes no shrinkage of the destructed region at a fixed propagation velocity of the detonation wave. Simultaneously, a decrease in the propagation velocity of the detonation wave results in an appreciable shrinkage of this region.

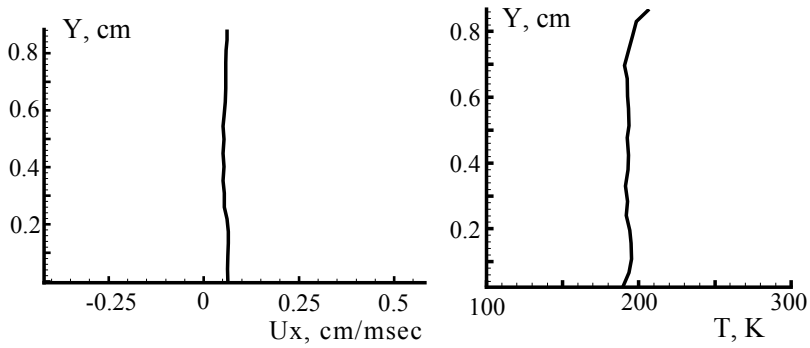

Figure 18: Distributions of the longitudinal velocity u_x (a) and temperature T (b) across the compacted region of the sample for the detonation velocity $D = 3$ km/s.

CONCLUSIONS

Joint theoretical and experimental studies have allowed to implement an approach that uses mathematical and physical simulation of shock-wave loading of powdered materials. A numerical simulation of shock wave propagation and deformation of the experimental assembly has been performed.

The temperature distributions over the sample thickness in the compacted zone for several values of detonation velocity show that at higher speeds there is considerable heterogeneity in the temperature distribution over the sample thickness. Near the axis of the sample the temperature has a higher value than in distance from it.

An increase in the pressure decay time due to increasing either the explosive thickness or the external loading intensity causes no shrinkage of the destruction zone at a fixed propagation velocity of the detonation wave. Compaction of powders with low detonation velocities results in a considerable shrinkage of destruction zones in finish samples and in a uniform distribution of material parameters in the compacted region.

REFERENCES

[1] V.F. Nesterenko, High-rate deformation of heterogeneous materials, Nauka, Novosibirsk (1992) (in Russian).
[2] R. Prümmer, Powder compaction. Explosive welding, forming and compaction, London; New York: Appl. Sci. Publ., (1983).
[3] S.P. Kiselev, V.M. Fomin, J. of Applied Mechanics and Technical Physics. 34(6) (1993) 861.
[4] V.V. Pai, G.E. Kuz'min, I.V. Yakovlev, Combustion, Explosion, and Shock Waves, 31(3) (1995) 124.
[5] A.I. Gulidov, I.I. Shabalin, Numerical Realization of the Boundary Conditions in Dynamic Contact Problems, Preprint ITAM SB RAS, Novosibirsk (1987) (in Russian).
[6] M. L. Wilkins, Computer simulation of dynamic phenomena, Springer, Berlin, Heidelberg (1999).
[7] E. I. Kraus, Vestnik NGU. Fizika, 2(2) (2007) 65 (in Russian).
[8] C. Slater, Introduction in the chemical physics.– New-York-London: McGraw Book company, Inc., (1935) 239.
[9] L. D. Landau, K.P. Stanyukovich, Dokl. Akad. Nauk SSSR, 46 (1945) 399 (in Russian).
[10] J. S. Dugdale, D. McDonald, Phys. Rev., 89 (1953) 832.
[11] V.Ya. Vaschenko, V.N. Zubarev, Sov. Phys. Solid State, 5 (1963) 653.
[12] R. G. McQueen, S. P. Marsh, J. W. Taylor, J. N. Fritz, High-Velocity Impact Phenomena, ed. by R. Kinslow, New York: Academic Press (1970) 293.

Temporal peculiarities of brittle fracture of rocks and concrete

Y. Petrov, I. Smirnov, A. Evstifeev, N. Selyutina
St. Petersburg State University, Universitetsky prospekt, 28, Peterhof, 198504, St. Petersburg (Russian Federation)
yp@YP1004.spb.edu; ivansmirnov@math.spbu.ru

ABSTRACT. When we want to compare the strength of two materials, we compare the table values of quasi-static strength. However results of some experiments show that the strength ratio of the materials can change with increase in rate of loading. Such "substitution effect" of material strength at different strain rates is studied in this paper. It is shown that one material can have a lower dynamic strength for a higher static strength compared to the other material. Tests of two different materials, tests of mortar and concrete, and tests of concrete with different water content are considered. It is shown that load-carrying capacity of materials and the substitution effect of material strength in a wide range of loading rates can be predicted by the incubation time criterion.

KEYWORDS. Static strength; Dynamic strength; Incubation time; Substitution effect.

INTRODUCTION

In selecting a material of construction an engineer is usually guided by the values of mechanical parameters obtained in quasi-static tests. A construction material is selected on the basis of its ability to withstand a certain stress (as one of the defining parameters). There is a set of test standards governing determination of the ultimate strength of a material under quasi-static tension, compression, bending, etc. However tests under dynamic loading conditions show essential differences of dynamic strength characteristics in comparison with those of quasi-static tests.

These differences relate to the dependence of the mechanical characteristics on the history (duration, intensity, shape of the stress pulse, etc.) and method of loading [1]. A critical value can be considered as a material constant only under quasi-static loading conditions. Under dynamic loading, the critical properties are characterized by very strong instabilities and can vary by several orders of magnitude. As a result, the dynamic system behaviour often appears unpredictable.

Importance of studying rocks and concrete dynamic strength is not in doubt. These materials are highly suitable materials for building structures in the energy sector, for instance solar energy storage water tanks, nuclear containment vessels, etc. However, such civil and military infrastructures (e.g. buildings, barracks, bridges, tunnels, containment structures for hazardous, toxic and inflammable materials, etc) are susceptible to catastrophic failure under intense sudden overloading (e.g. due to blasts, explosions) for which they are not designed. A correct and rational analysis of dynamically loaded structures requires an understanding of the behaviour of the mechanical properties of materials at high strain rates. Therefore a study of the behaviour of rocks and concrete at high rates of deformation and fracture is necessary.

Dependence of rocks on the extraction quarry, as well as numerous admixtures of concrete makes the research of strength characteristics a complex task. Moreover, various heterogeneity and impurity content can lead to various dynamic effects of fracture.

One of such effects is the change of the dominant strength between the two materials. A material, which has a lower strength compared to another material in quasi-static tests, can have greater strength under dynamic loading.

In this paper we consider such "substitution effect" of strength of two materials in three cases: tests of two different materials; tests of mortar and concrete; tests of concrete under different environmental conditions. As experimental data we used the results of [2-5]. The theoretical analysis is based on the criterion of the incubation time of fracture [1, 6, 7]. This criterion provides correct transition between quasi-static and dynamic loadings. Introduction of the additional measured characteristic of strength (the incubation time) to the already known "quasi-static" parameter of strength (limit stress) allows us to build dependences of maximal fracture stress on a loading (deformation) rate without numerous experiments for any type and character of loading.

THE INCUBATION TIME CRITERION

The criterion of fracture based on the concept of incubation time, proposed in [6-8], makes it possible to predict the unstable behaviour of the dynamic-strength characteristics observed in experiments on the dynamic fracture of solids. The fracture criterion can be written in the following general form:

$$\frac{1}{\tau}\cdot\int_{t-\tau}^{t}\left(\frac{F(t')}{F_c}\right)^{\alpha}dt' \le 1 \qquad (1)$$

Here, $F(t)$ is the intensity of the local force field causing the fracture (or structural transformation) of the medium, F_c is the static limit of the local force field, and τ is the incubation time associated with the dynamics of the relaxation processes preceding the fracture. It actually characterizes *the strain (stress) rate sensitivity* of the material. The fracture time t^* is defined as the time at which equality sign is reached in Eq. (1). The parameter α characterizes *the sensitivity of the material to the intensity (amplitude)* of the force field causing the fracture (or structural transformation). Often, $a = 1$ gives a good agreement with test data.

One of the possible means of interpreting and determining the parameter τ is proposed here on the example of the mechanical rupture of a material. Let us assume that a standard test specimen made of the material in question is subjected to tension and is broken into two parts under a stress P arising at a certain time $t = 0$: $F(t) = PH(t)$, where $H(t)$ is the Heaviside step function. In the case of quasi-brittle fracture, the material would unload, and the local stress at the break point would decrease rapidly (*but not instantaneously*) from P to 0. In this case, a corresponding unloading wave is generated which propagates over the sample and can be detected by standard (e.g., inter-ferometry) methods. The stress variation at the break point can be conditionally represented by the relation $\sigma(t) = P - Pf(t)$, where $f(t)$ varies from 0 to 1 (Fig. 1) within a certain time interval T.

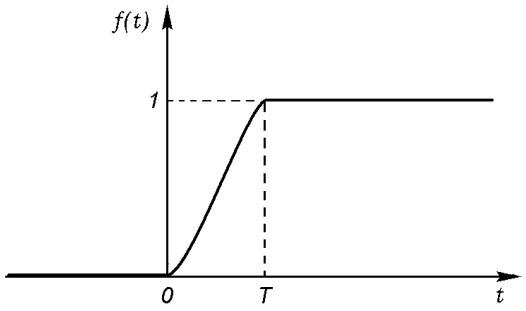

Figure 1: Schematic of fracture kinetics at the place of rupture.

The case $f(t) = H(t)$ corresponds to the classical strength theory. In other words, according to the classical approach, rupture occurs instantaneously ($T = 0$). In practice, the rupture of a material (sample) is a process in time, and the function $f(t)$ describes the *micro- scale level* kinetics of the transition from a conditionally defect-free state ($f(0) = 0$) to a completely broken state at the given point $f(t^*) = 1$ that can be associated with the macro-fracture event. On the other hand, application of the fracture criterion (1) to *macro-level* situation ($F(t) = PH(t)$), gives the time to fracture $t^* = T = \tau$ at $P = F_c$.

In other words, the incubation time introduced above is equal to the duration of the fracture process after the stress in the material has reached the static strength *on the given scale level* [9]. This duration can be measured experimentally by statically fracturing the samples and controlling the rupture process by different possible methods, e.g., by measuring the time of

the increase in pressure at the unloading wave front based on the recorded velocity profile of points (by interferometry) on the sample boundary. Below, we apply the general fracture criterion Eq. (1) to three problems.

CALCULATION PROCEDURE

Let us consider application of the criterion (1) for calculation of carrying capacity of a material for different strain rate. Note that we understand the carrying capacity as the maximum stress that the material can withstand without fracture. However according to the criterion of incubatory time, dynamic strength is characterized by the incubatory time, but not the maximum stress.

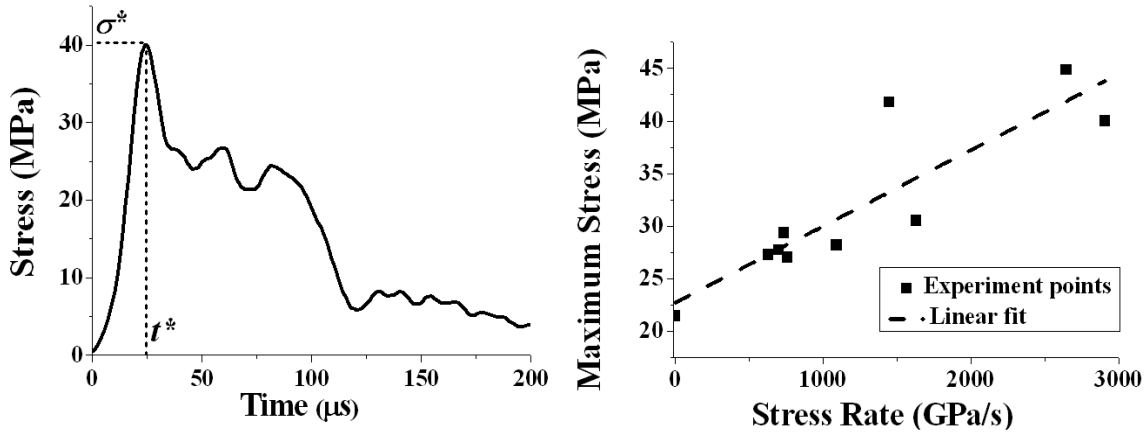

Figure 2: Test results of CARDIFRC in dynamic splitting [2]. a) Typical stress diagram (σ^* is the maximum stress; t^* is the fracture time). b) Maximum stress vs stress rate.

For simplicity of understanding, we consider simple test methods, such as the split Hopkinson bar test (the Kolsky method) [10-12] and the spall test [13]. Such tests allow to carry out calculations in one-dimensional statement. For example, Fig. 2 shows the results of dynamic splitting of CARDIFRC (fibre reinforced concrete) [14], which were carried out in the Laboratory of Material Mechanics at the Nizhny Novgorod State University [2].

The initial part of the loading branch (Fig. 2a) corresponds to the growth of the stress and strain. After the stress in the specimen reaches a limiting value, the material begins to fail rapidly accompanied by the formation of micro and macro cracks leading to a significant reduction in the stress with increasing strain.

In spite of the scatter in the data, it is reasonable to conclude that the maximum stress increases with increasing stress rate. The observed time dependence of the maximum stress can be predicted on the basis of the incubation time criterion (1), which in this particular case of fracture takes the form:

$$\frac{1}{\tau}\int_{t-\tau}^{t}\sigma\,(t')\,dt' \le \sigma_c \qquad (2)$$

where $\sigma(t)$ is the time dependence of stress in point of fracture (the average stress in the specimen in case of the SHPB test); σ_c is static strength of the material for given type of loading; τ is the fracture incubation time of the material.

For the well-known formulae from the Strength of Materials we can get a fairly simple relation to calculate the rate dependence of strength. These formulae allow engineers to obtain the values of the material strength, for a given character of loading and specimen geometry, without resorting to lengthy and laborious calculations. In our case, a simple analytical rate dependence of the limit stress can be obtained in the following manner. According to Fig. 2a an increase in the tensile stress with strain rate can be assumed to be linear until it reaches the maximum value σ^*, so that

$$\sigma(t) = \dot{\sigma}\cdot t\ \cdot H(t) = E\cdot\ \dot{\varepsilon}\cdot\ t\ \cdot H(t) \qquad (3)$$

where $\dot{\sigma}$ and $\dot{\varepsilon}$ are the rates of growth of the stress and strain respectively, which we assume to be constant, E is the modulus of elasticity, and $H(t)$ is the Heaviside function. Stress rate determines as the ratio of the maximum stress to the fracture time. We substitute this function into the stress criterion Eq. (2) and find the value of the time to failure t^* (using the equality sign) and get

$$t^* = \begin{cases} \tau/2 + \sigma_c/\dot{\sigma}, & t^* \geq \tau \\ \sqrt{2\sigma_c \cdot \tau/\dot{\sigma}}, & t^* < \tau \end{cases}$$

which yields the following expression for the limiting stress:

$$\sigma^* = \sigma(t^*) = \begin{cases} \sigma_c + \dot{\sigma} \cdot \tau/2 & t^* \geq \tau \\ \sqrt{2\dot{\sigma} \cdot \sigma_c \cdot \tau} & t^* < \tau \end{cases} \quad (4)$$

The incubation time of fracture τ can be determined by a semi-empirical method. The semi-empirical method consists in fitting of the calculated dependence $\sigma^*(\dot{\sigma})$ to the experimental dependence $\sigma^*(\dot{\sigma})$ by means of τ variation. The different algorithms (Gauss-Newton method, the steepest descent method, etc.) can be used to adjust the parameter values in the iterative procedure. The standard way of finding the best fit is to choose the parameters that would minimize the deviations of the theoretical curve(s) from the experimental points. Thereby nonlinear fitting was made to estimate the incubation time values which best describe the data.

It is clear that the experimental values of the studied parameters can deviate from this simple dependence as a result of a scatter. Note that more complex schemes of loading (non-linear loading, three-dimensional problem, etc.) will lead to more complicated analytical expressions. It is more convenient to consider such problems numerically [15].

STRENGTH OF TWO DIFFERENT MATERIALS

In this part, we compare the strength of gabbro-diabase and fibre reinforced concrete (CARDIFRC). Gabbro-diabase is dense, solid, homogeneous rock, characterized by a low degree of resistance to abrasion, frost resistance, and durability. CARDIFRC [14] is an ultra high performance fibre reinforced cement based composite characterised by high compressive and flexural strengths and high toughness. The tests have been performed using the modification of Kolsky method for dynamic splitting (the Brazil test) [16]. Detailed schemes of tests and results were presented in [3] for gabbro-diabase and in [2] for CARDIFRC.

Fig. 3 summarizes the split tests of the fibre reinforced concrete and gabbro-diabase under quasi-static and high strain rates on a semi-logarithmic scale. The curves in Fig. 3 correspond to the calculation by Eq. (2) with the following parameter values: σ_c = 23 MPa and τ = 15 μs for concrete and σ_c = 18 MPa and τ = 70 μs for gabbro-diabase.

It is clear from the picture that carrying capacity of both materials increases with the growth of loading rate. However although CARDIFRC has a higher quasi-static split strength than that of gabbro-diabase, its dynamic carrying capacity in splitting is lower at high stress rates (>$10^{2.5}$).

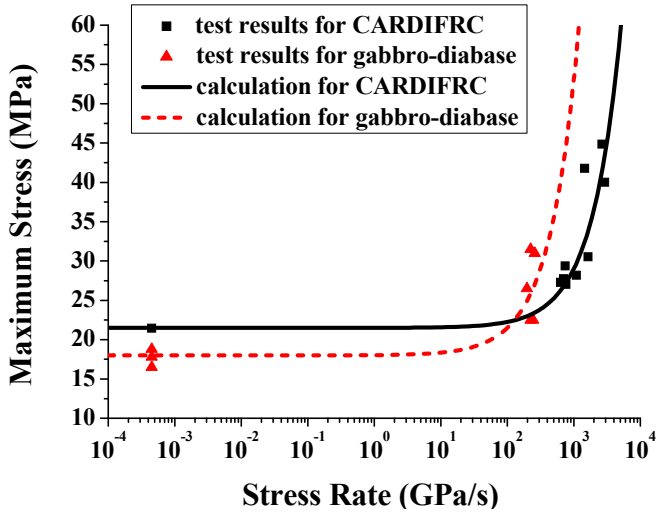

Figure 3: The split tests of CARDIFRC and gabbro-diabase; black squares are the experimental values for CARDIFRC [2]; black line is predictions of Eq. (2) for CARDIFRC (σ_c = 23 MPa and τ = 15 μs); red triangles are the experimental values for gabro-diabase [3]; and red dashed is predictions of Eq. (2) for gabbro-diabase (σ_c = 18 MPa and τ = 70 μs).

STRENGTH OF MORTAR AND CONCRETE

The experimental study of the behavior of concrete and mortar at high strain rates in compression were conducted in [4]. Application of techniques of the split Hopkinson bar (SHPB) and plate impact have allowed us to consider a range of loading rates of 10^2-10^4 s^{-1} with an amplitude of pulses up to 1.5 GPa. Both materials have the same processing conditions, and the pure mortar has the same composition as the mortar phase in the concrete. The parameters of the test materials are shown in Tab. 1. The quasi-static compressive strength was determined according to the standard ASTM C39-96. The tests by the Kolsky method were carried out only for mortar.
The results of these experiments are shown in Fig. 4. The curves correspond to the calculation of the maximum stress by the criterion (2). The value of the incubation time τ can be determined by Eq. (4) (see Table 1). We received the same incubation time for the mortar and concrete. However, despite the lower quasi-static strength compared with that of the mortar, the concrete can show greater strength under dynamic loading (at a given strain rate).

	ϱ, kg/m³	ν	E, GPa	σ_c^{comp}, MPa	τ, μs
Concrete	2100	0.2	20	46	6.5
Pure mortar	2600	0.29	45	30	6.5

Table 1: Parameters of concrete and mortar.

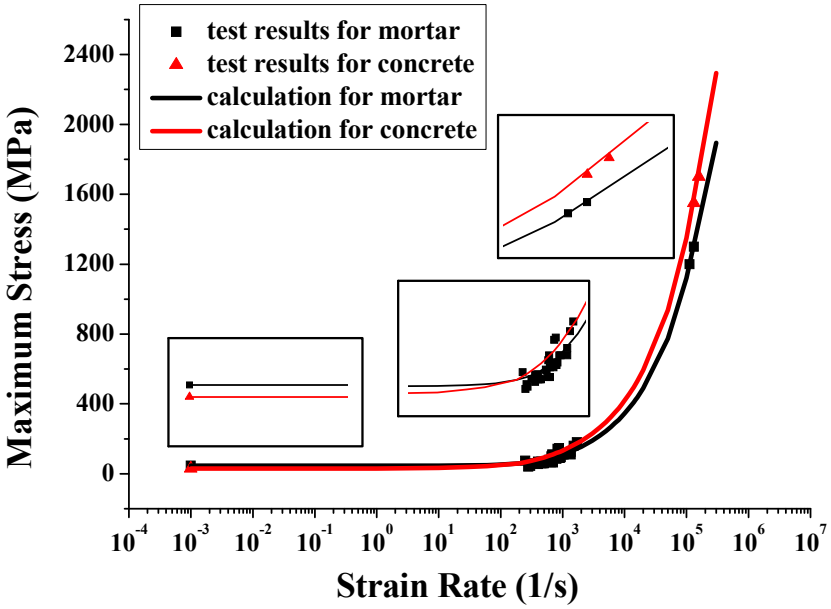

Figure 4: Dependence of limit compression stress on strain rate. Black squares are the experimental values for concrete [4]; black line is predictions of Eq. (2) for concrete; red triangles are the experimental values for mortar [4]; and red line is predictions of Eq. (2) for mortar.

The authors of the experiments [4] explain this effect by existence of hydrostatic pressure in a sample at high speeds of loading that leads to "compression" of microdefects and microcracks in material structure. As concrete can contain many defects (voids, cracks between the cement and the inclusion, etc.), its carrying capacity increases by limiting of the development of defects.
Nevertheless, this effect can be explained with a simple argument, without assumptions about the mechanisms of deformation and fracture. Since the load is linear (see Eq. 3), at high strain rates the limit stress will depend on the modulus of elasticity, that is, the quasi-static strength does not affect on the strength under dynamic loading. Thus, we can set the carrying capacity of concrete by the elasticity of fillers.

STRENGTH OF DRY AND SATURATED CONCRETE

In the paper [5] the influence of relative humidity of concrete subjected to a large range of stress rate was analyzed and discussed. The Hopkinson Bar Bundle (HBB) was realized to study the high loading rate tensile properties of plain concrete cubes. The experiments were carried out on concrete cured at three different curing conditions (drying at 50 °C; 20 °C - 50% RH; and saturated) and tested at three strain rates. The results showed that level of free water inside the concrete has an important influence on the carrying capacity of concrete.

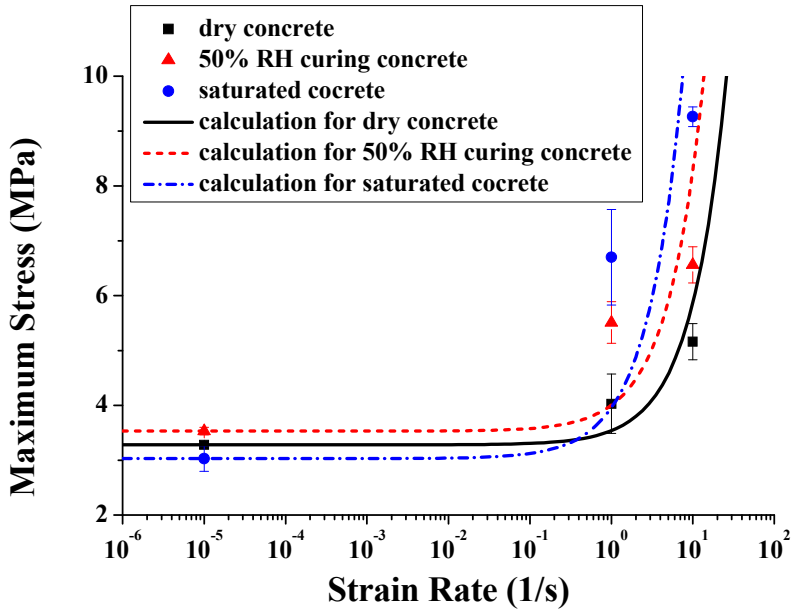

Figure 5: Strain rate effect on maximum tensile stress of concrete with three different curing states. Black squares are the experimental values for dry concrete [5]; black line is predictions of Eq. (2) for dry concrete; red triangles are the experimental values for 50% RH curing concrete [5]; and red dash line is predictions of Eq. (2) for 50% RH curing concrete; blue circles are the experimental values for saturated concrete [5]; blue dash-dot line is predictions of Eq. (2) for saturated concrete.

	Dry concrete	50% RH curing concrete	Saturated concrete
σ_c, MPa	3.3	3.5	3
τ, μs	12	22	44

Table 2: Parameters of concrete at different curing conditions.

The results of experiments (points) and the prediction of these results by Eq. (2) (curves) are shown in Fig. 5. The calculations were performed on the basis of the parameters in Table 2. It is clearly seen that the saturated concrete has a lower static strength (limit stress in statics) of the three materials, but one has a higher dynamic strength (the incubation time of fracture). Humidity increases the carrying capacity of concrete at high strain rates and vice versa in statics.

CONCLUSIONS

In this paper, we have analyzed the "effect of substitution" of load-carrying capacity of materials at different strain (stress) rate. The substitution effect means that in spite of the fact that static strength of one material is smaller than that of another one, its dynamic strength measured in terms of incubation time can be essentially higher.
The analysis was conducted based on the incubation time approach, which allows one to separate static strength (limit stress in statics) and dynamic strength (the incubation time of fracture). As the incubation time is a material parameter,

independent of the loading history, we can estimate and compare load-carrying capacity of materials in a wide range of loading rates.

Three cases of the substitution effect were examined. In the first case, two different materials were compared. It is shown that the fibre reinforced concrete (CARDIFRC) has a lower dynamic strength for a higher static strength compared to the gabbro-diabase.

In the second case, mortar and concrete were considered. It is shown that the substitution effect is also in this case. Moreover the difference between load-carrying capacity of concrete and mortar can depend on the elasticity of aggregate in concrete.

In the third case, concrete with different water saturation was studied. It is shown that saturated concrete has a greater dynamic strength than dry concrete. Thus, humidity can increase the carrying capacity of concrete under dynamic loads, and vice verse under quasi-static loads.

Thus, one of the central problems in testing of dynamic strength properties of rocks and concrete can be associated with measurements of the incubation time parameter. Studies of strain rate (loading rate) phenomenon provide an effective opportunity to examine the incubation stage of the fracture process that is important for predicting critical parameters of external action in a wide range of loading conditions.

REFERENCES

[1] N.F. Morozov, Y.V. Petrov, Dynamics of fracture. Berlin-Heidelberg-New York: Springer-Velrag (2000).
[2] A.M. Bragov, B.L. Karihaloo, Yu.V. Petrov, A.Yu. Konstantinov, D.A. Lamzin, A.K. Lomunov, I.V. Smirnov, J. of Applied Mechanics and Technical Physics, 53(6) (2012) 926.
[3] A.M. Bragov, A.P. Bolshakov, N.N. Gerdyukov, A.K. Lomunov, S.A. Novikov, I.V. Sergeichev, In: International Conference "V Kharitonov thematic scientific reading" (Sarov, VNIIEF, 2003).
[4] D.L. Grote, S.W. Park, M. Zhou, Int. J. of Impact Eng., 25 (2001) 869.
[5] E. Cadoni, K. Labibes, C. Albertini, M. Berra, M. Giangrasso, Materials and structures, 34 (2001) 21.
[6] Y.V. Petrov, A.A. Utkin, Material Science, 25 (1989) 153.
[7] Y.V. Petrov, N.F. Morozov, ASME J. Appl. Mech., 61 (1994) 710.
[8] Y.V. Petrov, Dokl. Phys., 49 (2004) 246.
[9] Y.V. Petrov, B.L. Karihaloo, V.A. Bratov, A.M. Bragov, Int. J. of Engng. Sci., 61(1) (2012) 3.
[10] A.C. Ross, E.Y. Thompson, J.W. ACI Mater. J., 86(5) (1989) 475.
[11] P.H. Bischoff, S.H. Perry, Mater. Struct., 24 (1991) 425.
[12] F. Akopov, A.M. Bragov, P. Demenko, L. Kruszka, A.K. Lomunov, V. Mineev, L.V. Sergeichev, J. de Physique IV, 110 (2003) 225.
[13] T. Antoun, L. Seaman, D.R. Curran, G.I. Kanel, S.V. Razorenov, A.V. Utkin, Spall Fracture. Springer-Verlag New York (2003).
[14] S.D.P. Benson, B.L. Karihaloo, Magazine Concrete Research, 57 (2005) 347.
[15] V. Bratov, N. Morozov, Y. Petrov. Dynamic Strength of Continuum. St.-Petersburg University Press (2009).
[16] T. Rodriguez, C. Navarro, V. Sanchez-Galvez, Journal de Physique IV, 4(C8) (1994) 101.
[17] A.M. Bragov, B.L. Karihaloo, A.Yu. Konstantinov, D.A. Lamzin, A.K. Lomunov, Bulletin of Nizhny Novgorod University N. Lobachevsky, 4 (2011) 123. (in Russian)

The failure criterion based on hydrogen distribution ahead of the fatigue crack tip

Yu. G. Matvienko
Mechanical Engineering Research Institute of the Russian Academy of Sciences, 4 M. Kharitonievsky Per., 101990 Moscow, Russia
matvienko7@yahoo.com

ABSTRACT. The hydrogen effect on the fracture toughness and fatigue crack growth behaviour in the martensitic high strength steel is investigated. The secondary ion mass spectrometry method has been employed to analyse the distribution of hydrogen concentration in the zone of the crack tip and at its edges. Changes in hydrogen concentration are observed in the vicinity of the propagating crack tip and at a remote site. The hydrogen peak C_H is reduced and moves away from the fatigue crack tip with the increase of the maximum stress intensity factor $K_{\max}$. The concept of damage evolution is used to explain fatigue crack propagation in connection with the hydrogen redistribution ahead of the crack tip. The physical failure criterion based on the hydrogen peak in the vicinity of the fatigue crack tip and the maximum stress intensity factor has been proposed. The criterion reflects changes in the hydrogen peak which resulted from the hydrogen redistribution due to the increase of the maximum stress intensity factor as the crack length increases under fatigue loading.

KEYWORDS. Hydrogen distribution ahead of the crack tip; Fatigue crack growth; SIMS; Local failure criterion; High strength steel.

INTRODUCTION

Recently many works have been performed on the hydrogen embrittlement of high strength steels (e.g., [1-4]). The deleterious effects of hydrogen on the mechanical properties of high strength martensitic steels are known to have caused premature failures. For example, it was found that the threshold stress intensity factor in steels decreases drastically in response to increased dissolved hydrogen concentration (e.g., [2, 5, 6]). Although it has been reported that hydrogen degrades mechanical properties of metallic materials, there have been few studies on the effect of hydrogen on fatigue behaviour ([7-9]).

It has been known that the fracture initiates in region of highly localized stress in which hydrogen is concentrated as a result of an augmented diffusion of hydrogen. To explain this phenomenon in the case of monotonic loading, a diffusion model was proposed by Liu [10] and developed by Kim et al. [3] introducing a fracture criterion as the critical hydrogen concentration at a critical distance ahead of the crack tip. However, until recently only a few papers [11-13] have reported on the experimental distribution of hydrogen ahead of a crack tip. Under monotonic mixed (I/II) mode loading there are two hydrogen accumulation peaks ahead of the crack tip [13], which correspond to the maximum hydrostatic stress and the maximum equivalent plastic strain, respectively. The experimental results also revealed that hydrogen distribution in the vicinity of the fatigue crack tip is related to the stress-strain fields surrounding the crack tip [12, 14]. It should be also

noted that the most essential results on the numerical analysis of the effect of cyclic loading on hydrogen diffusion and concentration around a crack tip was published by A.T. Yokobori et al. [15].
In this research, experimental analysis of the distribution of hydrogen concentration ahead of the crack tip in the martensitic high strength steel under hydrogen induced cracking and fatigue I mode loading conditions has been carried out. The generalized concept of damage evolution has been employed to explain fatigue crack propagation in connection with the hydrogen redistribution ahead of the crack tip. The physical criterion of local failure based on the hydrogen peak in the fracture process zone and the maximum stress intensity factor has been suggested.

EXPERIMENTAL PROCEDURES

The martensitic high strength steel is investigated to analyse the effect of hydrogen charge on the fracture toughness, the fatigue crack growth rate and the distribution of hydrogen concentration ahead of the crack tip. The fraction of retained austenite in the steel did not exceed 10%. Chemical composition of the studied steels is given in Tab. 1. Mechanical properties of the steel at room temperature are the following: the Young's modulus E=210 GPa, yield strength σ_y =850 MPa and ultimate strength σ_u =1150 MPa.

C	Cr	Ni	Si	Mn	P	S
0.06	16	7	<0.8	<0.8	<0.03	<0.02

Table 1: Chemical composition of high strength steel (weight %).

The hydrogen-charged and pre-fatigued specimens were employed. Hydrogen was artificially charged into specimens by a cathodic charging method before the tests. The solution used for the cathodic charging was a 10 mass% H_2SO_4 aqueous solution with an addition of SeO_2. The current density was i=1 A/dm^2 and charging time was 5 hours. Prior to immersing the specimen in the solution, its surface (with the exception of the crack surface) was coated with a chemically stable lacquer.
The testes were carried out on HUS-1025 machine at room temperature in laboratory air. The fracture toughness K_C was measured using compact-tension specimens (60x60 mm) with 5 mm thickness according to the standard method reported in the ASTM Standard E399.
The fatigue crack growth tests were conducted in order to clarify the hydrogen effect on fatigue crack growth behaviour and the distribution of hydrogen concentration ahead of the fatigue crack tip. Rectangular specimens 50 mm high and 5 mm thick with an edge crack loaded in cantilever bending were employed. The loading frequency was 20 Hz with a constant amplitude sinusoidal waveform for the applied load. The stress ratio was maintained at R=-0.3. The length of a growing fatigue crack was recorded by an optical microscope. At the given load or fatigue crack length the specimen was unloaded and 10x10 mm templates, which included the zone of the crack tip, were cut out from it. Template sizes were caused by sizes of the analytical chamber of the mass spectrometer.
The secondary ion mass spectrometry method was then used to analyse the distribution of hydrogen in the zone of the crack tip and at its edges [12]. The small size of the analysed area (5 μm) was ensured using a molybdenum diaphragm placed on the specimen. Prior to this, molybdenum was degassed in vacuum. The sensitivity of analysis for hydrogen was 10^{-2} cm^3/100 g. The reproducibility of the results of determining the intensities of the spectral lines was high. The mass spectrometric results were calibrated using reference specimens employed in installations for vacuum heating manufactured by LECO Company with linear grain sizes in the metal larger than 30 μm. This eliminated the apparatus error in recording local hydrogen concentrations associated with segregations of hydrogen at the grain boundary in the reference specimen since the size of the ion beam in analysis was smaller than the size of the grain within which the distribution of hydrogen was usually uniform. It should be noted that secondary ion mass spectrometry was successfully employed for an analyses of the hydrogen distribution around the fatigue crack on type 304 stainless steel [16]. According to the reported data [17], the fatigue crack growth is accompanied by microplastic deformation and formation of hydrogen collectors and traps. This greatly reduces the diffusion mobility of hydrogen in the zone of the crack tip.
The curve of hydrogen distribution through thickness for the specimen during removal of layers of the material was constructed (Fig. 1). It can be seen that the position of the maximum hydrogen concentration remains unchanged in specimens with different crack lengths. After finding the depth with the maximum concentration of hydrogen, the distribution of hydrogen ahead of the fatigue crack tip was measured at this depth.

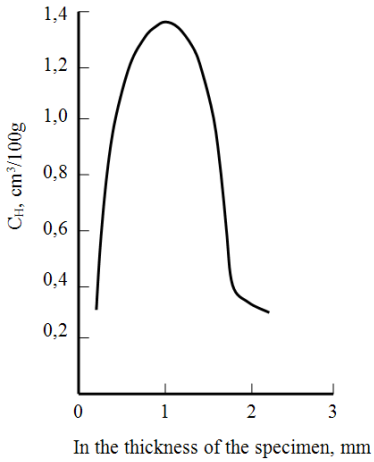

Figure 1: Hydrogen distribution C_H through the thickness for the hydrogen-charged specimen at the distance of 30 μm from the crack tip ($K_{max} = 20\ MPa\sqrt{m}$).

HYDROGEN CHARGING CONDITIONS

The problem of the effect of hydrogen charging conditions on the character of the hydrogen distribution in the specimen with a crack has been analysed. For this reason, the fatigue pre-cracked CT specimens were hydrogen charged in the same solution as the main set of the specimens at different values of the current density over a period of 2 hours under constant static load corresponding to two applied (constant) stress intensity factor values K_{10} (Tab. 2).

K_{10} ($MPa\sqrt{m}$)	Current density (A/dm²)	C_H / C_0
30	6	2.9
	10	3.0
50	6	3.8
	10	3.8

Table 2: The effect of hydrogen charging conditions on the hydrogen distribution ahead of the crack tip on crack extension line.

The distribution of hydrogen ahead of the crack tip was measured by the same procedure as for the specimens after the fatigue test [12]. The values of the ratio of the maximum local concentration C_H of hydrogen ahead of the crack tip to the volume concentration C_0 of hydrogen in the specimen were estimated. The results clearly show that the variation of the cathodic current density in these ranges does not influence on the C_H / C_0 ratio which is determined only by the value of the applied stress intensity factor K_{10}.

THE EFFECT OF HYDROGEN ON FATIGUE CRACK BEHAVIOUR

A negligible crack tip plastic zone is created due to the hydrogen embrittlement, mechanical properties of the high-strength steel and a low applied stress. It means that a linear elastic fracture mechanics methodology can be used to quantify the fracture toughness and fatigue crack growth behaviour. It follows that the maximum stress intensity factor must have an influence on fatigue damage evolution and the hydrogen distribution in the vicinity of the crack tip and, as a result, the physical growth of the fatigue crack.

Material	$K_C\,(MPa\sqrt{m})$	$C\left(\frac{m/cycle}{\left(MPa\sqrt{m}\right)^n}\right)$	m	$V^*\,(micron/cycle)$ [1]
Uncharged	85	$2.53\cdot10^{-12}$	2.74	3.84
Hydrogen-charged	75	$4.62\cdot10^{-12}$	2.95	3.36

Table 3: The fracture toughness and the fatigue crack growth rate parameters

[1] *The value of V^* corresponds to the stress intensity factor range ΔK varied from 20 MPa•m$^{1/2}$ to 50 MPa•m$^{1/2}$.*

To analyse the effect of hydrogen on the fracture toughness and fatigue crack propagation, the procedure, described in *Experimental procedures* section for hydrogen charged specimens and tests, has been employed. Experimental results revealed that the fracture toughness K_C and fatigue crack growth behaviour in the high-strength steel are in general dependent on the hydrogen content (Tab. 3). The fatigue crack growth rate parameters C and m refers to the Paris relationship. The fatigue crack growth rate dl/dN versus the stress intensity factor range ΔK curve in the uncharged specimen is lower than that in the hydrogen-charged specimens (Fig. 2). The fatigue crack in the hydrogen-charged specimens propagates at the same value of dl/dN as in the uncharged specimen at lower (by 30-40%) values of ΔK in the near-threshold region. However, there is no significant difference in the fatigue fracture toughness K_{fC} of the uncharged and hydrogen-charged specimens.

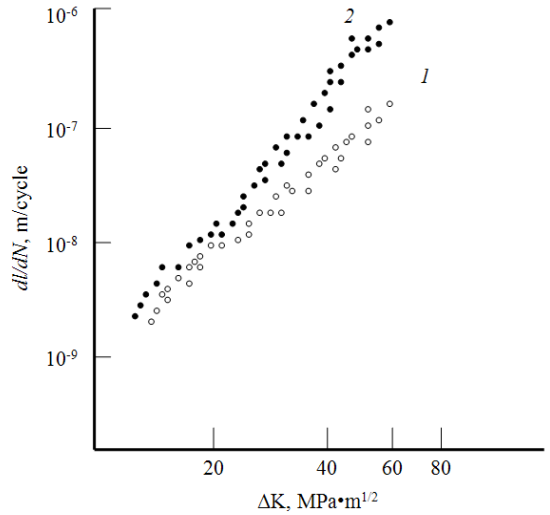

Figure 2: Fatigue crack growth behaviour: 1 - uncharged specimens, 2 - hydrogen-charged specimens

Experimental analysis of the distribution of hydrogen ahead of the crack tip under hydrogen induced cracking and fatigue I mode loading conditions has been carried out on a secondary ion mass spectroscope. The results on the distribution of hydrogen had been obtained and summarized for various periods of fatigue crack growth (or the maximum stress intensity factor) [12]. The concentration curves of hydrogen distribution in the sections normal to the crack surface and ahead of the crack tip on the crack extension line are plotted in Fig. 3 and 4, where C_H is the local hydrogen concentration. It can be seen that there is a hydrogen accumulation peak ahead of the crack tip, which is located on some distance ahead of the crack tip (Fig. 4). Changes in the hydrogen concentration were observed in the vicinity of the propagating crack tip and at a remote site. The hydrogen peak C_H is reduced and moves away from the crack tip as the maximum stress intensity factor $K_{\max}$ increases. The hydrogen concentration gradient also decreases. At the same time, the hydrogen concentration far away from the crack tip is increased by increasing the value of $K_{\max}$. So, the values and sites of hydrogen accumulation under fatigue loading are dependent on the magnitude of the maximum stress intensity factor.

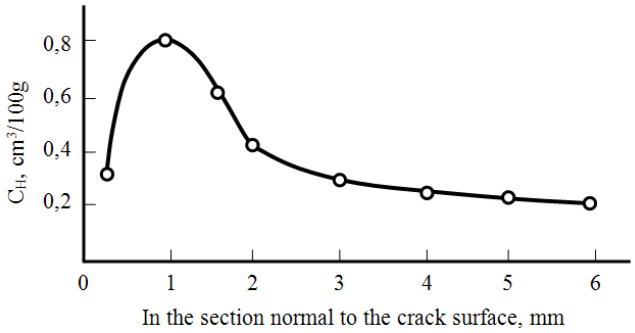

Figure 3: Hydrogen distribution C_H in the section normal to the crack surface at a distance of 3 mm behind the crack tip.

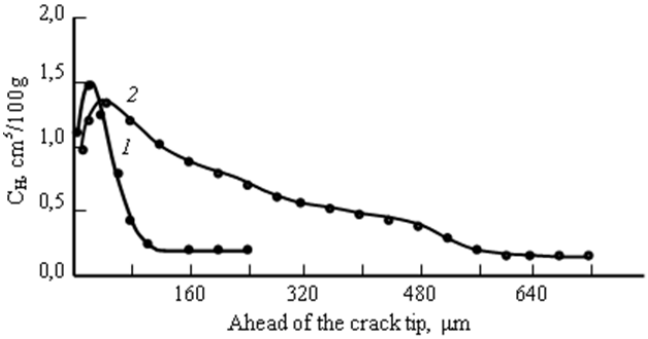

Figure 4: Hydrogen distribution C_H ahead of the crack tip on the crack extension line: line 1 corresponds to $K_{max} = 20\ MPa\sqrt{m}$, line 2 corresponds to $K_{max} = 68\ MPa\sqrt{m}$.

The trend of the redistribution of hydrogen ahead of the propagating fatigue crack tip can be reflected on the basis of the generalized concept of damage evolution [12, 14].

THE CONCEPT OF DAMAGE EVOLUTION

The evolution approach [18] has been extended to deformation and fracture processes of a mechanical loaded system, i.e. "solid - damage". It is assumed [14] that the accumulation of damage (the system state) is determined by the scalar $0 \le \Psi \le 1$ which is the single state variable $q = \Psi$. The controlling parameters ξ for deformation and failure processes of solids could be stress and strain, the stress intensity factor, temperature and other parameters, which are essential in the consideration of the damage accumulation process.

It is postulated that deformation and fracture processes are governed by some general functional law of damage accumulation [14]. For a simple case the damage evolution law can be formulated as

$$\frac{d\Psi}{d\tau} = -A\left(\frac{\xi}{\Psi}\right)^n \qquad (1)$$

where $A > 0$, $n \ge 0$ are material (the "solid - damage" system) constants for the fracture process under study. The evolution law (1) can be made more precise when the physical and mechanical aspects of a failure process are more clearly understood by examining the fracture mechanisms of the solid and the type of loading under study. The value of Ψ decreases with an increase of time τ during the process of the accumulation of damage in a solid. The value $\Psi = 1$ corresponds to the non-damaged state of a solid when $\tau = 0$, and the value $\Psi = \Psi_c$ corresponds to the critical state when $\tau = \tau_c$, where τ_c is the critical time. So, failure occurs in a solid if the damage reaches the critical value $\Psi = \Psi_c$ at $\tau = \tau_c$. The following relationship can be written as follows by integrating Eq. (1) from $\Psi = 1$ to $\Psi = \Psi_c$

$$\Psi_c^{1+n} = 1 - A(1+n)\int_0^{\tau_c} \xi^n d\tau \tag{2}$$

Eq. (2) is transformed into the following equation for the determination of the critical time τ_c

$$\tau_c = \frac{1-\Psi_c^{1+n}}{A(1+n)\xi^n} \tag{3}$$

if the controlling parameter ξ is constant. Taking into account Eqs. (1) and (3), the cumulative damage law is expressed in the integral form

$$\int_0^{\tau_c} \frac{d\tau}{\tau_c} = 1 \tag{4}$$

The influence of the controlling parameter ξ on the critical time may now be analysed for damage evolution in solids. First it is assumed that the critical value Ψ_c is constant for the deformation and failure process under study, and the critical state of a damaged solid can be reached for various combinations of the controlling parameter and time τ. It has been suggested therefore that the critical value Ψ_c [Eq. (2)] is also reached when the controlling parameter ξ is equal to the critical value ξ_c at some fixed time (or a unit of time) $\tau = \tau^* < \tau_c$, that is

$$\Psi_c^{1+n} = 1 - A(1+n)\xi_c^n \tau^* \tag{5}$$

The evolution equation at $\Psi_c = const$ is derived from Eqs. (2) and (5), namely

$$\int_0^{\tau_c} \xi^n d\tau = \xi_c^n \tau^* \tag{6}$$

This equation may be rewritten at $\xi = const$ as

$$\tau_c = \tau^* \left(\frac{\xi_c}{\xi}\right)^n \tag{7}$$

The damage evolution equation allows one to estimate the critical time for a solid to reach its critical state under the given controlling parameter for the deformation and fracture processes being studied.
It should be noted that exponent n in basic equations has different physical meaning for different physical phenomena and corresponding equations. What is why, this exponent has different table of symbols for below-mentioned equations.

THE FAILURE CRITERION

According to the above-mentioned concept, using the maximum stress intensity factor $K_{\max}$ as the controlling parameter ξ and replacing critical time τ_c with the critical hydrogen accumulation peak (maximum local hydrogen concentration) $C_{H\max}$ ahead of the crack tip, the damage evolution equation can be written as

$$C_{H\max} K_{\max}^b = const \tag{8}$$

It is assumed that the shape of the loading cycle is not changed. Eq. (8) gives the physical criterion for local fatigue failure in the fracture process zone, i.e. in the vicinity of the fatigue crack tip, and reflects changes in the hydrogen peak which resulted from the hydrogen redistribution due to the increase of the maximum stress intensity factor as the crack length increases under fatigue loading. This conclusion is in agreement with the observed experimental results (Fig. 4) for different values of the maximum stress intensity factor.
Fatigue crack growth behaviour can be described by the following equation [12]

$$\frac{dl}{dN} = V^* \left(\frac{K_{\max}}{K_{fC}} \right)^k = C' \left(1 - R\right)^k K_{\max}^k \tag{9}$$

where $V^* = C' \left(1 - R\right)^k K_{fC}^k$, C' and k are constants of the material and loading conditions. The process of local failure in the vicinity of the crack tip has interrupted nature and the crack propagates by means of discrete extension (crack jump) by the value Δa_i. After the jump, further crack propagation requires a certain time (cycle ΔN of loading) to accumulate fatigue damage and redistribute hydrogen in the vicinity of the crack tip until the condition (8) is reached. Thus, the parameter $V^* = \Delta a_i / \Delta N$ is connected with the discrete nature of fatigue crack propagation. The value V^* slightly decreases for the hydrogen-charged specimens (Tab. 3). This variation is associated with a reduction of the crack increment Δa_i in the hydrogen-charged specimen rather than with an increase of ΔN. It should be also mentioned that in the presence of a microcracks, the steel with internal hydrogen can be regarded as a system subjected to the effect of an external hydrogen environment. In this case, the localisation of deformation caused by hydrogen can be considered as one of the hydrogen embrittlement mechanisms [17]. It is obvious that more intensive localisation of deformation caused by interaction of hydrogen with moving dislocations and by activation of their sources will be also observed if the steel contains steep hydrogen concentration gradients.

CONCLUSIONS

The effect of hydrogen, which was artificially charged into specimens by a cathodic charging method, on the fracture toughness and fatigue crack growth behaviour in the martensitic high strength steel has been investigated. The distribution of hydrogen concentration in the zone of the fatigue crack tip and at its edges has been analysed by the secondary ion mass spectrometry method. The following conclusions can be drawn from the present study.

The variation of the cathodic current density does not influence on the ratio of the maximum local concentration C_H of hydrogen ahead of the crack tip to the volume concentration C_0 of hydrogen which is determined by the value of the applied stress intensity factor K_{10}.

The generalized concept of damage evolution has been employed to describe fatigue crack propagation in connection with the hydrogen redistribution ahead of the crack tip. The failure criterion based on the hydrogen peak in the vicinity of the fatigue crack tip and the maximum stress intensity factor has been proposed. The local concentration of hydrogen in the vicinity of the crack tip is a function of the stress intensity factor, i.e. higher values of $K_{\max}$ lead to the lower hydrogen peak. The criterion explains experimentally observed changes in the hydrogen peak which resulted from the hydrogen redistribution due to the increase of the maximum stress intensity factor as the crack length increases under fatigue loading.

REFERENCES

[1] S.A. Ahmad, D.A. Ryder, T.A. Davis, Engineering Fracture Mechanics, 7 (1975) 357.
[2] R.L.S. Thomas, J.R. Scully, R.P. Gangloff, Metallurgical and Materials Transactions, 34(A) (2003) 327.
[3] Y. Kim, Y. J. Chao, Marty J. Pechersky, Michael J. Morgan, Int. J. of Fracture, 134 (2005) 339.
[4] J. Capelle, J. Gilgert, I. Dmytrakh, G. Pluvinage, Engineering Fracture Mechanics, 78 (2011) 364.
[5] C.J. McMahon, Engineering Fracture Mechanics, 68 (2001) 773.
[6] A.T. Yokobori, Int. J. of Fracture, 128 (2004) 121.
[7] Y. Oda, H. Noguchi, Int. J. of Fracture, 132 (2005) 99.
[8] Y. Murakami, Int. J. of Fracture, 138 (2006) 167.
[9] I. Dmytrakh, O. Smiyan, A. Syrotyuk, In: Proceedings of the 18th European Conference on Fracture. Fracture of Materials and Structures from Micro to Macro Scale. Dresden, Germany. (2010) 13.
[10] H.W. Liu, Transaction of ASME: J of Basic Engineering, 92 (1070) 633.
[11] S. Wu, L. Chen, M. Liu, Acta Metall. Sinica., 26 (1990) A86.
[12] Yu.G. Matvienko, V. E. Vygovskii, E. N. Lubnin, V. B. Spiridonov, Materials Sciences, 26 (3) (1990) 251.

[13] H. Gao, W. Cao, C. Fang, E. R. de los Rios, Fatigue and Fracture of Engineering Materials and Structures, 17 (1994) 1213.
[14] Yu.G. Matvienko, In: Integrity of Pipelines Transporting Hydrocarbons, NATO Science for Peace and Security Series C: Environmental Security / eds.: G. Bolzon, T. Boukharouba, G. Gabetta, M. Elboujdaini and M. Mellas, Springer Netherlands: (2011) 227.
[15] A. T. Uesugi, M. Sendoh, and M. Shibata, Strength, Fracture and Complexity, 1 (4) (2003) 187.
[16] N. Saintier, T. Awane, J.M. Olive, S. Matsuoka, Y. Murakami. International journal of Hydrogen Energy, 36 (2011) 8630.
[17] M.R. Louthan, Scripta Metall., 17 (1983) 451.
[18] H. Haken Advanced Synergetic: Instability Hierarchies of Self-Organizing Systems and Devices. Berlin, Heidelberg, New York, Tokyo: Springer-Verlag, (1983).

The numerical simulation of ceramic composites failure at axial compression

P.V. Makarov, M.O. Eremin

Institute of Strength Physics and Material Science Siberian Branch of Russian Academy of Science, National Researching Tomsk State University

bacardi@sibmail.com

ABSTRACT. On the basis of the developed model of quasibrittle medium the brittle and quasibrittle failure of composite ceramic materials with zirconium dioxide matrix and various percentage of hardening particles of corundum are studied numerically. The theory of the damaged media is applied in the calculations. It is shown that failure process educes in 2 stages - a relatively slow quasistationary phase of accumulation of inelastic deformations and damages in all hierarchy of scales and superfast catastrophic phase - a blow-up regime when the failure process reaches the macro-scale and there is a macro-crack formation. The failure process in the proposed model assumes to be completed when the damage function reaches its maximum value and the strength of the composite evolve to zero.

KEYWORDS. Brittle and quasi-brittle failure; Quasistationary phase; Blow-up regime.

INTRODUCTION

Constructional ceramic composites have received a wide practical application in the industry because of their high unit strength, the raised toughness, hardness, crack stability, high resistivity to fatigue breakdown etc. Constructional ceramics on the basis of strong oxides of various metals (zirconium, aluminum, etc.) are capable to resist the intensive mechanical loads effectively. However the brittle properties of ceramic composites, their rather low stability to shock loads strongly confine the ranges of their application. Studying the mechanisms and features of brittle and quasibrittle failure of ceramic materials is one of the most urgent problems of modern fracture mechanics.

According to the approach of physical mesomechanics [1] and ideas of paper [2] the loaded solid is the nonlinear dynamic system which evolution in fields of operating forces completely corresponds to the fundamental features of evolution of nonlinear dynamic systems.

In the present paper the basic attention is given to the character of failure of quasibrittle solids and media – the presence of two stages of failure: rather slow quasistationary and superfast catastrophic stage – the blow-up regime according to the S.P. Kurdyumov terminology [3] as it is the fundamental feature of evolution of the nonlinear dynamic systems possessing the self-organized criticality [4].

One of the central problems of solid mechanics is a problem of the formulation of the fracture criteria or conditions when the crack formation starts. Many papers are dedicated to the problems of crack-growing in non-homogeneous media, such as rocks [19], polycrystalline materials or ceramics and ceramic composites [18]. For example, in paper [21] the equation of state is built on the basis of crack interaction and crack density accounting and strain rate dependency and used for simulation of macroscopic stress-strain curves. Such approach gives good qualitative and quantitative results in calculation of the degradation stage in stress-strain curves, strain rate dependency and defects density evolution. However

in the present paper the main accent is made on studying the transition from the quasistationary phase of media evolution to the blow-up regime which is assumed as local failure at crack formation which applies to be the new vision of the failure process.
In the present paper these problem also dares on the basis of ideas of the mathematical theory of evolution of loaded solids and media [2].
According to traditional ideas of fracture mechanics a local fracture in solids occurs when a maximum load is reached. All experience of application of this approach to the problem of limiting design has shown its comprehensible working capacity and correctness for many practical problems. However we can tell nothing about the failure process especially about its forecast. If a certain constant or changing load is enclosed to solid it is only possible to calculate the conforming stress-strain state and to answer a question whether a maximum load is reached or not somewhere. Such answers appear useful and sufficient in a number of important engineer cases but to tell something about the mechanisms and scenarios of failure locus formation is impossible.
The fundamental law of fracture of any materials has been investigated in the 70s of the XX century: the final failure (not only fatigue but any) precedes more or less significant preparatory stage. For example for the silicate glasses which failure was considered as instant the speed of crack propagation in the beginning of failure has appeared in thousands times less than at the final stage [5] and this is with the fact that the whole failure process takes some ms.
Rapid development of ideas and methods of nonlinear dynamics at the same years and the next decades have allowed the group of S.P. Kurdyumov to formulate the new concept of superfast catastrophic stages of evolution of nonlinear systems – the blow-up regimes [3] and both analytically and numerically to study the kinds and features of these regimes.
These ideas and the qualitative results obtained on their basis are the key-ideas for understanding the failure process. In the considered case of brittle or quasibrittle failure (and also the failure of any materials and constructions, plastic metals, brittle concrete, rocks, geomedia etc.) the preparatory process of accumulation of inelastic deformations and damages in brittle media is localized in certain areas. This preparatory quasistationary stage because of the self-organized criticality of solid as nonlinear dynamic system passes sooner or later in the superfast catastrophic stage – blow-up regime by S.P. Kurdyumov [2, 4, 7]. It is clear that any failure forecast basically is not possible without studying the features of development of these stages and conditions of transferring of one stage of sustainable development of failure to unstable superfast regime.

MATHEMATICAL STATEMENT OF A PROBLEM. MODEL OF QUASI-BRITTLE MEDIUM

According to the evolutionary concept of the description of inelastic deforming and the subsequent failure processes [2, 4, 6-9] the full set of equations includes:
1. Fundamental conservation laws:

– Mass $$\frac{d\rho}{dt}+\rho div\bar{\upsilon}=0 \tag{1}$$

– Impulse $$\rho\frac{d\upsilon_i}{dt}=\frac{\partial\sigma_{ij}}{\partial x^j}+\rho F_i \tag{2}$$

– Energy $$\frac{dE}{dt}=\frac{1}{\rho}\sigma_{ij}\frac{d\varepsilon_{ij}}{dt} \tag{3}$$

where ρ is the material density, υ_i is the *i*-component of the speed vector, F_i is the *i*-component of the massive force, is energy, t is time.
2. The evolutionary equations of the first group which have been written down in the relaxation form in which increments of stresses $\Delta\sigma_{ij}=\dot{\sigma}\Delta t$ are proportional to increments of total deformations $\dot{\varepsilon}_{ij}^{T}$ and relax proportionally to the development of inelastic deformation $\dot{\varepsilon}_{ij}^{P}$. The procedure of stresses reduction to the instant limiting surface means the instant stress relaxation on each time layer to some dynamic equilibrium state defined both by relaxation and the rate of strength and elastic parameters of medium degradation. At $\dot{\varepsilon}_{ij}^{P}>\dot{\varepsilon}_{ij}^{T}\quad\Delta\sigma_{ij}<0$, there is a relaxation, at $\dot{\varepsilon}_{ij}^{P}<\dot{\varepsilon}_{ij}^{T}\quad\Delta\sigma_{ij}>0$ and stresses steepen:

$$\dot{\sigma}_{ij}=\lambda\left(\dot{\theta}^{T}-\dot{\theta}^{P}\right)\delta_{ij}+2\mu\left(\dot{\varepsilon}_{ij}^{T}-\dot{\varepsilon}_{ij}^{P}\right) \tag{4}$$

$$\sigma_{ij} = \left(-P\delta_{ij} + S_{ij}\right) \tag{5}$$

$$\dot{P} = -K\frac{\dot{V}}{V} \tag{6}$$

$$\frac{DS_{ij}}{Dt} = 2\mu\left(\dot{\varepsilon}_{ij} - \frac{1}{3}\dot{\theta}\delta_{ij}\right) \tag{7}$$

$$\frac{DS_{ij}}{Dt} = \dot{S}_{ij} - S_{ik}\dot{\omega}_{jk} - S_{jk}\dot{\omega}_{ik} \tag{8}$$

$$\dot{\varepsilon}_{ij}^{T} = \frac{1}{2}\left(\frac{\partial \upsilon_i}{\partial x^j} + \frac{\partial \upsilon_j}{\partial x^i}\right) \tag{9}$$

$$\dot{\omega}_{ij} = \frac{1}{2}\left(\frac{\partial \upsilon_i}{\partial x^j} - \frac{\partial \upsilon_j}{\partial x^i}\right) \tag{10}$$

$\dot{\theta}$ is the rate of volumetric strain, λ, μ are the Lame constants, K is the bulk modulus, P is pressure, σ_{ij} are the components of deviator stress tensor, $\frac{D}{Dt}$ is the co-rotation derivative of Yauman considering the rotation of the medium elements at deforming, $\dot{\omega}_{ij}$ are the components of the rotation strain rate tensor.

3. The problem of the evolutionary equations of the second group is the definitions of rates of inelastic deformations in the Eq. (4). Generally it is the kinetic equations setting the rates of inelastic deformations and providing the relaxation of elastic stresses in (4). In the present paper the components of rates of inelastic deformations tensor are identified according to the theory of plasticity and instant stress relaxation on each time layer.

The limiting surface of stresses is written down in the form of Mises-Schleicher that allows to satisfy the requirement of generalization of plasticity and brittle failure conditions: the form of a limiting surface and its properties are completely defined by three parameters of a stressed state - octahedral normal stress octahedral shear stress σ_{oct} and a kind of the stressed state μ_σ (parameter of Lode-Nadai)

$$f = \frac{\alpha}{3}J_1(\sigma_{ij}) + J_2^{1/2}(\sigma_{ij}) - Y \tag{11}$$

where f is the yield surface and J_1, J_2 are the first, the second invariants of the stress tensor and Y - current strength. Eq. (11) is a generalization of plasticity criterion of Coulomb-More. The model of Drucker-Prager-Nikolaevskiy with non-associated flow law is taken as basis allowing describing the dilatation and internal friction processes independently. In the case of non-associated flow law the plastic potential $g\left(\sigma_{ij}\right)$ does not coincide with a function of plasticity and for a limiting surface (11) is written as follows [10]:

$$g\left(\sigma_{ij}\right) = J_2 + \frac{\Lambda}{3}J_1\left(2Y - \frac{\alpha}{3}J_1\right) + const \tag{12}$$

Components of rates of inelastic deformations tensor will be defined as follows:

$$\dot{\varepsilon}_{ij}^{p} = \dot{\lambda}\frac{\partial g}{\partial \sigma_{ij}} = (s_{ij} + \frac{2}{3}\Lambda(Y - \frac{\alpha}{3}I_1)\delta_{ij})\dot{\lambda} \tag{13}$$

where $\dot{\lambda}$ is the plasticity multiplier in the theory of plasticity.

$$\dot{I}_1^P = 2\Lambda(\dot{I}_2^P)^{1/2} \tag{14}$$

That allows to establish the connection between volumetric $\dot{I}_1^P$ and shear $\dot{I}_2^P$ components of inelastic strain (14) [7] where Λ is a speed of dilatation. However the model is not bound yet to the kind of stressed state. That dependence will be defined within the function of damages accumulation.

4. Failure in the educed approach is considered as a process of avalanche degradation of material strength to zero at macro-cracking during the superfast catastrophic stage of stress-strain state evolution which is the closing stage of pre-failure. However the medium remains consolidated macroscopically hence all the equations of inelastic deforming (1) ÷ (14) are fair. There is no need to introduce the strength parameters defining the "limiting" state of material into model. According to the ideas of the present paper the "limiting" condition should be formed in the loaded medium during the process of inelastic deformations and damages accumulation. It is necessary to set the initial strength of the material .
According to the classic ideas of the failure kinetic concept (N.S. Zhurkov, A.V. Stepanov, R. Bekker, Ja.I. Frenkel and others) [11-15] to lead an ideal crystal to a state of local shear it is necessary to make a work proportional to the difference of free energies F of an ideal crystal and a crystal in current state $A(\sigma)\sim V\frac{\sigma_0^2-\sigma^2}{2\mu}$ (V - volume, σ_0 – the value of theoretical strength, σ is the current stress).
Orowan modified this idea and put the critical increment of energy depending only on the size of plastic (inelastic) deformation [16] $F(\sigma)\sim h^2 V\frac{\varepsilon_p^2}{2\mu}$, where h is the strain hardening parameter, ε_p is the accumulated inelastic strain.

We use this idea and put the function of medium degradation $D=D(t,\varepsilon_p,\mu_\sigma)$ in the form of dependence on inelastic deformation accumulated by medium $\varepsilon_p=\varepsilon_{cur}-\varepsilon_0$ and the kind of stressed state:

$$D=\int_{t_0}^{t}\frac{(\varepsilon_{cur}-\varepsilon_0)^2\,dt}{\varepsilon_*^2 t_*} \qquad (15)$$

$$\varepsilon_*=\varepsilon_{0*}(1+\mu_\sigma)^n \quad , \quad Y=Y_0(1-D),\ D\le 1$$

$$\mu_\sigma=2\frac{S_2-S_3}{S_1-S_3}-1 \qquad (16)$$

ε_{cur} is the current mean of total deformation intensity, ε_0 is the initial deformation when the damage accumulation begins. ε_0 is different for areas of compression and tension and makes 0.2 - 0.5 from the elasticity limit depending on a solved problem. Such approach allows accumulating the damages at macroscopically elastic stage of deforming. Rates of damage accumulation for local tension-shift areas where $\mu_\sigma<0$ are essentially bigger than in compression-shift areas where $\mu_\sigma>0$. This process is controlled by the parameter $\varepsilon_*=\varepsilon_*(\mu_\sigma)$ in (15). Thus the medium response (its current strength) is formed during loading. Hence the strength and elastic parameters will degrade essentially faster in those areas (particles) of medium where the Lode-Nadai parameter $\mu_\sigma<0$ that corresponds to tension-shift areas. This response depends also on the loading history. Changing the deforming regime from tension-shear to compression-shear might mean the transition to another scenario of evolution and regeneration of the medium properties. ε_{0*} is the model parameter, t_* makes sense of the characteristic time of the process, S_1,S_2,S_3 – are the main deviatric stresses.
Calculations were made in 2D under the condition of a plane deformation and 3D with the scheme of the second order of accuracy described in detail in paper [17].

THE NUMERICAL SIMULATION RESULTS OF BRITTLE AND QUASI-BRITTLE FAILURE OF COMPOSITE CERAMIC MATERIALS

The model specimens of ceramic composites with zirconium dioxide ZrO_2 matrix and various content of hardening particles (15% (a) and 40% (b)) of corundum Al_2O_3 are represented on Fig. 1. The content of the second phase was chosen as 15% and 40% to study the qualitative changes in the mechanical behavior of the composites. The presented structural models were developed on the basis of the well-known typical quasi-homogeneous distribution of the hardening particles within the matrix. In paper [22] the experimental study of uniaxial compression of porous ceramic on the base of zirconium dioxide was carried out and it's structure and phase content were also studied. Using the observations of structure from several papers of the author of paper [22] we developed the model of ceramic

composites presented on the Fig. 1. The uniaxial compression of specimens was carried out in the calculations. The dimensions of the specimens are $100 \times 140 \mu m$.

In paper [18] it has been shown that in loaded ceramic composites there are local areas of tension stresses on the interphase borders. Formation of mesocracks occurs in these areas of tension stresses. We will show that failure of composites in the majority of cases occurs in tension areas. It is caused by two reasons: 1) the presence of structural heterogeneities always leads to the formation of local tension areas in composite; 2) strength of quasibrittle materials at tension is essentially low than at compression. Rates of damages accumulation in tension areas are also essentially bigger.

In Tab. 1 the physical-mechanical properties of the materials compounding the composite are presented.

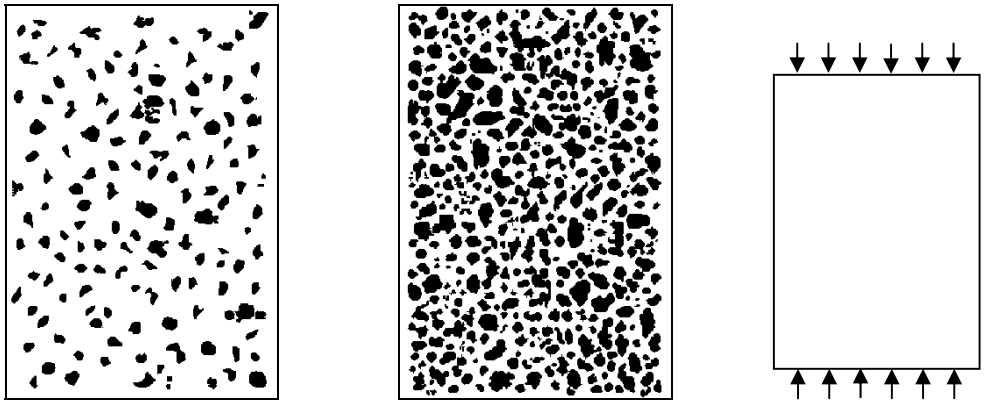

(a) (b) (c)

Figure 1: The model specimens of composites with 15% (a) and 40% (b) content of the hardening particles and the principle loading scheme (c).

Parameter	Material density, kg/m³	Bulk modulus, MPa	Shear modulus, MPa	Strength, MPa	Λ speed of dilatation	α, internal friction coefficient
ZrO_2	5700	$1.433 \cdot 10^5$	$0.6615 \cdot 10^5$	2100	0.22	0.62
Al_2O_3	3984	$3.46 \cdot 10^5$	$1.6 \cdot 10^5$	3740	0.12	0.6

Table 1: The physical-mechanical properties of the materials compounding the composite.

The macroscopic behavior

The $\sigma - \varepsilon$ diagrams for composite specimens are shown under various loading conditions on Fig. 2 - ideal sliding (Fig. 2a) and friction (Fig. 2b) on the loading border.

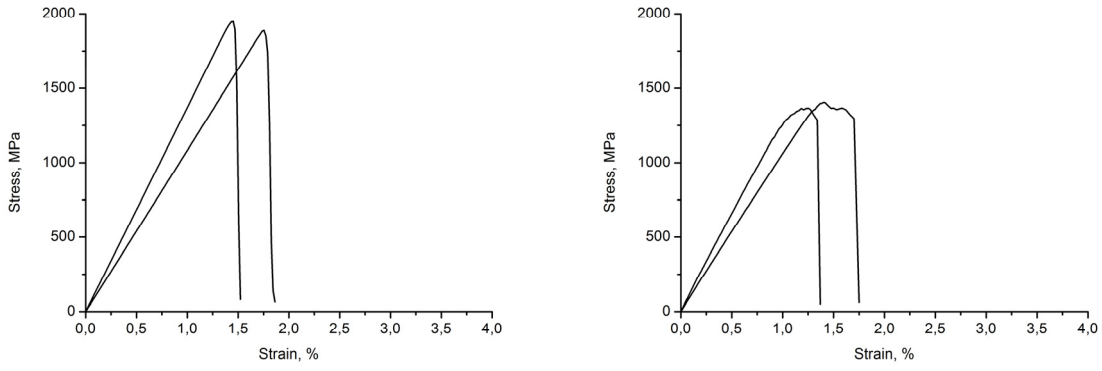

(a) (b)

Figure 2: The $\sigma - \varepsilon$ diagrams in case of: ideal sliding (a), friction (b) on the loading border.

The general for two variants of loading is the strength evolution of composites in the blow-up regime at final stage of deforming. Steady slow accumulation of inelastic deformations and damages at lower structural levels than considered macrolevel is replaced by the stage of unstable avalanche accumulation of damages (the blow-up regime) which occupies the tenth lobes of macrodeformation. It means that there is a localization of failure process in time. During the blow-up regime the global loss of stability, strength and elastic moduli of composites degradation to zero occur very quickly.
In the case of ideal sliding on the loading border (Fig. 2a) the brittle failure of specimens occurs that is the sharp break on the $\sigma - \varepsilon$ diagram and the system evolution is observed in the blow-up regime. The stage of the linear stress growth is followed by the blow-up regime with the global strength degradation. The feature of the deformation response in the case of friction on the loading border (Fig. 2b) is the presence of the stage of inelastic deforming of specimens because of the compression-shear areas formation near the friction border that sharply reduces the rate of damages accumulation. This process detains the phase of the blow-up regime and the global degradation of physical-mechanical properties of medium. Thus the stage of inelastic deformation occupies some % of macrodeformation.
Other scenario educes in the case of a lateral pressure (Fig. 3). Constraint of the deformation leads to tightening of the catastrophic phase of evolution of the system. The strength resource is spent gradually in this case, the sequence of relaxations and growths of stresses is observed. The similar situation is observed in geomedia at so-called "slow" earthquakes when the features of constraint of deformation lead to the tightening of the local failure process.

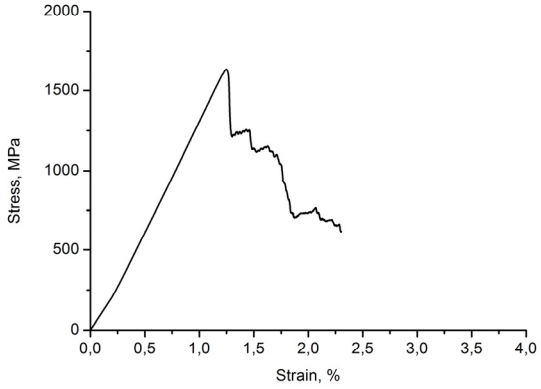

Figure 3: The $\sigma - \varepsilon$ diagram in the case of the lateral pressure.

The behavior on the meso-scale

The part of specimen area reflecting the kind of the stressed state in a composite defined by the Lode-Nadai parameter is represented on Fig. 4. First of all the formation of a strip of the localized failure occurs in a narrow regions of normal tension stresses $\mu_\sigma \to -1$.

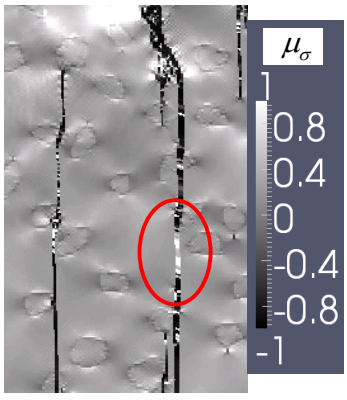

Figure 4: The part of specimen area reflecting the kind of the stressed state in the composite defined by the Lode-Nadai parameter μ_σ.

Besides in the generated mesocrack in the noted area the stressed state was replaced with compression-shears that means transferring to the compaction mode at the steepening of the deformation constraint due to the presence of the hardening

particles. At the same time in the generated mesocrack areas neighboring with the compaction zone are in dilatation regime. This process of failure delay in matrix shows one more positive role of the hardening particles.

On Fig. 5 - 8 the calculated patterns of inelastic deformations in composites for three consecutive times ($t_1 = 4000\mu s, t_2 = 6000\mu s, t_3 = 8000\mu s$), the stressed state (by the Lode-Nadai parameter), damage function are presented at 2 variants of boundary conditions.

In all presented cases the incipient states of specimens deforming accompanied with a vertical crack growing that also show the experiments [20].

Comparison of failure patterns of composites with various percentage of hardening particles shows the distinction in mechanisms of their destruction. In the composite with 40 % content of corundum the great number of hardening particles simultaneously creates the possibility for formation of the of local tension stresses areas on the phase border where the degradation of physical-mechanical properties of medium descends much faster. But also interferes with the macrocrack growing. On the pre-failure stage of the composite with 40% content of corundum the significant number of mesocrack is generated and this is more power-intensive process than formation of the small number of long cracks within the composite with 15% content of hardening particles (Fig. 5, 7).

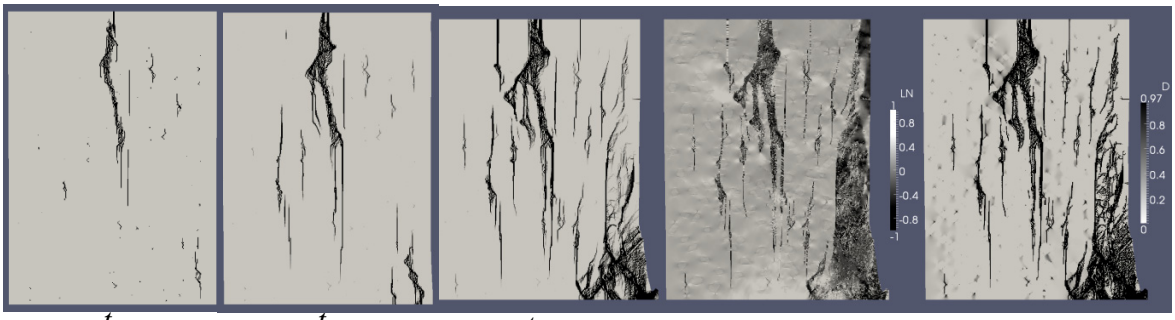

Figure 5. Simulation patterns: inelastic deformations (for three consecutive times), the stressed state (μ_σ), damage function (D) in the composite specimen with 15% content of hardening particles in the case of ideal sliding on the loading border.

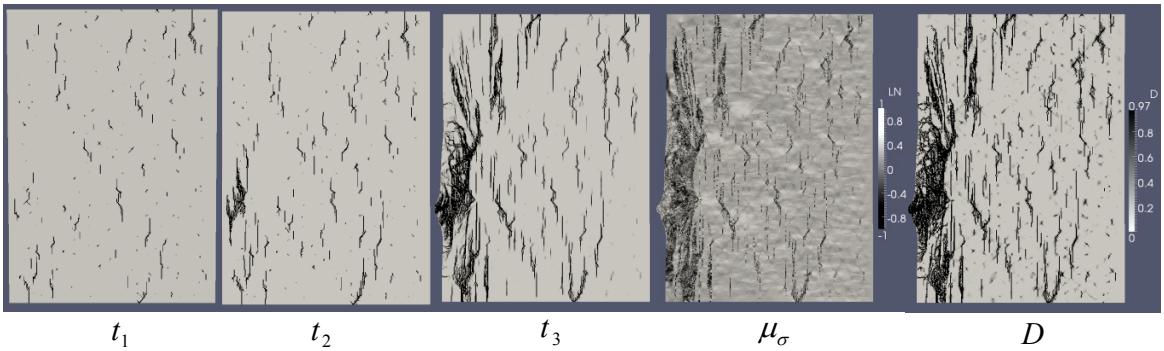

Figure 6: Simulation patterns: inelastic deformations (for three consecutive times), the stressed state (μ_σ), damage function (D) in the composite specimen with 40% content of hardening particles in the case of ideal sliding on the loading border.

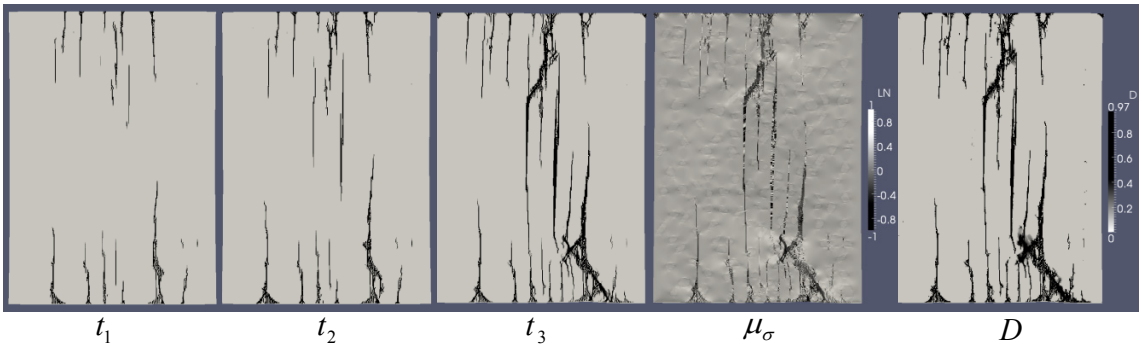

Figure 7: Simulation patterns: inelastic deformations (for three consecutive times), the stressed state (μ_σ), damage function (D) in the composite specimen with 15% content of hardening particles in the case of friction on the loading border.

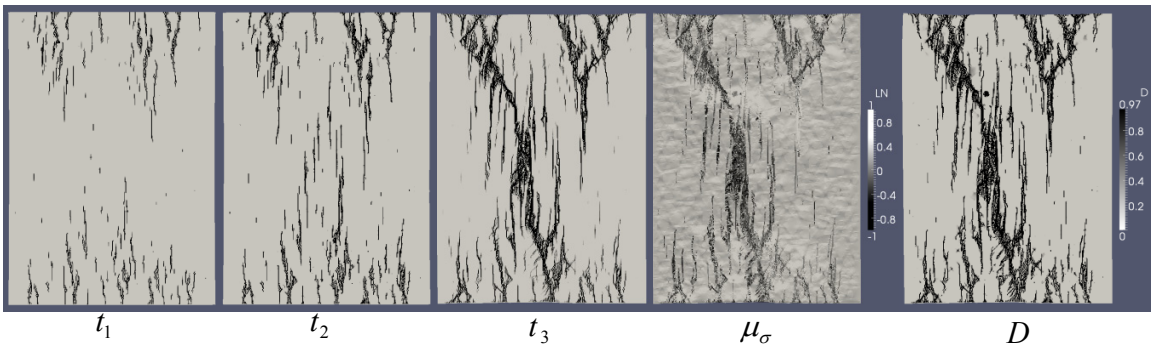

Figure 8: Simulation patterns: inelastic deformations (for three consecutive times), the stressed state (μ_σ), damage function (D) in the composite specimen with 40% content of hardening particles in the case of friction on the loading border.

Dynamics of crack growth in such composites (Fig. 6, 8) for three consecutive times shows that during the pre-failure stage there is a steady accumulation of inelastic deformations and damages in the whole considered volume of composites. The catastrophic superfast phase of system evolution – the blow-up regime occurs when the process of inelastic deformations and damages accumulation reaches the macrolevel. It is anticipated by the quasistationary preparation phase which is expressed in the formation of percolation net of mesocracks. At final stage of deforming there is a confluence of the generated mesocracks in main macrocrack.

Other situation is observed in the composite with 15 % content of hardening particles. Propagation of the crack fastigium generated on the interphase border is stopped by the smaller quantity of hardening particles that is the growing crack approximately three times rarely encounters the resistance of hardening particles. Thus the average length of an individual mesocrack for the composite with 15% content of corundum exceeds the similar length of an individual mesocrack for the composite with 40% content of corundum in 1.5 - 2 times. Such distinction at mesolevel leads to the distinction at macrolevel in characters of destruction of two composites. In the composite with 15% content of the hardening particles the macrocrack also has mainly vertical character. The mesocracks growing from the opposite edges of the specimen getting to a region of a dynamic influence and start to render the interference against each other that leads to their confluence at a final stage of deforming.

The particles flow characters in the composites are shown in the shift-fields. For example on the Fig. 9, 10 the shift-fields in composites related to the noted grain are presented for three consecutive times.

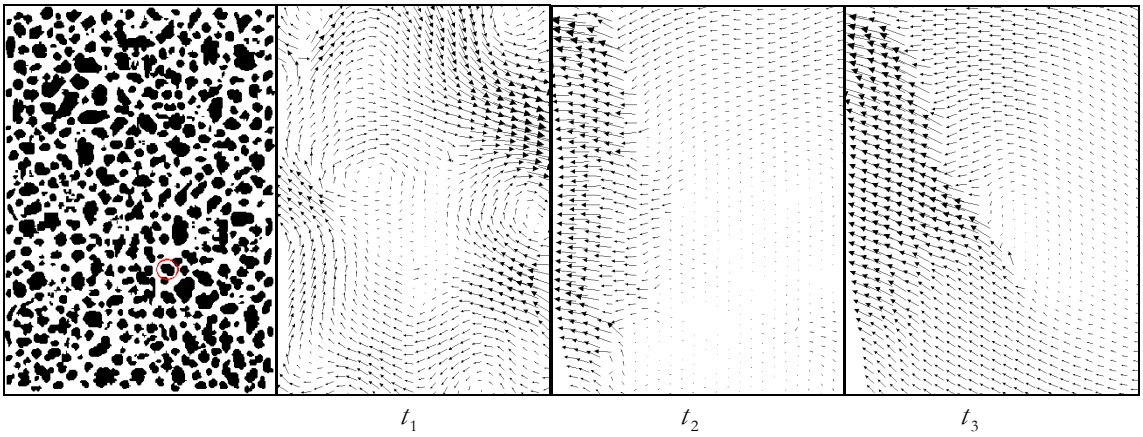

Figure 9: Simulation shift-fields for the composite with 40% content of the hardening particles in the case of ideal sliding on the loading border.

Shift-fields possess a strongly pronounced heterogeneity. The evolution of the shift-fields in time shows that the stress-strain state in the area of the fixed grain changes during the loading from compression on the incipient state of deforming then shears and formation of the curls and tension during the composite fragmentation. At main crack formation shift-field shows the correlated locomotion of composite fragments in the normal direction to main crack.

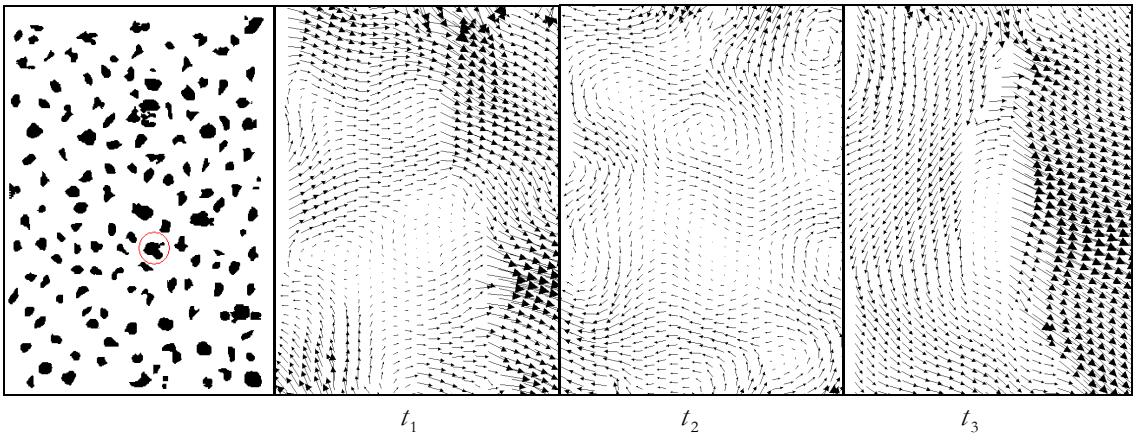

Figure 10: Simulation shift-fields for the composite with 15% content of the hardening particles in the case of friction on the loading border.

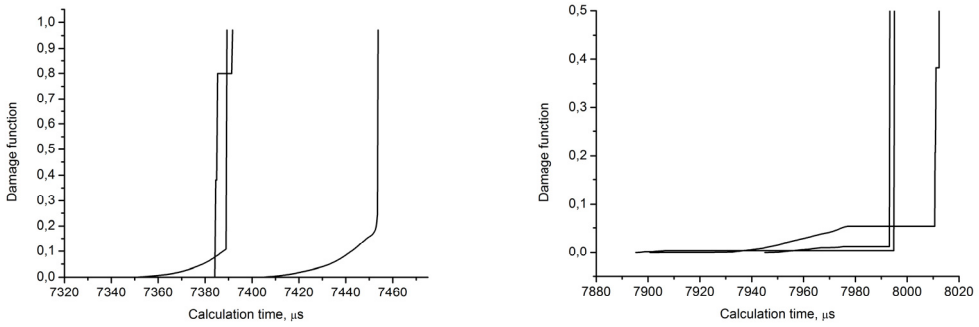

Figure 11: Damage function monitoring for several particles of the specimen which are in the region of a prospective dynamic influence in the composite with 15% content of hardening particles (a – in the case of friction on the loading border, b - in the case of ideal sliding on the loading border).

The pattern of damage function monitoring for several particles in the specimen volume located in the region of the prospective mutual dynamic influence (Fig. 11) shows the presence of slow quasistationary phase of damage growth and superfast phase of evolution – the blow-up regime with the damage growth in the particle of the composite to it's maximum value. From Fig. 11 also it is visible that damage in the particles consistently reaches the maximum value consecutively. The similar behavior can testify the migration of deformation activity. After the finish of the blow-up regime in one of the particles it begins in another (or the quasistationary phase in the next particle proceeds) and next the superfast phase of evolution occurs and there is a migration of deformation activity to the next particle.

A generalization of the quasi-brittle medium on the case of 3D simulation

The developed model of quasibrittle medium was applied for the 3D numerical simulation of the brittle failure of ceramic composites. The 3D stochastic structure of the composite with 15% content of the hardening particles with quasi-homogeneous distribution was generated and presented on the Fig. 12. The same parameters as for the 2D simulation presented in Tab. 1 were applied in 3D simulation. The results of uniaxial compression at different boundary conditions are presented on the Fig. 13.

From the simulation patterns presented on the Fig. 13 we can see that the generalization of the developed model on the case of 3D simulation qualitatively gives the same results. Particularly we have the formation of the meso-cracks on the incipient stages of deforming mainly co-directed with the loading force. At later stages of deforming we can see that the formation of bridges between meso-cracks leads to the macro-crack formation which can be either co-directed with the loading force or disoriented to some angle with the loading force. In several cases the growing meso-crack change it's direction on the angle of 90° when it gets into the region of the high compression near the hardening particle; such behavior at crack growing was observed in the experiments [23].

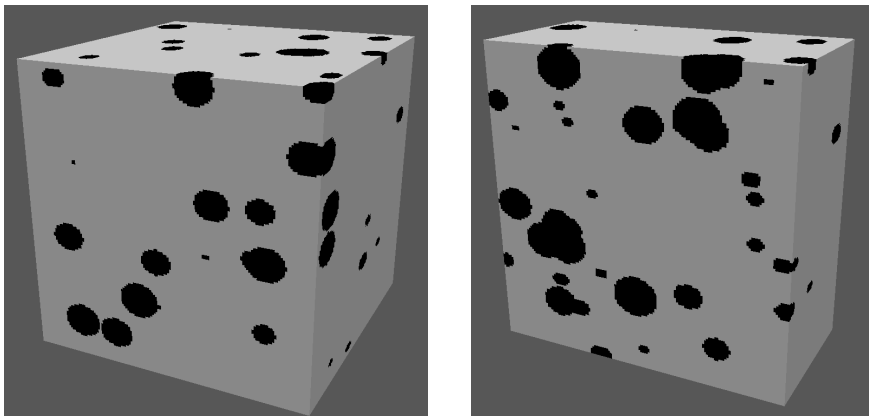

(a) (b)

Figure 12: The 3D generated structural model of the ceramic composite with 15% contain of the hardening particles: the whole specimen (a) and a middle clip (b).

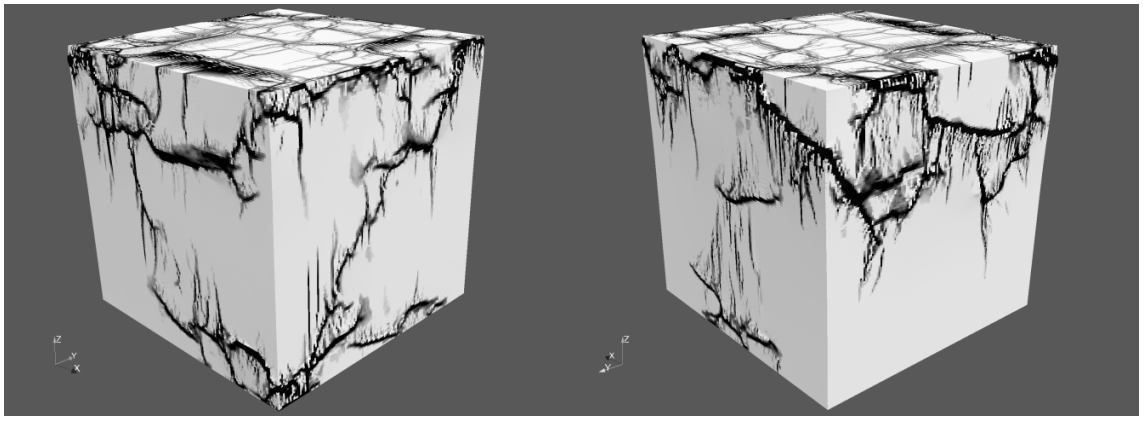

(a)

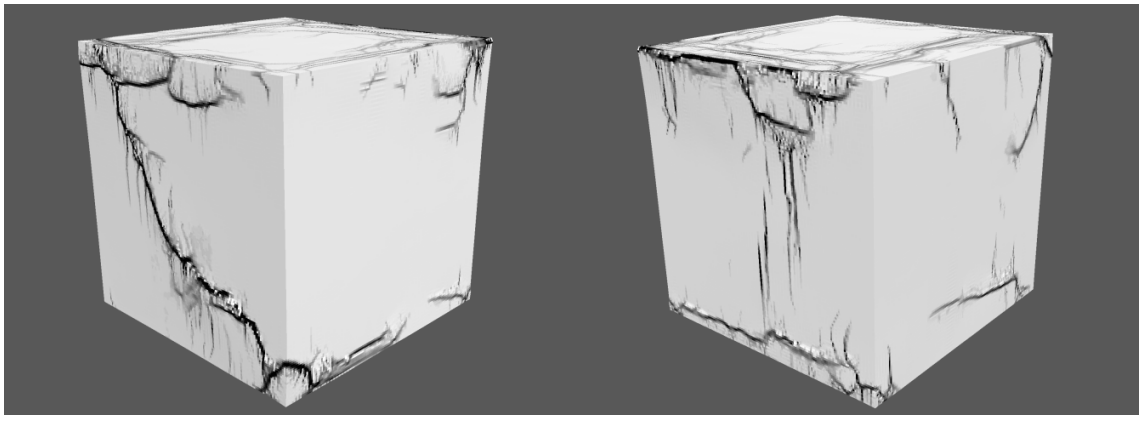

(b)

Figure 13: Simulation patterns: cracking of the ceramic composite with 15% content of hardening particles (2 views from opposite sides) at ideal sliding (a) and fixing (b) on the loading border.

CONCLUSIONS

In the considered model of medium the limiting condition in the loaded material is formed during loading and depends on the stressed state kind.

Studying the laws of brittle and quasibrittle failure of composite ceramic materials with the usage of the developed model of quasibrittle medium it was shown that failure process always educes in two stages - slow steady accumulation of inelastic deformations and damages in all hierarchy of structurally-scale levels as the quasistationary phase is replaced by the blow-up regime – the superfast catastrophic phase of evolution of system when the failure process reaches the macrolevel.

At ideal sliding on the loading border failure has a brittle character when the linear steepening of stresses is followed by the global loss of stability and degradation of elastic and strength properties of composites to zero. At friction on the loading border the stage of pre-failure inelastic deforming of the composites with formation of the local areas of the strength loss which occupies some percent of macrodeformation is observed. Thus the stage of evolution of system in the blow-up regime is tightened.

In the case of constrained deformation the other scenario of the composite evolution is observed. The resource of elastic and strength properties of medium is spent gradually. During the general evolution of the system in the blow-up regime the sequence of steepens and relaxations of stresses on the $\sigma - \varepsilon$ diagram is observed.

It is shown that brittle and quasibrittle failure of materials descends mainly in the tension stresses areas where the rate of elastic and strength properties degradation of medium is bigger on several orders. At pre-failure stage the confluence of the mesocracks in percolation net evolves in the macrocracking at the final stage of deforming.

REFERENCES

[1] V.E. Panin, A.D. Korotaev, P.V. Makarov, V.M. Kuznetsov, Izvestiya of the High schools. Physics, 9 (1998) 8.
[2] P.V. Makarov, Phys. Mesomech, 11 (3) (2008) 19.
[3] S.P. Kurdyumov, Blow-up regimes. Idea evolution, Ed. G.G. Malinetsky, 2nd ed., Fizmatlit, (2006) 312.
[4] P.V. Makarov, Phys. Mesomech, 13(5) (2010) 97.
[5] V.Z. Parton, E. M. Morozov, Mechanics of elasto-plastic failure, Science, (1974) 416.
[6] P.V. Makarov, Geology and geophysics, 48(7) (2007) 724.
[7] P. V. Makarov, I. Yu. Smolin, Yu. P. Stefanov, Nonlinear mechanics of geomaterials and geomedia, Novosibirsk, SB RAS Geo, (2007) 235 .
[8] P.V. Makarov, Phys. Mesomech, 8 (6) (2005) 39.
[9] E. P. Evtushenko, M. O. Eremin, Yu. A. Kostandov, P.V. Makarov et alii, Phys. Mesomech, 15(3) (2012) 35.
[10] I. A. Garagash, V. N. Nikolaevskiy, Successes of mechanics, 12(1) (1989) 131.
[11] S. N. Zhurkov, B. N. Narzulaev, ZhTF, XXIII(10) (1953) 1677.
[12] A.V. Stepanov, Basics of the practical crystal strength, Science (1974) 131.
[13] V. R. Regel, A. I. Slutzker, E. E. Tomashevskiy, Science, (1974) 560.
[14] I.I. Frenkel, Introduction to the metals theory, Fizmatlit, (1958) 424.
[15] R. Becker, Physikalische zeitschrift, 25(7) (1925) 919.
[16] E. J. Orowan, The creep of metals, West Scot. Iron and steel Inst., 54 (1947) 45.
[17] M. L. Wilkins, Computer simulation of dynamic phenomena, Heidelberg, Springer, (1999) 265.
[18] G. I. Barenblatt, G.P. Cherepanov, Izv. Of USSR AS, Mechanics and Mechanical engineering, 3 (1960).
[19] Yu. P. Stefanov, Phys. Mesomech, 8(3) (2005) 129.
[20] Yu. A. Kostandov, P. V. Makarov, M. O. Eremin, I. Yu. Smolin, I. E. Shipovskii, International Applied Mechanics, 49 (1) (2013) 95.
[21] B. Paliwal, K. T. Ramesh, J. of the Mechanics and Physics of Solids, 56 (2008) 896.
[22] S. V. Panin, P. S. Lyubutin, S. P.Buyakova, S. N. Kulkov, Phys. Mesomech, 11(6) (2008) 77.
[23] J. D. Kuntz, G. D. Zhan, A. K. Mukherjee, MRS Bull., 29 (2004) 22.

Impact loading of a space nuclear powerplant

Evgeny I. Kraus, Ivan I. Shabalin
Khristianovich Institute of Theoretical and Applied Mechanics of Siberian Branch of RAS
Institutskaya str. 4/1, Novosibirsk 630090, Russia
kraus@itam.nsc.ru

ABSTRACT. Preferred formulation of the problem in two space dimensions are described for solving the three fundamental equations of mechanics (conservation of mass, conservation of momentum, and conservation of energy). Models of the behavior of materials provide the closure to the three fundamentals equations for applications to problems in compressible fluid flow and solid mechanics. Models of fracture and damage are described. A caloric model of the equation of state is proposed to describe thermodynamic properties of solid materials with the phase transitions. Two-dimensional problems of a high-velocity impact of a space nuclear propulsion system reactor are solved. High-velocity impact problems of destruction of reactor are solved for the two cases:
1) at its crash landing on the Earth surface (the impact velocity being up to 400 m/s);
2) at its impact (with velocity up to 16 km/s) with the space debris fragments.

KEYWORDS. Equation of state; Shock waves; High-velocity impact.

INTRODUCTION

The problem of quantitative description of the impact is a rather complex task, therefore it is connected with a whole scientific and technical research area rapidly developing lately. The bodies collision is accompanied by various processes, which emergence and relative role depend on the shape and physical characteristics of the objects and, more importantly, on the relative velocity of their collision. Moreover, the collision is often accompanied by penetration of one body into the other. In the process of high-speed collision, one or both of the bodies collided can collapse, scatter, or disperse, followed by dissipation of a significant amount of energy.
In emergency situations, modern space vehicles with thermionic reactors "shoot off" (jettison) the nuclear powerplants (a simplified sketch of such a powerplant is shown in Fig. 1). There is a certain probability, however, that the reactor fragment containing the nuclear fuel reaches the Earth's surface despite considerable thermal and mechanical loads in dense atmospheric layers. The velocity of the impact of the remaining part of the reactor system can reach 400 m/s.
It is next to impossible to solve impact problems of real engineering objects though the computational engineering development level is rather high and fairly realistic mathematical models of material behavior are available. The reasons are the complicated spatial locations of the reactor fragments and the multiscale character of the problem. In such situations, the object considered is simplified, which makes it possible to construct a number of models aimed at studying the influence of the impact parameters on particular basic fragment of the object.
The simplification used implies that the materials of small-scale parts were averaged inside the reactor zone in the additive approximation. The mass of the non-principal materials was assumed to be too small (beryllium, uranium dioxide and zirconium hydride compose 95—97 % of the reactor mass) to exert any significant effect on the shock-wave amplitude. As such a medium (mixture) does not have the volume defects, its specific volume on the wave front can be calculated as

$$V_{\text{mix}}(P)=\sum_{i=1}^{n}\alpha_i V_i(P),\ \alpha_i=\frac{m_i}{\sum_{i=1}^{n}m_i},\quad \sum_{i=1}^{n}\alpha_i=1,$$

where V_i is the specific volume of the i-th species under shock compression of each species separately, n is the number of species in the mixture, and α_i is the mass concentration, m_i is the mass of the i-th species.
Thus, our study is based on the assumption that the additivity rule is satisfied rather accurately. In the additive approximation, the volume of the shock-compressed mixture is assumed to be equal to the sum of the volume of the species obtained at the same pressure with their separate shock compression in the form of homogeneous monolithic samples.

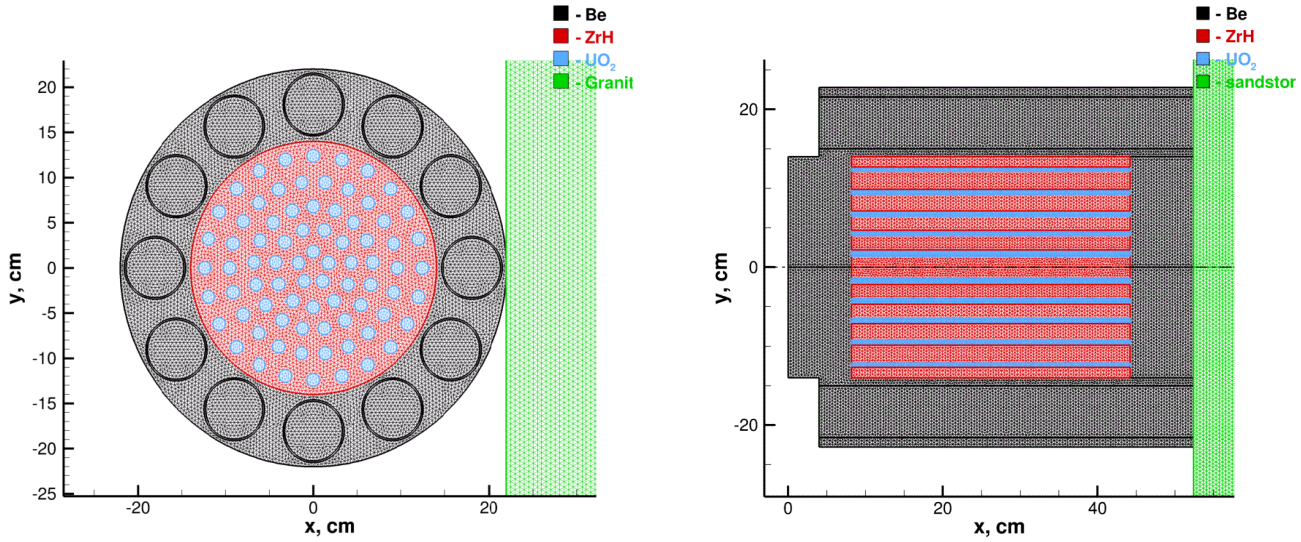

(a) (b)

Figure 1: (a) Reactor "Topaz" with plane geometry; (b) Reactor "Topaz" with axial geometry.

It was further assumed that the external elements of the structure burn down when the reactor enters the dense atmospheric layers, and the reactor remainder is an object with a complicated internal structure illustrated in Figs. 1. The reactor consists of a beryllium shell, uranium dioxide fuel cells, and zirconium hydride fillers. The end-face (longitudinal) and side impacts were considered. In the first case, we have a problem of an impact of the cylinder side surface onto a deformed target. A specific feature of this formulation of the problem is a multiply connected computational domain with a large number of contact surfaces. In the second case, the reactor model is formed as a ring-shaped structure, while the computational domain is again multiply connected and numerous contact surfaces are formed (Fig. 1).

MATHEMATICAL PROBLEM

The problem was solved in a formulation proposed by Wilkins [1] with the symmetric algorithm of contact boundary calculation [2]. Previously, we proposed the process of automatic construction of a triangular grid for an arbitrary multiply connected domain [3-4].
According to [1] we used Lagrange coordinates permits the history of mass elements to be followed where the integrated effects of plasticity and external loads change the material physical properties. In order to describe all the dynamic processes, firstly, the main conservation laws must be taken into account (mass, momentum, energy and equation of state), elastic and Prandtl-Reuss stress-strain relations:

- equations for tracks of the material particles: $\dot{x}_i = u_i$
- conservation of mass: $V_0\rho_0 = V\rho$
- conservation of momentum: $\rho\dot{u}_i = \sigma_{ij,j}$

- conservation of energy: $\rho\dot{e} = \sigma_{ij}\dot{\varepsilon}_{ij}$

- the strain rate tensor: $\dot{\varepsilon}_{ij} = 0,5(u_{i,j} + u_{j,i})$

Stress tensor is represented in the conventional $\sigma_{ij} = -\delta_{ij}P + s_{ij}$, where

- s_{ij} : deviator of the stress tensor
- P: pressure
- ρ: density
- u: speed

Prandtl-Reuss stress-strain relations

$$\overset{\nabla}{s}_{ij} + d\lambda' s_{ij} = 2G\dot{\varepsilon}'_{ij}, \qquad \dot{\varepsilon}'_{ij} = \dot{\varepsilon}_{ij} - \dot{\varepsilon}_{ij}\frac{\delta_{ij}}{3}$$

with the plastic strain increments given by Levy-Mises Equation

$$s_{ij}s_{ij} \le \frac{2}{3}Y_0^2$$

where G -shear modulus, Y_0 - dynamic yield stress, for definition scalar $d\lambda'$ known procedure used to bring to the yield circle.

The plastic flow will be described by conserving the deviator of stress tensor at the elastic limit. We will assume that after the deformation increase, the stresses change and exceed the yield circle. This contradicts the yield condition and cannot be realized. Instead, we will assume that a plastic flow takes place in the material and the stresses remain at the elastic limit, i.e. on the yield circle.

The plastic part of the deformations is perpendicular to the yield surface that leads to limitation of exactly those stresses which are connected with this part of the deformations. Thus, summarizing the assumption about the yield, we can write down the yield condition in the terms of the stress tensor deviator.

An algorithm realizing such a condition was proposed by M.L. Wilkins [1]. If a redundant change of the stresses in a particular element has led to a law violation, then the main values of the stress tensor deviator have to be corrected in such a way, that the condition is met again.

EQUATION OF STATE

We consider the three-term Mie-Grüneisen equation of state with the solid-phase free energy being determined as

$$F(V,T) = E_x(V) + c_{v,l}T\ln\left(\frac{\theta(V)}{T}\right) - \frac{1}{2}c_{v,e0}T^2\left(\frac{V}{V_0}\right)^{2/3} \qquad (1)$$

where V is the specific volume, $E_x(V)$ is the "cold" energy, T is the temperature, $c_{v,l} = 3R/A$ is the specific heat of the lattice at constant volume, A is the mean atomic weight, R is the gas constant, $\theta(V)$ is the Debye temperature, and $c_{v,e0}$ is the experimental value of the electron heat capacity under standard conditions. The elastic (cold) component of energy $E_x(V)$ is related exclusively to interaction forces between the body atoms and is equal (including the energy of zero vibrations) to the specific internal energy at the absolute zero temperature.

The thermodynamic model of a few-parameter equation of state is based on the dependence of the Grüneisen parameter γ on the volume

$$\gamma(V) = \frac{2}{3} - \frac{2}{(1 - aV_0/V)} \quad a = 1 + \frac{2}{(\gamma_s - 2/3)} + \frac{2P_{t,0}}{K_s} \qquad (2)$$

where $\gamma_s = \beta K_s V_0 / c_v$, K_s is the adiabatic modulus of volume compression, c_v is the specific heat at constant volume, and $P_{t,0}$ is the thermal pressure in the initial state.

The general expression for the volume dependence of the Grüneisen parameter has the form

$$\gamma(V)=-\left(\frac{2-t}{3}\right)-\frac{V}{2}\left[\frac{d^2}{dV^2}\left(P_x V^{\frac{2t}{3}}\right)\Big/\frac{d}{dV}\left(P_x V^{\frac{2t}{3}}\right)\right] \tag{3}$$

In Eq. (3), the situation value corresponds to the Landau-Slater theory [5, 6] at *t=0*, to the Dugdale-McDonald theory [7] at *t=1*, and to the free-volume theory [8] at *t=2*.

To determine the zero isotherm, we equated the expression for the Grüneisen parameter (2) at the zero temperature ($T=0\mathrm{K}$) to the expression for the generalized Grüneisen parameter (3):

$$\frac{2}{3}-\frac{2}{1-a_x V_0/V}=-\left(\frac{2-t}{3}\right)-\frac{V}{2}\left[\frac{d^2}{dV^2}\left(P_x V^{\frac{2t}{3}}\right)\Big/\frac{d}{dV}\left(P_x V^{\frac{2t}{3}}\right)\right] \tag{4}$$

Here, a_x is the value of the parameter $a\big|_{T=0}$ at the zero temperature in Eq. (2), which can be taken $a_x=a(0)=1+2/(\gamma_s-2/3)$ as the first approximation.

The differential Eq. (4) has an analytical solution for "cold" pressure and energy:

$$P_x(V)=C_1V^{-2t/3}+C_2H_2(V) \qquad E_x(V)=-\left(C_1V^{1-2t/3}/(1-2t/3)+C_2H_1(V)\right)+C_3 \tag{5}$$

Using the definition of the Grüneisen parameter in the Debye approximation $\gamma=-\left(d\ln\theta/d\ln V\right)\big|_T$ and Eq. (2), we obtain the characteristic Debye temperature on the volume:

$$\theta(V)=\theta_0\left[\frac{(a-V/V_0)}{(a-1)}\right]^2\left(\frac{V_0}{V}\right)^{\frac{2}{3}}$$

where $\theta_0=\theta(V_0)$ is the Debye temperature at the initial conditions.

The constants for Eq. (5) were determined and calculated in Fig.2 and [9]. It was also demonstrated there that the set of semi-empirical relations (1)-(5) describes the behavior of thermodynamic properties of solids within 5-10% in a wide range of pressures and temperatures. For the equation of state to be applied, it is sufficient to know only six constants V_0, β, K_t, c_v, Θ_0, and $c_{v,e0}$ corresponding to the values of these quantities under standard conditions, which can be found in reference books on physical and mechanical properties of substances.

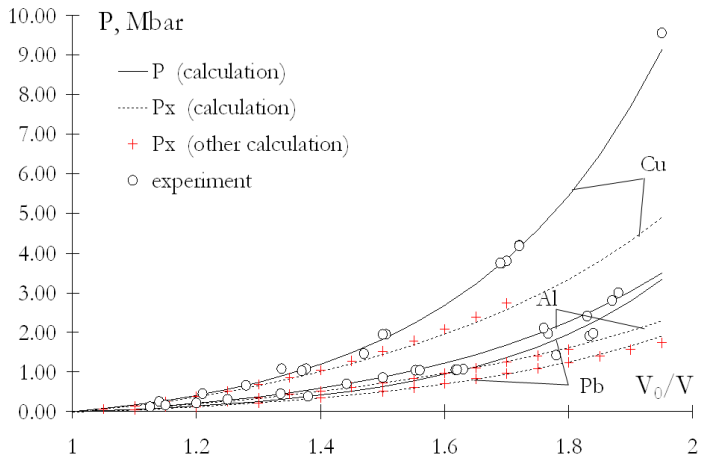

Figure 2: Adiabat solid. Experiments [10]

MODIFICATION OF THE EQUATION OF STATE.

Thermodynamic and kinetic properties of liquids usually cannot be predicted theoretically on the basis of the first principles only. The calculation of phase diagrams is additionally complicated by the fact that the most important characteristics of phase transitions (heat of transition, difference in phase densities, etc.) are small differences in

quantities that have large values and cannot be calculated with sufficient accuracy. Because of thermodynamic nonequilibrium typical for polymorphic transformations in shock waves, the general thermodynamic relations for phase transitions (equality of chemical potential in the region of simultaneous existence of the phases and Clausius-Clapeyron equation) as applied to shock-wave processes can only be used as approximate estimates. Therefore, beginning from the famous van der Waals' paper, numerous attempts have been made to construct the dynamics of a liquid substance by extrapolating the known thermodynamic functions from different areas of the phase diagram. The absence of a commonly accepted thermodynamic model for liquids, which would be equivalent to the Debye approximation for the crystalline state, is a severe obstacle for constructing the equation of state for liquids.

In studying particular models of thermodynamic states, it is clear that the usual classification of states in the region of high pressures and temperatures often loses its definiteness and becomes conventional, while the boundaries between the phases either disappear altogether or get fuzzy and actually correspond to continuous mutual transformation of states close to each other. The substance is both compressed and heated in the shock wave. In comparatively weak shock waves propagating over a cold substance, however, the pressure is mainly increased owing to compression. The pressure growth rate in relative units exceeds the temperature growth rate, and the increase in the "cold" compression energy is much greater than the increase in the thermal energy. As the shock wave intensity increases, the relative contribution of the thermal components of pressure and energy increases and becomes prevailing in strong shock waves.

To take into account melting, the equation for a solid body (1) is modified. Though the phonon spectrum in the liquid phase is obviously a non-Debye spectrum (as the liquid does not have the far order, its molecules do not have forbidden states; hence, the molecular motion is not discrete), such a modified model can provide positive results at sufficiently high densities of the liquid near the line of phase equilibrium between the liquid and solid phases, because the motion of a liquid molecule within the first coordination sphere at rather high densities can be conventionally considered as vibrational motion. Thus, the higher the pressure, the more precisely the model is satisfied.

The expression for the free energy $F_L(V,T)$ of a monatomic liquid in the so-called rough classical model of the harmonic oscillator has the form

$$F_L(V,T) = E_{x,L}(V) + c_{v,l}T\ln\left(\frac{\theta_L(V)}{T}\right) - \frac{1}{2}c_{v,e0}T^2\left(\frac{V}{V_{0,L}}\right)^{2/3} - \frac{RT}{A} \qquad (6)$$

where $E_{x,L}(V)$ is the "cold" component of the internal energy of the liquid and $\theta_L(V)$ is the characteristic "Debye temperature" of the liquid.

Formally, the expression for the free energy of the liquid (6) differs from the expression for the free energy of the solid (1) only by the presence of an additional entropy term $F_c = -RT/A$. Nevertheless, the differences between the solid and liquid states are much more essential. Thus, different cold curves are used to describe the solid and liquid states.

First, the major part of the entropy jump is related to the change in the solid structure due to the transition to the liquid state, which is caused by the loss of the far order and leads to the formation of a collective or configuration entropy (equal to zero in an ideal crystal) in thermodynamic models of the liquid. The configuration part of the entropy $S_c = -\partial F_c/\partial T$ characterizes the measure of liquid disordering and should remain a finite quantity (similar to the entropy of amorphous solids) as the temperature formally tends to zero $T = 0K$.

Second, the zero isotherm of the liquid is shifted with respect to the zero isotherm of the solid toward lower densities. The primary reason is that the liquid-phase density extrapolated to the domain of low temperatures is somewhat lower than the density of the solid substance.

These principal differences between the thermodynamic descriptions of the liquid and solid states form the basis for the thermodynamic model modification considered in the present work. Thermodynamic functions of both solids and liquids are formally examined in the entire temperature range, including the domain close to $T = 0K$. This is convenient for a unified description of both phases and allows functions typical for the solid state (such as the density at the temperature $T = 0\mathrm{K}$, zero isotherm, etc.) to be used to describe the liquid state thermodynamics. We assumed that the physically meaningful branches are those at $T > T_m$ for the liquid state and at $T < T_m$ for the solid state (T_m is the melting temperature).

To "control" the configuration entropy we introduced a certain parameter a_s, which has the meaning of the residual entropy at the temperature $T = 0K$. Then, the entropy term of the free energy of the liquid in Eq. (6) takes the form $F_c = -a_s RT/A$, which does not contradict the approximation of the "rough" model of the liquid at $a_s = 1$. This

fitting parameter makes it possible to define correct values of the entropy and specific volume jumps on the melting curve.

Considerations used to derive the expression for the Grüneisen parameter are not confined to the condensed phase. For this reason, all relations in contain only the general thermophysical properties of the material, which are defined and have an identical meaning both for the solid and form the liquid states. Therefore, repeating all transformations applied in solid, we can obtain equations for $E_x(V)$, $P_x(V)$, etc., whose functional form is similar to those for the solid state. The differences are only in the parameters determined by particular initial conditions. Therefore, the use of the modified equation of state requires only six constants, as the equation for the solid phase. The constants for several liquid metals can be found in. Moreover, the liquid model requires the jumps of the volume ΔV and entropy ΔS due to melting to be known.

MELTING AT HIGH PRESSURES BEHIND THE FRONT OF A STRONG SHOCKWAVE

The phase transition of the first kind (melting) is understood as an equilibrium transition of the substance from one phase to another with jump-like changes in the first derivatives of the Gibbs energy G with respect to temperature and pressure, i.e., the entropy S and specific volume V experience jump-like changes during melting:

$$S = -\left(\frac{\partial G}{\partial T}\right)_p \qquad V = \left(\frac{\partial G}{\partial P}\right)_T$$

The entropy of the liquid phase is always greater than the entropy of the solid; therefore, the entropy change during melting is always positive. The change in the volume during melting, however, can be either positive or negative. The inequalities $\Delta S > 0$ and $\Delta V > 0$, which mean greater orderliness and density of the crystalline phase as compared with the melt, seem to be natural. They are valid for most substances and ensure a positive slope of the melting curve $dP/dT > 0$. At the same time, there are some substances (e.g., gallium, bismuth, and water) with negative values of this derivative $dP/dT < 0$.

As the shock-wave pressure increases, the thermal energy imparted to the substance continuously increases and the transition of the initially solid substance to the liquid state is expected to start at a certain pressure level. The further behavior of the dependence $T(P)$ along the dynamic adiabat can be understood by analogy with melting at atmospheric pressure, where an increase in the energy imparted to the substance starting to melt does not lead to an increase in temperature until the substance becomes completely melted. Further heating of the liquid is accompanied by an increase in temperature. A similar pattern should also be observed under shock compression, with the only difference that a certain increase in temperature can be expected in the domain of simultaneous existence of two phases (segment of the melting curve between the shock adiabats for the solid and liquid substances, in Fig. 3), because $dT / dP > 0$ for the melting curve of the majority of substances (so-called "standard" substances).

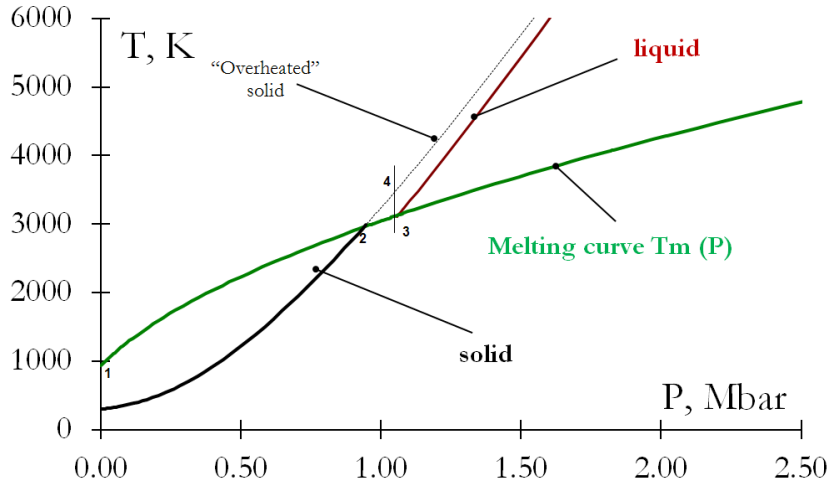

Figure 3: Melting curve and shock adiabats in the domains of the solid and liquid phases.

To construct the melting curve, we use the phase equilibrium condition

$$\begin{cases} P_L = P_S \\ T_L = T_S \\ F_L = F_S + P\Delta V_m \end{cases} \quad (7)$$

The last equation in (7) is the equality of the chemical potentials of both phases per 1 mole of the substance. The subscripts refer to the solid state (S), liquid state (L), and values on the melting curve (m).

CALCULATION RESULTS OF EOS

Using the system of equations of state of the solid (1) and liquid (6) phases and taking into account the phase equilibrium condition (7), we calculated the dynamic adiabats and the melting curves for several metals.

The numerical calculations were performed by an iterative method. The shock adiabat of the solid body was used as the reference curve. In this case, we first assumed that $a_s = 1$ in Eq. (6) and chose a value of a_x in Eq. (4) that ensured the minimum difference between the calculated and the reference shock adiabats of the liquid. After that, for this value of a_x, we found the value of as from the condition of identical chemical potentials of the solid and liquid phases for specified entropy and volume jumps on the melting curve. After that, the procedure was repeated with the new value of a_s.

The calculated adiabats with the phase transition in the $T-P$ coordinates are shown in Fig. 3. The correctness of taking into account melting behind the shock-wave front in the equation of state derived is indirectly confirmed in the paper of Sakharov [11] who measured the viscosity behind the shock-wave front in aluminum and concluded that it remains in the solid phase up to pressures of 1 Mbar. The calculations show (see Fig. 4) that aluminum melting begins at the pressure P=1.07 Mbar. The transition of Al to the liquid state is finalized at the pressure P=1.2 Mbar.

The calculation for lead shows (see Fig. 4) that Pb melting begins at the pressure P=0.36 Mbar. The transition of Pb to the liquid state ends at the pressure P=0.41 Mbar. The result obtained is in reasonable agreement with the data [12], where it was noted that melting in the shock wave begins when the mass velocity reaches ~ 650-700 m/s, which corresponds to pressures of 0.23–0.25 Mbar. In [13] experiment, lead behind the shock-wave front is already in the melted state at pressures of 0.4 Mbar.

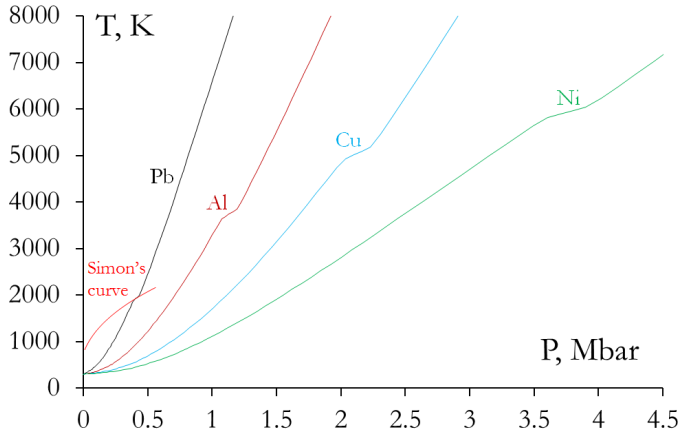

Figure 4: Shock adiabats of metals with allowance for melting.

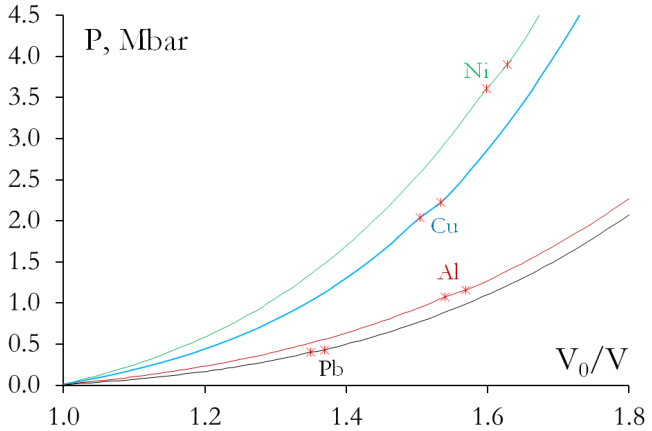

Figure 5: Shock adiabats of metals with allowance for melting.

In accordance with Urlin theoretical predictions [14], we performed calculations (Fig. 5), which show that melting exerts a minor effect on the adiabat shape in the $P-V$ coordinates. The inflections on the diagram in Fig. 5 are so small (the melting zone is indicated by the asterisks) that they can be hardly distinguished visually. The values of these inflections are comparable with the error of data obtained in shock experiments.

Now let us consider the melting curve found as the boundary between the phases with the corresponding equations of state. Fig. 6 shows the melting curve calculated for aluminum, the experimental data and Simon's melting curve. The calculated melting curve lies somewhat lower than the optimal curve, and the error of calculating the temperature on the melting curve is smaller than 10% in the entire range of pressures considered.

Fig. 7 shows the lead melting curve and the experimental data; the results are seen to be in good agreement. As an estimate, the figure also contains Simon's melting curve for lead extrapolated to the range of high pressures. As the parameters were chosen on the basis of low-temperature experiments, Simon's melting curve underestimates the melting temperatures in the high-pressure domain.

Comparing the calculated results with available experimental data, we can conclude that the calculation accuracy is fairly high and the phase equilibrium condition (7) can be used for calculating the melting curves for the metals considered.

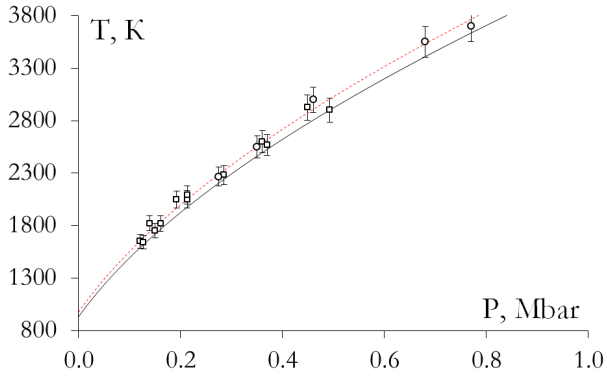

Figure 6: Melting curve for Al. The solid curve is the present calculation; the experimental data ☐ and ○ [15, 16]. The dashed curve is Simon's melting curve.

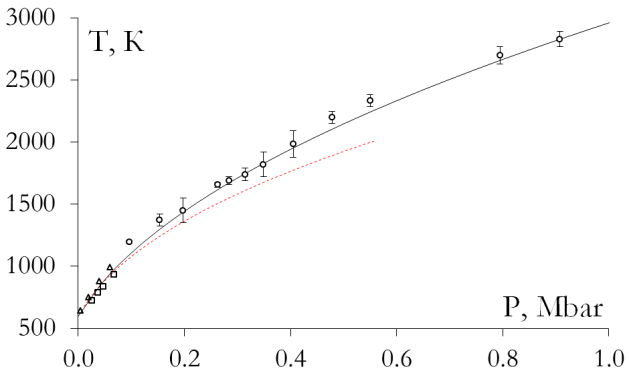

Figure 7: Melting curve for Pb. The solid curve is the present calculation; the experimental data are indicated by ○ , △ , and ☐ [17-19]. The dashed curve is Simon's melting curve.

FRACTURE

Kinematic strength characteristics include the limiting values of elongation (usually under uniaxial tension) and shear. Brittle materials are also destroyed by compressive strains. Kinematic characteristics are accumulated quantities incorporating the entire history of the process. The most frequently used quantities are the limiting elongation and shear strain. Finding these quantities involves calculation of the primary tensile and compressive strains

$$\varepsilon_1 = \frac{\varepsilon_{xx} + \varepsilon_{yy}}{2} + \sqrt{\left(\frac{\varepsilon_{xx} - \varepsilon_{yy}}{2}\right)^2 + \varepsilon_{xy}^2}$$

$$\varepsilon_2 = \frac{\varepsilon_{xx} + \varepsilon_{yy}}{2} - \sqrt{\left(\frac{\varepsilon_{xx} - \varepsilon_{yy}}{2}\right)^2 + \varepsilon_{xy}^2}$$

and also the shear strain

$$\varepsilon_\tau = \frac{(\varepsilon_1 - \varepsilon_2)}{2}$$

If the tensile strains in the course of deformation exceed the limiting elongation ε_1^* (i.e., $\varepsilon_1 > \varepsilon_1^*$) or the limiting shear strain $\varepsilon_\tau > \varepsilon_\tau^*$, ε_τ^*, then the element material is assumed to be fractured, i.e., it has no longer resistance to tension and shear, but still has resistance to compression.

Force strength parameters include the limiting values of tensile [20], compressive, and shear stresses. If the stresses proper are used, then they are instantaneous criteria, i.e., as soon as the principal stresses exceed the limiting values, the element material is assumed to be fractured:

$$\begin{cases} \sigma_1 > \sigma_1^* \\ \sigma_2 > \sigma_2^* \\ \sigma_\tau = \dfrac{(\sigma_1 - \sigma_2)}{2} > \sigma_\tau^* \end{cases}$$

Most material, however, possess properties of plasticity and viscosity; therefore, their fracture requires a time interval during which the material is under overstrain. The code involves one of such criteria (it is demonstrated by an example of the principal tensile stress) [21]:

$$\sigma_t = \frac{\sum_{i=n_1}^{n_2} (\sigma_1 - \sigma_1^*)_i \Delta t_i}{\sum_{i=n_1}^{n_2} \Delta t_i} > \sigma_t^* \qquad \sigma_1 - \sigma_1^* > 0$$

CONVERSION OF FRACTURED ELEMENTS TO PARTICLES

If the element is at the boundary of the computational domain and the parameters of the material reaches a limited value, the material of the element is replaced by discrete particles. Radius of the particle is calculated from the condition of incorporating one or more of the particles in the element. Mass of the element is allocated between the discrete particles. For one time step is only one layer of boundary elements can be converted into discrete particles, as is that the velocity of the wave front of destruction does not exceed the speed of disturbances in the medium [2]. Fig. 8 shows conversion of triangle elements (A, B and others) to particles [22]:

- ✓ Element A is removed from the element grid;
- ✓ Particle A is added as a particle node;
- ✓ All of the element variables (stress, strain, damage, etc.) are transferred to the particle;
- ✓ The mass, velocity and center of gravity of the particle node are set to those of the replaced element. The nodal velocity is obtained from the momentum of the element (three nodal masses and velocities);
- ✓ The masses of nodes b, c and k are reduced by the removal of element A;
- ✓ For the conversion of element B (which has two sides on the surface) to node B; most of the steps are similar to those used for element A.

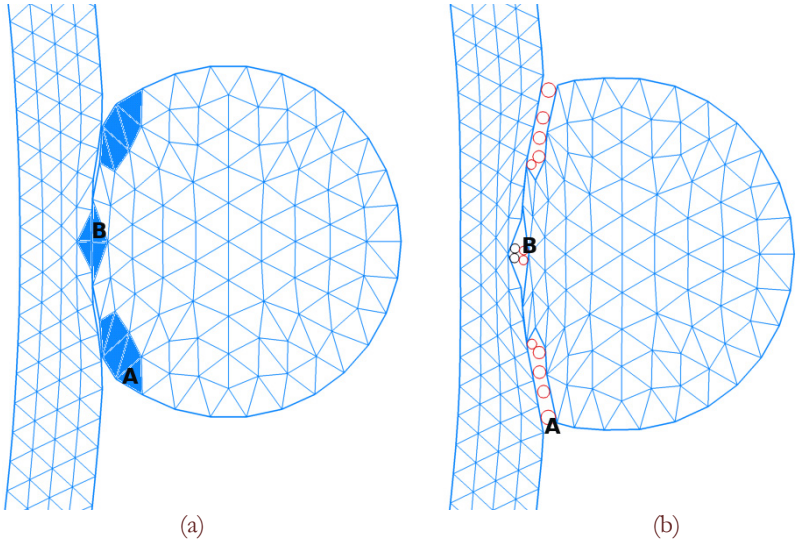

Figure 8: Conversion of triangle elements to particles: (a) interface nodes and elements before conversion; (b) interface after conversion of elements.

TWO-DIMENSIONAL PROBLEM OF THE IMPACT OF A MODEL NUCLEAR POWERPLANT "TOPAZ" ONTO THE EARTH'S SURFACE

As the first example, we consider an impact of the reactor on sandstone with the initial velocity of 400 m/s in the axial formulation. Realistic photo of the nuclear powerplant with thermionic reactors for space applications "Topaz" is illustrated in Fig. 9. Geometry of the reactors is illustrated in Fig. 1. In the case of the reactor impact

onto sandstone, the wave pattern is complicated by the fact that sandstone is destroyed by compressive stresses. This specific feature is induced by the inner structure of sandstone where strong crystals of sand are bound with brittle cement mass. As sand and cement have different compressibility, the shock wave forms shear stresses on interfaces between the media, which destroy the connections on the boundary, i.e., the resultant product is sand with a fine fraction of cement. Free sand exerts practically no resistance to shear strains. Thus, the impact compression forms a domain of a fractured material near the reactor-sandstone contact surface and, as a consequence, an unloading wave. The interaction of the side unloading waves and the unloading wave from the fracture zone leads to formation of a zone of tensile stresses with a higher amplitude, leading to fracture of the reactor materials (zirconium hydride filler and fuel cells). Beryllium shell fracture follows the mechanism of shear-induced quasi-static fracture. Fig. 10 shows the frames of the impact of the reactor model onto sandstone.

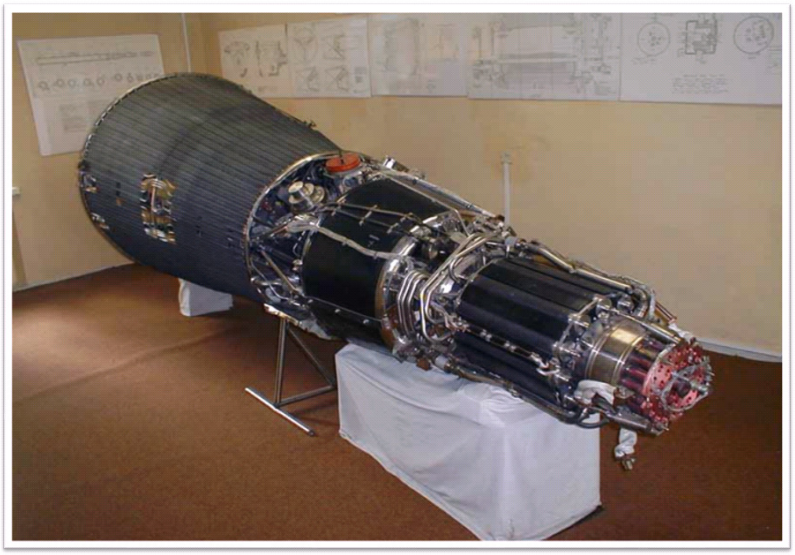

Figure 9: Nuclear powerplant with thermionic reactors for space applications "Topaz".

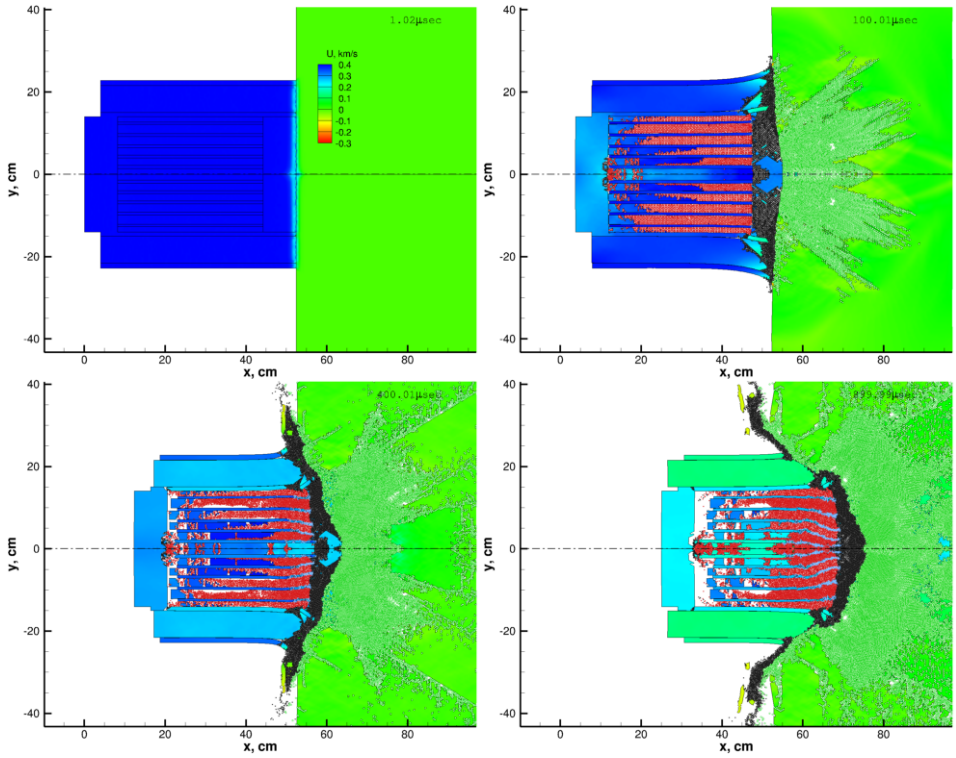

Figure 10: Impact of a reactor model with a sandstone plate surface.

Let us further consider the computation of the side impact of the nuclear powerplant. Fig. 11 shows the frames of the computed side impact of the reactor on a granite plate with an impact velocity of 400 m/s. This computation shows that the side impact of the reactor is more critical in terms of the impact velocity than the end-face impact because of higher strains in the contact area. While moving, the reactor filler (which is heavier) weighs on the beryllium shell, thus, inducing shear fracture in the contact area with the granite plate and inner fracture of the casing material, which violates the reactor proofness. Numerous cracks appear in the ZrH filler, which results in disintegration of fuel cells and, as a consequence, possible radioactive contamination of the place of incidence of the reactor.
It should be noted that the results of calculations in the 2D planar case show a loss of symmetry in space. This is because the build perfectly symmetrical grid for complex bodies is not possible. Enough small deviations from symmetry lead to small differences in the strains, but near the critical values of this causes no symmetry of fracture in the space. To impact at the normal calculation can be performed in one half of that mathematically ensures symmetry of fracture. However, in practice we generally are not spatially symmetric picture of damage.

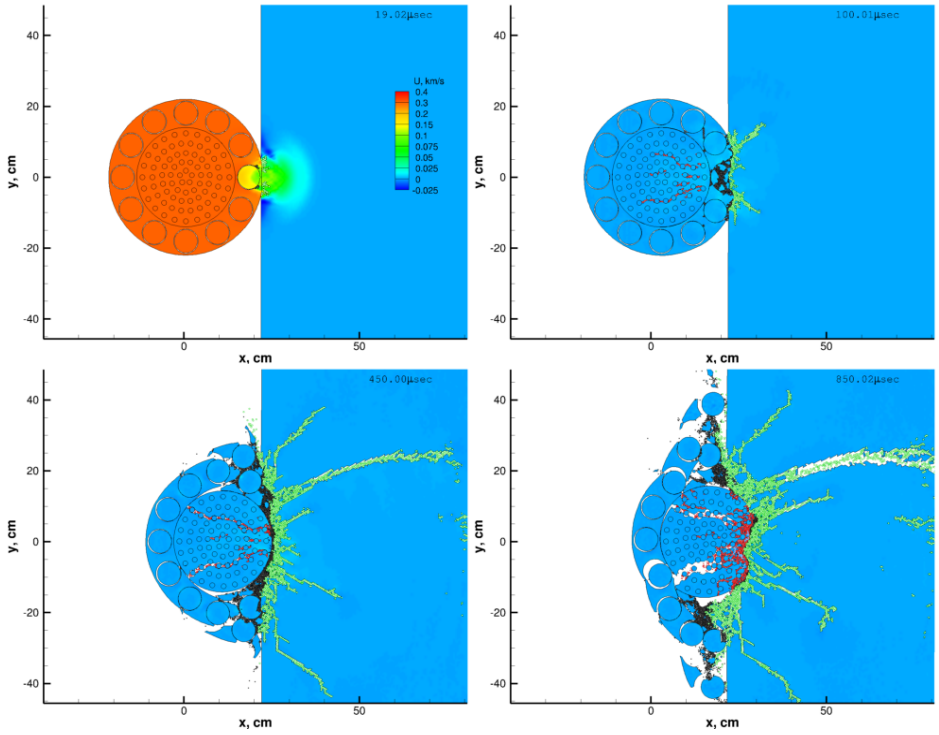

Figure 11: Frames of the calculated side impact of the reactor model onto the granite plate surface

Calculations of reactor destruction due to its collision with space debris on the orbit ("Topaz")

In the first calculation, a two-dimensional reactor model interacts with a steel object 3 cm in diameter with a velocity of 11.7 km/s. This velocity is the most probable one for collisions with space debris fragments. The calculation is performed for a reactor model protected by the Whipple shield (aluminum sheet 2mm thick surrounding the reactor). The experiment shows that the kinetic energy of the object with such a velocity is sufficient for penetration through the target, acceleration of the expelled mass, and fragmentation of the impinging object and expelled part of the target. Shock waves arising during target penetration are reflected from free surfaces as unloading waves whose interference generates strong tensile waves in the materials of the Whipple shield and the impinging object. The parameters of the resultant waves are substantially higher than the strength characteristics of the materials, which leads to fragmentation of the structure and to formation of a cloud of fragments behind the target. The further interaction between the cloud and the reactor model proceeds in accordance with the following scenario: the cloud of fragments of the destroyed projectile almost with the initial impact velocity reaches the beryllium shell of the reactor. The remaining part of the cloud also contacts the reactor shell with a certain delay. Despite the presence of the Whipple shield, the kinetic energy of the cloud

of particles is sufficient for destroying the reactor shell made of beryllium. Multiple interactions of particles form a stable spherical shock wave, which destroys not only the shell, but also the zirconium hydride interior and uranium fuel cells. Fig. 12 shows the frames of the interaction of the cloud of fragments with the reactor. The presence of beryllium cylinders in the shell structure is manifested only as an additional stress concentrator and results in more expressed destruction on the shell edges, but exerts practically no effect on the overall pattern of shell failure.

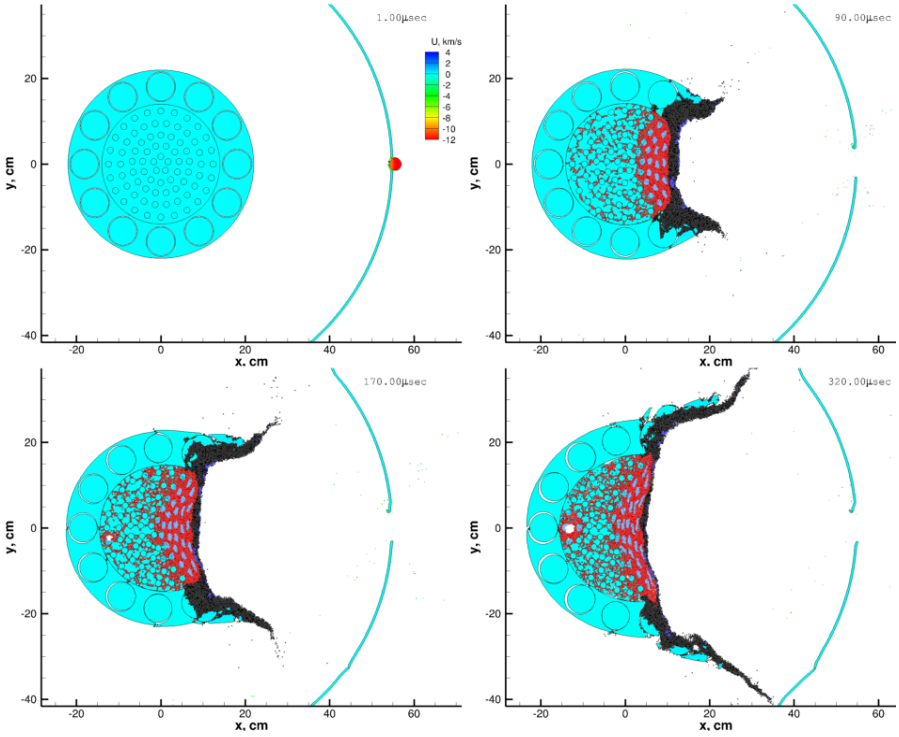

Figure 12: Photographic records of the impact of space debris with a reactor equipped with the Whipple shield.

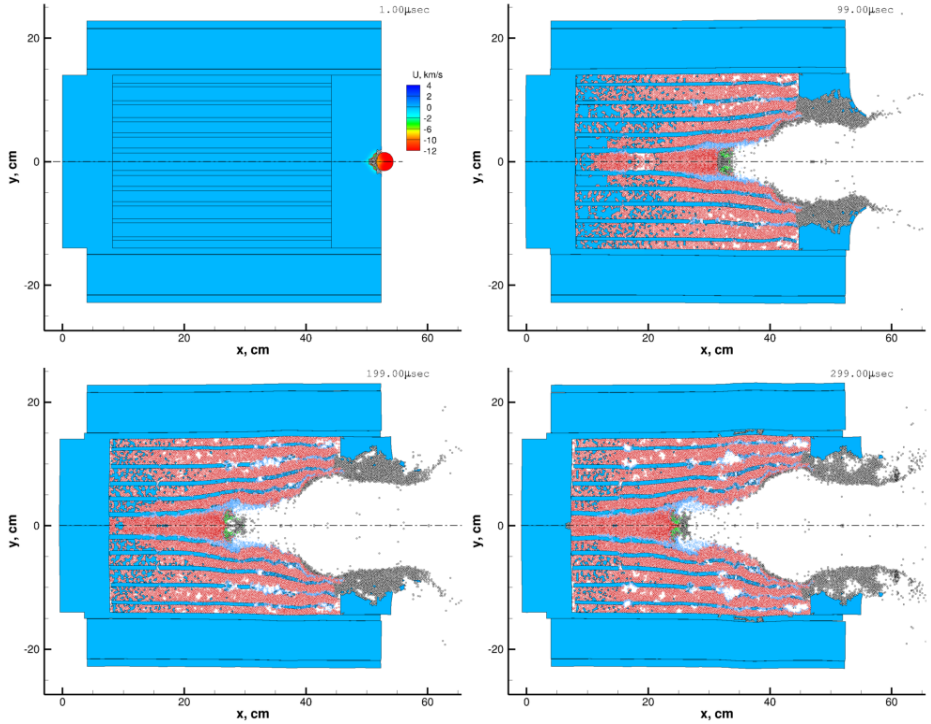

Figure 13: Photographic records of the impact of space debris with a reactor (axial formulation).

After that, the interaction of a steel object 3 cm in diameter impinging along the reactor axis with a velocity of 11.7 km/s is calculated. Fig. 13 shows the photographic records of the impact process. A powerful spherical shock wave propagates from the contact surface. Free surfaces at the periphery of interacting bodies allow the materials of these bodies to unload by acquiring velocities directed away from the "center of pressure", thus forming zones of tensile strains and stresses. The destruction process begins. As the size of the impinging particle are small, as compared with the reactor size, an analogy can be found with a point source of pressure applied on the boundary of interaction of bodies, moving along the reactor axis. As the central part of the reactor has a complicated structure, multiple interactions of compression-unloading waves lead to its failure even at the stage of overall compression behind the shock wave front (mainly due to shear strains). The acquired velocity induces systematic tensile strains, which rapidly reach critical values, and fragmentation of the materials of the central part of the reactor. Massive deformation of the central part appreciably alleviates peripheral loads, which allows the beryllium shell to remain in the non-destroyed state.

CONCLUSIONS

1. Calculations show that the high-speed impact of space debris leads to full failure of the reactor.
2. Impact of the reactor onto Earth's surface at a speed of 400 m/s leads to decompression of the reactor and radioactive contamination of the fall.

REFERENCES

[1] M.L. Wilkins, Computer Simulation of Dynamic Phenomena, Springer, (1999) 246.
[2] V. M. Fomin, A.I. Gulidov, G.A. Sapozhnikov, et al., High-Velocity Interaction of Solids, 1999 (in Russian).
[3] E.I. Kraus, V.M. Fomin, I.I. Shabalin, Vych. Tekhnol., 14 (2009) 40 (in Russian).
[4] E.I. Kraus, V.M. Fomin, I.I. Shabalin, Vych. Tekhnol., 11 (2006) 104 (in Russian).
[5] L.D. Landau., K.P. Stanyukovich, Dokl. Akad. Nauk SSSR, 46 (1945) 399 (in Russian).
[6] I.C. Slater, Introduction in the Chemical Physics, McGraw Book company, (1935).
[7] J.S. Dugdale, D. McDonald, Phys. Rev, 89 (1953) 832.
[8] V.Ya. Vaschenko, V.N. Zubarev, Sov. Phys. Solid State, 5 (1963) 653.
[9] V.M Fomin, E.I. Kraus, I.I. Shabalin, Mater. Phys. Mech., 7(1) (2004) 23.
[10] L.V. Altshuler, Usp. Fiz. Nauk, 85 (2) (1965) 197.
[11] A.D. Sakharov et alii, Dokl. USSR, 159 (1964) 1019 (in Russian).
[12] L.V. Belyakov et alii, Dokl. USSR 170 (1966) 540 (in Russian).
[13] S.A. Novikov, L.M. Sinitsina, Zh. Eksp. Teor. Fiz., 6 (970) 107 (in Russian).
[14] V. D. Urlin, Zh. Eksp. Teor. Fiz., 49-2(8) (1965).
[15] A. Hänström, P. Lazor, J. Alloys Comp., 305 (2000) 209.
[16] R. Boehler, M. Ross, Earth Plan. Sci. Lett., 153 (1997) 223.
[17] B.K. Godwal, C. Meader, Science, 248(4954) (1990) 462.
[18] P.W. Mirwald, G.C. Kennedy, J. Phys. Chem. Solids, 37 (1976) 795.
[19] M. Akaishi, H. Kanda, N. Setaka, O. Fukunaga, Japan J. Appl. Phys., 16(6) (1977) 1077.
[20] G. Maenchen, S. Sack, In: Methods in Computational Physics, B. Adler, S. Fembach, and M. Rotenberg (eds.), 3: Fundamental Methods in Hydrodynamics, Academic Press, New York (1964).
[21] F.R. Tyler, B.M. Butcher, Int. J. Fract. Mech., 4 (1968) 431.
[22] G.R. Johnson, R.A. Stryk, Int. J. of Impact Engineering, 28 (2003).

Effect of weld parameter on mechanical and metallurgical properties of dissimilar joints AA6082–AA6061 in T_6 condition produced by FSW

H. S. Patil
Department of Mechanical Engineering, Pacific School of Engineering, Surat, India
hspatil12@rediffmail.com

S. N. Soman
Department of Metallurgy & Material Engineering, Faculty of Engineering & Technology, M. S. University of Baroda, India

ABSTRACT. The effect of processing parameters on the mechanical and metallurgical properties of dissimilar joints of AA6082–AA6061 produced by friction stir welding was analysed in this study. Different FSW samples were produced by varying the welding speeds of the tool as 50 and 62 mm/min and by varying the alloy positioned on the advancing side of the tool. In all the experiments the rotating speed is fixed at 1600rpm. All the welds were produced perpendicularly to the rolling direction for both the alloys. Microhardness (HV) and tensile tests performed at room temperature were used to evaluate the mechanical properties of the joints. In order to analyse the microstructural evolution of the material, the weld's cross-sections were observed optically and SEM observations were made of the fracture surfaces. The corrosion tests of base alloy and welded joints were carried out in 3.5%NaCl solution at a room temperature. Corrosion current and potential were determined using potentiostatic polarization measurements. It was found that the corrosion rates of welded joints were higher than that of base alloy.

KEYWORDS. FSW; Aluminium alloys AA6082-AA6061; Mechanical and metallurgical characterization.

INTRODUCTION

Modern aerospace concepts demand reductions in both the weight as well as cost of production of materials. Under such conditions, welding processes have proven most attractive, and programs have been set up to study their potential. Car manufacturers and shipyards are also evaluating new production methods. Increasing operating expenses are driving manufacturers to reduce weight in many manufacturing applications, particularly in aerospace sector. The goal is to reduce the costs associated with manufacturing techniques to result in considerable cost and weight savings by reducing riveted/fastened joints and part count. One way of achieving this goal is by utilising a novel welding technology known as Friction Stir Welding (FSW). Friction stir welding is a solid-state joining process developed and patented by the The Welding Institute (TWI) in 1991 by Thomas et al and it is emerged as a welding technique to be used in high strength alloys (2xxx, 6xxx, 7xxx and 8xxx series) for aerospace, automotive and marine applications that were difficult to join with conventional techniques[1,2]. This technique is attractive for joining high strength aluminium alloys since there is far lower heat input during the process compared with conventional welding methods such as Tungsten Inert Gas (TIG) or Metal Inert Gas (MIG). This solid state process leads to low distortion in long welds, excellent mechanical properties in the weld and heat-affected zone, no fumes or spatters, low shrinkage, as well as being energy efficient. Furthermore, other cost reductions are realized in that the process uses a non-consumable

welding tool. The process was developed initially for aluminium alloys, but since then FSW was found suitable for joining a large number of materials.
In FSW a non-consumable rotating tool with a specially designed pin and shoulder is inserted into the abutting edges of sheets or plates to be joined and traversed along the line of joint. The tool serves two primary functions: (a) heating of work piece, and (b) movement of material to produce the joint. The heating is accomplished by friction between the tool and the work piece and plastic deformation of work piece. The localized heating softens the material around the pin and combination of tool rotation and translation leads to movement of material from the front of the pin to the back of the pin. As a result of this process a joint is produced in 'solid state'. During FSW process, the material undergoes intense plastic deformation at elevated temperature, resulting in generation of fine and equiaxed recrystallized grains. The fine microstructure in friction stir welds produces good mechanical properties. Fig. 1 shows a schematic diagram of the FSW process.

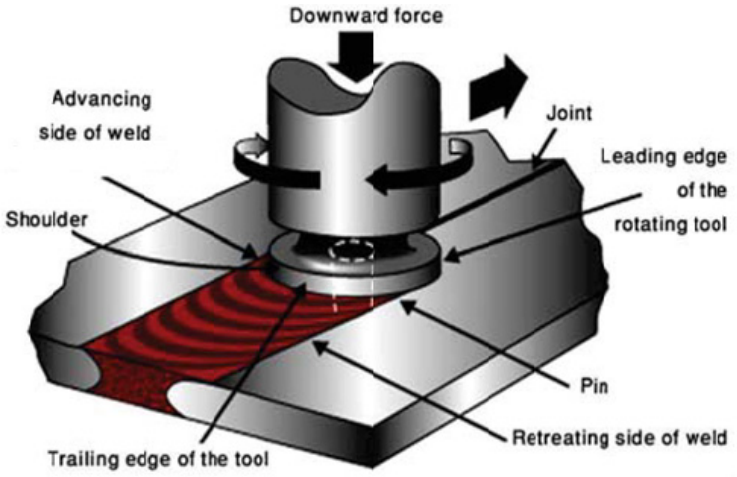

Figure 1: Schematic diagram of the FSW process.

Many papers are present in the literature regarding this field. Further to joints of similar alloys, FSW is being studied for welding dissimilar alloys which can be of particular interest in some industrial applications. Some works can be found in the literature [3–7], but data is still scarce on the characterisation of 6082-6061 joint type. Some authors have demonstrated that the microstructure of the weld nugget of strongly different aluminium alloys is mainly fixed at the retreating side of the material [3]. Murr et al. [8] showed the properties of dissimilar casting alloys by FSW. The microstructural evolution of dissimilar welds as a function of processing parameters has been widely studied in [9], showing the behaviour of AA6061–AA2024 materials. Dickerson et al. [10] found that friction-stir-welded butt joints are generally defect free if welding process conditions (welding speed and sheet thickness) are properly tuned within a 'tolerance box' for a particular alloy. It is not possible to assume that FSW will be free of flaws, however, because manufacturers may want to run FSW outside the tolerance box in order to increase productivity.
The weld zones are more susceptible to corrosion than the parent metal [11-16]. Generally, it has been found that Friction stir (FS) welds of aluminium alloys such as 2219, 2195, 2024, 7075 and 6013 did not exhibit enhanced corrosion of the weld zones. FSW of aluminium alloys exhibit intergranular corrosion mainly located along the nugget's heat-affected zone (HAZ) and enhanced by the coarsening of the grain boundary precipitates. Coarse precipitates and wide precipitate-free zones promoted by the thermal excursion during the welding are correlated with the intergranular corrosion. The effect of FSW parameters on corrosion behaviour of friction stir welded joints was reported by many workers [14, 16]. The effect of processing parameters such as rotation speed and traverse speed on corrosion behaviour of friction stir processed high strength precipitation hardenable AA2219-T87 alloy was investigated by Surekha et al. [16]. However, researchers have nevertheless been strained to study competent study of the mechanical properties in terms of UTS, YS and % elongation, microhardness test, fractography analysis, metallurgical properties, and corrosion behaviour and the main causes of developing defects with changing FSW parameters for a dissimilar aluminium joint of AA6082 with AA6061. Selection of process parameters is an important issue in the FSW process, particularly in the case of joining dissimilar alloys. In the present paper, the effect of different welding speeds on the weld characteristics of advancing and retreating side of AA6082-T6 and AA6061-T6 fabricated by a hexagonal tool pin profile is investigated.

EXPERIMENTAL PROCEDURE

The experiments were conducted on the aluminium alloy AA6082-T6 and AA6061-T6, its chemical composition and mechanical properties are respectively presented in Tabs. 1 and 2.

The rolled plates of 5mm thickness were cut into the required size (300mm×150 mm) by power hacksaw cutting and grinding. Square butt joint configuration was prepared to fabricate FSW joints. The initial joint configuration was obtained by securing the plates in position using mechanical clamps. The direction of welding was normal to the rolling direction. Single pass welding procedure was used to fabricate the joints. In present work hexagonal tool pin profile was used for the welds, made of cold work die steel. The tool dimensions are shown in Fig. 2. The machine used for the production of the joints was vertical machining centre. Different materials positioned on the advancing side of the tool allowed four different welding conditions described in Tab. 3.

Chemical Composition								
Element	Si	Fe	Cu	Mn	Mg	Cr	Zn	Ti
Required	0.7-1.3	0.5	0.1	0.4-1.0	0.6-1.2	0.25	0.2	0.1
Contents	0.9	0.24	0.9	0.7	0.7	0.06	0.04	0.05
Mechanical Properties								
Tensile Strength (MPa)		Yield Strength MPa)		Elongation (%)		Hardness(HV)		
Min	Max	Min	Max	Min	Max			
295	--	240	--	8	--	89		
324	332	308	319	9	12	90		

Table 1: Chemical composition and mechanical properties AA6082-T6.

Chemical Composition								
Element	Si	Fe	Cu	Mn	Mg	Cr	Zn	Ti
Required	0.4-0.8	0.7	0.15-0.4	0.15	0.8-1.2	0.04-0.35	0.25	0.15
Contents	0.62	0.45	0.2	0.18	1.05	0.09	0.03	0.07
Mechanical Properties								
Tensile Strength (MPa)		Yield Strength MPa)		Elongation (%)		Hardness(HV)		
Min	Max	Min	Max	Min	Max			
300	--	241	--	6	--	95		
328.57	335.71	282	296	11	11.8	98		

Table 2: Chemical composition and mechanical properties AA6061-T6.

Materials of Joints	Rotational Speed (rpm)	Welding Speed (mm/min)	Tool Depth (mm)	Downward Force(KN)
6082T6-6061T6	1600	50	4.6	14
6082T6-6061T6	1600	62	4.6	11
6061T6-6082T6	1600	50	4.6	11
6061T6-6082T6	1600	62	4.6	11

Table 3: Welding conditions employed to join the AA6082–AA6061 plates.

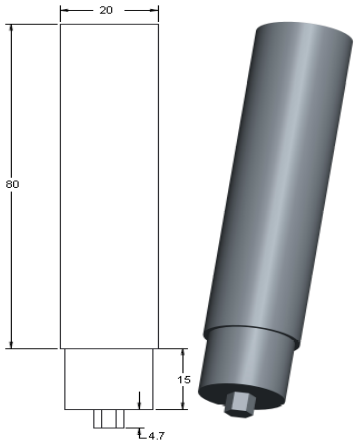

Figure 2: Geometry of the hexagonal tool pin profile used in the present study.

All welded samples were visually inspected in order to verify the presence of possible macroscopic external defects, such as surface irregularities, excessive flash, and surface-open tunnels. By using Radiographic unit, X-Ray radiographic inspection was carried out on FSW samples. In radiographic test 6Ci & Ir192 used as radioactive source. The film used was Agfa D-4 and the radiographs indicated defect free weld as well as weld with defects like insufficient fusion and cavity.

Mechanical properties of the test welds were assessed by means of tensile tests and the ultimate tensile stress (UTS) yield strength (YS) and % elongation were measured in the tensile test. Microindentation hardness test as per ASTM E-384:2006 has been used to measure the Vickers hardness of FSW joints. The Vickers microhardness indenter is made of diamond in the form of a square-base pyramid. The test load applied was 100gram and the dwell time was 15 seconds. The indentations were made at midsection of the thickness of the plates across the joint. The tensile fractured surfaces were analyzed by using scanning electron microscopy (SEM).

Metallographic specimens were cut mechanically from the welds, embedded in resin and mechanically ground and polished using abrasive disks and cloths with water suspension of diamond particles. The chemical etchant was the Keller's reagent. The microstructures were observed on optical microscope.

Potentiodynamic polarization tests were used to study the pitting corrosion behaviour of AA6082-AA6061 alloys. In the tests, cell current readings were taken during a short, slow sweep of the potential. The sweep was taken in the range of 0.5V to 1V. The potentiodynamic scan was performed at scan rate of 0.5mV/sec.

RESULT AND DISCUSSION

Mechanical Properties

The mechanical and metallurgical behaviour of dissimilar FSW AA6082–AA6061 was studied in this research. Transverse tensile properties of FSW joints such as yield strength, tensile strength, percentage of elongation and joint efficiency on transverse tensile specimens are presented in Tab. 4. The strength and ductility in the as-welded condition are lower than the parent metal in T_6 condition.

Material of FSW Joint	YS (N/mm^2)	UTS (N/mm^2)	% Elongation	% Joint Efficiency
$6082T_6$-$6061T_6$	167	183	5.14	50.13-49.03
$6082T_6$-$6061T_6$	101	170	4	46.57-45.57
$6061T_6$-$6082T_6$	91	173	4.29	47.39-46.38
$6061T_6$-$6082T_6$	95	154	4.43	42.19-41.28
AA6082-T_6	117	365	14	--
AA6061-T_6	99.84	373.12	16.56	--

Table 4: Mechanical properties of dissimilar FSW joints.

The joints were produced with different alloy positioned on the advancing side of the tool. The joints were realized with a rotation speed of 1600 rpm and by changing the advancing speed from 50 to 62 mm/min. From the Fig. 3 it can be inferred that the welding speed and alloy positions are having influence on tensile properties of the FSW joints.

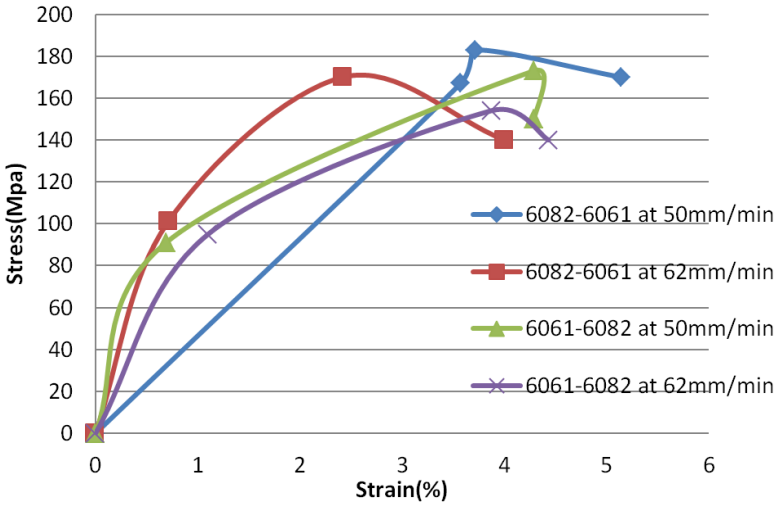

Figure 3: Stress-Strain curves for dissimilar alloys AA6082-AA6061.

The ductility is higher with decreasing the weld speed in the case of AA6082 on the advancing side, while it decreases in the case of AA6061 on the advancing side (Fig. 4). Such dependence of the strength on the material position was previously observed. The best conditions of strength and ductility are reached in the joints welded with AA6082 on the advancing side and weld speed of 50 mm/min. In joint efficiency table, the first efficiency represents the weld joint efficiency with AA6082 as a base metal and second efficiency represent with AA6061 as a base metal. The joint efficiency is higher with decreasing the weld speed in the case of AA6082 on the advancing side, while it is lower in the case of AA6061 on the advancing side. Fig. 5 shows the effect of welding speed on microhardness of dissimilar welds. The highest value of microhardness is reached in AA6061-6082 at welding speed of 50mm/min. The lowest value of microhardness is reached when the AA6061 alloy is on the advancing side of the tool at welding speed of 62 mm/min. When AA6082 alloy is employed on the advancing side of the tool, the microhardness appears more uniform, indicating a better mixing of the material as shown in Fig. 5. Furthermore, the maximum hardness values in the nugget zone correspond to the welds with AA6082 on the advancing side.

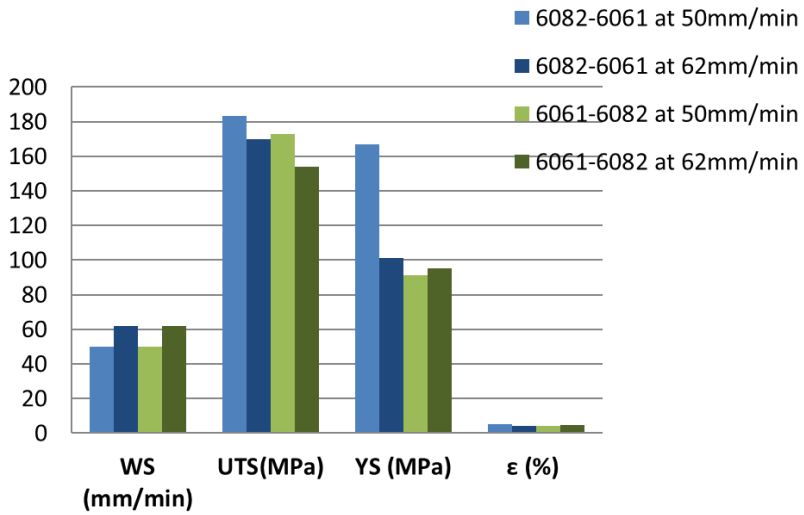

Figure 4: Effect of welding speed on mechanical properties for dissimilar alloys 6082-6061.

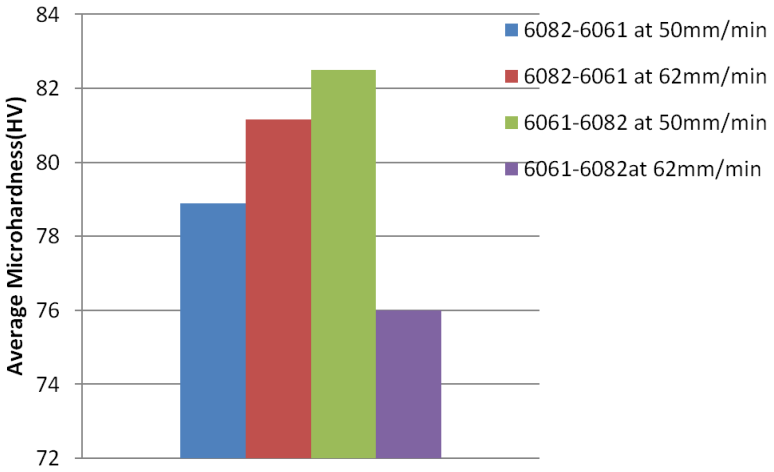

Figure 5: Effect of welding speed on microhardness for dissimilar alloys 6082-6061

Micro-structural Evolution

Based on optical micro structural characterization of grains and precipitates, three distinct zones have been identified such as weld nugget zone, thermo-mechanically affected zone (TMAZ) and heat affected zone (HAZ). Microstructural details of the base metals (BM) and dissimilar joint are presented in Figs. 6-8. Examination of onion rings in the AA6082-AA6061 at 50mm/min has shown that these onion rings are a result of shell extrusions in the dynamically recrystalized zone (DXZ). In AA6061-6082 at 62mm/min, it can be seen that the root flaw looks like a crack in the root part of the friction stir welds. The root flaw usually occurs if the pin length is too short for the plate thickness being welded, and this may also occur due to low heat input or incorrect tool orientation.

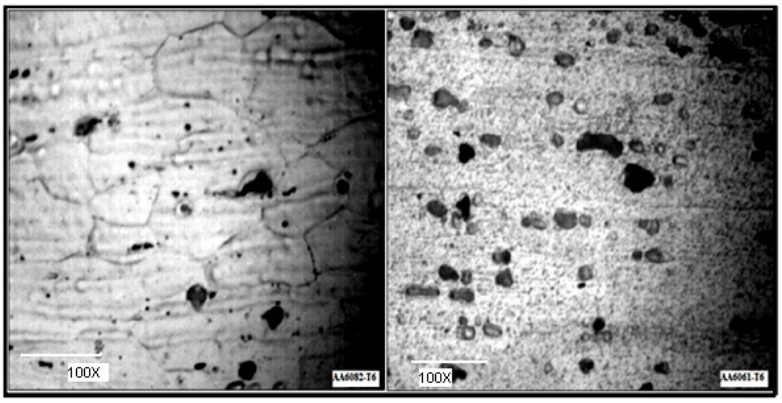

Figure 6: Optical micrograph of base metals AA6082 and AA6061.

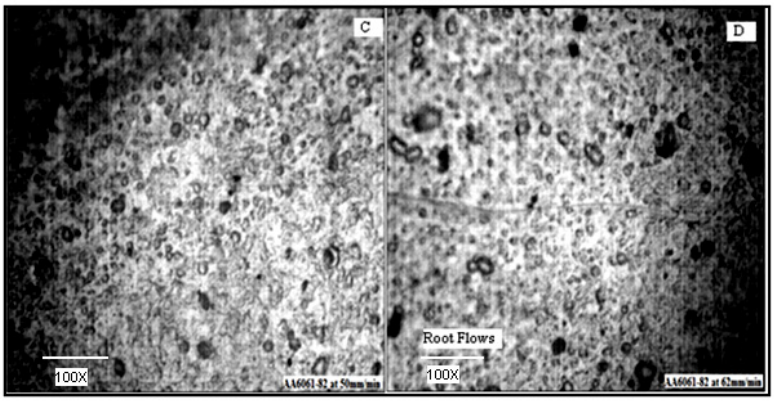

Figure 7: Optical micrograph of AA6082-6061(A) at 50mm/min (B) at 62mm/min

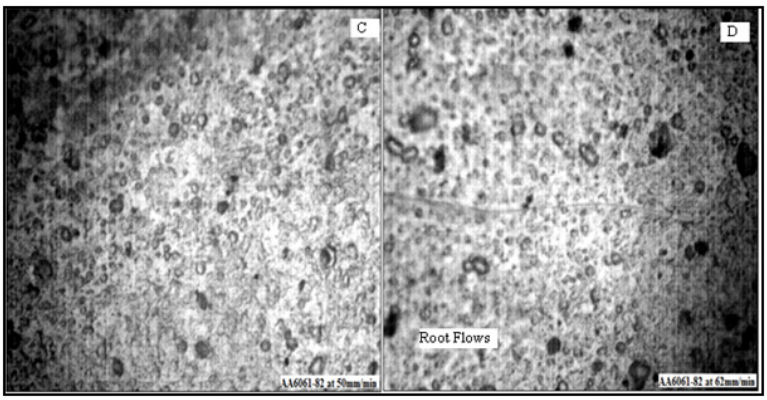

Figure 8: Optical micrograph of AA6061-6082 (C) at 50mm/min (D) at 62mm/min.

Fractography Analysis

Examination of the tensile fracture surfaces of the FSW joints was done at low magnification as well as at higher magnification in order to identify the fracture mechanisms.According to Figs. 9-10, it may be predicted that the fracture mechanism in the mixing of these alloys will be dimpled rupture. The dimpled rupture fracture mechanism indicates that the fracture occurred with some degree of ductility, but the existence of the defect can always cause a stress concentration around the defect zone during the tension test; therefore, this phenomenon results in a strain locality that is higher than the yield strength in the turbulence zone of the weld, a sudden crack in the specimen, and consequently, a low elongation in the connection.

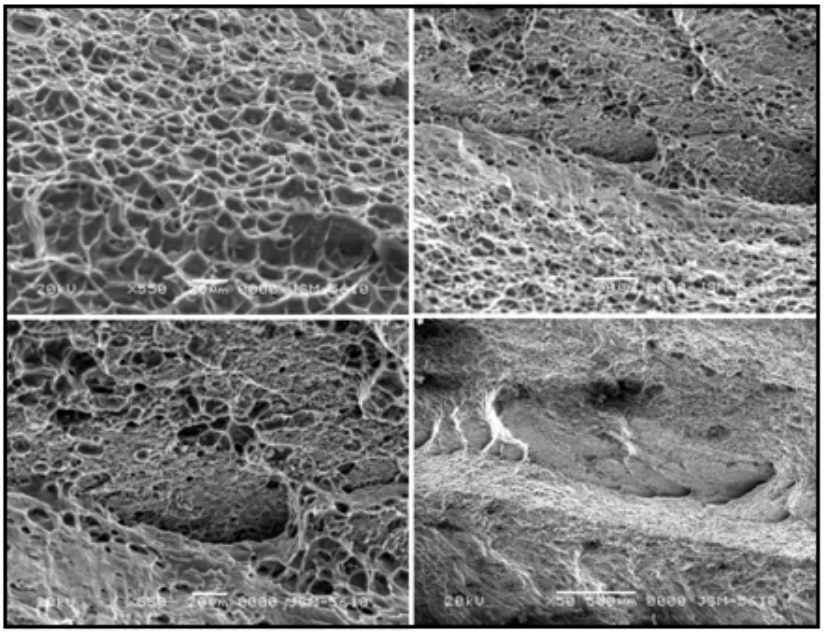

Figure 9: SEM images of tensile fracture surface of 6082-6061 at 50mm/min.

Corrosion Behaviour

The potentiostatic polarization curves for the base alloy and FSW samples in 3.5%NaCl at room temperature are given in Figs. 11-13. It is shown that the corrosion behavior of base alloy significantly varies from that of welded joints.

From Tab. 5 it is observed that the pitting potentials of corrosion tested samples at various process parameters clearly indicated a greater corrosion resistance of weld metal than base metal. This is attributed to the precipitates present in the alloy promote matrix dissolution through selective dissolution of aluminium from the particle. These precipitate deposits are highly cathodic compared to the metallic matrix, which initiates pitting at the surrounding matrix and also enhances pit growth. During FSW process only coarser precipitates could nucleate and grow but not finer ones. This aids in formation of passive film, which remained more intact on surface of the sample. It is also found that in AA6082-6061 at 50mm/min,

the corrosion resistance is very poor. The poor pitting corrosion resistance of weld joint is due to difference in pitting potentials across the weld region or stir nugget because of inhomogeneity of microstructures in those regions. With AA6082 on the advancing side, the corrosion rate is higher with respect to increasing welding speed of the tool while corrosion rate decreased in case of AA6061 on advancing side (Tab. 5). Such dependence of the corrosion behaviour on the material position was observed. All FSW samples show passivation after longer time of exposure to corrosion media. AA6082-61 at 62mm/min has highest active potential (-1.16V). The active E_{corr} increased with increasing the weld speed in case advancing and retreating side of 6082T6-6061T6.

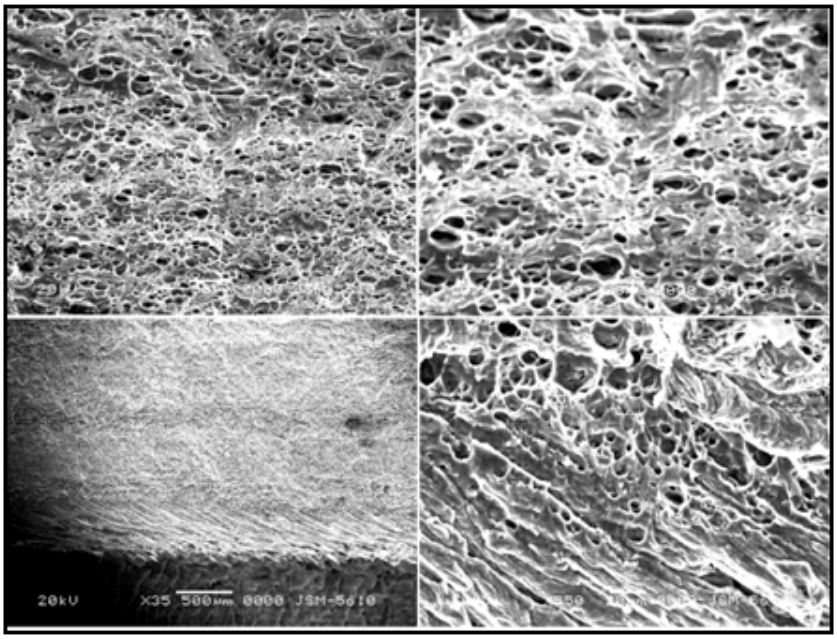

Figure 10: SEM images of tensile fracture surface of 6061-6082 at 62mm/min.

Material of FSW Joint	I_{corr} (μA/cm²)	E_{corr} (mV)	Corrosion Rate (mpy)
$6082T_6$-$6061T_6$	55.00	-938	25.14
$6082T_6$-$6061T_6$	3.33	-1160	1.520
$6061T_6$-$6082T_6$	836nA	-732	382 e^{-3}
$6061T_6$-$6082T_6$	1.590	-920	726.60 e^{-3}
AA6082-T_6	4.270	-1380	1.95
AA6061-T_6	1.820	-1160	832.1 e^{-3}

Table 5: Result analysis of corrosion test.

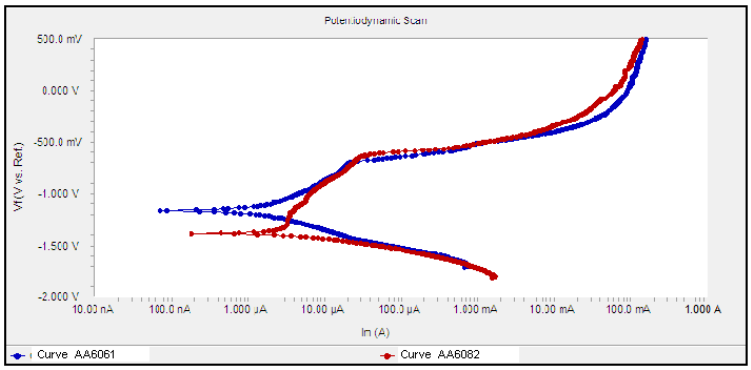

Figure 11: Polarization curves of base metals AA6082 and AA6061

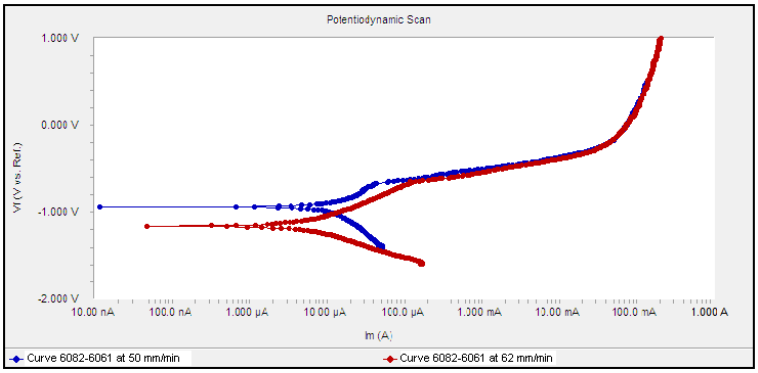

Figure 12: Polarization curves of AA6082-AA6061 at 50-62 mm/min.

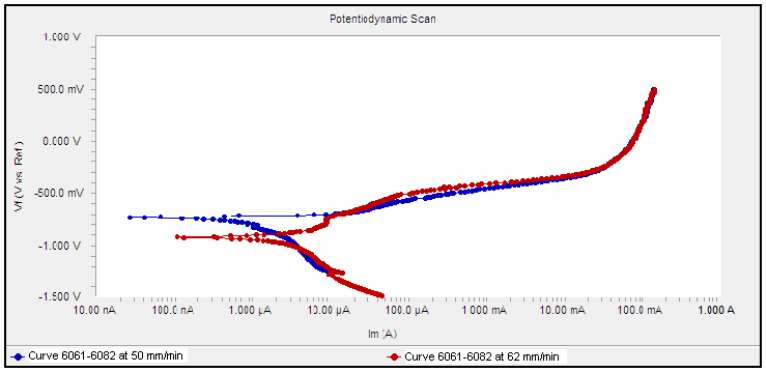

Figure 13: Polarization curves of AA6061-AA6082 at 50-62 mm/min

CONCLUSIONS

The mechanical and metallurgical behaviour of dissimilar FSW AA6082–AA6061 was studied in this paper. The joints were produced with different alloy positioned on the advancing side of the tool. The joints were realized with a rotation speed of 1600 rpm and by changing the welding speed from 50 to 62mm/min. The downward force was observed to be constant as the welding speed for all the produced joints increases. The tensile strength of the dissimilar joint is lower than that of the parent metal. With the 6082 alloy positioned on the advancing side of the tool, the dissimilar joints exhibited good mechanical properties with respect to AA6061. Microstructural changes induced by the friction stir welding process were clearly identified in this study. Friction stir welding of dissimilar alloys AA6082T6-6060T6 resulted in a dynamically recrystalized zone, TMAZ and HAZ. A softened region has clearly occurred in the friction stir welded joints, due to dissolution of strengthening precipitates.With AA6082 on the advancing side; the corrosion rate is higher with respect to increasing welding speed of the tool while corrosion rate decreased in case of AA6061 on advancing side.

REFERENCES

[1] W. M. Thomas, E. D. Nicholas, Materials & Design, 18 (1997) 269.
[2] W. M. Thomas, E. D. Nicholas, J. C. Needham, M. G. Nurch, P. Temple-Smith, C. Dawes, Patents on Friction Stir Butt Welding, International: PCT/GB92/02203; British: 9125978.8; USA: 5460317, (1991-1995).
[3] W. B. Lee, Y. M. Yeon, S. B. Jung, J. Mater. Sci., 38 (2003) 4183.
[4] W. B. Lee, Y. M. Yeon, S. B. Jung, Scripta Materialia, 49 (2003) 423.
[5] P. Cavaliere, R. Nobile, F.W. Panella, A. Squillace, Int. J. Machine Tools Manufacturing, 46 (2006) 588.
[6] P. Cavaliere, A. De Santis, F. Panella, A. Squillace, Material & Design, 30 (2008) 609.
[7] A. Scialpi, M. de Giorgi, L. A. C. de Filippis, R. Nobile, F.W. Panella, Material & Design, 29 (2008) 928.
[8] L. E. Murr, N. A. Rodriguez, E. Almanza, C. J. Alvarez, J. of Material Science, 40 (2005) 4307.

[9] J. H. Ouyang, R. Kovacevic, J. Material Engineering, 11 (2002) 51.
[10] T. L. Dickerson, J. Przydatek, Int. J. Fatigue, 25 (2003) 1399.
[11] C.S. Paglia, K.V. Jata, R.G. Buchheit, Material Science Engineering A, 424 (2006) 196.
[12] R.W. Fonda, P.S. Pao, H.N. Jones, C.R. Feng, B.J. Connolly, A.J. Davenport, Material Science Engineering A, 519 (2009) 1.
[13] D.A. Wadeson, X. Zhou, G.E. Thompson, P. Skeldon, L. Djapic Oosterkamp, G. Scamans, Corrosion Science, 48 (2006) 887.
[14] M. Jariyaboon, A.J. Davenport, R. Ambat, B.J. Connolly, S.W. Williams, D.A. Price, Corrosion Science, 49 (2007) 877.
[15] P. S. Pao, S. J. Gill, C. R. Feng, K. K. Sankaran, Scripta Materiala, 45 (2001) 605.
[16] K. Surekha, B. S. Murty, K. Prasad Rao, Solid State Sciences, 11 (2009) 907.

A consistent use of the Gurson-Tvergaard-Needleman damage model for the R-curve calculation

Gabriele Cricrì
Department of Mechanical Engineering, University of Salerno, Italy
gcricri@unisa.it

ABSTRACT. The scope of the present work is to point out a consistent simulation procedure for the quasi-static fracture processes, starting from the micro-structural characteristics of the material. To this aim, a local nine-parameters Gurson-Tvergaard-Needleman (GTN) damage law has been used. The damage parameters depend on the micro-structural characteristics and must be calculated, measured or opportunely tuned. This can be done, as proposed by the author, by using an opportunely tuned GTN model for the representative volume element simulations, in order to enrich the original damage model by considering also the defect size distribution. Once determined all the material parameters, an MT fracture test has been simulated by a FE code, to calculate the R-curve in an aeronautical Al-based alloy. The simulation procedure produced results in a very good agreement with the experimental data.

KEYWORDS. GTN model; Ductile fracture; Cell calibration; R-curve.

INTRODUCTION

Aluminium alloys are widely used in aircraft structures, transportation industries and civil engineering due to their relative lightness and versatility. In particular, the fuselage skin, which thickness ranges from 1 to 3 mm, is often made of aluminium alloys capable of fully ductile behaviour. Thus, in order to better take advantage from the material metallurgical characteristics, the damage tolerance design concept is often used in the aircraft structures sizing. Following this approach, the presence of macroscopic cracks during the ordinary service life can be tolerated, as long as they are under control. For this reason, in this field the study of both the static and the dynamic response of cracked panels in ductile regime, in terms of residual strength it assumes a relevance that can hardly be overestimated [1]. The so-called R-curve, that represents the critical stress intensity factor versus the crack length for a given structure, is a widely used tool to design by following the above criteria. Unfortunately the R-curve behaviour depends both from material and geometrical properties and then it changes as the test set-up changes [2, 3]. A reliable calculation model of the R-curve is, for this reasons, very important for the design purposes, in order to drastically decrease the amount of the very expensive physical tests.

From a micro-mechanical point of view, ductile failure is typically characterized by three coupled stages: nucleation, growth and coalescence of voids, which are induced in the metal alloy matrix by the presence of a variety of microscopic defects. In order to consider the effects of these voids evolution on the stress-carrying capability of a mechanical continuum during simulations, damage mechanics models are often used. Many models for ductile fracture growth have been proposed in the past [4 - 11] and, for their relative simplicity and efficiency the Gurson-Tvergaard-Needleman (GTN) model and many of its variants are proposed by several authors and also included in some public FE codes, like WARP3D [12]. These kinds of models for ductile fracture include the micro-mechanical effects of void nucleation, growth, and coalescence of micro-voids in the constitutive equation used to describe the mechanical continuum. The coalescence mechanism, in particular, induces a strain softening at the large-scale material response. Therefore, the

material becomes susceptible of bifurcations, instabilities and localized deformation modes. This is because the governing equations become hyperbolic in some unknown area of the continuum and make ill-posed the boundary value problem. As a consequence, numerical solutions chronically suffer from mesh dependency [13 - 15].
A popular and well proven in literature way to avoid this problem is the use some nonlocal formulations of the damaged material model. This is done by replacing the local variables denoting stress and strain fields, as well as the damage variables and the other internal ones, with nonlocal variables, which are space-weighted averages of the local ones. The averaging volume is related to a characteristic length l_c depending from the failure evolution at the micro-structural scale. The nonlocal formulations are capable to regularize ill-posed problems associated with damage, but require a very large increasing of the computational amount with respect to the local damage formulations [16 - 19]. From the computational point of view, the regularization is strictly related to the characteristic length; in fact, with l_c a constraint to the material law is introduced in addition to the large scale material behavior [20].
Also the local models can be regularized, and the easiest way to do this in a FE analysis is introducing the characteristic length not at the material model level, but more roughly at the element level. In other words, the element dimension will be strictly related to the characteristic length lc. In many works the latter computational strategy is adopted [21 - 24]. They typically present many free parameters that should be calibrated and fixed in a physically consistent way in order to make the calculation procedure effective.
In the present work, a complete procedure to calculate the R-curve starting from a local form of the GTN model is presented and a numerical application on a widely used aeronautical alloy, 2024A-T351, is reported, using material and test data provided by industrial research offices. Differently from the purely phenomenological approach that is usually employed to calculate all the model parameters, a procedure to consistently calculate some of these parameters on the basis of objective micro-structural data has been performed. In order to enrich the original damage model also the defect size distribution has been considered. With such methodology, the arbitrariness of the parameters tuning is strongly reduced, and a double result is attained: the number of the FE run needed to simulate the R-curve behaviour drastically decreases, and the transferability of the whole methodology to different geometries and boundary conditions is improved. Once determined all the material parameters, to calculate the R-curve an MT fracture test has been simulated by the free FE code WARP3D.

THE GTN MODEL FOR DUCTILE FRACTURE

In a homogeneous ductile metal model, the total strain amount usually leaves unchanged the volume, because the plastic part of the strain is dominant with respect to the elastic one. On the other hand, in a material model containing voids which matrix phase is ductile, the volume can *globally* change, due to the local plastic flow arising around the voids boundary and, consequently, the void volume change. Then, the material model response to an imposed global strain will be a stress-strain curve presenting a softening curve, nevertheless the matrix material model have hardening behaviour. In such model, the voids can grow until the global load carry capability becomes negligible.
The Gurson-Tvergaard (GT) model is able to explain the local strength decreasing during the fracture process of ductile metals in the intermediate phase between the *nucleation* and the *coalescence* of voids. Standing this characteristic, in the void growth model the number of voids is kept constant. Nucleation and coalescence are taken into account before the homogenization of the material model, applying some opportune corrections, originally proposed by Needleman et al., directly to the stress-strain cell response. Updated in this way the GT model, it is usually named GTN model.

Gurson-Tvergaard model

The homogenization technique is based on the stress-strain characterization of a Representative Volume Element (RVE), that can be roughly defined as the minimum material volume containing all the micro-structural information of a heterogeneous material, related to the specific problem under investigation (see, e.g., [25 - 27]). In the Gurson-Tvergaard void growth model, the RVE of the material is considered as a cubic volume with a single void, yet existing in the virgin material. The initial void volume fraction f_0 should be chosen as the 'equivalent' volume fraction corresponding to the physical distribution of voids inside the RVE (Fig.1).
The resulting homogenized material model was defined by modifying the analytical solution of the single void cell (Fig. 1) performed by Gurson and limited to a rigid-plastic material model of the matrix. The corrections take into account for the hardening of the matrix material and for the presence of void cell array instead of a single void cell. They are represented by the coefficients q_1, q_2, q_3 in the critical surface definition, originally introduced by Tvergaard.

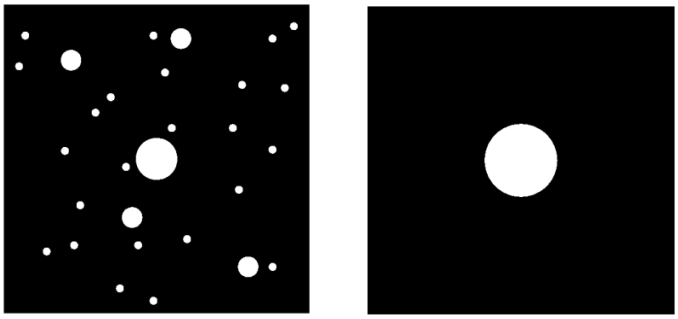

Figure 1: Physical vs. equivalent voids distribution (plane representation).

The homogenized constitutive law is defined by (tensors are indicated with bold characters):

$$\phi\left(\sigma_{eq},\sigma_m,\bar{\sigma},f\right)=\left(\frac{\sigma_{eq}}{\bar{\sigma}}\right)^2+2q_1 f\cosh\left(\frac{3q_2\sigma_m}{2\bar{\sigma}}\right)-\left(1+q_3 f\right)^2=0 \tag{1}$$

$$d\boldsymbol{\varepsilon}^p=d\lambda\frac{\partial\phi}{\partial\boldsymbol{\sigma}} \tag{2}$$

$$df=\left(1-f\right)d\boldsymbol{\varepsilon}^p:\boldsymbol{I} \tag{3}$$

$$(1-f)\bar{\sigma}\,d\bar{\varepsilon}=\boldsymbol{\sigma}:d\boldsymbol{\varepsilon}^p \tag{4}$$

$$\boldsymbol{\sigma}=\boldsymbol{C}\left(\boldsymbol{\varepsilon}-\boldsymbol{\varepsilon}^p\right) \tag{5}$$

$$d\bar{\varepsilon}=\begin{cases}\dfrac{N\varepsilon_0}{\sigma_0}\left(\dfrac{\bar{\sigma}}{\sigma_0}\right)^{N-1} & \text{if } \phi=0 \text{ and } d\bar{\sigma}>0\\ 0 & \text{otherwise}\end{cases} \tag{6}$$

Where:

Eq. (1) defines the plastic surface;
Eq. (2) is the plastic flow rule;
Eq. (3) is the void growth rate definition;
Eq. (4) imposes the equivalence between micro and macro-mechanical plastic work;
Eq. (5) is the global stress-strain relationship;
Eq. (6) is the plastic hardening power law for the matrix material.

Further, the symbols indicate:

$\boldsymbol{\sigma}$	: stress tensor;
$\boldsymbol{\varepsilon}$, $\boldsymbol{\varepsilon}^p$	: total and plastic strain tensors;
$\boldsymbol{C}$	: constitutive elastic law;
$\boldsymbol{\sigma}_{eq}$	: Von Mises equivalent global stress;
$\boldsymbol{\sigma}_m$	: global mean stress;
$\bar{\sigma}$	: current matrix flow stress (internal variable of the model);
$\bar{\varepsilon}$	: current matrix equivalent strain (internal variable);
f	: voids volume fraction (internal variable);
N	: hardening coefficient;
$\boldsymbol{\sigma}_0$, $\boldsymbol{\varepsilon}_0$	: yield equivalent stress and strain;
q_1, q_2, q_3	: Tvergaard correction coefficients.

Voids nucleation model

The nucleation of the first void in an array of cells is implicit in the above model. With the increasing load, further voids can nucleate in the RVE, and this fact is *indirectly* taken into account in the homogenized material law by increasing the void growth rate defined in Eq. (3).
In the present study the following relation is used:

$$df_{nuc} = A(\bar{\varepsilon})d\bar{\varepsilon} \tag{7}$$

where:

$$A(\bar{\varepsilon}) = \frac{f_N}{S_N\sqrt{2\pi}} exp\left[-\frac{1}{2}\left(\frac{\bar{\varepsilon}-\varepsilon_N}{S_N}\right)^2\right] \tag{8}$$

The corrected void growth rate becomes:

$$df = (1-f)d\boldsymbol{\varepsilon}^p : \boldsymbol{I} + A(\bar{\varepsilon})d\bar{\varepsilon} \tag{9}$$

The expressions (7-9) relate the voids growth rate due to the nucleation process to the internal equivalent strain rate $d\bar{\varepsilon}$. This acceleration is driven by the parameter A and it is limited to an internal strain condition in which $\bar{\varepsilon}$ is quite close to a certain value ε_N, representing the matrix strain value where the nucleation takes place.
Three new parameters are so introduced in the constitutive law (1-6):

f_N : magnitude of the volume fraction rate increasing;
ε_N : main value of the internal strain for which the nucleation takes place
S_N : standard deviation of the Gaussian distribution.

The void nucleation law completes the analytical description of the GTN model.

Cell dimension

It is well known that the undefined equilibrium problem in a material domain which constitutive law has softening branches loses ellipticity near the critical point and then it is hill-posed [27].
If the finite element method is used to search a solution, disregarding the above problem, the resulting discrete equation can be solved, but the solution is chronically mesh dependent and the convergence can't be reached. This occurs because near the softening condition the strain field would become discontinuous and, correspondently, in the discrete problem the strain tends to concentrate in a small zone, which size depends on the elements size. Smaller the element size, smaller the zone affected by the strain concentration. This behaviour is commonly named *strain localization*.
If the softening law derives from a physical model of the material, the incongruence can be explained noting that, at the micro-structural scale, the material domain can't be longer be considered homogeneous, so the softening at the large scale material law can be attributed to the micro-structural *geometric* changes.
Apparently, the consequence of this fact is that we can't use local homogenization techniques if the global material law presents a softening behaviour. In practice, using a local FE model, we can avoid the mesh dependence by keeping fix the element dimensions in the fracture zone, regardless with the macroscopic geometry of the domain. In particular, the dimension D_0 to be mandatory controlled is the cell length in the direction perpendicular to the crack plane. The correct value of the element dimension depends on the scale of the local fracture process related to the particular material under consideration. In this way, the element dimension becomes a further parameter of the material constitutive law. In other words, we couldn't use a local homogenized law because the analytical equilibrium problem is hill-posed, but the error that cannot be eliminated in the FE solution of this problem can be *driven* in order to reach a numerically correct result.

Voids coalescence

In the constitutive law (1-6) the internal strain state is represented by a *unique* variable $\bar{\varepsilon}$. This simplification can be accepted only in the early phases of the void growth, in which the internal strain (and stress) distribution doesn't vary too much. In the following load phase the matrix material model becomes unrealistic. In fact, in this phase the fracture advances between two consecutive voids (coalescence) and then the RVE model with the single equivalent void itself becomes unrealistic.
The voids coalescence, and the consequent crack advancing, is modelled in the FE code by eliminating the corresponding element (named killed element) when a critical volume fraction value f_c is reached. Many studies have demonstrated that

the critical value should be much less than 1, which is the value rigorously provided by the theory. For many ductile materials the critical volume fraction can be set-up between 0.15 ÷ 0.25, and a phenomenological correlation furnishes the following empirical law [21, 22]:

$$f_c = 0.15 + 2f_0 \tag{10}$$

Along the crack plane, the element traction forces are still present in this condition ($f = f_c$) and they are gradually decreased until zero is reached, using a multiplicative coefficient γ, related to the cell dimension D_0 and depending from a further parameter λ, to be set.

$$\gamma = 1 - \frac{D - D_c}{\lambda D_0} \qquad 0 \le \gamma \le 1 \tag{11}$$

In Eq. (11) D and D_c indicates respectively the actual and the critical value of D_0, averaged over the cell volume.

CELL CALIBRATION

The material model described above needs the calculation, the measurement or the phenomenological tuning of (at least) 13 parameters:

- ✓ The internal plastic-hardening parameters N, σ_0, ε_0.
- ✓ The Tvergaard correction coefficients q_1, q_2, q_3.
- ✓ The nucleation parameters f_N, ε_N, S_N.
- ✓ The cell height D_0.
- ✓ The initial and critical void volume fractions f_0, f_c.
- ✓ The force release parameter λ.

Critical void volume fraction and force release parameter

These parameters are related to the coalescence phase. For the present calibration they have been chosen as mean values from the ones present in literature [21, 22].

$$f_c = 0.2; \qquad \lambda = 0.1$$

Notwithstanding the above position, the release forces parameter λ contributes to form the energy released in the element extinction process, so it can't be rigorously considered a merely calculation parameter. The γ coefficient defined in (11) depends on the component of the strain orthogonal to the crack plane. In fact, we can write:

$$\gamma = 1 - \frac{D - D_c}{\lambda D_0} = 1 - \frac{D/D_0 - D_c/D_0}{\lambda} \cong 1 - \frac{\exp(\varepsilon) - \exp(\varepsilon_c)}{\lambda}$$

$$\sigma_{rel} = \gamma \sigma_c$$

where σ_{rel} is the stress value present during the force release process (coalescence). Thus, the corresponding energy density w released in the coalescence phase can be evaluated, for small λ, ε_c:

$$w = \int_{\varepsilon_c}^{\varepsilon|\gamma=0} \gamma \sigma_c \, d\varepsilon \cong \sigma_c \frac{\lambda}{2} \Rightarrow \lambda = \frac{2w}{\sigma_c}$$

where σ_c is the stress corresponding to the critical strain ε_c (reached when $f = f_c$).
Then, the parameter λ is related to the energy released during the coalescence process.

Cell height and initial void volume fraction

Both the cell height D_0 and the initial void volume fraction can be estimated considering as a starting point the defect size distribution.

2024A-T351 All Three Directions							
Equivalent Diameter (μm)	Volume Fraction (%)	Standard Deviation	Nearest Neighbour (μm)	Nearest Neighbour Standard Deviation (μm)	Minimum Separation Distance (μm)	Minimum Separation Distance Standard Deviation (μm)	Average Diam of particles in size category (μm)
All Sizes	0.76	0.33	10.61	8.01	8.55	8.09	1.75
1:2	0.13	0.06	16.14	12.11	14.65	12.39	1.41
2:3	0.10	0.05	35.18	26.48	32.82	27.30	2.41
3:4	0.07	0.04	62.38	46.78	59.61	48.71	3.41
4:6	0.12	0.07	58.90	40.68	53.76	42.22	4.87
6:8	0.11	0.08	93.54	64.45	86.12	66.44	6.88
8:10	0.09	0.09	130.27	96.68	122.14	101.91	8.86
10+	0.14	0.21	126.95	97.90	111.94	99.72	13.23

Tabella 1: Defects size distribution.

As shown above, the cell dimension, and in particular the cell height, is a fundamental parameter because, when the strain localization occurs, the cell height coincides with the localized strip of material. So, from this point, the most of the energy released is proportional to this parameter. On the other side, in the present model the energy released is also influenced by the coalescence parameters and by the shape of the stress-strain curve (that depends on the nucleation and Tvergaard parameters). Then, the correct cell height should be chosen taking into account the influence of all the above parameters in the fracture process.

If we consider the cell as a representative volume element (as it is usually done) it should contain a sufficiently representative voids distribution. Of course, a greater RVE contains more micro-structural information, but it is less useful in the present model because the strain would localize in a strip with *fixed* height. In conclusion, the cell height can't be precisely defined without a critical consideration of all the constitutive law parameters influence.

As an approximated evaluation, we can consider the bigger defects above the last 20% of the total volume fraction as it were the driving defects of the localization process. In this way, with reference to the Tab.1, an RVE, which dimension is coincident with the cell height, will contain *one* defect with 10+ μm diameter and the appropriate number of minor defects as deduced from the size distribution (Tab. 2).

Category	Volume fraction	Average diameter (μm)	Spherical average diameter (μm)	Volume (μm^3)	Density (defects/ mm^3)	Defects in the RVE
1:2	0.0013	1.41	1.79	3.00	433000	904
2:3	0.0010	2.41	3.07	15.1	66200	138
3:4	0.0007	3.41	4.34	42.8	16300	34
4:6	0.0012	4.87	6.20	125	8810	18
6:8	0.0011	6.88	8.50	322	3410	7
8:10	0.0009	8.86	11.3	752	1200	2
10+	0.0014	13.23	17.7	2920	479	1

Tabella 2: Defects distribution in the RVE (from Tab. 1 data rearranging).

The cell height and the initial void volume fraction can be finally estimated:

$$D = (10+ \text{ category density})^{1/3} \approx 130 \ \mu m; \quad f_0 = 0.0014$$

The D value is in good agreement with the literature values that range between 80÷200 μm.

This procedure can appear quite arbitrary. In fact, if the categories were chosen in a different way (for instance the last category could be 8+ or 12+), the resulting D and f_0 parameters were different. On the other side, this can be avoided if we consider for all the distribution, as stated above, the bigger defects above the last 20% of the total volume fraction; in this case, is arbitrary the 20% value.
As discussed above, a certain degree of arbitrariness is un-eliminable because the cell height (and consequently the initial volume fraction) has the double role of dimension of the RVE and dimension of the strain localization zone. Then, once established the cell height on the basis of a reasonable RVE choice, the effect of the strain localization should be taken into account by tuning both the nucleation parameters (that can be considered responsible for the minor defects growth) and the coalescence parameters f_c , λ.
As an example, in the pictures below (Fig. 2) is reported the equivalent strain distribution inside two different two-dimensional RVEs with the same initial volume fraction (see Fig.1 for the unstrained configurations). The first, is the simplified Gurson RVE with a single void; the second, has a void distribution compatible with the Tab. 2 distribution.

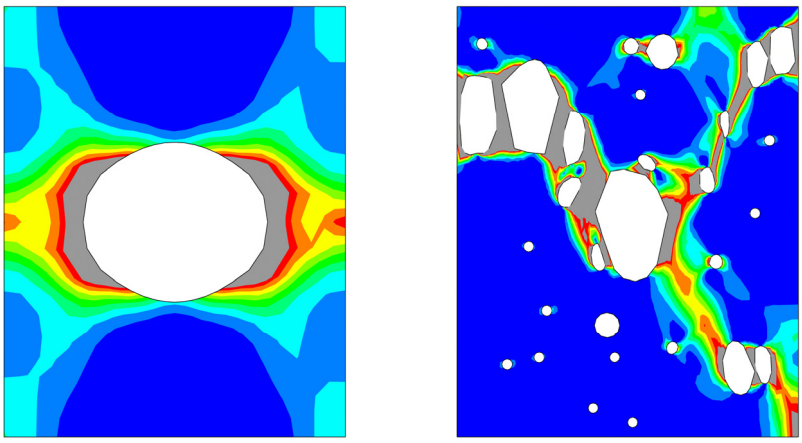

Figure 2: Equivalent strain distribution inside two RVE.

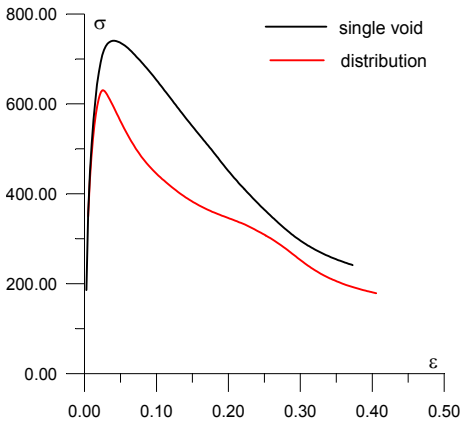

Figure 3: Global cell response.

It can be deduced that the localization zone dimension is larger in the first that in the second RVE. This fact influences the global cell response (Fig. 3). A more general discussion on this topic can is presented in [28]. Supposing that the second RVE represents a sufficiently accurate evaluation of the material behaviour, the pre-defined cell height seems too large in relation to the 'true' localization zone, as it results comparing the different entity of energy involved in the load process. Once established a compromise value D = 100 μm < 130 μm, the residual difference should be taken into account by tuning, as written above, the nucleation and the coalescence parameters.

Tvergaard correction coefficients

The correction coefficients q_1, q_2, q_3 can be calculated from a single void RVE model.
The global cell behaviour has been calculated for two different load conditions:

1) Imposed global strain $\varepsilon_x > 0$ and free surface condition for y and z direction.
2) Imposed global strain $\varepsilon_x > 0$ and $\varepsilon_y = \varepsilon_z = -0.2\varepsilon_x$.

In the following pictures 4-5 are presented the cell mesh and the resulting strain distribution in the x direction for the two considered load cases.

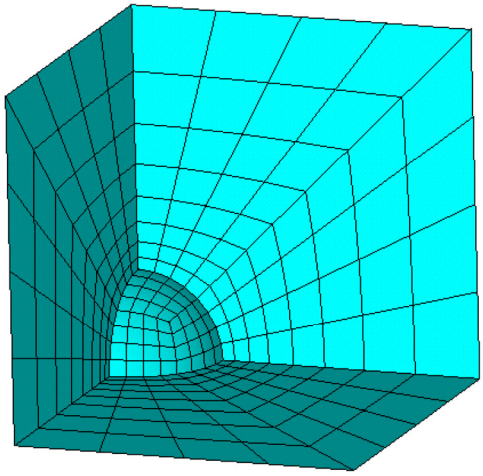

Figure 4: FE model of the single void cell.

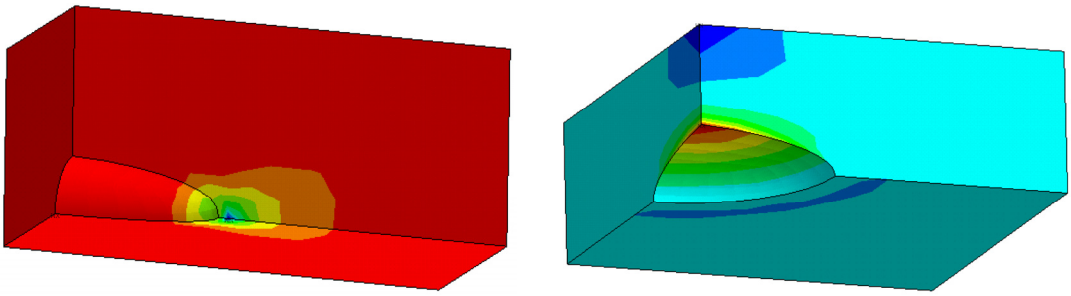

Figure 5: Strain (ε_x) distribution for the two load cases.

It can be noted that in the first case the x-direction strain is about uniform, but in the second there is a consistent strain concentration on the void boundary. This agrees with the constitutive law (1-6), that attributes the void volume fraction growth to the mean stress (Eq. 3) that in the first case is much lower than in the second one.
The global RVE responses have to be compared with the eq. (1-6) stress-strain curves resulting from an equivalent load process. This comparison allows to determine the Tvergaard correction coefficients. In the present work, the analytically derived relation is adopted [23], that:

$$q_3 = q_1^2$$

In the subsequent refinement of the model calibration the parameter q_3 could be left free.
The two remaining free parameters q_1, q_2 are determined by imposing on the homogenized law the condition that the characteristic values:

$$\sigma_{max};\ \ w_c = \int_0^{\varepsilon_c} \sigma d\varepsilon$$

are equal to that resulting from the FEM calculation.
The first load case (uniaxial strain) is quite insensitive to the parameter variation, due to the very slow void growth rate present in this condition, so the calibration has been done with reference to the second load case. Finally, the resulting values are:

$q_1 = 1.25$; $q_2 = 0.98$; $q_3 = 1.56$

In Fig. 6, the comparison between the FE model of the cell and the homogenized law (1-6) stress-strain curve is reported for the two load cases.

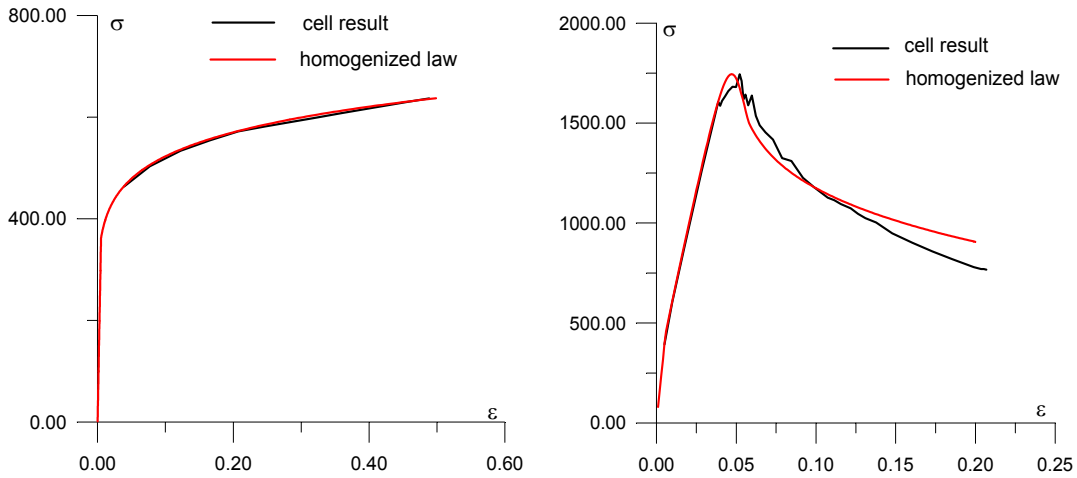

Figure 6: Global cell response compared with eq. (1-6) for the two load cases.

Nucleation parameters

In the present work, the nucleation parameters have been considered as correction parameters, not directly related to the microstructure. Then, the parameters f_N, ε_N , S_N have been used to fit the experimental-numerical results in the residual strength curve, and their values are reported in the following section.

In Fig. 7 the coalescence law (11) has been included into the constitutive law, with the imposed values $f_c = 0.2$ for the starting point, and $\lambda = 0.1$ for the curve slope, as established before. It is shown that the energy related to the coalescence process is a non negligible part of the total cell energy.

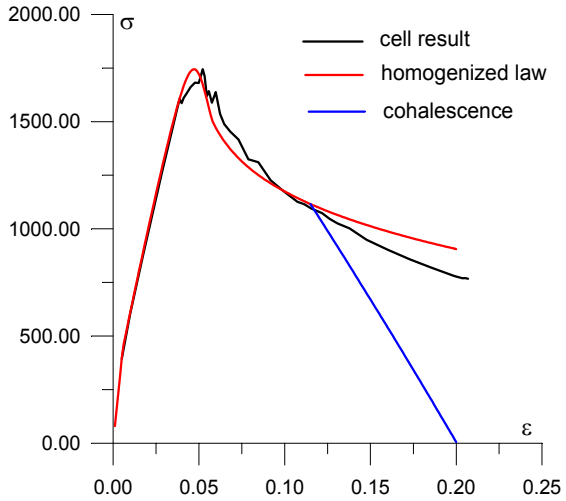

Figure 7: Global cell response compared with eq. (1) and the coalescence law.

R-CURVE DETERMINATION

The R-curve calculation procedure has been tested on an M(T) specimen model, which experimental results have been published in [2].

The M(T) specimen used for the residual strength results is made by a 1.28 mm thick 2024 sheet material. The

panel width is H = 500 mm and the initial half crack length is a_0 = 49.78 mm. Testing and data evaluation were done according to ASTM specification E561-86 for R-curve determination. The residual strength tests were done under displacement control.

Mesh generation

The FEM mesh has been generated within the ANSYS code pre-processor module. All the elements are eight nodes brick, in order to be allowable for the subsequent calculations with the WARP3D [12] solver. The specimen has been modelled taking into account the three symmetry conditions. Along the crack plane, all the elements are cubic with length D_0 = 106.667 μm (see the calibration section). Along the thickness t, six elements have been generated, so that $t/2$ = 0.64 mm = $6D_0$. In Fig. 8 some particulars of the mesh generation are reported.

It should be noted that, as shown in the last picture, there the row of elements before the initial crack front is not present. Further, the elements that will be killed during the crack advance simulation are indicated with a different colour, that indicates two different materials. In fact, for computational reasons, the killable elements have to be separated from the non-killable ones; otherwise, the solver can try to kill the above elements in contrast with the crack plane definition. This contrast will produce a program error (the limitation is related only to the force-release kill procedure). The elements immediately before the initial crack front have been deleted in order to avoid an undesired 'collaboration' to the initial crack strength.

The as generated mesh, and the boundary conditions have been 'translated' into the corresponding WARP3D commands by using a Fortran routine.

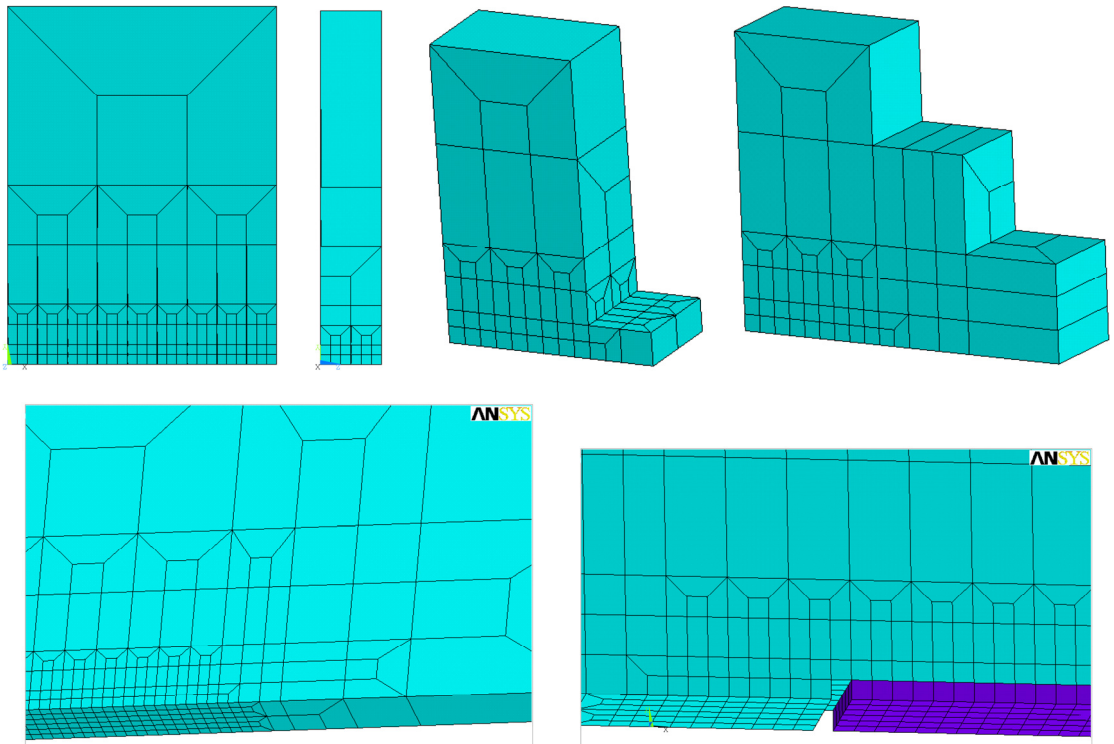

Figure 8: Mesh generation.

Results: Load vs. crack length curve

From the experimental test data, the following material parameters have been chosen for the numerical analysis:

E = 71100 MPa
σ_y = 366 MPa
σ_u = 482 MPa
ε_f = 0.173

So, the internal stress parameters are:

$\sigma_0 = \sigma_y = 366$ MPa
$\varepsilon_o = \sigma_y / E = 0.00515$
$\varepsilon_{f,log} = log(1 + \varepsilon_f) = 0.1596$
$\sigma_{u,\text{true}} = \sigma_u (1 + \varepsilon_f) = 565$ MPa
$N = log(\varepsilon_{f,log} / \varepsilon_o) / log(\sigma_{u,\text{true}} / \sigma_0) = 8.0$

The other constitutive law parameters values, calculated in the above section, are:

$q_1 = 1.25$
$q_2 = 0.98$
$q_3 = 1.56$
$f_0 = 0.0014$
$D = 0.107$ mm
$F_c = 0.2$
$\lambda = 0.1$

After the solution has been calculated, by using a Fortran routine, the WARP3D output file can be read and interpreted. For every step, the total reaction value R_y in the traction direction and the total number of killed elements N_k are stored. Then, with simple data manipulations, the gross stress S and the half crack length a are pointed out:

$S = R_y / (t \cdot H/4)$
$a = N_k / (t/2) \cdot D^2$

The resulting curve $S(a)$ has to be compared with the experimental curve in order to perform the tuning of the nucleation parameters.

Nucleation parameters tuning

From the afore cited experimental test data, the following experimental stress vs. crack length curve results (Fig. 9).
By varying the nucleation parameters ε_N, S_N, f_N, different curves have been calculated . The parameter f_N gets down the curve when it is increased; S_N has the opposite effect, with a little influence on the shape of the curve; the increasing of ε_N can slightly move the curve maximum value versus the increasing Δa. The best nucleation parameter values are:

$\varepsilon_N = 0.09$
$S_N = 0.09$
$f_N = 0.2$

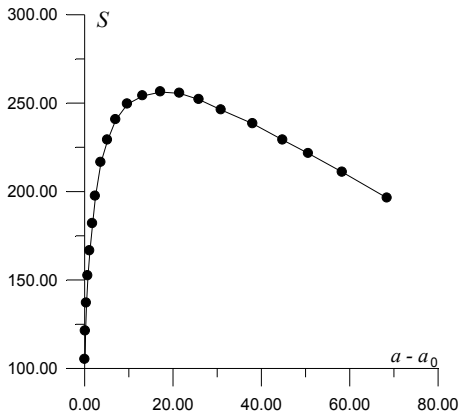

Figure 9: Experimental stress vs. crack length curve.

Final results and R-curve

The ASTM specification E561-86 for R-curve determination imposes that the curves have to be expressed in terms of equivalent stress intensity factor and equivalent crack length, in order to take into account for the plastic deformation around the crack tip. For the M(T) central crack specimen, the equivalent SIF is defined by:

$$K_{eq} = sec\left(\frac{\pi a_{eq}}{H}\right) S\sqrt{\pi a_{eq}} = \beta\left(a_{eq}\right) S\sqrt{\pi a_{eq}} \tag{12}$$

The equivalent crack length has two alternative definitions: the one, based on the Crack Opening Displacement in the traction direction of the centre of the crack; the other, which has been adopted in the present work, based on the plastic radius evaluation. The plasticity contribution to the equivalent crack length is done by:

$$r_p = \frac{1}{2\pi}\left(\frac{K_{eq}}{\sigma_y}\right)^2 \tag{13}$$

Then, the equivalent crack length is defined by:

$$a_{eq} = a + r_p;\ \Delta a_{eq} = a_{eq} - a_0 \tag{14}$$

The plastic radius definition (13) contains the equivalent SIF and, vice-versa, the expression (12) contains the equivalent crack length. It is then necessary to calculate iteratively the two expressions (12), (13-14) up to the convergence is reached. The current plastic radius value is then done, in an iterative formulation by:

$$r_p^{i+1} = \frac{1}{2\pi}\left(\frac{\beta\left(a + r_p^i\right) S\sqrt{\pi\left(a + r_p^i\right)}}{\sigma_y}\right)^2;\ r_p^1 = \frac{1}{2\pi}\left(\frac{\beta(a) S\sqrt{\pi a}}{\sigma_y}\right)^2$$

The convergence is reached when the $(i+1)$-th value of the plastic radius differs from the i-th value for a small enough quantity.

By using the $S(a)$ values calculated before, and after the above descript transformation $(S, a) \rightarrow (K_{eq}, a_{eq})$, we can compare the calculated and experimental R-curves, as reported in Fig. 10. As a result, the calculated R-curve is in very good agreement with the experimental test.

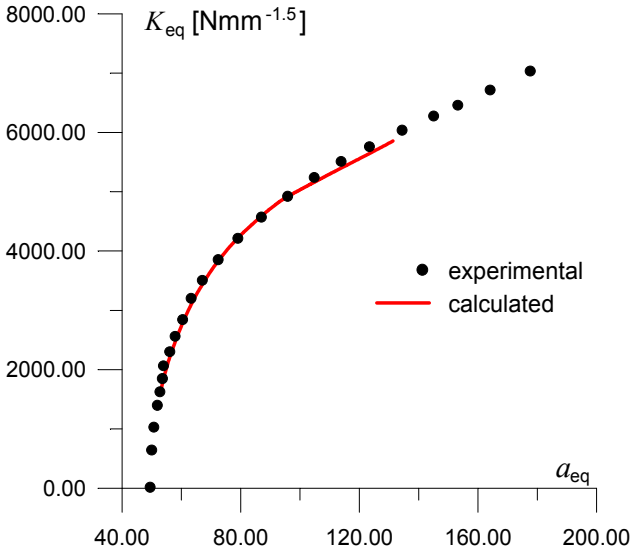

Figure 10: Comparison between calculated and experimental R-curve.

In the following pictures, some results from the FE solution are reported. The WARP3D solution data stored during the calculation has been 'translated' in ANSYS commands with a Fortran routine, in order to use its postprocessor module.

In Fig. 11 the calculated stress distribution in the traction direction (y) for the half-crack length increasing Δa = 25 mm is reported for the whole model and near the crack front. It is possible to appreciate the thorough-the-thickness distribution (remember that symmetry conditions have been imposed). In the following Fig. 12, the crack front shape is pointed out. It results from the elements extinction procedure described above.

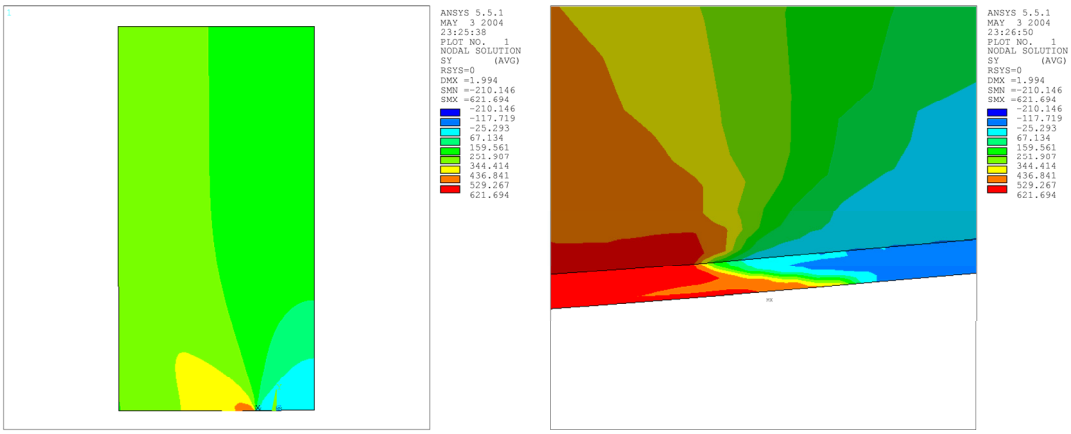

Figure 11: Calculated stress distribution in the traction direction (y) for Δa = 25 mm.

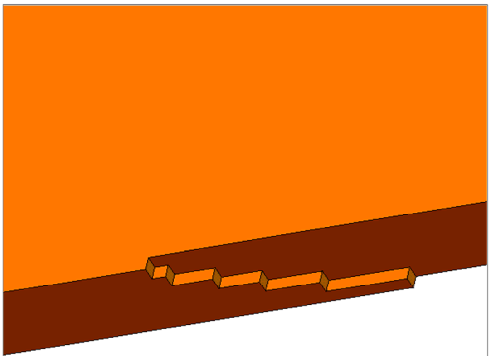

Figure 12: Crack front shape resulting from elements extinction.

In Fig. 13, the enhanced deformed configuration is reported, for Δa = 25 mm. In the first picture, the deformation around the crack tip is pointed out and it is possible to appreciate the strain localization effect. In the last picture, the residual strain near the initial crack length is shown. Considering that the crack surface is stress free, the deformation is totally plastic. Further, the difference between the residual strain on the symmetry surface (the visible surface) and the external one is shown, were for the external surface (near the plane stress condition) the plastic strain is much higher.

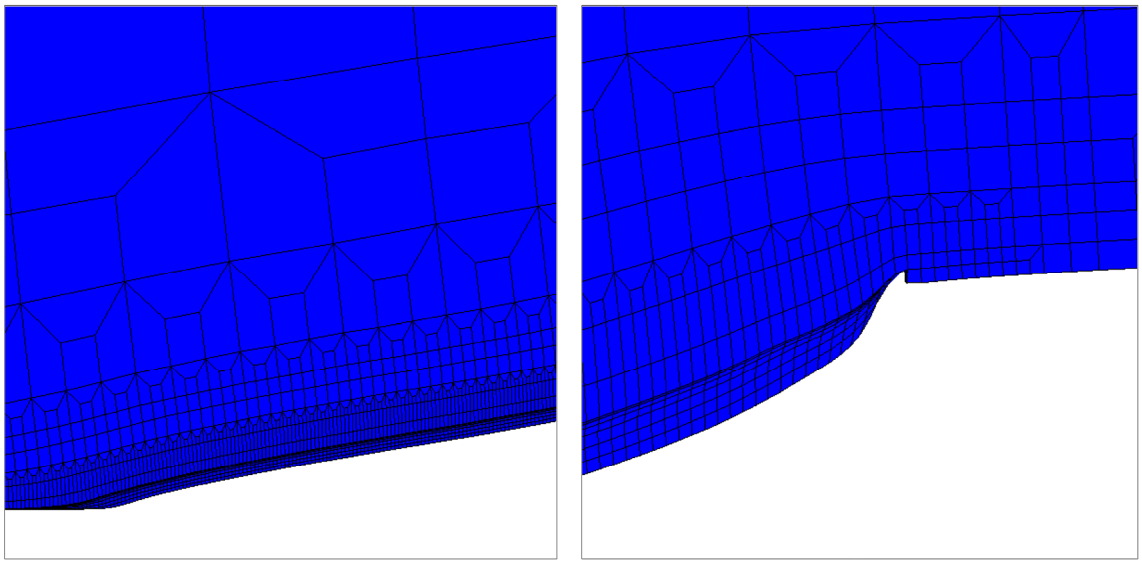

Figure 13: Deformed configuration near the crack tip and the initial crack length.

CONCLUSIONS

A complete procedure for the R-curve calculation has been presented, tested on a MT test specimen simulation reproducing a widely used aeronautical alloy, 2024A-T351, which gives results in a very good agreement with the experimental tests. The algorithm was based on the local form of the Gurson – Tvergaard –Needleman damage model and, differently from the purely phenomenological approach that is usually employed to calculate all the model parameters, it uses a preliminary RVE definition, partially based on microstructural information on the material, to determine most of the continuum-scaled model. In order to enrich the original damage model also the defect size distribution has been considered. Only few parameters are tuned on the basis of an experimental test: they are the nucleation parameters f_N, ε_N, S_N. They are related to the material behaviour, nor to the geometry of the test specimen. For this reason, they can reasonably be determined with a single test result, as is done in the present work, and the same values can be used for different geometries, as the design process requires.

REFERENCES

[1] R. Citarella, G. Cricrì, Advances in Engineering Software, 40 (2009) 363–377.
[2] Office of Aviation Research - Residual Strength Test on Stiffened Panels With Multiple-Site Damage, technical report, Washington, D.C. 20591 [www.tc.faa.gov/its/act141/reportpage.html].
[3] T. V. Pavankumar, M. K. Samal, J. Chattopadhyay, B. K. Dutta, H. S. Kushwaha, E. Roos, M. Seidenfuss, Int. J. of Pressure Vessels and Piping, 82 (2005) 386.
[4] B. Dodd, B. Yilong, Ductile Fracture and Ductility, Academic Press Inc. Ldt., Orlando, Florida, (1987).
[5] M. Li, Int. J. Mech. Science, 42 (2000) 907.
[6] L. Xia, C. Fong Shih, J. W. Hutchinson, J.Mech. Phys. Solids, 43(3) (1995) 389.
[7] L. Xia, C. Fong Shih, J.Mech. Phys. Solids, 43(2) (1995) 233.
[8] L. Xia, C. Fong Shih, J.Mech. Phys., Solids, 43(12) (1995) 1953.
[9] L. Xia, C. Fong Shih, J.Mech. Phys., Solids, 44(4) (1996) 603.
[10] C. Ruggieri, T. L. Panontin, R. H. Jr. Dodds, Int. J. of Fracture, 82 (1996) 67.
[11] L. Malcher, F. M. Andrade Pires, J. M. A. César De Sá, Int. J. of Plasticity, 30-31 (2012) 81.
[12] A. S. Gullerud, K. C. Koppenhoefer, A. Roy, R. H. Jr. Dodds. WARP3D–Release 13.9 - Department of Civil Engineering, University of Illinois at Urbana–Champaign Urbana, Illinois, (2000), ISSN: 0069–4274.
[13] H. L. Schreyer, M. K. Neilsen, Int. J. Numer. Methods Engrg., 39 (10) (1996) 1721.
[14] G. Cricrì, R. Luciano, Simulation Modelling Practice and Theory, Elsevier, 11 (2003) 433.
[15] G. Cricrì, M. Perrella, C. Calì, Composites Part B: Engineering, 45(1) (2013) 1079.
[16] S. D'hers, E. N. Dvorkin, In: Mecánica Computacional, Buenos Aires, Argentina, XXIX (2010) 5189.
[17] M. K. Samal, M. Seidenfuss, E. Roos, B. D. Dutta, H. S. Kushwaha, In: Proceedings of the Institution of Mechanical Engineers, Part C: Journal of Mechanical Engineering Science (2009) 223.
[18] X. Lu, J. P. Bardet, M. Huang, Comput. Methods Appl. Mech. Engrg., 198 (2009) 3702.
[19] G. Hütter, T. Linse, U. Mühlich, M. Kuna, Int. J. of Solids and Structures, 50(5) (2013) 662.
[20] P. J. Sanchez, A. E. Huespe, J. Oliver, Int. J. of Plasticity, 24 (2008) 1008.
[21] J. Faleskog, X. Gao, C. F. Shih, Int. J. of Fracture, 89 (1998) 355.
[22] X. Gao, J. Faleskog, C. F. Shih, Int. J. of Fracture, 89 (1998) 375.
[23] Z. L. Zhang, C. Thaulow, J. Odegard, Engineering Fracture Mechanics, 67 (2000) 155.
[24] P. Negre, D. Steglich, W. Brocks, Engineering Fracture Mechanics, 71 (2004) 2365.
[25] G. Cricrì, E. Garofalo, F. Naddeo, L. Incarnato, J. of Polymer Science Part B: Polymer Physics, 50(3) (2012) 207.
[26] M. Hori, S. Nemat-Nasser, Mech. of Materials, 31 (1999) 667.
[27] J. F. Ganghoffer, L. J. Sluys, R. De Borst, Eur. J. Mech. Solids, 18 (1999) 17.
[28] H. Fei, K. Yazzie, N. Chawla, H. Jiang, J. of Electronic Materials, 41(2) (2012) 177.